



City Research Online

City, University of London Institutional Repository

Citation: Mashoof, S. (1989). The mathematical modelling of concrete constitutive relationships. (Unpublished Doctoral thesis, City University London)

This is the accepted version of the paper.

This version of the publication may differ from the final published version.

Permanent repository link: <https://openaccess.city.ac.uk/id/eprint/7952/>

Link to published version:

Copyright: City Research Online aims to make research outputs of City, University of London available to a wider audience. Copyright and Moral Rights remain with the author(s) and/or copyright holders. URLs from City Research Online may be freely distributed and linked to.

Reuse: Copies of full items can be used for personal research or study, educational, or not-for-profit purposes without prior permission or charge. Provided that the authors, title and full bibliographic details are credited, a hyperlink and/or URL is given for the original metadata page and the content is not changed in any way.

THE MATHEMATICAL MODELLING OF CONCRETE
CONSTITUTIVE RELATIONSHIPS

BY

SAID MASHOOF, B.Sc., M.Eng.

A THESIS SUBMITTED FOR THE DEGREE OF DOCTOR
OF PHILOSOPHY IN THE DEPARTMENT OF CIVIL
ENGINEERING AT CITY UNIVERSITY.

CITY UNIVERSITY

1989

A B S T R A C T

The available experimental evidence demonstrates the extreme nonlinear material behaviour of reinforced concrete structures. These nonlinear effects are attributed to the collective behaviour of the constituent materials in addition to factors such as cracking, crushing, aggregate interlock, creep, shrinkage, bond slip and rate of loading. Analytical methods have been improved in the past two decades as a result of the availability of more powerful computers. It is, therefore, feasible to model these nonlinear features in order to conduct an analysis of the behaviour of reinforced concrete structures. The present research is concerned with some of these nonlinear effects. These include the formulation of a constitutive model for the three-dimensional stress-strain relationships of concrete and the mathematical modelling of cracked and crushed concrete. The proposed models have been implemented into a finite element system for the analysis of reinforced and pre-stressed concrete structures.

Chapter One is a general introduction to structural nonlinearities and the finite element method. The structure of the thesis is also outlined. Chapter Two reviews available theoretical approaches used for the formulation of the concrete behaviour and assesses their relative advantages. The theory of plasticity is discussed in greater depth as it forms the foundation of the work in Chapter Three.

A three-dimensional concrete yield surface is developed in Chapter Three. This yield surface is used in the theory of hardening plasticity to establish the incremental constitutive relationships for concrete. Furthermore, this model is extended to represent the strain-softening effect in concrete. The hardening and softening rule which has been developed is based on experimental results obtained from the literature. The results of the proposed model are compared with these experimental data.

The cracking and crushing of concrete have been studied in Chapter Four. A rough crack model is developed for concrete and crack stress-displacement relationships due to aggregate interlock are formulated. A mathematical model is proposed for the effect of dowel forces in cracked reinforced concrete structures. The effect of bond stress between a steel bar and concrete has been introduced by a tension-stiffening factor and suitable formulations has been proposed. The results from the crack related models have also been compared with experimental data from the literature. Finally, stiffness matrices for cracked plain and reinforced concrete have been developed using a smeared crack approach.

The concrete constitutive model and the crack model developed in Chapters Three and Four have been implemented into a finite element program for the numerical analyses given in Chapter Five. This implementation has been carried out for plane stress and axisymmetric solid stress problems. A reinforced concrete beam and a prestressed concrete reactor vessel have been analysed and the results compared with experimental data. Finally Chapter Six presents the overall conclusions and recommendations for further research.

C O N T E N T S

	PAGE
ABSTRACT	I
CONTENTS	II
ACKNOWLEDGEMENTS	VIII
TABLES	IX
FIGURES	X
NOTATIONS	XVI

CHAPTER ONE - INTRODUCTION

1.1	General	1
1.2	Finite Element Method	2
1.3	Objectives of the Research	5
1.4	Outline of the Research	6

CHAPTER TWO - REVIEW OF LITERATURE

2.1	Introduction	10
2.2	Review of Different Theories for the Concrete Modelling	10
2.2.1	Elasticity Theory	10
2.2.2	Plasticity Theory	12
2.2.3	Plastic-Fracturing Theory	14
2.2.4	Endochronic Theory	16
2.2.5	General Remarks on Different Theories for Concrete Modelling	18
2.3	Concrete Models Based on the Theory of Plasticity	20
2.3.1	A Review of the Available Yield Surfaces	22
2.3.2	Work-Hardening Plasticity Models	30

2.4	Conclusions	37
-----	-------------	----

CHAPTER THREE - THE MATHEMATICAL MODELLING OF THE STRESS-STRAIN RELATIONSHIP OF CONCRETE

3.1	Introduction	54
3.2	Work-Hardening Plasticity for Concrete	55
3.3	The Proposed Triaxial Failure Surface	58
3.3.1	Meridional Definition of the Yield Surface	59
3.3.2	Deviatoric Definition of the Proposed Yield Surface	64
3.4	The Proposed Failure Criterion	66
3.5	Mathematical Definition of the Proposed Hardening and Softening Parameter	68
3.5.1	Determination of the Effective Plastic Strain at Peak Stress	71
3.6	Incremental Stress-Strain Relationship for Concrete	74
3.7	Comparison of the Proposed Constitutive Model with Experimental Results	79
3.8	Conclusions	81

CHAPTER FOUR - FRACTURE MODELLING OF CONCRETE AND EFFECT OF DOWEL ACTION AND TENSION-STIFFENING

4.1	Introduction	118
4.2	The Proposed Fracture Criteria	120
4.3	The Adopted Procedures for Cracking	122
4.4	Crack Idealisation in Concrete	123
4.5	Fracture Treatment in Concrete	124
4.6	The Proposed Models for a Cracked Concrete Element	126
4.6.1	Aggregate Shear Transfer	126

4.6.1.1	The Proposed Cross Crack Stress-Displacement Mathematical Model	128
4.6.1.2	The Crack Stiffness Matrix due to Aggregate Interlock	131
4.6.2	Dowel Action	132
4.6.2.1	The Proposed Dowel Force-Displacement Mathematical Model	133
4.6.2.2	Dowel Stiffness	137
4.6.3	Tension Stiffening	138
4.6.3.1	The Proposed Tension-Stiffening Factor	139
4.7	The Proposed Crack Concrete Stiffness Matrices	142
4.7.1	The Stiffness Matrix of Cracked Plain Concrete	143
4.7.2	The Stiffness Matrix of Cracked Reinforced Concrete	147
4.8	Conclusions	152

CHAPTER FIVE - IMPLEMENTATION OF THE PROPOSED CONCRETE CONSTITUTIVE AND FRACTURE MODELS AND ASSOCIATED ANALYTICAL RESULTS

5.1	Introduction	173
5.2	The Finite Element System Used - LUSAS	174
5.2.1	Nonlinear Analysis in LUSAS	175
5.2.2	LUSAS Element Library	175
5.3	The Finite Element Implementation of the Proposed Concrete Model	178
5.4	Material Modelling of the Fractured Concrete	185
5.4.1	Compressive Failure	185
5.4.2	Tensile Failure and Crack Formation	185
5.4.2.1	Cracked Concrete Properties	186
5.4.2.2	Crack Opening and Closing	188
5.4.2.3	Cracking Verification	189

5.5	Modelling of the Reinforcement Bars	190
5.5.1	The Material Behaviour of Steel Bars	190
5.5.2	Finite Element Idealisation of Steel Bars	191
5.6	Numerical Analysis and Examples	192
5.6.1	Plane Stress Flexural Beam	193
5.6.2	Axisymmetric Solid Stress Reactor Vessel	196
5.7	Conclusions	199

CHAPTER SIX - CONCLUSIONS AND RECOMMENDATIONS

6.1	Conclusions	221
6.2	Recommendations for Further Research	226

APPENDIX A - DESCRIPTION OF THE MATHEMATICAL RELATIONS USED FOR THEORETICAL DEVELOPMENT IN CHAPTER THREE

A.1	Mathematical Definitions	228
-----	--------------------------	-----

APPENDIX B - ELLIPTIC TRACE OF THE YIELD SURFACE

B.1	Derivation of the Elliptic Trace	231
-----	----------------------------------	-----

APPENDIX C - DERIVATION OF ϵ_p IN TERMS OF OCTAHEDRAL STRAINS^p

C.1	Derivation of ϵ_p	236
-----	----------------------------	-----

APPENDIX D - DERIVATIVES OF YIELD SURFACE AND EXPRESSIONS FOR ζ , χ , ψ AND γ

D.1	Derivatives of Yield Surface	238
-----	------------------------------	-----

D.1.1	Calculation of ζ	241
D.1.2	Calculation of χ	243
D.1.3	Calculation of ψ	245
D.2	Calculation of γ	247

APPENDIX E - DERIVATION OF TENSORIAL ELASTIC-PLASTIC MODULAR MATRIX

E.1	Derivation of Tensorial D-Matrix	250
E.1.1	Calculation of $D_{ijmn}^e \frac{\partial f}{\partial \sigma_{mn}} \frac{\partial f^T}{\partial \sigma_{rs}} D_{rskl}^e$	251
E.1.2	Calculation of $\frac{\partial f^T}{\partial \sigma_{mn}} D_{mnr s}^e \frac{\partial f}{\partial \sigma_{rs}}$	253
E.1.3	Calculation of h	254
E.1.4	Elastic-Plastic Modular Matrix	255

APPENDIX F - CLASSIFICATION OF DIFFERENT STRESS ZONES ON THE YIELD SURFACE

F.1	Introduction	257
F.2	Calculation of the Boundaries	257
F.3	Classification of the Stress Zones	259

APPENDIX G - EXPLICIT EXPRESSIONS FOR CRACK STIFFNESS MATRIX

G.1	Crack Stress-Displacement Relationship	264
G.2	Derivation of K_{nn} , K_{nt} , K_{tn} and K_{tt}	265

APPENDIX H - EXPLICIT EXPRESSIONS FOR DOWEL STIFFNESS MATRIX

H.1 Dowel Force-Displacement Relationship 267

H.2 Derivation of H_{nn} , H_{nt} , H_{tt} and H_{tn} 268

APPENDIX I - DERIVATION OF THE SLIP FREE LENGTH AND THE TENSION-STIFFENING FACTOR

I.1 Derivation of the Slip free Length, L_s 269

I.2 Derivation of the Tension Stiffening Factor, α_t 271

REFERENCES 275

A C K N O W L E D G M E N T S

The author wishes to express his gratitude to Dr. L.F. Boswell for his support, guidance and most of all his firendship throughout the course of this reseach.

Sincere thanks are due to Dr. P. Lyons for his valuable help, constructive criticism and providing computer facilities for the use of the LUSAS system in F.E.A. Ltd.

The work has been partially supported by the award of a research studentship from the Science and Engineering Research Council.

Many thanks to my wife for her love, patience, friendship and moral support without which this research would have never been completed.

T A B L E S

PAGE

CHAPTER THREE

Table 3.1	Boundary Conditions Used for the Yield Surface	61
-----------	--	----

CHAPTER FOUR

Table 4.1	A comparison of the contribution of shear stress due to dowel force with shear stress due to the aggregate interlock, experimental results of Walraven et al [87] versus Eq. 4.8	136
-----------	--	-----

CHAPTER FIVE

Table 5.1	Details of the Flexure Beam OB-1 used in the Finite Element Analysis.	194
Table 5.2	Details of the Pressure Vessel PV9 used in the Finite Element Analysis.	197

F I G U R E S

		PAGE
 CHAPTER TWO		
Fig. 2.1	Characteristic uniaxial response of plastic material.	40
Fig. 2.2	Characteristic uniaxial response of fracturing material.	40
Fig. 2.3	Characteristic uniaxial response of plastic-fracturing material.	40
Fig. 2.4	Idealised stress-strain curve for perfectly plastic-brittle-fracture concrete material.	41
Fig. 2.5	Loading surfaces of concrete in biaxial plane.	41
Fig. 2.6	Rankin's maximum principal stress criterion.	42
Fig. 2.7	Representation of Von Mises and Tresca's failure criteria.	42
Fig. 2.8	Three dimensional representation of Von Mises and Tresca's failure surfaces.	43
Fig. 2.9	Representation of the relationship between the principal stresses for the Mohr-Coulomb criterion.	44
Fig. 2.10	Curved Mohr-Coulomb failure envelope for concrete.	44
Fig. 2.11	Representation of Mohr-Coulomb failure criterion.	45
Fig. 2.12	Representation of Drucker-Prager failure criterion.	45
Fig. 2.13	Comparison between Mohr-Coulomb and Drucker-Prager failure criteria.	46
Fig. 2.14	Elliptic trace of the failure surface of Willam and Warnke.	47
Fig. 2.15	Representation of Willam-Warnke three-parameter failure criteria.	47
Fig. 2.16	Comparison of Willam-Warnke three-parameter failure surface with experimental results.	48

Fig. 2.17	Comparison of Willam-Warnke five-parameter failure surface with experimental results.	48
Fig. 2.18	Comparison of Kotsovos's failure surface with experimental results.	49
Fig. 2.19	Comparison of Ottossen's failure surface with experimental results.	49
Fig. 2.20	Comparison of Hsieh et. al. failure criterion with experimental results.	50
Fig. 2.21	Comparison of Hsieh et. al. failure criterion with experimental results.	50
Fig. 2.22	Chen and Schnobrich failure surface: hyperbolic curve fitting to the corners of Mohr-Coulomb failure surface.	51
Fig. 2.23	Representation of Nilsson and Glemberg's generalised ellipsoidal failure surface.	51
Fig. 2.24	Representation of Chen and Chen's failure and initial loading surfaces.	52
Fig. 2.25	Comparison of Chen and Chen's failure envelopes with experimental results.	53

CHAPTER THREE

Fig. 3.1	Schematic representation of a yield surface.	83
Fig. 3.2	Schematic representation of plastic material behaviour.	83
Fig. 3.3	Isotropic hardening expansion of the failure surface.	84
Fig. 3.4	Schematic representation of plastic strain hardening material behaviour.	85
Fig. 3.5	General shape of the proposed failure surface.	86
Fig. 3.6	Deviatoric and hydrostatic sections of the proposed failure surface.	87
Fig. 3.7	Schematic representation of the boundary conditions for the proposed failure surface.	87
Fig. 3.8	Comparison of the proposed compressive and tensile meridians with experimental results.	88

Fig. 3.9	Comparison of the recommended compressive and tensile meridians with experimental results.	93
Fig. 3.10	Geometry of the proposed failure surface at the deviatoric section.	96
Fig. 3.11	Fit of the proposed failure surface to biaxial and triaxial experimental results.	97
Fig. 3.12	Definition of the hardening parameter β .	100
Fig. 3.13	Geometrical relationship between the intermediate failure surface and the ultimate yield surface.	100
Fig. 3.14	Variation of the hardening parameter β , with plastic strain.	101
Fig. 3.15	Variation of β with nondimensional parameter X .	101
Fig. 3.16	Comparison of the hardening model with experimental results.	102
Fig. 3.17	Geometrical definition of the ultimate stress vector from the current stress vector.	103
Fig. 3.18	Representation of normality rule.	104
Fig. 3.19	Schematic representation of plastic flow.	104
Fig. 3.20	Comparison of the performance of the proposed concrete constitutive model with uniaxial and biaxial experimental results.	105
Fig. 3.21	Comparison of the performance of the proposed concrete constitutive model with triaxial compression experimental results.	107
Fig. 3.22	Comparison of the performance of the proposed concrete constitutive model with triaxial extension experimental results.	110
Fig. 3.23	Comparison of volumetric response of the proposed concrete constitutive model with experimental results.	113

CHAPTER FOUR

Fig. 4.1	Representation of different mechanisms for cracked reinforced concrete.	155
Fig. 4.2	Possible crack formations and crack opening and closure.	156

Fig. 4.3	Crack idealisation in the finite element method.	157
Fig. 4.4	Schematic representation of different crack models.	158
Fig. 4.5	Rough crack representaiton.	158
Fig. 4.6	Crushed concrete representation.	159
Fig. 4.7	Three-dimensional representation of a single crack.	159
Fig. 4.8	Two-dimensional representation of a single crack and associated crack stresses and displacements.	159
Fig. 4.9	General shear stress-displacement behaviour of cracked concrete.	160
Fig. 4.10	Comparison of the proposed aggregate interlock model with experimental results.	161
Fig. 4.11	Comparison of the proposed aggregate interlock model with theoretical and experimental results of Leober.	165
Fig. 4.12	Model representation of dowel force-displacement relationship.	166
Fig. 4.13	Non-dimensional dowel force curve.	166
Fig. 4.14	Comparison of the proposed dowel force model with experimental results.	167
Fig. 4.15	Schematic representation of dowel force and stresses on a cracked concrete element.	168
Fig. 4.16	Actual and idealised bond stress distribution for an embedded bar subjected to pull-out force.	169
Fig. 4.17	Proposed tension-stiffening model for different steel ratio.	170
Fig. 4.18	Cracked plain concrete with smeared cracking.	171
Fig. 4.19	Cracked reinforced concrete with smeared cracking.	172

CHAPTER FIVE

Fig. 5.1	Two-dimensional two and three noded bar elements.	200
----------	---	-----

Fig. 5.2	A two-dimensional eight noded plane stress element.	200
Fig. 5.3	A three noded axisymmetric membrane element.	201
Fig. 5.4	An eight noded axisymmetric solid element.	201
Fig. 5.5	Deviatoric representation of transition from elastic zone to plastic zone.	202
Fig. 5.6	Schematic representation of the stresses returned to the yield surface.	203
Fig. 5.7	Crack representation for plane stress elements.	204
Fig. 5.8	Crack representation for axisymmetric solid stress elements.	205
Fig. 5.9	Stress states of the solid concrete between cracks.	206
Fig. 5.10	Crack loading and unloading.	207
Fig. 5.11	Single element tests for crack formation.	208
Fig. 5.12	Schematic representation of the steel elasto-plastic model 62 in LUSAS.	209
Fig. 5.13	Geometry and the general layout of the flexural beam.	210
Fig. 5.14	Finite element mesh of the flexural beam.	211
Fig. 5.15	Comparison between the analytical and experimental mid-span load-deflection curves of the flexural beam.	212
Fig. 5.16	Analytical zones of tensile failure of the flexural beam.	213
Fig. 5.17	Comparison between the analytical and experimental crack pattern of the flexural beam at failure.	214
Fig. 5.18	Details of the section and the prestressing arrangement of the reactor vessel.	215
Fig. 5.19	Finite element mesh of the reactor vessel.	216
Fig. 5.20	Comparison between the analytical and experimental central load-deflection curves of the reactor vessel.	218
Fig. 5.21	Analytical zones of tensile failure of the reactor vessel.	219
Fig. 5.22	Comparison between the analytical and experimental crack pattern of the reactor vessel.	220

APPENDIX A

Fig. A.1 Haigh-Westegard coordinate system. 230

APPENDIX B

Fig. B.1 Geometry of the proposed elliptic yield surface. 235

APPENDIX F

Fig. F.1 Schematic representation of intersection between planes of zero stress and the proposed yield surface. 261

Fig. F.2 Intersection of the plane of $\sigma_1=0$ with the proposed yield surface. 262

Fig. F.3 Two-dimensional representation of the intersection points on the proposed yield surface. 263

APPENDIX I

Fig. I.1 Reinforcement bar crossing a sharp crack and the associated stresses. 274

N O T A T I O N S

In the following, a list of main symbols used in this thesis is presented. All the symbols are also defined in the text as they occur. Occasionally, to be consistent with the literature, a symbol may have been used for different meanings in the text. These are separated by a '/' in the list below.

A	hardening modulus
A_b	cross-sectional area of a steel bar
A_c	area of concrete
A_s	area of steel reinforcement
B	strain matrix
b_1	deviatoric component of yield surface at $\theta = 0^\circ$
b_2	deviatoric component of yield surface at $\theta = 60^\circ$
$b(\theta)$	deviatoric component of yield surface as a function of angle of similarity
C^{cc}	cracked concrete flexibility matrix
C^{ccd}	cracked concrete flexibility matrix with dowel action effect
C^{cr}	crack flexibility matrix
C^{sc}	uncracked concrete flexibility matrix
C_i	slope of i th hardening section of steel stress-effective strain curve
C_{ijkl}	elastic modular tensor
c	cohesion
D	modular matrix
D^{cc}	cracked concrete modular matrix
D^d	dowel modular matrix
D^e, D^{el}	elastic modular matrices

D^{epf}	elasto-plastic-fracturing modular matrix
D^{fr}	fracture modular matrix
D^p, D^{pl}	plastic modular matrices
D^{rd}	reinforced concrete modular matrix
D^{rccd}	cracked reinforced concrete modular matrix including dowel action and tension-stiffening effects
D^s	steel reinforcement modular matrix
D^{sc}	uncracked concrete modular matrix
D_{max}	maximum aggregate particle size
D_{elem}^{cc}	cracked concrete modular matrix in element coordinate system
D_{ijkl}^e	elastic modular tensor
D_{ijkl}^{ep}	elasto-plastic modular tensor
D_{ijkl}^p	plastic modular tensor
D_{elem}^{rccd}	cracked reinforced concrete modular matrix including dowel action and tension-stiffening effects in element coordinate system
D_i^s	steel reinforcement modular matrix of the i th reinforcement system
d	external diameter of pressure vessel
$df, df(\sigma_{ij})$	changes of yield surface
$df(\sigma_{ij}, \beta)$	change of hardening yield surface
de_{ij}	increment of strain deviator tensor
de_{ij}^{fr}	increment of fracture strain deviator tensor
de_{ij}^{pl}	increment of plastic strain deviator tensor
ds_{ij}	increment of stress deviator tensor
ds_{ij}^{fr}	increment of fracture stress deviator tensor
$d\beta$	change of hardening parameter
$d\gamma_{nt}^{cr}$	average crack shear strain increment
$d\delta_n$	crack normal displacement increment

$d\delta_t$	crack shear displacement increment
$d\varepsilon$	strain increment / volumetric strain increment
$d\varepsilon^{cr}$	crack strain increment
$d\varepsilon^e, d\varepsilon^{el}$	elastic strain increments
$d\varepsilon^p, d\varepsilon^{pl}$	plastic strain increments
$d\varepsilon^{sc}$	uncracked concrete strain increment
$d\varepsilon_{ij}$	increment of strain tensor
$d\varepsilon_p$	effective plastic strain increment
$d\varepsilon_{nn}^{cr}, d\varepsilon_{tt}^{cr}, d\varepsilon_{nt}^{cr}$	components of crack strain increment
$d\varepsilon_{ij}^e$	increment of elastic strain tensor
$d\varepsilon_{ij}^p$	increment of plastic strain tensor
$d\varepsilon_{ij}^{pi}$	increment of plastic strain tensor due to isotropic hardening
$d\varepsilon_{ij}^{pk}$	increment of plastic strain tensor due to kinematic hardening
$d\zeta$	plastic intrinsic time
dk	fracture intrinsic time
$d\lambda$	inelastic dilatancy due to shear / plasticity proportionality parameter
$d\lambda'$	hydrostatic compaction due to normal stress
$d\lambda''$	shear compaction due to deviatoric strain
$d\sigma$	stress increment / volumetric stress increment
$d\sigma^{cr}$	crack stress increment
$d\sigma^d$	dowel stress increment
$d\sigma^{fr}$	fracture stress increment
$d\sigma^{sc}$	uncracked concrete stress increment
$d\sigma_{ij}$	increment of stress tensor
$d\sigma_{nn}^{cr}, d\sigma_{tt}^{cr}, d\sigma_{nt}^{cr}$	components of crack stress increment
$d\sigma_{nn}^d, d\sigma_{tt}^d, d\sigma_{nt}^d$	components of dowel stress increment
$d\tau_{nt}^{cr}$	average crack shear strain increment

$d\tau_{nt}^d$	average dowel shear strain increment
E	Young's modulus
E_c	concrete Young's modulus
E_p	slope of the <i>i</i> th hardening section of steel stress-strain curve
E_s	steel Young's modulus
$E_{s,i}$	Young's modulus of <i>i</i> th steel reinforcement system
E_t	tangential Young's modulus
E_{ijkl}	plastic modular tensor
E_s^*	steel Young's modulus with tension-stiffening effect
e_{ij}	strain deviator tensor
F	yield surface / body force / crack flexibility matrix
F_d	dowel force
$F_{d,u}$	ultimate dowel force
$F_{nn}, F_{nt}, F_{tn}, F_{tt}$	components of crack flexibility matrix
f	applied load / yield surface
f_{bc}	biaxial compressive strength of concrete
f_{cu}	uniaxial compressive strength of concrete
f_{tu}	uniaxial tensile strength of concrete
f_y	steel yield stress
$f_n(\delta_n, \delta_t), f_n(\delta_n, \delta_t)$	functions of crack displacements
$f(\sigma), f(\sigma_{ij})$	yield surface functions
$f(\sigma_{ij}, \beta)$	hardening yield surface
$f(\epsilon_{ij}^p)$	a function of plastic strain
$f(\epsilon_p)$	a function of effective plastic strain
G	shear modulus
G_0	initial shear modulus
$g, g(\sigma)$	plastic potential
H	strain hardening rate / dowel stiffness matrix

H_i	dowel stiffness matrix of i th reinforcement system
$H_{nn}, H_{nt}, H_{tn}, H_{tt}$	components of dowel stiffness matrix
H_{ijkl}	elastic compliance tensor
H_w	height of pressure vessel
h	a function of stress
I	unit matrix
I_1, I_2, I_3	invariants of stress
$\bar{I}_1, \bar{I}_2, \bar{I}_3$	normalised invariants of stress
J_1, J_2, J_3	invariants of stress deviator
$\bar{J}_1, \bar{J}_2, \bar{J}_3$	normalised invariants of stress deviator
J_4, J_5	functions of stress
K	stiffness matrix / bulk modulus / crack stiffness matrix
K_0	initial bulk modulus
$K_{nn}, K_{nt}, K_{tn}, K_{tt}$	components of crack stiffness matrix
K_t	tangential stiffness matrix
k	element stiffness matrix
L_i	effective plastic strain of the i th hardening section of steel stress-effective strain curve
L_s	slip free length
l	distance along reinforcement bar measured from crack face
m	number of sub-increments
m_p	equivalent uniaxial plastic strain scaling factor
N	displacement function
$\bar{N}_{p,x}$	X-direction cosine of yield surface at P
$\bar{N}_{p,y}$	Y-direction cosine of yield surface at P
n	ratio of steel Young's modulus to concrete Young's modulus
P	total potential energy

P_e	external potential energy
P_h	equivalent hoop pressure
P_i	internal strain energy
P_l	equivalent pressure from longitudinal prestressing tendons
P_w	equivalent pressure from hoop prestressing wires
p	steel percentage
P_i	steel percentage of i th reinforcement system
R	current stress position vector
R_{max}	ultimate stress position vector
r	strain scaling factor
r_1	deviatoric component of yield surface at $\theta = 0^\circ$
r_2	deviatoric component of yield surface at $\theta = 60^\circ$
$r(\theta)$	deviatoric component of yield surface as a function of angle of similarity
$r(\sigma_a, \theta)$	deviatoric component of yield surface as a function of stress and angle of similarity
s	crack spacing measured normal to the crack direction
s'	crack spacing measured parallel to x-axis
s_{ij}	stress deviator tensor
T	surface traction / transformation matrix
t_h	equivalent thickness of hoop prestressing wires
t_l	equivalent thickness of longitudinal prestressing tendons
t_s	thickness of pressure vessel end-slab
t_w	thickness of pressure vessel wall
U	a function of r_1 , r_2 and θ

U_b	bond force per unit length of reinforcement bar
u	internal element displacement
V	a function of r_1 , r_2 and θ
v	a percentage of yield stress used as tolerance for keeping the stress vector on the yield surface
W	a function of r_1 , r_2 and θ
X	ratio of ϵ_p to $\epsilon_{p,u}$
Z	a function of concrete strength
α	kinematic hardening parameter / shear retention factor / a function of Poisson's ratio, Young's modulus and stress
α_{bc}	a function of concrete strength
α_{ij}	kinematic hardening parameter
α_t	tension-stiffening parameter
α_{tu}	a function of concrete strength
$\alpha(\epsilon^P)$	kinematic hardening function
β	isotropic hardening or softening parameter
β_0	initial value of hardening parameter
β_r	residual value of hardening parameter
β_u	ultimate value of hardening parameter
$\beta(\epsilon^P)$	isotropic hardening function
γ	a derivative of yield surface
$\gamma_{0,u}$	ultimate octahedral shear strain
γ_{cr}	average crack shear strain
γ_{nt}	average crack shear strain
γ_0^e	elastic octahedral shear strain
$\gamma_{0,u}^e$	ultimate elastic octahedral shear strain
γ_0^p	plastic octahedral shear strain
$\gamma_{0,u}^p$	ultimate plastic octahedral shear strain
$(\gamma_{0,u})_{uni}$	ultimate uniaxial octahedral shear strain
Δ	dowel displacement

$-\Delta f$	applied load increment
$\Delta \epsilon$	strain increment
$\Delta \delta$	applied nodal displacement increment
$\Delta \sigma$	stress increment
$\Delta \sigma_{adj}$	stress adjustment increment
$\Delta \sigma_e$	elastic stress increment
$\Delta \sigma_{ep}$	elasto-plastic stress increment
δ	nodal displacement
δ_b	bond slip
δ_{ij}	Kronecker delta
δ_n	crack normal displacement
δ_t	crack shear displacement
ϵ	strain
ϵ^{cr}	crack strain
ϵ^e	elastic strain
ϵ^p	plastic strain / effective plastic strain
ϵ^{sc}	uncracked concrete strain
ϵ^v_p	volumetric effective plastic strain
ϵ_0	octahedral normal strain
$\epsilon_{0,u}$	ultimate octahedral normal strain
$\epsilon_1, \epsilon_2, \epsilon_3$	principal strains
ϵ_i	strain of i th hardening section of steel stress-strain curve
ϵ_{ij}	strain tensor
ϵ_{nn}	strain normal to crack direction
ϵ_p	effective plastic strain
ϵ_{pu}	peak uniaxial compressive strain
$\epsilon_{p,u}$	ultimate effective plastic strain
ϵ_s	steel strain
$\epsilon_{nn}^{cr}, \epsilon_{tt}^{cr}, \epsilon_{nt}^{cr}$	components of crack strain
ϵ_0^e	elastic octahedral normal strain

$\epsilon_{0,u}^e$	ultimate elastic octahedral normal strain
ϵ_p^i	effective plastic strain due to isotropic hardening
ϵ_0^p	plastic octahedral normal strain
$\epsilon_{0,u}^p$	ultimate plastic octahedral normal strain
$\epsilon_1^p, \epsilon_2^p, \epsilon_3^p$	principal plastic strains
$\epsilon_c(L_s)$	concrete strain at the end of slip free length
$\epsilon_c(l)$	concrete strain at distance l from crack face
$\epsilon_s(L_s)$	steel strain at the end of slip free length
$\epsilon_s(l)$	steel strain at distance l from crack face
$(\epsilon_{0,u})_{uni}$	ultimate uniaxial octahedral normal strain
ζ	a derivative of yield surface
η_{ij}	a tensor of stress deviator
θ, θ_1	angle of similarity
θ_{cr}	crack angle
θ_{bc}	angle between reinforcement bar and crack
θ_{bc1}	angle between first set of reinforcement bar and crack
θ_{bc2}	angle between second set of reinforcement bar and crack
$\kappa_1, \kappa_2, \kappa_3$	functions of Poisson's ratio and stress
λ	a function of angle of similarity
μ	a function of Poisson's ratio, Young's modulus and stress
ν	Poisson's ratio
ν_c	concrete Poisson's ratio
ν_s	steel Poisson's ratio
ξ	volumetric component of stress
$\bar{\xi}$	normalised volumetric component of stress

ξ_1	volumetric coordinate of intersection point of yield surface with hydrostatic axis / hydrostatic boundary of elliptic cap
$\bar{\xi}_1$	normalised hydrostatic boundary of elliptic cap
$\bar{\xi}_c$	normalised volumetric coordinate of intersection point of yield surface with hydrostatic axis in compression zone
$\bar{\xi}_{c1}, \bar{\xi}_{c2}$	normalised volumetric coordinates of intersection points of yield surface with planes of zero stress in compression zone
$\bar{\xi}_{c0}$	normalised hydrostatic boundary of compressive meridian of yield surface
$\bar{\xi}_t$	normalised volumetric coordinate of intersection point of yield surface with hydrostatic axis in tension zone
$\bar{\xi}_{t1}, \bar{\xi}_{t2}$	normalised volumetric coordinates of intersection points of yield surface with planes of zero stress in tension zone
$\bar{\xi}_{t0}$	normalised hydrostatic boundary of tensile meridian of yield surface
ξ_u	volumetric coordinate of intersection point of yield surface with hydrostatic axis / volumetric component of ultimate stress
$\bar{\xi}_u$	normalised volumetric component of ultimate stress
ρ	deviatoric component of stress / polar coordinate of yield surface
$\bar{\rho}$	normalised polar coordinate of yield surface
ρ_1, ρ_2	functions of compressive and tensile meridians of yield surface
ρ_c	compressive meridian of yield surface
$\bar{\rho}_c$	normalised compressive meridian of yield surface
$\bar{\rho}_{c0}$	normalised deviatoric boundary of compressive meridian
$\bar{\rho}_{c1}$	normalised deviatoric boundary of compressive part of elliptic cap
ρ_t	tensile meridian of yield surface

\bar{p}_t	normalised tensile meridian of yield surface
\bar{p}_{t0}	normalised deviatoric boundary of tensile meridian
\bar{p}_{t1}	normalised deviatoric boundary of tensile part of elliptic cap
ρ_u	deviatoric component of ultimate yield surface
$\bar{\rho}_u$	normalised deviatoric component of ultimate yield surface
σ	stress
σ^{cr}	crack stress
σ^d	dowel stress
σ^{sc}	uncracked concrete stress
σ_0	octahedral normal stress
$\sigma_{o,u}$	ultimate octahedral normal stress
$\sigma_1, \sigma_2, \sigma_3$	principal stresses
$\bar{\sigma}_1, \bar{\sigma}_2, \bar{\sigma}_3$	normalised principal stresses
σ_a	mean normal stress
σ_{eq}	equivalent uniaxial stress
σ_{ij}	stress tensor
σ_{oct}	octahedral normal stress
σ_s	steel stress
σ'_s	steel stress at the end of slip free length
$\sigma_{nn}^{cr}, \sigma_{tt}^{cr}, \sigma_{nt}^{cr}$	components of crack stress
$\sigma_{nn,0}^{cr}$	limiting value of ultimate crack normal stress
$\sigma_{nn,u}^{cr}$	ultimate crack normal stress
$\sigma_{nt,0}^{cr}$	limiting value of ultimate crack shear stress
$\sigma_{nt,u}^{cr}$	ultimate crack shear stress
$\sigma_{nn}^d, \sigma_{tt}^d, \sigma_{nt}^d$	components of dowel stress
$\sigma_c(L_s)$	concrete stress at the end of slip free length

$\sigma_c(l)$	concrete stress at distance l from crack face
$\sigma_s(L_s)$	steel stress at the end of slip free length
$\sigma_s(l)$	steel stress at distance l from crack face
τ	shear stress
τ_0	octahedral shear stress
τ_{0c}	octahedral shear stress for compressive meridian
τ_{0e}	octahedral shear stress for tensile meridian
$\tau_{u,0}$	ultimate octahedral shear stress
τ_a	mean shear stress
τ_b	bond stress
τ_d	shear stress due to dowel action
τ_i	shear stress due to dowel action and aggregate interlock combined
τ_{oct}	octahedral shear stress
τ_u	ultimate shear stress
$\tau(\epsilon_p^i)$	isotropic hardening function
ϕ	fracture loading surface
ϕ_{ijkl}	plastic modular tensor
ϕ	bar diameter
χ	a derivative of yield surface
ψ	a derivative of yield surface / residual force
ω	hardening parameter / a function of stress
ω_i	angle of ith reinforcement system

CHAPTER ONE

INTRODUCTION

1.1 General

The nature and behaviour of reinforced concrete is extremely complex and except in limited circumstances its behaviour is nonlinear. Current design methods are usually dictated by international codes of practice which seek to simplify the behaviour of reinforced concrete structures to provide practical methods for design.

Certain types of structure such as nuclear pressure vessels, offshore structures, large span bridges and earthquake resistant structures, however, require special design considerations. The nonlinear characteristics of these structures is required to be known in order to determine their ultimate load behaviour.

Modern computational techniques, in particular the finite element method, offer general and powerful analytical techniques in which important parameters affecting the nonlinear behaviour of reinforced concrete structures can be conveniently and systematically varied. These techniques provide verification of the design codes. The finite element method can trace the entire history of structural behaviour up to the failure limit and may be used for studying constitutive assumptions and their effects on the overall structural performance rather than the development of a new design method.

In general, the design procedure is based upon good practice to determine an initial structural configuration. Once this configuration is known, a refined finite element analysis may be carried out to determine internal forces and moments which enables the designer to check the concrete dimensions and steel requirements. An ideal analytical procedure should accommodate both material and geometrical nonlinearities. The main obstacles impeding the development of an implicit analytical approach are an adequate description of the mechanical properties of concrete and steel and their interaction. These obstacles give rise to associated computational complexities. Research continues to remove both these obstacles.

1.2 Finite Element Method

The finite element method is a solution technique for structural analysis in which a domain of arbitrary shape and boundary condition is simulated by an assemblage of finite elements interconnected at a finite number of nodes for which a solution is available within the laws of continuum mechanics. The technique relies on minimising the total potential energy to achieve an approximate solution.

The total potential energy P , due to an arbitrary nodal displacement δ , is the summation of the internal strain energy P_i , and potential energy of the external loads P_e . To achieve equilibrium, the total potential energy P , must be zero.

Thus

$$P = P_i - P_e = 0 \quad (1.1)$$

where $P_i = \int_v \epsilon^T \sigma \, dv \quad (1.2)$

$$P_e = \int_v \epsilon^T F \, dv + \int_s \delta^T T \, ds \quad (1.3)$$

in which ϵ is the strain tensor, σ stress tensor, F is the vector of body force and T is the vector of surface traction.

The internal displacement u , at any point within the element can be expressed in terms of nodal displacement δ , by means of the displacement function N , as

$$u = N \delta \quad (1.4)$$

Differentiation of Eq. 1.4 establishes the relationship between the strain ϵ , and the nodal displacement δ , as

$$\epsilon = B \delta \quad (1.5)$$

in which B is the strain matrix. The element stress tensor σ , is related to the strain tensor ϵ , by means of modular matrix D

$$\sigma = D \epsilon \quad (1.6)$$

Combining Eq's. 1.1 to 1.6, leads to

$$\delta^T \left(\int_V B^T D B dv \right) - \delta^T \left(\int_V F dv + \int_S T ds \right) = 0 \quad (1.7)$$

dividing Eq. 1.7 by δ^T produces the general stiffness relationships

$$f = K \delta \quad (1.8)$$

where

$$f = \int_V F dv + \int_S T ds$$

= total applied loads, and

$$K = \int_V B^T D B dv$$

= stiffness matrix

For known applied nodal loads f , the nodal displacements δ , are calculated from Eq. 1.8 which can be used in Eq's. 1.5 and 1.6 to calculate the element strains and stresses. This procedure is termed the 'Displacement Method'.

In nonlinear finite element analysis the total applied load f , is added in increments of Δf and for each load step the increments of nodal displacement $\Delta \delta$, are related to the load increments by the tangent stiffness matrix K_t , as

$$\Delta f = K_t \Delta \delta \quad (1.9)$$

In addition, for every load step the residual forces ψ , are calculated as

$$\psi = \int_V B^T \sigma dv - f \quad (1.10)$$

for every incorrect stress and displacement non-zero residual forces are obtained. The residual forces ψ , are applied as additional nodal forces to bring the forces associated the assumed displacement into nodal equilibrium. For each load increment an iterative procedure such as Newton-Raphson must be performed until negligible residual forces are obtained thus satisfying equilibrium.

1.3 Objectives of the Research

Although the fundamentals of the finite element method of structural analysis are well established, the application of the method to investigate the nonlinear behaviour of structures is a current subject of research activity. This thesis concentrates on the nonlinear material behaviour of concrete. This nonlinearity is observed in all reinforced concrete structures and it is essential to consider its effect for an exact analysis.

Nonlinear material behaviour can be separated into time-independent effect and time-dependent effects such as creep and shrinkage. This thesis is concerned with time-independent nonlinear effects, namely the stress-strain relationships and cracking of reinforced concrete. Concrete properties vary widely and depend upon such factors as design mix, curing cycle and the rate of loading. Concrete is generally in a biaxial or triaxial state of stress unlike the steel reinforcement which is usually subjected to an uniaxial state of stress within structural elements prior to cracking. During the formation of sharp cracks the steel reinforcement

can be subjected to kinking and shear as a result of the relative movements of crack surfaces. A major part of the research reported in this thesis is, therefore, related to establishing general constitutive relations for concrete subjected to multiaxial loading.

Although concrete is strong in compression, reinforced concrete structures which are subjected to tensile stresses can crack at relatively low load. Cracks can propagate at increasing load which then affect local stresses and displacements as well as the overall structural behaviour. Consequently a further part of this investigation is concerned with modelling the behaviour of cracked reinforced concrete. This requires a mathematical definition of aggregate interlock, dowel action of steel reinforcements and tension-stiffening effects due to bar-to-concrete bond. It is also essential to adopt suitable procedures to represent crack propagation so that a numerically stable solution is achieved.

1.4 Outline of the Research

The work reported in this thesis is concerned with the establishment of constitutive equations to represent the stress-strain behaviour of concrete. A mathematical description of the behaviour of cracked reinforced concrete is also given. The theoretical work has been implemented within the finite element method to enable the analysis of concrete structures to be undertaken. The chapters which follow the Introduction are now briefly described

- i) Chapter Two represents a review and summary of the different constitutive models for concrete. The subject of constitutive laws governing the behaviour of the concrete material is classified into four groups: elastic, plastic, plastic-fracturing and endochronic. These models are described and their merits are assessed. Throughout this chapter the performance of each model is reviewed.
- ii) The concept of the theory of hardening plasticity is used to describe the constitutive equations of concrete subjected to a multi-axial state of stress in Chapter Three. Firstly, a triaxial failure surface is developed for which the shape can be defined by the appropriate strength properties of concrete. Secondly, the incremental stress-strain relationships of concrete are obtained using a flow rule and the consistency condition for plastic flow. Finally, an isotropic hardening law is used to model the nonlinearity in the pre-ultimate region. The uniform expansion of the loading surface is controlled by the hardening parameter β , which is mathematically defined as a function of non-recoverable strains. Furthermore, the proposed model is extended to define the post-ultimate behaviour of concrete. This is achieved by a progressively collapsing failure surface after the ultimate strength is reached. The collapse of the failure surface is monitored by the hardening parameter β , which has a value less than unity in the strain-softening region and progressively decreases with non-recoverable strains. The results are compared with published work.

iii) Chapter Four considers the subject of cracking in concrete and the effects of steel reinforcement on the behaviour of cracked concrete. A crack theory is developed by considering aggregate interlock between crack surfaces of concrete. The mathematical model for the interlock shear transfer is obtained empirically. The effects of dowel forces due to bars crossing a crack and the tension-stiffening which results from bar-to-concrete bond are included in the theory. Stiffness matrices which represent the effects of aggregate interlock, dowel action and tension-stiffening are developed for cracked plain and cracked reinforced concrete elements.

iv) Chapter Five deals with the application of the constitutive laws developed in Chapter Three and the cracking models developed in Chapter Four using the finite element method for the analysis of reinforced concrete structures. The proposed material model is used for the analysis of plane stress and axisymmetric problems. The proposed material model has been incorporated into a general purpose nonlinear finite element system called LUSAS.

The crack mechanism in reinforced concrete structures has been dealt with using the 'smeared' crack theory rather than the 'discrete' crack approach. That is, the effect of cracking is considered by modifying the constitutive relations for uncracked concrete and an

average effect of the cracks being introduced into the theory. This has been achieved by using the proposed crack theory developed in Chapter Four.

The steel reinforcement has been modelled as isolated members interconnected to the concrete elements in the numerical examples which are presented in Chapter Five. The reinforcement was assumed to be rigidly bonded to the concrete at the nodal points. It is an approximate method which ignores the bond slip between steel and concrete. Analytical results obtained from the proposed concrete model are compared with published experimental data.

- v) In Chapter Six the general conclusions from this research are considered together with recommendations for further research.

C H A P T E R T W O

REVIEW OF LITERATURE

2.1 Introduction

Many different constitutive models have been developed in the last two decades to define the stress-strain relationship of concrete subjected to different states of stress. Both empirical and theoretical approaches have been adopted to represent the complex stress-strain behaviour of concrete. The theories which have been developed can be classified into the following groups: elastic, plastic, plastic-fracturing and an endochronic theory of plasticity. These groups include a wide range of concrete models which vary in simplicity, accuracy and applicability. At the present time, however, research is needed to describe special features such as the behaviour of high strength concrete and microcracking. In addition, new experimental evidence is needed to understand the general behaviour of concrete subjected to dynamic and non-proportional loading.

2.2 Review of Different Theories for the Concrete Modelling

2.2.1 Elasticity Theory

Elastic and nonlinear elastic models, in general, obey the Hookean formulation either in the form of incremental or total stress-strain relationships given as

$$\sigma = D \epsilon \quad (2.1)$$

or $d\sigma = D d\epsilon \quad (2.2)$

The constitutive matrix relating stresses to strains is obtained by approximate or empirical techniques which avoid the use of more theoretical concepts such as yield surface, flow rule or intrinsic time which are commonly used in the plasticity and endochronic theories. As a result, the variable material stiffness matrix is obtained without resorting to complex equations.

The majority of elasticity models, however, are primarily limited to concrete material subjected to monotonic or proportional loading only. There are two types of nonlinear elastic formulation in this category known as the 'secant' and the 'tangential' relations. The 'secant' or 'total' formulation relates the current stress state to the current strain state and assumes that there is a unique relationship between them at any loading level. The disadvantage of this type of modelling is that it is 'path-dependent' which is not the case for a granular type material such as concrete. These models may be applied during monotonic or proportional loading.

The incremental formulation also known as 'hypo-elastic' assumes that the increments of stress and strain are linearly related by a modular matrix which is dependent on the current state of stress or strain or both. This type of formulation is 'path-dependent' and provides a more realistic method for predicting the concrete behaviour under general loading conditions.

2.2.2 Plasticity Theory

Experimental evidence show that the nonlinear deformation of concrete is inelastic and by implication only a portion of strain would be recovered upon unloading. The recoverable portion of strain is elastic while the irrecoverable portion can be represented by the plasticity theory. At each stage of loading, therefore, the deformation is the summation of elastic and inelastic (or plastic) strains, Fig. 2.1, and may be written as

$$\epsilon = \epsilon^e + \epsilon^p \quad (2.3)$$

or
$$d\epsilon = d\epsilon^e + d\epsilon^p \quad (2.4)$$

The elastic portion of strain is defined by the Hookean law. The plastic portion of strain is defined by a flow rule as follows

$$d\epsilon^p = d\lambda \frac{\partial g}{\partial \sigma} \quad (2.5)$$

where g = the plastic potential, and

$d\lambda$ = proportionality parameter

According to the plasticity theory the material flows plastically when a certain limiting stress state is reached. This limiting stress is defined by a surface in the stress space known as the yield surface, $f(\sigma)$. Plastic flow occurs when

$$f(\sigma) = 0 \quad (2.6)$$

The stresses must remain unchanged during the plastic flow which requires the stress vector to remain on the yield surface. This requirement is known as the 'consistency condition' and may be expressed as follows

$$df = \frac{\partial f}{\partial \sigma} d\sigma = 0 \quad (2.7)$$

Combining these assumptions, the elasto-plastic stress-strain relationship is given as

$$d\sigma = D^{ep} d\epsilon \quad (2.8)$$

where $D^{ep} = D^e - D^p$
 D^e = elastic modular matrix,
 D^p = plastic modular matrix

$$= \frac{D^e \frac{\partial g}{\partial \sigma} \frac{\partial f}{\partial \sigma} D^e}{A + \frac{\partial f}{\partial \sigma} D^e \frac{\partial g}{\partial \sigma}}, \text{ and}$$

A = hardening modulus

There are two types of plasticity model, elastic perfectly plastic and elastic strain-hardening plastic. Most plastic models use the concept of 'associated plasticity' where it is assumed that the plastic potential g , has the same shape, size and configuration as the yield surface f . It is only required, therefore, to define the yield surface for an associated plasticity model. The accuracy of a plasticity model depends upon how accurate the yield surface can

represent the material strength.

2.2.3 Plastic-Fracturing Theory

The concept of 'progressively fracturing' solids was developed by Dougill [1] for heterogeneous materials such as rock and concrete which contains many fractures. It was suggested that cracks propagate at different rate from many fracture sites implying a general process which causes a reduction in the stiffness of the material. It was proposed, therefore, to treat stable progressive fracture in heterogeneous solids within the theory of continuum mechanics. Dougill's theory assumes that fracturing causes an irreversible degradation of elastic moduli and leads to a decline of stress at increasing strain and the deformation is reversible upon complete unloading, Fig 2.2.

The theory of plasticity considers nonlinearity effects as a dissipation of energy due to dislocation and sliding of material particles while the fracturing theory associates nonlinearity to progressive fracturing which results in the loss of stiffness. Concrete exhibits energy dissipation, however, by both fracturing and yielding. The former prevails at low hydrostatic pressure and the latter dominates the material behaviour at high hydrostatic pressure.

Bazant and Kim [2] developed a technique by combining the hardening plasticity and the progressively fracturing theories to propose a theory of 'plastic-fracturing' for concrete, Fig 2.3. Increments of stress for the plastic-

fracturing theory are combination of stresses . due to the elastic and the plastic deformation and the decrement of fracture stresses. The deviatoric and hydrostatic stress increments are given as

$$ds_{ij} = 2G(de_{ij} - de_{ij}^{pl}) - ds_{ij}^{fr} \quad (2.9)$$

$$d\sigma = 3K(d\epsilon - d\epsilon^{pl}) - d\sigma^{fr} \quad (2.10)$$

where

$$\sigma = \frac{\sigma_{kk}}{3} = \text{mean normal stress,}$$

$$\epsilon = \frac{\epsilon_{kk}}{3} = \text{mean normal strain,}$$

$$s_{ij} = \sigma_{ij} - \frac{1}{3} \delta_{ij} \sigma_{kk}$$

= deviator of stress,

$$e_{ij} = \epsilon_{ij} - \frac{1}{3} \delta_{ij} \epsilon_{kk}$$

= deviator of strain,

$$\delta_{ij} = \text{Kronecker delta,}$$

$$K = \text{bulk modulus,}$$

$$G = \text{shear modulus, and}$$

$$i, j = 1, 2 \text{ or } 3$$

indices fr and pl indicate plastic and fracture respectively.

Plastic strains are obtained from the flow rule and a yield surface. The decrement of fracture stresses is calculated by a flow rule in conjunction with a surface analagous to the yield surface . This yield surface is defined in the space of strains and is called the 'fracture surface'.

By combining Eq's 2.9 and 2.10 the incremental stress-strain relationship of concrete is obtained as

$$d\sigma = D^{epf} d\varepsilon \quad (2.11)$$

where $D^{epf} = D^{el} - D^{pl} - D^{fr}$
 D^{el} = elastic modular matrix,
 D^{pl} = plastic modular matrix, and
 D^{fr} = fracture modular matrix

2.2.4 Endochronic Theory

The endochronic theory is a novel form of constitutive relation for time-independent as well as time-dependent inelastic materials. The major difference between this theory and those previously described is that the incremental stress-strain relationship is nonlinear. This theory is a special case of viscoplasticity in which the plastic rate coefficient depends on stress and strain as well as strain rate [3]. The theory was originally proposed by Schaperg [4], and Valanis [5] showed the capabilities of this theory to model the loading and unloading irreversibility.

The endochronic theory is characterised by the use of a non-decreasing scalar variable known as 'intrinsic time'. The increments of this variable depend on strain increments and are assumed to control the magnitude of the inelastic strain increments. The first application of this theory to concrete was proposed by Bazant and Bhat [6] which was later improved to overcome the problems concerning its uniqueness,

stability, continuity and energy dissipation during a load cycle [7,8]. The most recent endochronic theory for concrete has been suggested by Bazant and Shieh [8] in which the incremental stress-strain relationship is written in the form of deviatoric and hydrostatic relations and given as follows

$$de_{ij} = \frac{ds_{ij}}{2G} + de_{ij}^{pl} + de_{ij}^{fr} \quad (2.12)$$

$$d\epsilon = \frac{d\sigma}{3K} + d\lambda + d\lambda' + d\lambda'' \quad (2.13)$$

where $\sigma = \frac{\sigma_{kk}}{3}$ = mean normal stress,
 $\epsilon = \frac{\epsilon_{kk}}{3}$ = mean normal strain,

$$s_{ij} = \sigma_{ij} - \frac{1}{3} \delta_{ij} \sigma_{kk}$$

= deviator of stress,

$$e_{ij} = \epsilon_{ij} - \frac{1}{3} \delta_{ij} \epsilon_{kk}$$

= deviator of strain,

δ_{ij} = Kronecker delta,

K = bulk modulus,

G = shear modulus,

$$de_{ij}^{pl} = \frac{1}{2G} \frac{\partial \psi}{\partial e_{ij}} d\zeta = \text{increment of plastic deviatoric strain,}$$

$$de_{ij}^{fr} = \frac{\partial \phi}{\partial e_{ij}} dk = \text{increment of fracture deviatoric strain,}$$

Ψ = plastic loading function,
 Φ = fracture loading function,
 $d\zeta$ = plastic intrinsic time,
 $d\kappa$ = fracture intrinsic time,
 $d\lambda$ = inelastic dilatancy parameter due to shear,
 $d\lambda'$ = hydrostatic compaction parameter due to
compressive mean normal stress,
 $d\lambda''$ = shear compaction parameter due to deviator
of strain, and
 $i, j = 1, 2 \text{ or } 3$

2.2.5 General Remarks on Different Theories for Concrete Modelling

In the previous sections different theories for modelling the stress-strain relationships of concrete were described. The stress-strain laws are in general classified into two groups: The 'total' stress-strain formulations and the 'incremental' stress-strain formulations.

The first group comes under the category of nonlinear elasticity theory (section 2.2.1). The main advantage of this type of formulation is the numerical simplicity in its application. The principal disadvantage is its range of application which is limited to monotonic and proportional loading regim because of inherent stress path-independent characteristics.

The second group includes hypo-elasticity, plasticity, plastic-fracturing, and endochronic theory. All these theories produce constitutive relations which are path-

dependent and offer a more realistic approach for the representation of concrete nonlinear behaviour without restriction on the range of application.

The application of the hypo-elasticity theory is limited by the number of parameters required to adequately model the concrete behaviour. This limitation has led to the use of linear elastic incremental stress-strain relationships with the tangential elastic moduli. Furthermore, uniqueness is not always satisfied in the hypo-elasticity theory when an arbitrary loading criterion is introduced to distinguish between loading and unloading. This may lead to a discontinuity at or near neutral loading.

Currently, the theory of plasticity is the basis for the most reliable type of constitutive laws for practical application. The use of the normality rule and the convexity of the yield surface guarantee a stable material law in accordance with Drucker's postulate which assures the uniqueness of the solution. The main shortcoming of the plasticity theory is, however, its inadequate capability to treat strain-softening in concrete.

The plastic-fracturing theory offers an attractive alternative to the theory of plasticity accounting for strain-softening and unloading stiffness degradation. The main difficulty in applying the plastic-fracturing theory is the large number of material parameters which have to be determined as well as the formulation of an unsymmetrical modular matrix which causes analytical difficulties .

The endochronic theory offers a very powerful method for predicting concrete behaviour but this theory is complex and requires many material dependent constants. In addition, because of its nonlinear incremental stress-strain relationship it requires very small load increments and a more complicated computational technique compared with the other incremental theories.

In the following sections the available concrete models which are based upon the theory of plasticity are reviewed.

2.3 Concrete Models Based on the Theory of Plasticity

In section 2.2.2 the principles of the theory of plasticity were described. It was mentioned that there are two types of plasticity models the 'elastic-perfectly plastic' models or the 'work-hardening plastic' model.

The elastic-perfectly plastic model consider concrete to be a ductile material and assumes it behaves elastically until the stresses reach a yield surface and the concrete can flow plastically on that surface before fracture takes place. The initial behaviour is modelled by either linear or nonlinear elasticity models (section 2.2.1). The plastic flow is represented by a flow rule. The increments of stress are represented by an elasto-plastic stiffness matrix (Eq. 2.8) in which the hardening modulus A , is zero. It is assumed that crushed concrete loses its resistance against further deformation and the current stresses reduce to zero, Fig 2.4.

The observation of experimental results suggests that the nonlinear behaviour of concrete begins at about 30-60 percent of the ultimate strength. This type of behaviour is characterised by work-hardening plasticity and is a generalisation of the perfectly plastic model. In this approach, the limiting elastic behaviour is modelled by an 'initial yield surface'. Any state of stress within this surface implies elastic material behaviour. A subsequent surface called the 'loading surface' is developed which replaces the initial surface when the material is stressed beyond the elastic limit surface. Any state of stress within this new surface is treated elastically. Further plastic deformation will result if loading is continued beyond this surface and a new loading surface will be developed. The process continues until an ultimate failure surface is reached when failure or partial failure occurs by crushing or cracking, Fig. 2.5.

The success of both perfect and work-hardening plasticity models relies on how accurately the failure surface represent the ultimate strength of concrete. The predominant nonlinear behaviour of concrete, from very low stress level, suggests that a work-hardening plasticity model provides a more realistic representation of the overall concrete behaviour. In the following sections a review of the available yield surfaces is presented and some work-hardening plasticity concrete models are critically reviewed.

2.3.1 A Review of the Available Yield Surfaces

The development of yield surfaces has been the subject of research since the mid-nineteenth century. Many failure surfaces have been proposed for use in plasticity models in general or merely to set a criterion for failure of the material. These surfaces vary in their degree of complexity and their application is limited to certain type of material.

Rankin [9] proposed a failure model known as the 'tension-cut-off'. The model has three planes perpendicular to the stresses σ_1 , σ_2 , and σ_3 , Fig 2.6. This surface is still used to distinguish between compressive and tensile type of failure. Later, Tresca [10] stated that the yielding begins when the maximum shear stress reaches a certain value. Von Mises [11] used the octahedral shear stress instead of the maximum shear stress as the critical value. The effect of hydrostatic pressure was not considered by Tresca and Von Mises. Therefore, the failure surface must represent a cylindrical surface with hexagonal or circular deviatoric sections, respectively, Fig's. 2.7 and 2.8.

Mohr [12] suggested a failure surface which is governed by the limiting shear stress τ . The simplest form of Mohr envelop is the straight line envelop of Coulomb [13], given as

$$\tau = c - \sigma \tan\phi \quad (2.14)$$

where c = cohesion, and
 ϕ = angle of friction

According to the Mohr-Coulomb theory, the critical failure of material will occur for all states of stress for which the largest of the Mohr's circles is just tangent to the envelop, Fig. 2.9. Experimental evidence of Richart et al [14], however, shows that a concrete failure envelop cannot be represented by straight lines. A more realistic shape would be a curved envelop for all the circles corresponding to the various states of stress representing failure, Fig. 2.10. A hydrostatic and deviatoric representation of the Mohr-Coulomb criterion is given in Fig. 2.11.

An approximation to the Mohr-Coulomb law was presented by Drucker and Prager [15]. For this approximation a smooth cross-section was obtained by simple modification of the Von Mises yield criterion. The resulting equation is as follows

$$f(I_1, J_2) = \alpha I_1 + \sqrt{J_2} - k \quad (2.15)$$

where I_1 = first stress invariant,
 J_2 = second stress deviator invariant, and
 α and k = constants

This model, which has been used in soil mechanics, has the advantage of using two stress invariants unlike the previous models, Fig. 2.12. A comparison between the surface of Drucker and Prager and of Mohr-Coulomb is given in Fig. 2.13. The idea of using two stress invariants was later adopted by Bresler and Pister [16]. They proposed their formulation in

terms of the octahedral stresses as follows

$$\frac{\tau_{\text{oct}}}{f_c} = a - b \frac{\sigma_{\text{oct}}}{f_c} + c \left(\frac{\sigma_{\text{oct}}}{f_c} \right)^2 \quad (2.16)$$

where σ_{oct} = octahedral normal stress,
 τ_{oct} = octahedral shear stress,
 f_c = uniaxial compressive strength
of concrete, and
a, b, and c = material constants

This criterion has shown good agreement with the experimental results of McHenry and Karni [17] and has been successfully used for the biaxial failure modelling of concrete [18]. Its accuracy, however, is not so good in the case of general triaxial loading [19]. The main reason may be attributed to the exclusion of the third stress invariant in this formulation.

Willam and Warnke [20] suggested a 'three parameter' failure surface for concrete in the tension and low compression regions. The surface has straight meridians and a non-circular cross-section. The failure surface is constructed by fitting an elliptic curve to the tensile meridian r_1 at $\theta = 0^\circ$, and the compressive meridian r_2 at $\theta = 60^\circ$, where θ is the angle of similarity, Fig. 2.14. The general elliptic trace is expressed in polar coordinates as

$$r(\theta) = \frac{U + V}{W} \quad (2.17)$$

where

$$U = 2r_2 (r_2^2 - r_1^2) \cos \theta$$

$$V = r_2 (2r_1 - r_2) [4(r_2^2 - r_1^2) \cos \theta + 5r_1^2 - 4r_1 r_2]^{1/2}$$

$$W = 4(r_2^2 - r_1^2) \cos^2 \theta + (2r_1 - r_2)$$

The terms r_1 and r_2 are obtained as functions of uniaxial and biaxial compressive strength and uniaxial tensile strength of concrete, Fig. 2.15. The general criterion for failure is written in terms of the average stresses σ_a and τ_a , and the angle of similarity θ , and given as

$$f(\sigma_a, \tau_a, \theta) = \frac{1}{Z} \frac{\sigma_a}{f_c} + \frac{1}{r(\theta)} \frac{\tau_a}{f_c} - 1 \quad (2.18)$$

where

- σ_a = average normal stress,
- τ_a = average shear stress,
- $r(\theta)$ = meridian of failure surface (Eq. 2.17)
- Z = a function of concrete strength, and
- f_c = uniaxial compressive strength of concrete

Fig. 2.16 shows the fit of this surface to triaxial strength data [21]. A good fit is shown in the low compression region. The model, however, deviates from the experimental values at high compressive stress. Willam and Warnke [20] proposed an improved formulation to include the high compressive region by replacing the straight meridians r_1 and r_2 , by second order parabolic curves expressed in terms of the average hydrostatic pressure σ_a , given by

$$r_1(\sigma_a) = a_0 + a_1 \frac{\sigma_a}{f_c} + a_2 \left(\frac{\sigma_a}{f_c} \right)^2 \quad (2.19)$$

$$r_2(\sigma_a) = b_0 + b_1 \frac{\sigma_a}{f_c} + b_2 \left(\frac{\sigma_a}{f_c} \right)^2 \quad (2.20)$$

where $a_0, a_1, a_2, b_0, b_1,$ and $b_2 =$ material parameters

Fig. 2.17 shows the agreement between the results obtained from the improved version and the triaxial strength data of Launay and Gachon [21]. The failure surface is known as the 'five-parameter' model and the failure criterion is given by

$$f(\sigma_a, \tau_a, \theta) = \frac{1}{r(\sigma_a, \theta)} \frac{\tau_a}{f_c} - 1 \quad (2.21)$$

where $r(\sigma_a, \theta)$ is given by Eq. 2.17 while r_1 and r_2 are obtained from Eq's. 2.19 and 2.20.

The general elliptic yield surface of Willam and Warnke [20] was later used by Kotsovos [22] to obtain a failure surface. He used the experimental results from the Concrete Material Research Group at the Imperial College to define the meridians of the failure surface in terms of the octahedral normal and shear stresses σ_0 and τ_0 , in the following forms

$$\frac{\tau_{0c}}{f_c} = 0.944 \left(\frac{\sigma_0}{f_c} + 0.05 \right)^{0.724} \quad \text{for } \theta = 60^\circ \quad (2.22)$$

$$\frac{\tau_{0e}}{f_c} = 0.633 \left(\frac{\sigma_0}{f_c} + 0.05 \right)^{0.857} \quad \text{for } \theta = 0^\circ \quad (2.23)$$

Fig. 2.18 shows the fit of Kotsovos's model to triaxial failure test results.

Ottosen [25] proposed a failure criterion which involves the three stress invariants I_1 , J_2 and J_3 as follows

$$f(I_1, J_2, \cos 3\theta) = A \frac{J_2}{f_c^2} + \lambda \frac{\sqrt{J_2}}{f_c} + B \frac{I_1}{f_c} - 1 \quad (2.24)$$

where A, B = shape parameters,
 λ = a function of the angle of similarity θ , and
 f_c = uniaxial compressive strength of concrete

Parameter A and B determine the curved shape meridians and λ is used to define the trace of the failure surface in the deviatoric section. The function of λ was proposed in the following form

$$\lambda = K_1 \cos \left[\frac{1}{3} \cos^{-1} (K_2 \cos 3\theta) \right] \quad \text{for } \cos 3\theta \geq 0^\circ \quad (2.25)$$

$$\lambda = K_1 \cos \left[\frac{\pi}{3} - \frac{1}{3} \cos^{-1} (-K_2 \cos 3\theta) \right] \quad \text{for } \cos 3\theta > 60^\circ \quad (2.26)$$

The constant parameters A , B , K_1 and K_2 were obtained from biaxial and triaxial failure test results. Fig. 2.19 shows a comparison of Ottosen's failure surface with experimental results.

Hsieh et al [28] suggested the following yield criterion involving the stress invariants I_1 and J_2 , and the maximum principal stress σ_1 , given as

$$f(I_1, J_2, \sigma_1) = A \bar{J}_2 + B \sqrt{\bar{J}_2} + C \bar{\sigma}_1 + D \bar{I}_1 - 1 \quad (2.27)$$

where the upper bar notation indicates normalisation with respect to the uniaxial compressive cylinder strength of concrete. Parameters A, B, C and D are material dependent and are obtained from biaxial and triaxial test results. Fig's. 2.20 and 2.21 give the comparison of this surface with experimental results.

Later, Chen and Schnobrich [31] proposed equations for the tensile and compressive meridians based on the test results and the least square fitting of Ottosen [25]. The results are expressed in terms of ρ and ξ which are measures of the deviatoric and the hydrostatic stresses, respectively

$$\frac{\rho_t}{f_c} = -6.4899 + 2.9458 \left(5.0343 - \frac{\xi}{f_c} \right)^{1/2} \quad \text{for } \theta = 0^\circ \quad (2.28)$$

$$\frac{\rho_c}{f_c} = -3.6199 + 2.9458 \left(1.6907 - \frac{\xi}{f_c} \right)^{1/2} \quad \text{for } \theta = 60^\circ \quad (2.29)$$

where $\rho = \sqrt{2J_2}$, and

$$\xi = \frac{I_1}{\sqrt{3}}$$

The ultimate strength surface was obtained by fitting hyperbolas to the corners of the Mohr-Coulomb failure locus on the deviatoric plane, Fig. 2.22. The failure criterion is defined as

$$f(\sigma_{ij}) = \sqrt{2J_2} - [(1 - S^2 \theta_1^2) \rho_1 + S^2 \theta_1^2 \rho_2] \quad (2.30)$$

where $S = \pi/3$,
 $\rho_1, \rho_2 =$ some function of ρ_t and ρ_c , and
 $\theta_1 =$ angle of similarity

Nilsson and Glemberg [32] proposed a closed yield surface which is generally suitable for granular material exhibiting strain-softening and dilatancy at low hydrostatic pressure and hardening and compaction at high hydrostatic pressure. The surface is defined by a general ellipsoidal surface as

$$F = \left[\left(\frac{2\sigma_0 - \xi_u - \xi_1}{\xi_u - \xi_1} \right)^2 + \left(\frac{\tau_0}{b(\theta)} \right)^2 - 1 \right]^{1/2} \quad (2.31)$$

where $\sigma_0 =$ octahedral normal stress,
 $\tau_0 =$ octahedral shear stress,
 $\xi_1 =$ yield surface intersection with the hydrostatic axis in the compression zone, and
 $\xi_u =$ yield surface intersection with the hydrostatic axis in the tension zone

The deviatoric semi-axis $b(\theta)$, is obtained in terms of the corresponding values of $b(\theta)$ at θ equals 0° , b_1 , and θ equals 60° , b_2 , using the elliptic deviatoric trace of Willam and Warnke [20] given by Eq. 2.17, Fig. 2.23.

In summary, Von Mises or Tresca types of failure surface are pressure independent and are suitable for pure shear problems in compression. They are usually augmented by Rankine type failure criterion (tension-cut-off) to model tensile failure. The Drucker -Prager surface is probably the simplest pressure dependent failure criterion, but it is not very suitable for concrete modelling. Firstly, the meridians are straight and secondly, the surface is not dependent on the angle of similarity θ . The Bresler and Pister criterion has parabolic meridians while the deviatoric section is independent of θ . On the other hand, the three-parameter surface of Willam and Warnke is dependent on θ , but the meridians are linear which makes it inadequate for high compression regions. The more refined surfaces of Willam and Warnke (five-parameter surface), Ottosen, Kotsosovos, Hsieh et al, Chen and Schnobrich, and Nilsson and Glemberg constitute both a nonlinear meridian and a θ dependence. Most of these models are in close agreement with test results and satisfy the basic requirements for characterising a stable failure surface for concrete. These requirements include smoothness, convexity, symmetry and curved meridians.

2.3.2 Work-Hardening Plasticity Models

Work-hardening models assume that material yield at some stress level below the ultimate strength level which

corresponds to an initial yield surface. Further intermediate yield surfaces develop as a result of plastic deformation and the process continues until the ultimate yield surface is achieved (section 2.3). A work-hardening plasticity formulation, therefore, requires three fundamental assumptions to be established:

- i) the shape of the initial yield surface,
- ii) the evaluation of the subsequent loading surface, and
- iii) a flow rule to evaluate the plastic deformation and its direction.

There are three general hardening rules, i.e. isotropic, kinematic and mixed hardening. The first rule assumes a uniform expansion of the initial yield surface as plastic flow occurs. In kinematic hardening, the yield surface is translated as plastic flow continues, thus maintaining the shape and size of the initial yield surface. Finally, mixed hardening is a combination of both the first and the second rules. In what follows, some different hardening plasticity models for concrete are described.

Chen and Chen [33] assumed that the criterion for failure of concrete is dependent on the deviatoric stress and the hydrostatic pressure and proposed the following yield criterion

$$f(\sigma_{ij}) = \frac{\frac{\kappa^2}{3} J_2 - \frac{\kappa^2}{36} I_1^2 \pm \frac{I_1^2}{12} + \frac{\beta}{3} I_1}{1 - \frac{\alpha}{3} I_1} = \tau_u^2 \quad (2.32)$$

in which the positive and negative signs indicate the loading surface in compression-compression and tension-compression states of stress, respectively. The constant parameter κ^2 is assumed to be three and α and β are material constants expressed in terms of the uniaxial and biaxial strength of concrete. Fig's. 2.24 and 2.25 show a triaxial representation and a fit of experimental results for this model. The variation of the yield surface for the initial elastic limit up to the failure surface is defined by the parameter τ , where $\tau = \tau_0$ represents the elastic limit and $\tau = \tau_u$ represents the ultimate failure surface. A subsequent loading surface is represented by the condition

$$\tau_0 < \tau < \tau_u$$

The incremental plastic stress-strain relationship is obtained from the flow rule and is given as

$$d\epsilon_{ij}^p = \frac{\frac{\partial f}{\partial \sigma_{ij}} \frac{\partial f}{\partial \sigma_{mn}}}{H \sqrt{\frac{\partial f}{\partial \sigma_{rs}} \frac{\partial f}{\partial \sigma_{sr}}}} d\sigma_{mn} \quad (2.33)$$

It is assumed that the total incremental strain is the summation of the incremental elastic and plastic strains. The

incremental elastic-plastic stress-strain relationship is obtained from Eq. 2.33 as

$$d\epsilon_{ij} = \left[H_{ijkl} + \frac{\frac{\partial f}{\partial \sigma_{ij}} \frac{\partial f}{\partial \sigma_{kl}}}{H \sqrt{\frac{\partial f}{\partial \sigma_{rs}} \frac{\partial f}{\partial \sigma_{sr}}}} \right] d\sigma_{kl} \quad (2.34)$$

where $\frac{\partial f}{\partial \sigma_{ij}}$ = gradient of yield surface,
 H_{ijkl} = elastic compliance matrix, and

$$H = \frac{df}{\sqrt{d\epsilon_{rs}^p d\epsilon_{sr}^p}}$$

= strain hardening rate

To obtain the hardening parameter H, the concept of the effective stress and effective plastic strain is used as follows. The effective stress is given as

$$f(\sigma_{ij}) = F(\epsilon_p) \quad (2.35)$$

and the effective plastic strain is obtained as follows

$$\epsilon_p = \int d\epsilon^p = \sqrt{d\epsilon_{rs}^p d\epsilon_{sr}^p} \quad (2.36)$$

Experimental results are used to obtain the plot of F versus ϵ_p from which the hardening parameter H, is the slope of this curve at each stress level [33]. This model has been used successfully in finite element analysis [35-38].

successfully in finite element analysis [35-38].

Similar isotropic hardening plasticity models were developed by Chen and Schnobrich [31], where the expansion of the yield surface is introduced into Eq. 2.30 by a hardening parameter ω , as

$$f(\sigma_{ij}, \omega) = \sqrt{2J_2} - \omega [(1 - S^2 \theta_1^2) \rho_1 + S^2 \theta_1^2 \rho_2] \quad (2.37)$$

The hardening parameter ω , is defined in terms of an equivalent uniaxial stress σ_{eq} , and a peak stress corresponding to the current stress level σ_0 , as

$$\omega = \frac{\sigma_{eq}}{|\sigma_0|} \quad (2.38)$$

The hardening modulus A , in Eq. 2.8 is obtained as

$$\begin{aligned} A &= - \frac{\partial f}{\partial \omega} \frac{\partial \omega}{\partial \lambda} \\ &= - \frac{\partial f}{\partial \omega} \frac{H}{|\sigma_0|} m_p \sqrt{\frac{\partial f}{\partial \sigma_{ij}} \frac{\partial f}{\partial \sigma_{ij}}} \end{aligned} \quad (2.39)$$

where

$$H = \frac{d\sigma_{eq}}{d\varepsilon_{eq}^p} = \frac{E_t}{1 - \frac{E_t}{E}},$$

E = initial Young's modulus,

E_t = tangential Young's modulus, and

m_p = equivalent uniaxial plastic strain scaling factor

Argyris et al [39] developed a mixed hardening plasticity model for concrete based on the five-parameter surface of Willam and Warnke (Eq. 2.21). This model is represented by

$$f(\sigma_a, \tau_a, \theta, \alpha, \beta) = \frac{1}{r(\sigma_a - \alpha\sigma_0, \theta)} \frac{\tau_a}{f_c} - \beta \quad (2.40)$$

where

- $\alpha = \alpha(\epsilon^p)$,
- $\beta = \beta(\epsilon^p)$,
- ϵ^p = effective plastic strain,
- ϵ^p = volumetric effective plastic strain, and
- σ_0 = maximum hydrostatic translation

The term α represents a translation of the yield surface along the hydrostatic axis (kinematic hardening) and the parameter β defines an expansion of the yield surface (isotropic hardening). An incremental work-hardening stress strain relationship was obtained using a flow rule. A modular matrix similar to that given by Eq. 2.8 was used with a hardening modulus A , given by

$$A = \left(\frac{\partial f}{\partial \beta} \frac{\partial \beta}{\partial \epsilon^p} - \frac{\partial f}{\partial \alpha} \frac{\partial \alpha}{\partial \epsilon^p} \frac{\partial f}{\partial \sigma_a} \right) \sqrt{\frac{\partial f}{\partial \sigma_{ij}} \frac{\partial f}{\partial \sigma_{ji}}} \quad (2.41)$$

Argyris et al [39] have not proposed any suitable formulation for the variation of the hardening parameters α and β , with the plastic strain.

Hsieh et al [40] expressed the isotropic hardening as a function of an effective plastic strain ϵ_p^i , and the kinematic hardening by the term α_{ij} , which characterises the movement of the centre of the yield surface. They introduced these parameters into Eq. 2.27 and represented their failure criterion as follows

$$f(\sigma_{ij}, \tau) = A \frac{J_2}{\tau(\epsilon_p^i)} + B \sqrt{J_2} + C \bar{\sigma}_1 + D \bar{I}_1 - \tau(\epsilon_p^i) \quad (2.42)$$

where $\sigma_{ij} = \sigma_{ij} - \alpha_{ij}$
 $\tau(\epsilon_p^i) =$ a function of plastic strain

To obtain the incremental relationships the increment of plastic strain $d\epsilon_{ij}^p$, is decomposed into increments of plastic strain due to isotropic hardening $d\epsilon_{ij}^{pi}$, and kinematic hardening $d\epsilon_{ij}^{pk}$, as

$$\begin{aligned} d\epsilon_{ij}^p &= d\epsilon_{ij}^{pi} + d\epsilon_{ij}^{pk} \\ &= M d\epsilon_{ij}^p + (1 - M) d\epsilon_{ij}^p \end{aligned} \quad (2.43)$$

where $M =$ a constant parameter

The hardening parameters corresponding to the two types of hardening were obtained using the concept of the effective plastic strain, Eq. 2.36. The incremental stress-strain relationship was proposed as follows

$$d\sigma_{ij} = (C_{ijkl} - E_{ijkl}) d\epsilon_{kl} \quad (2.44)$$

$$E_{ijkl} = \frac{C_{ijmn} C_{klrs} G_{mnr s}}{C_{mnr s} G_{mnr s} \left[c(1 - M) \frac{\partial f}{\partial \bar{\sigma}_{rs}} \partial \bar{\sigma}_{rv} - \bar{H} M \frac{\partial f}{\partial \tau} G_{mnr s}^{1/2} \right]} \quad (2.45)$$

where

$$G_{mnr s} = \frac{\partial f}{\partial \bar{\sigma}_{mn}} \frac{\partial f}{\partial \bar{\sigma}_{rs}},$$

$$\bar{H} = \text{slope of } \tau - \epsilon_p^i \text{ curve,}$$

$$\epsilon_p^i = \text{effective plastic strain,}$$

corresponding to $d\epsilon_{ij}^{pi}$, and

$$c = \text{constant parameter}$$

2.4 Conclusions

The following conclusions may be drawn from the review presented in this chapter.

- i) Elasticity based models are restricted to proportional loading and path-independent materials if they are used in the 'total' form. The hypo-elasticity models are also limited in their application by the number of parameters required to represent the material behaviour adequately. In addition, they may produce unrealistic results for cyclic loading.
- ii) The plastic-fracturing model relies on many material parameters and the incremental modular matrix is unsymmetrical which makes it unfavourable for finite element applications.

- iii) The endochronic theory of plasticity results in a nonlinear relationship between the increments of stress and strain which may produce a great deal of complexity in its application. This theory also depends on many material parameters to represent the concrete behaviour.
- iv) The theory of plasticity together with a suitable yield surface and an adequate hardening model seems to be the most reliable option for concrete modelling.
- v) The five-parameter surface of Willam and Warnke produces an adequate failure surface for concrete. The choice of the material constants for the definition of the yield surface is, however, an important task. It is, therefore, required to investigate the best values for these parameters to achieve the optimum fit.
- vi) The isotropic expansion of the yield surface for representing the material strain-hardening would appear to be adequate for concrete. The use of kinematic hardening requires many assumptions which may not be realistic due to the lack of experimental results and may lead to unnecessary complications.
- vii) The isotropic hardening parameter β , proposed by Argyris provides a simple and realistic representation of concrete hardening without resorting to concepts such as, 'equivalent' uniaxial stress for the representation of the triaxial state of stress. An explicit function is needed, however, to determine the variation of β with

the development of plastic strain.

viii)The use of a plasticity model to represent strain-softening in concrete requires immediate attention.

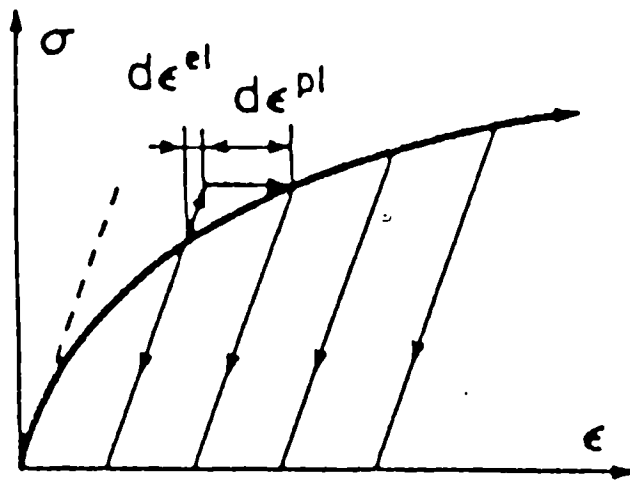


Fig. 2.1 Characteristic uniaxial response of plastic material.

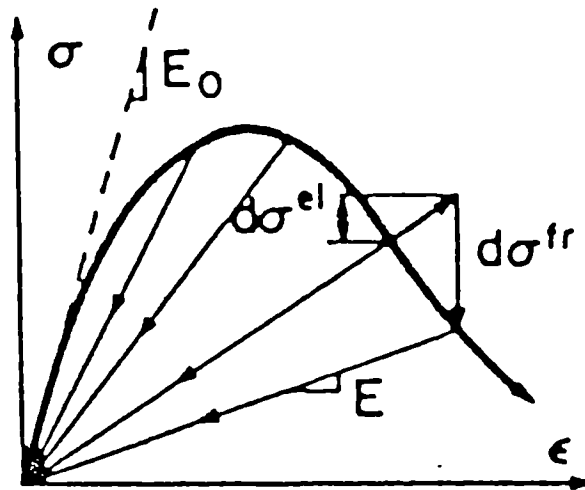


Fig. 2.2 Characteristic uniaxial response of fracturing material.

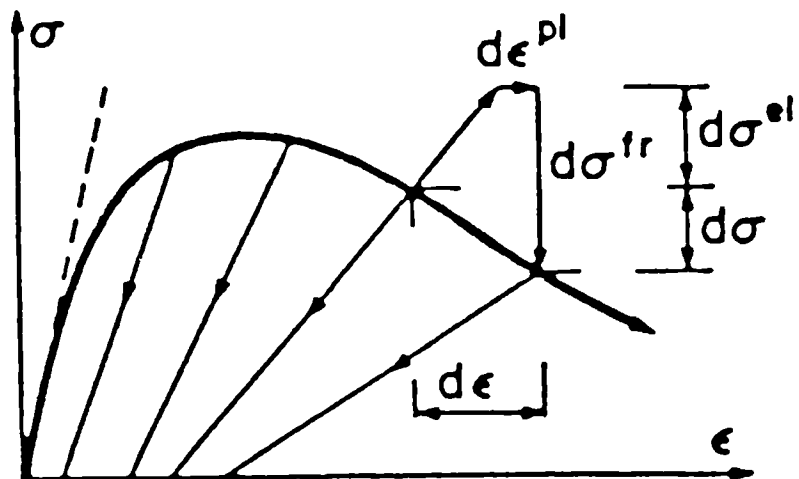


Fig. 2.3 Characteristic uniaxial response of plastic-fracturing material.

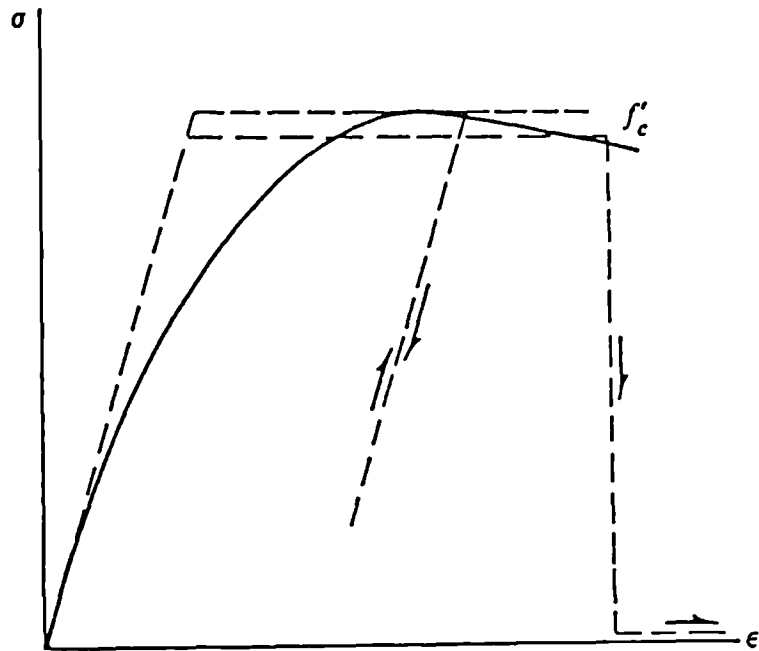


Fig. 2.4 Idealised stress-strain curve for perfectly plastic-brittle-fracture concrete material.

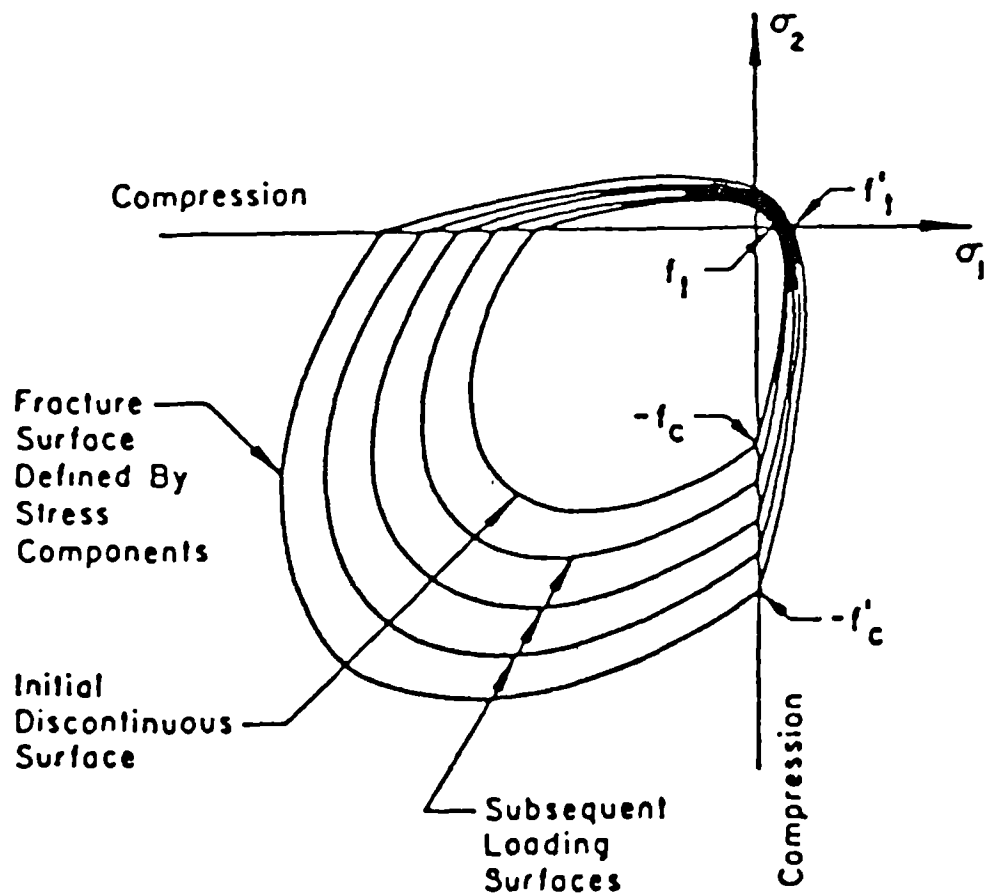
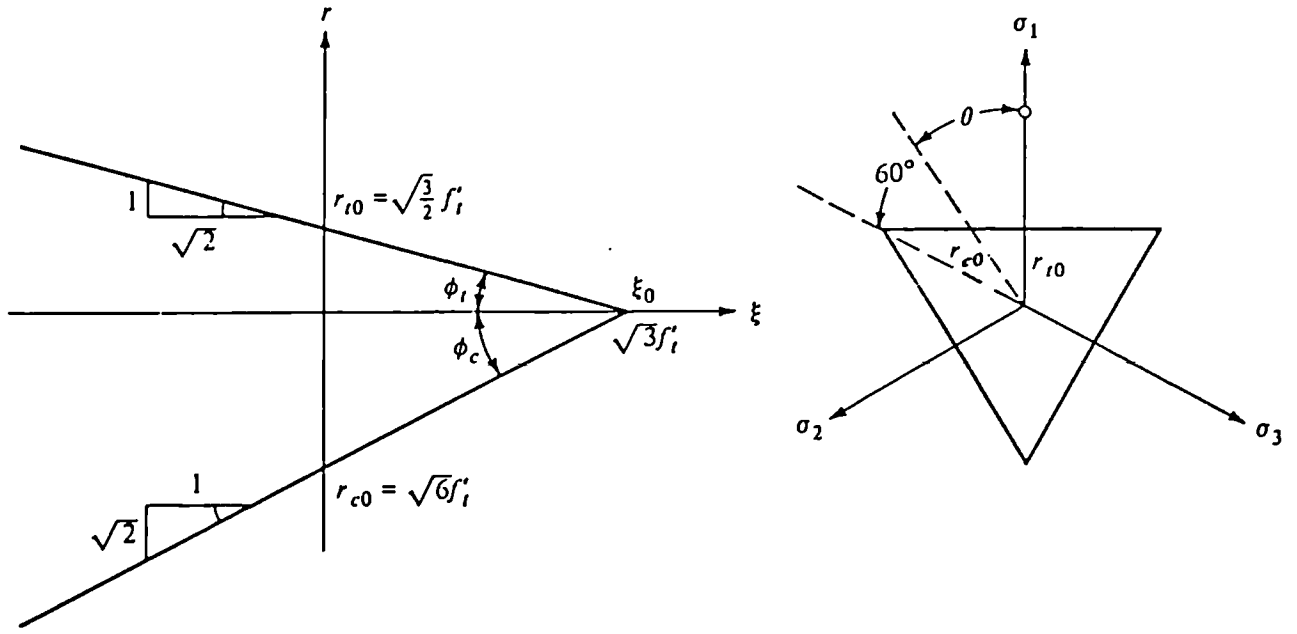


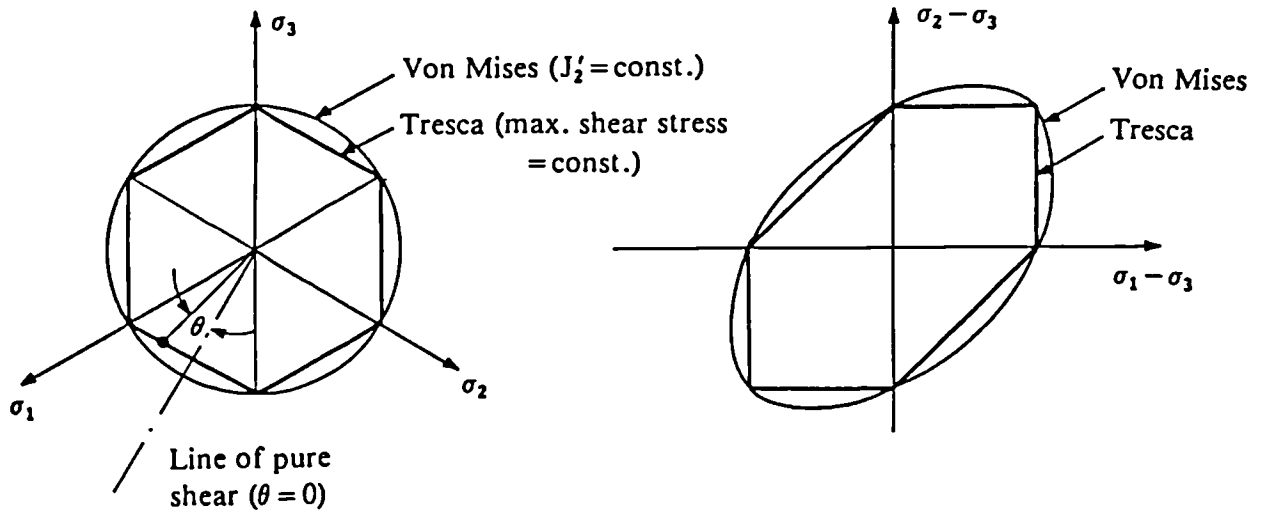
Fig. 2.5 Loading surfaces of concrete in biaxial plane.



(a) Hydrostatic Section

(b) Deviatoric Section

Fig. 2.6 Rankin's maximum principal stress criterion.



(a) Hydrostatic Section

(b) $\sigma_3 = 0$ Plane

Fig. 2.7 Representation of Von Mises and Tresca's failure criteria.

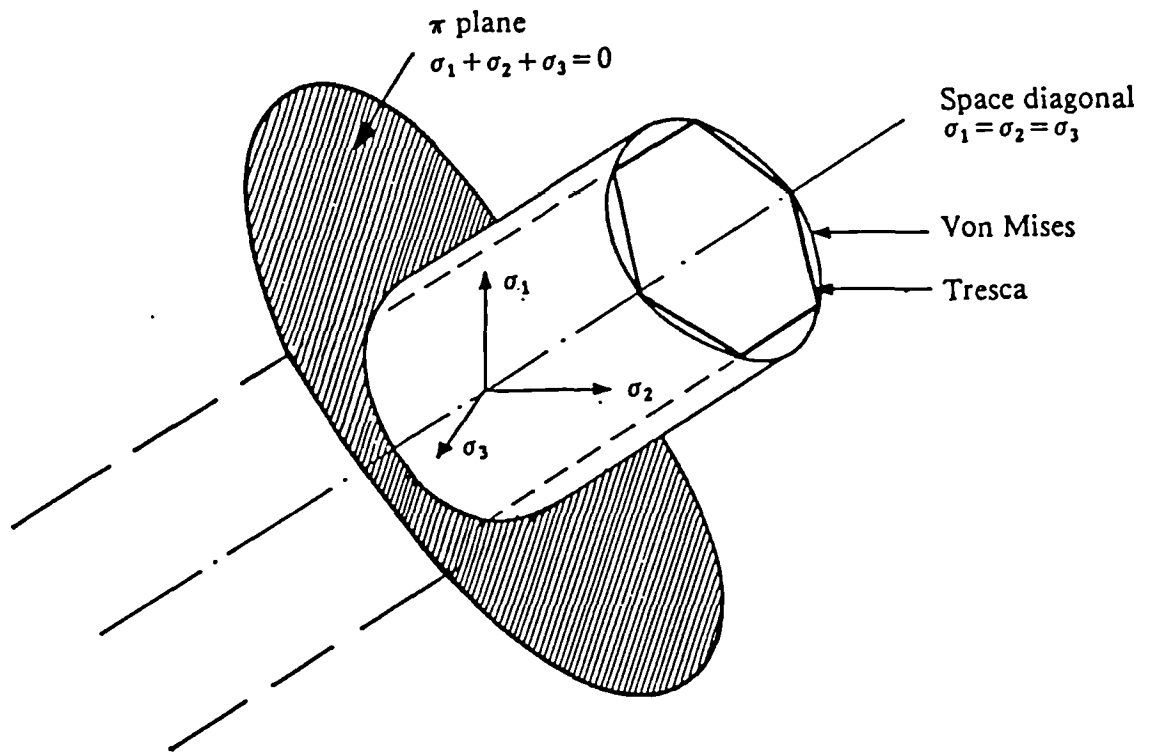


Fig. 2.8 Three dimensional representation of Von Mises and Tresca's failure surfaces.

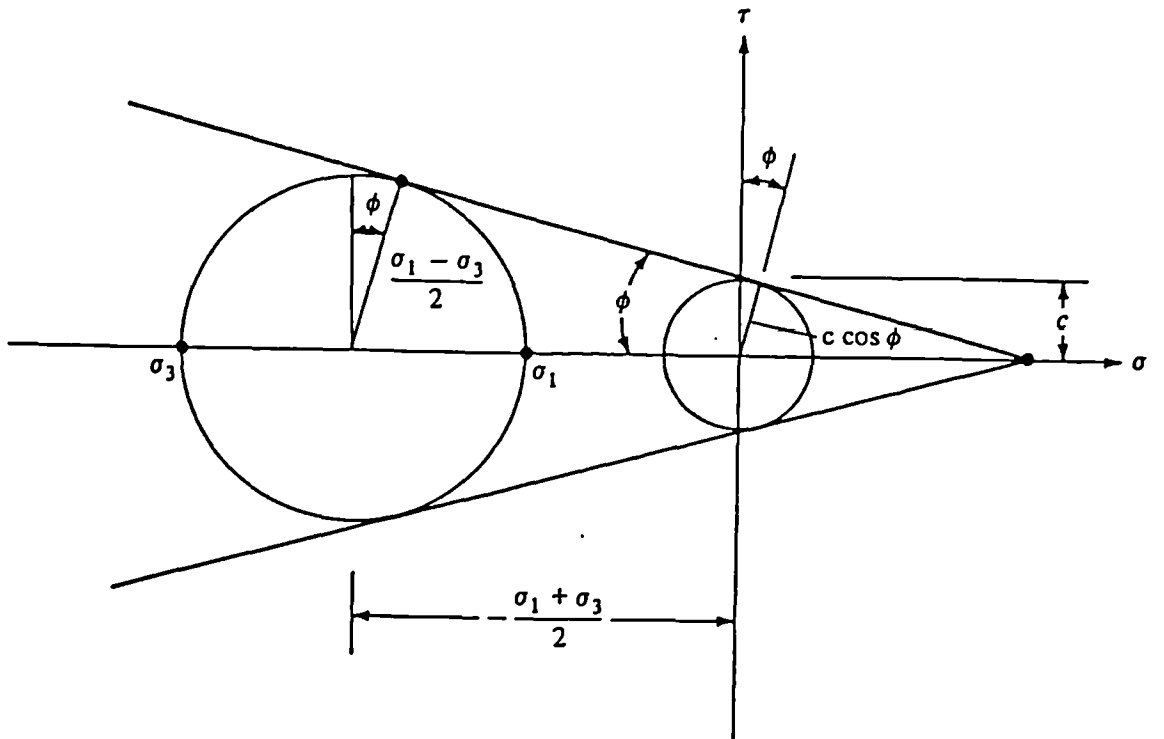


Fig. 2.9 Representation of the relationship between the principal stresses for the Mohr-Coulomb criterion.

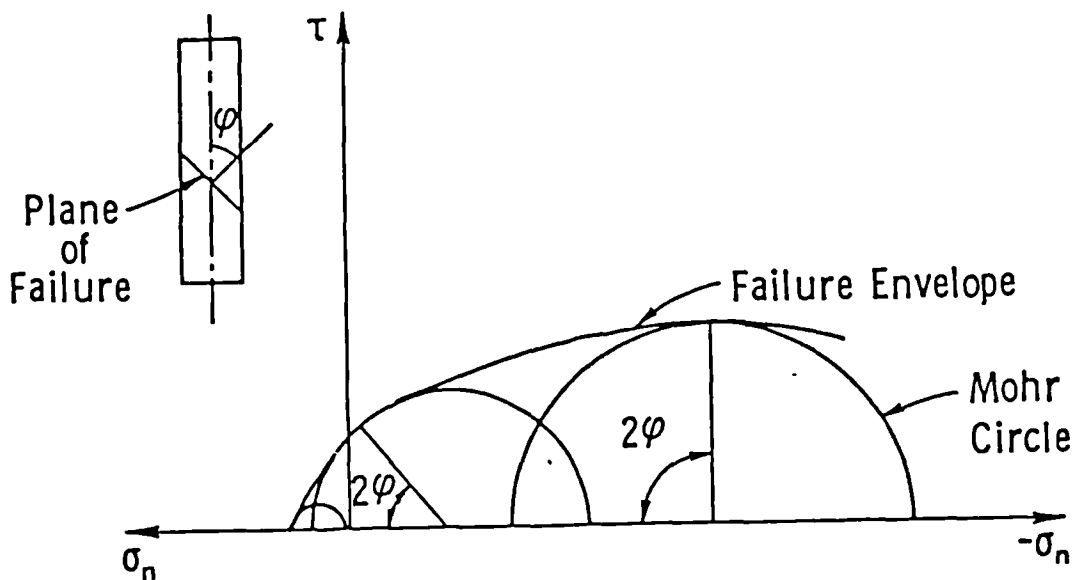
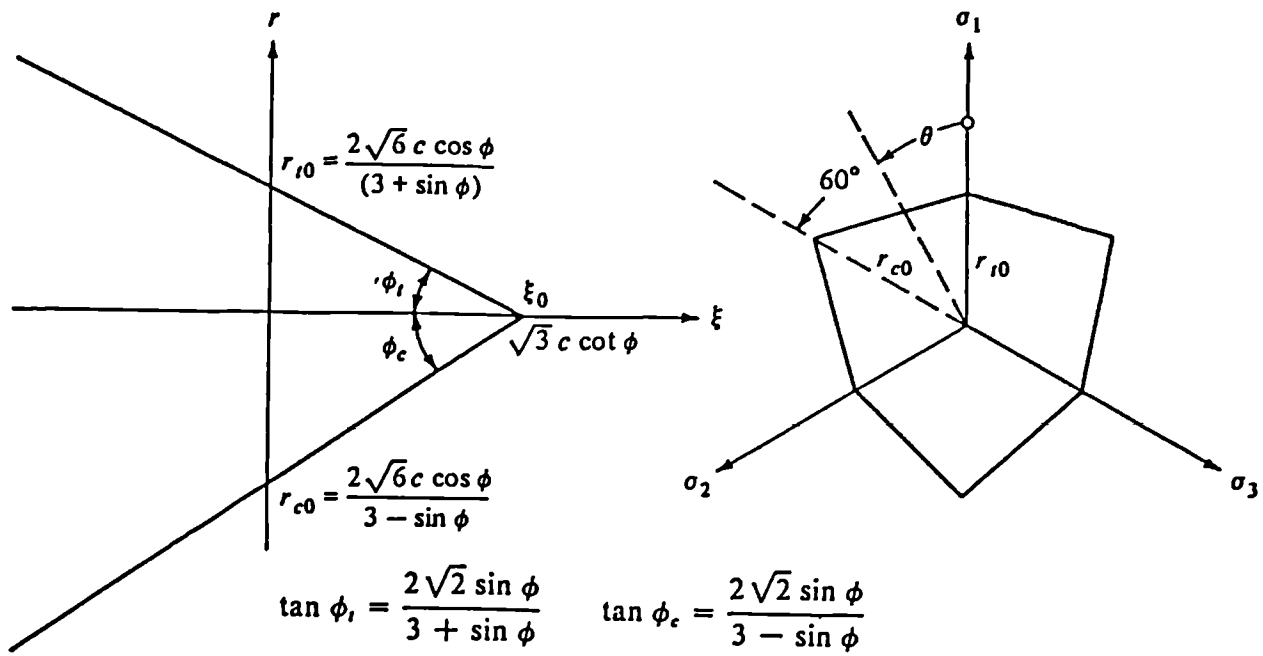


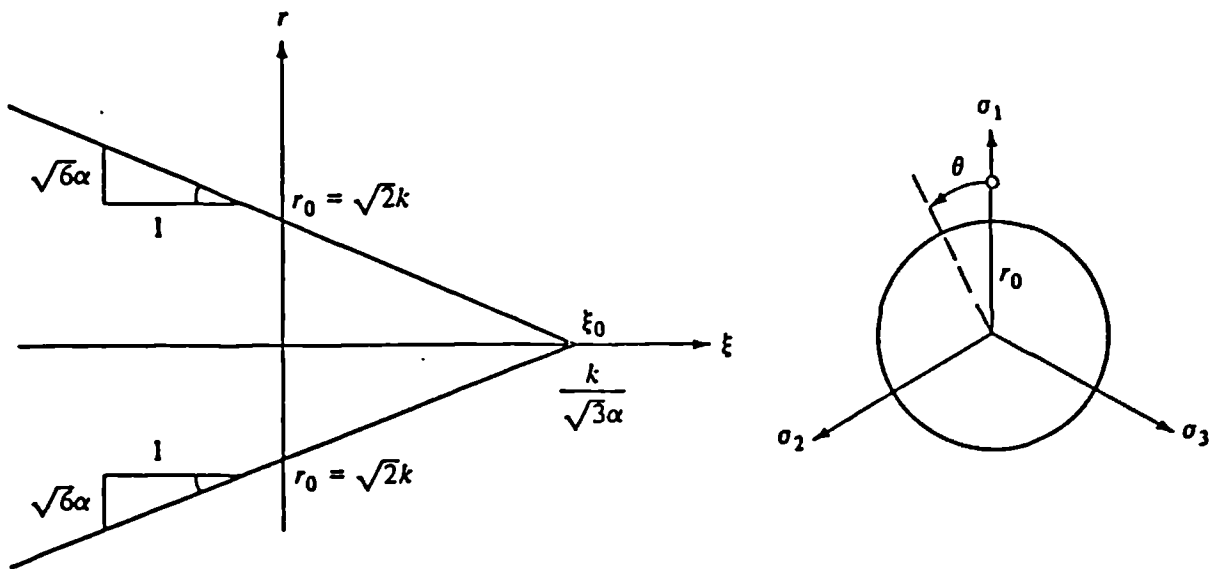
Fig. 2.10 Curved Mohr-Coulomb failure envelope for concrete.



(a) Hydrostatic Section

(b) Deviatoric Section

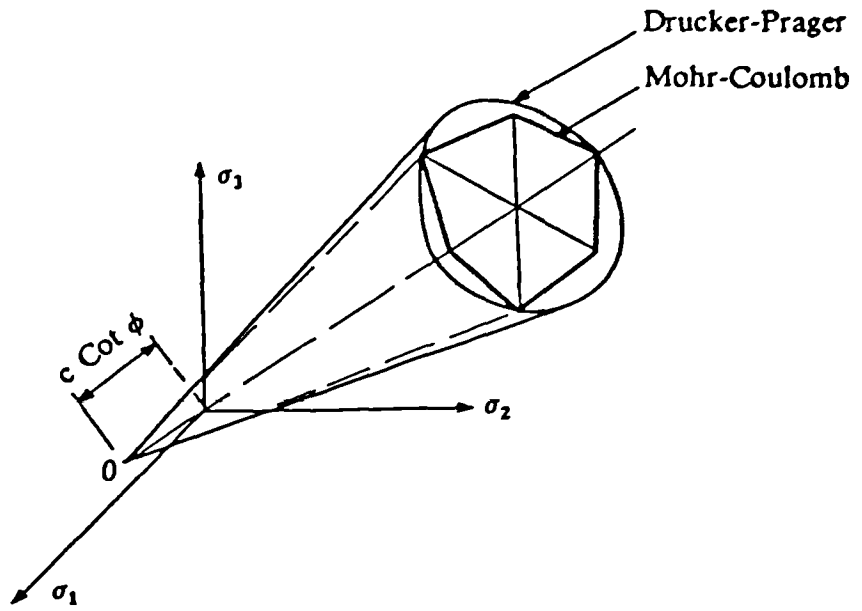
Fig. 2.11 Representation of Mohr-Coulomb failure criterion.



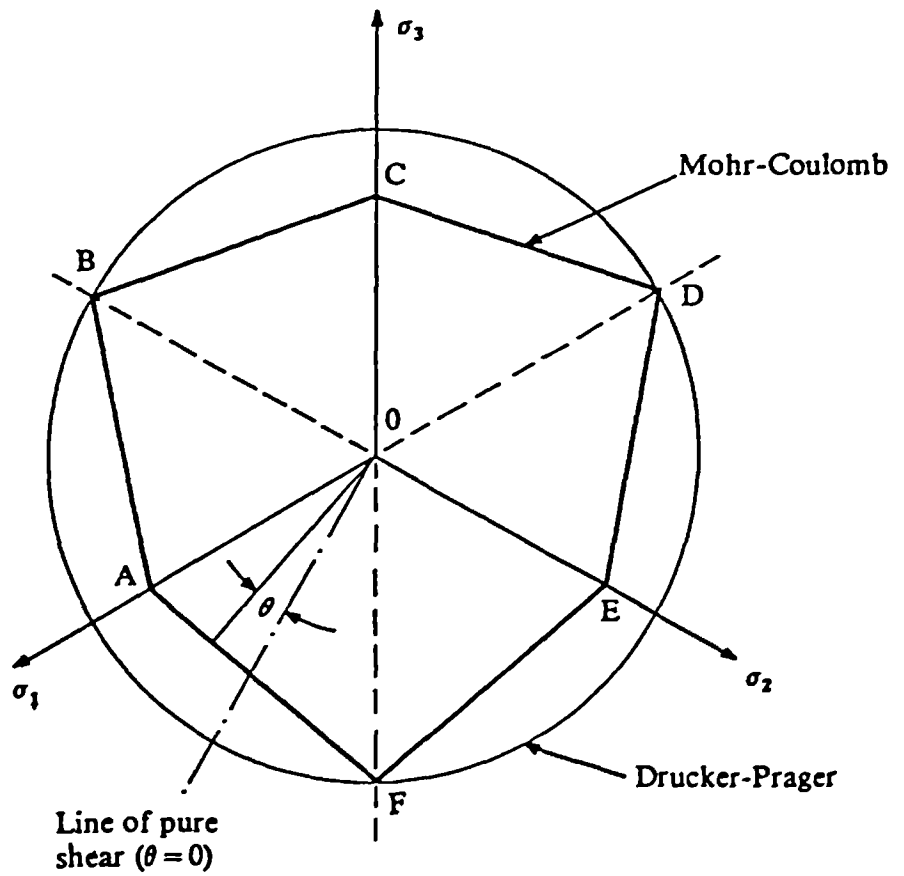
(a) Hydrostatic Section

(b) Deviatoric Section

Fig. 2.12 Representation of Drucker-Prager failure criterion.



(a) Stress Space



(b) Deviatoric Section

Fig. 2.13 Comparison between Mohr-Coulomb and Drucker-Prager failure criteria.

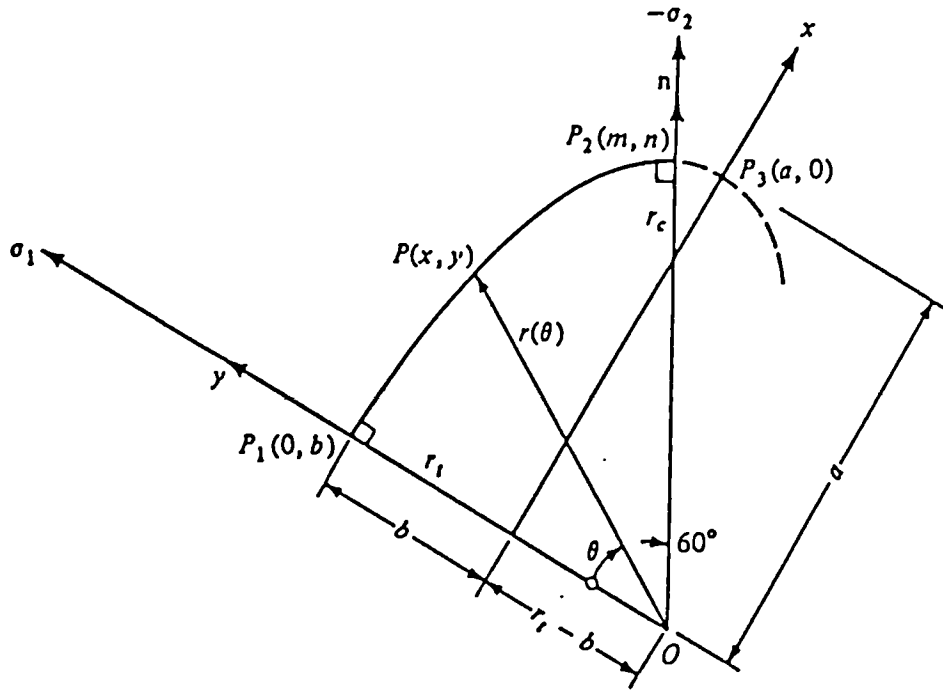


Fig. 2.14 Elliptic trace of the failure surface of Willam and Warnke.

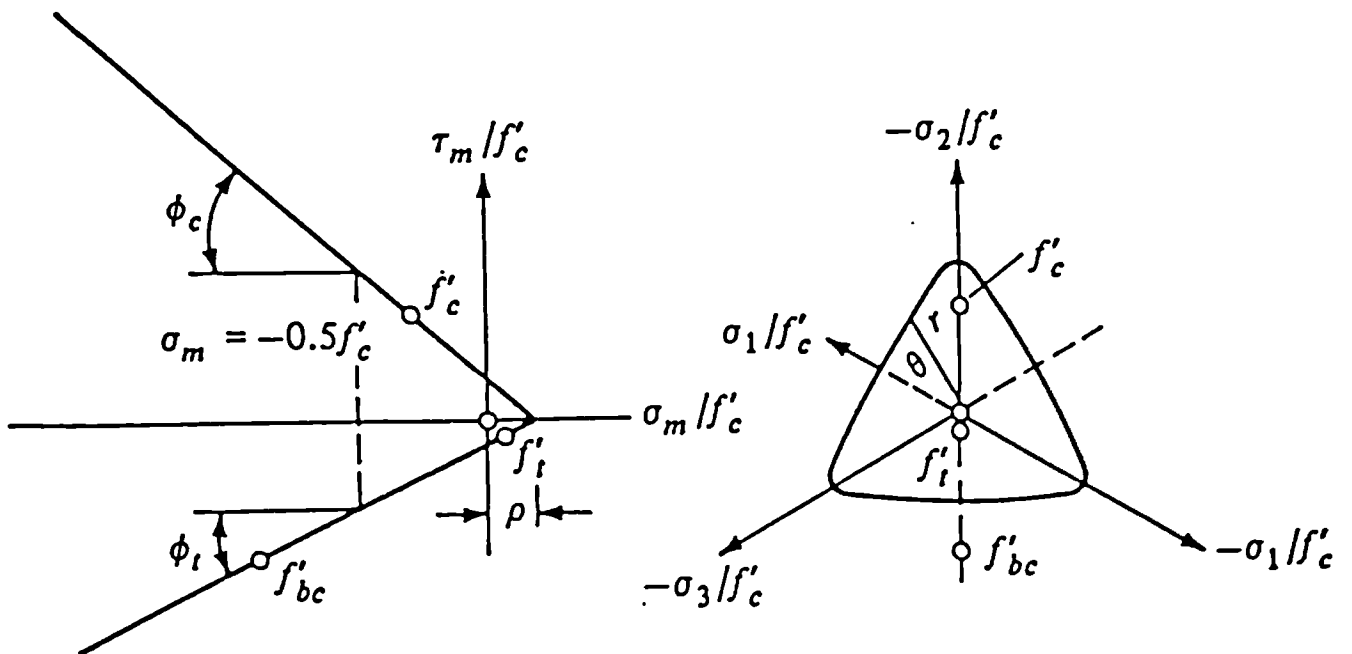
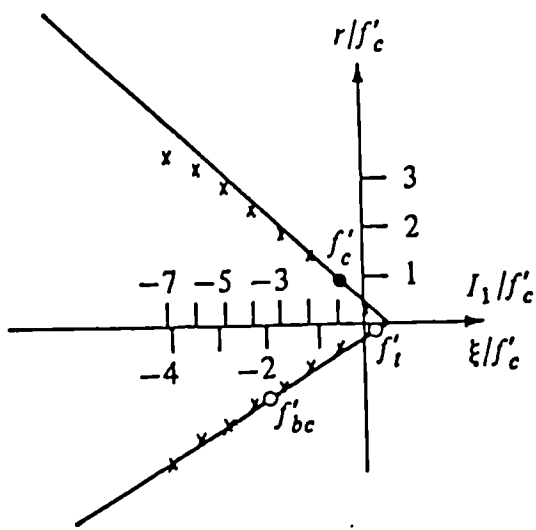
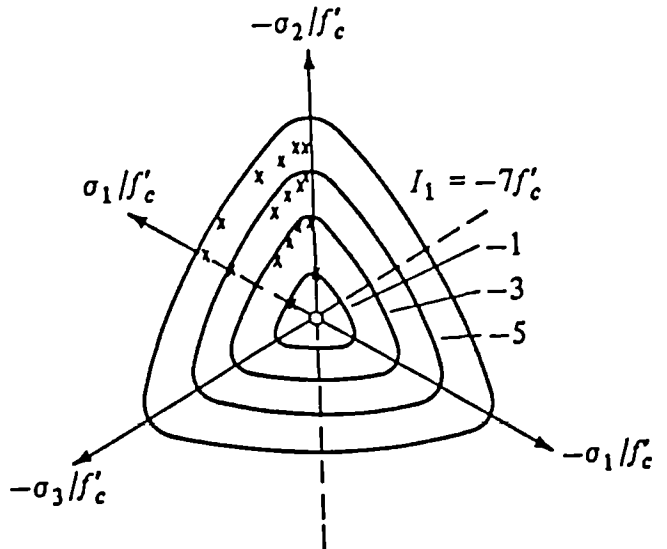


Fig. 2.15 Representation of Willam-Warnke three-parameter failure criteria.



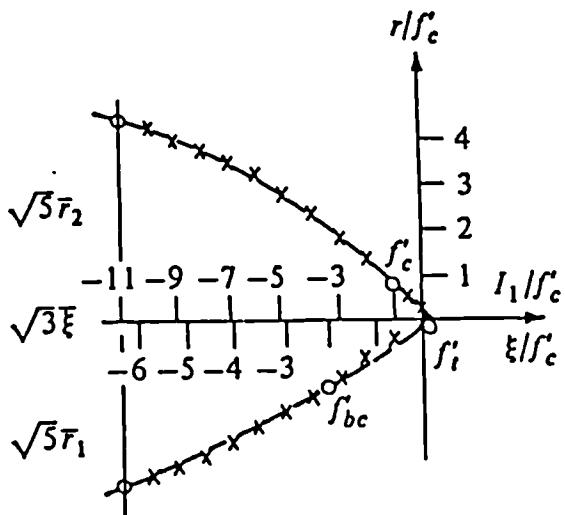
(a) Hydrostatic Section



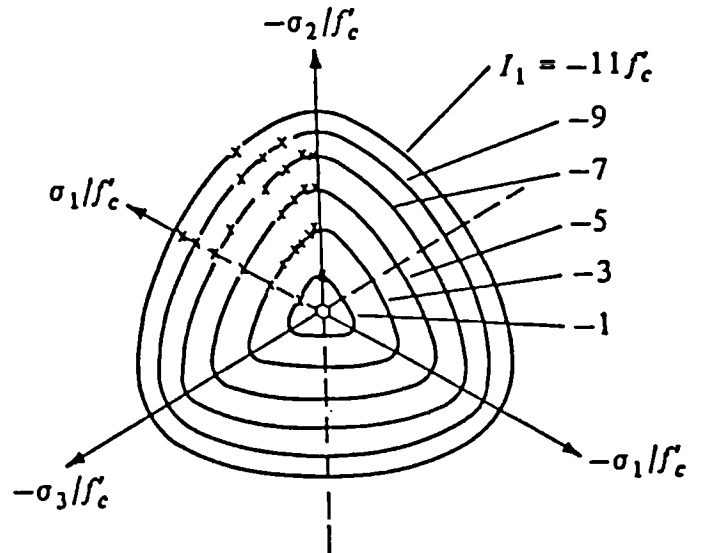
(b) Deviatoric Section

Experimental Results [22]

Fig. 2.16 Comparison of Willam-Warnke three-parameter failure surface with experimental results.



(a) Hydrostatic Section



(b) Deviatoric Section

Experimental Results [22]

Fig. 2.17 Comparison of Willam-Warnke five-parameter failure surface with experimental results.

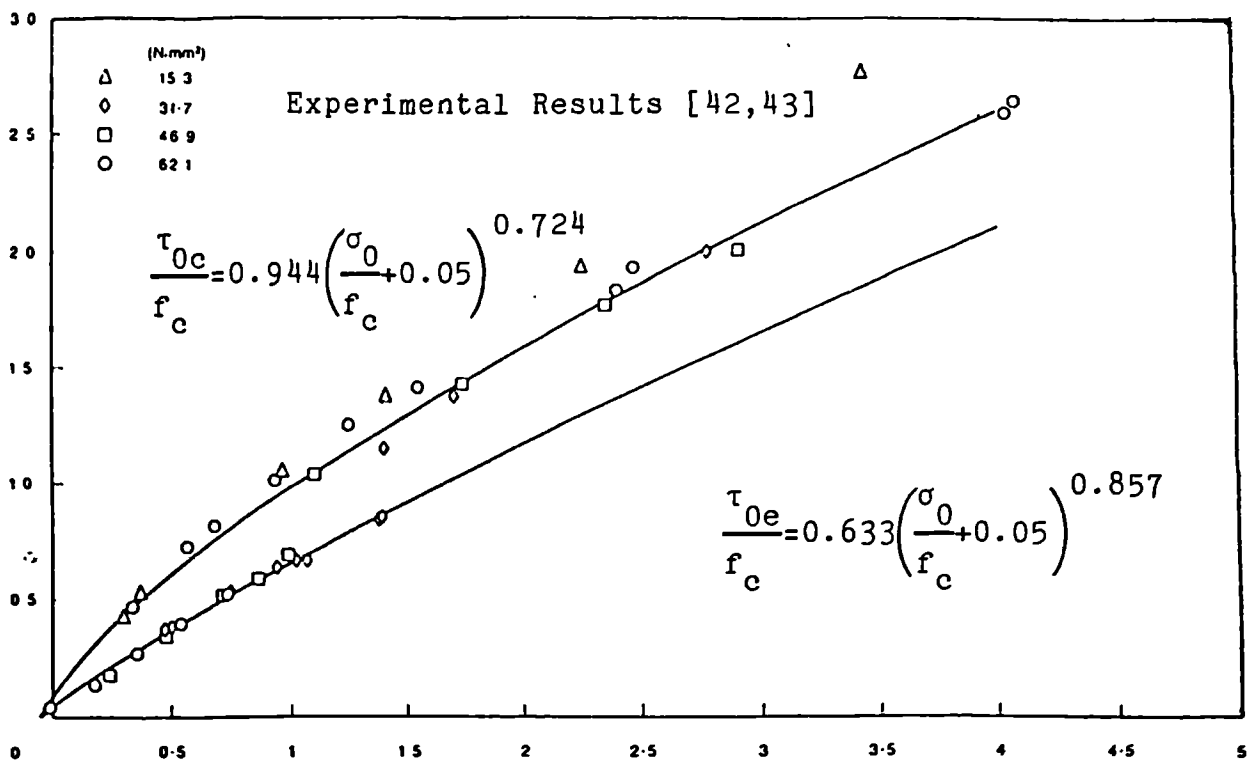


Fig. 2.18 Comparison of Kotsovos's failure surface with experimental results.

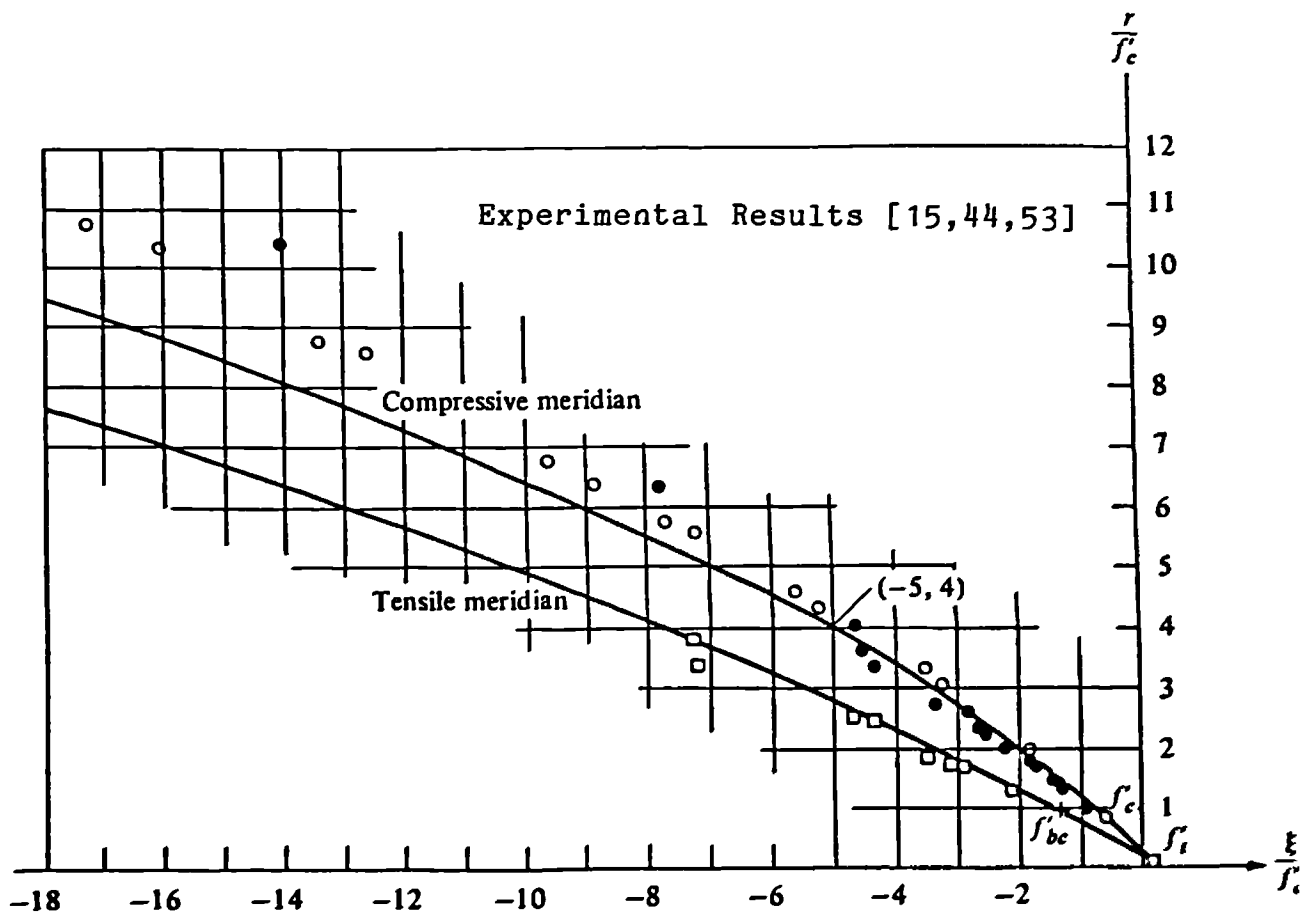


Fig. 2.19 Comparison of Ottosen's failure surface with experimental results.

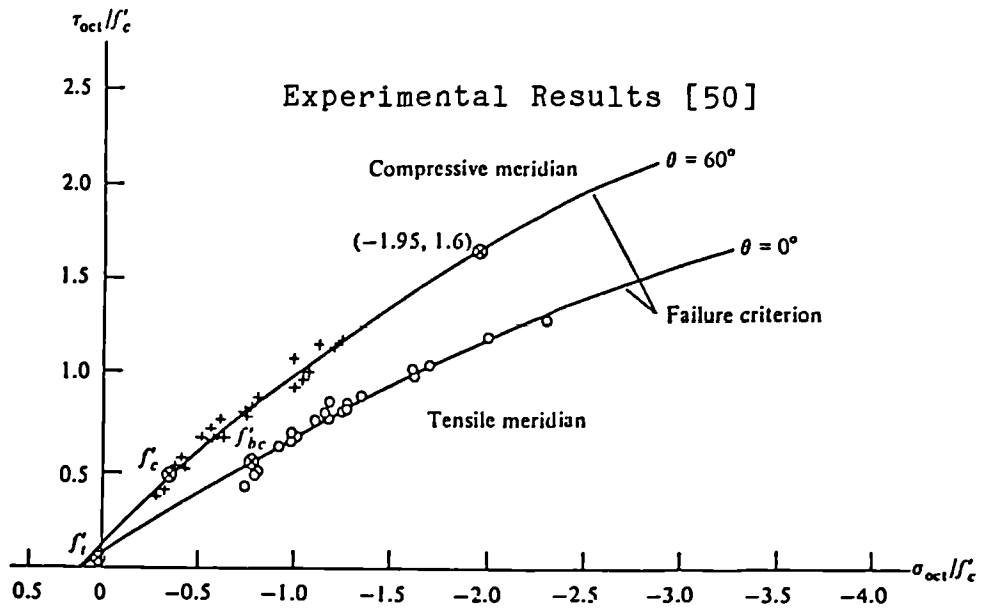


Fig. 2.20 Comparison of Hsieh et. al. failure criterion with experimental results.

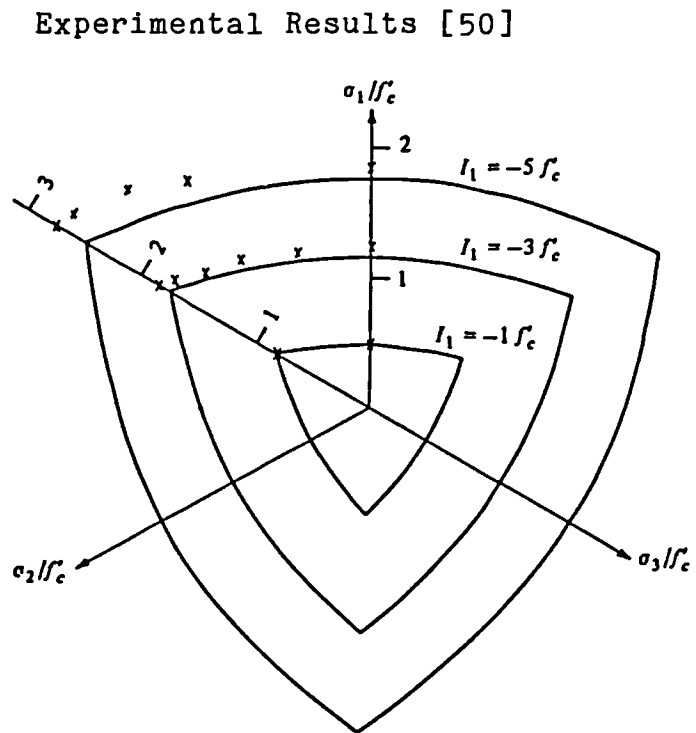


Fig. 2.21 Comparison of Hsieh et. al. failure criterion with experimental results.

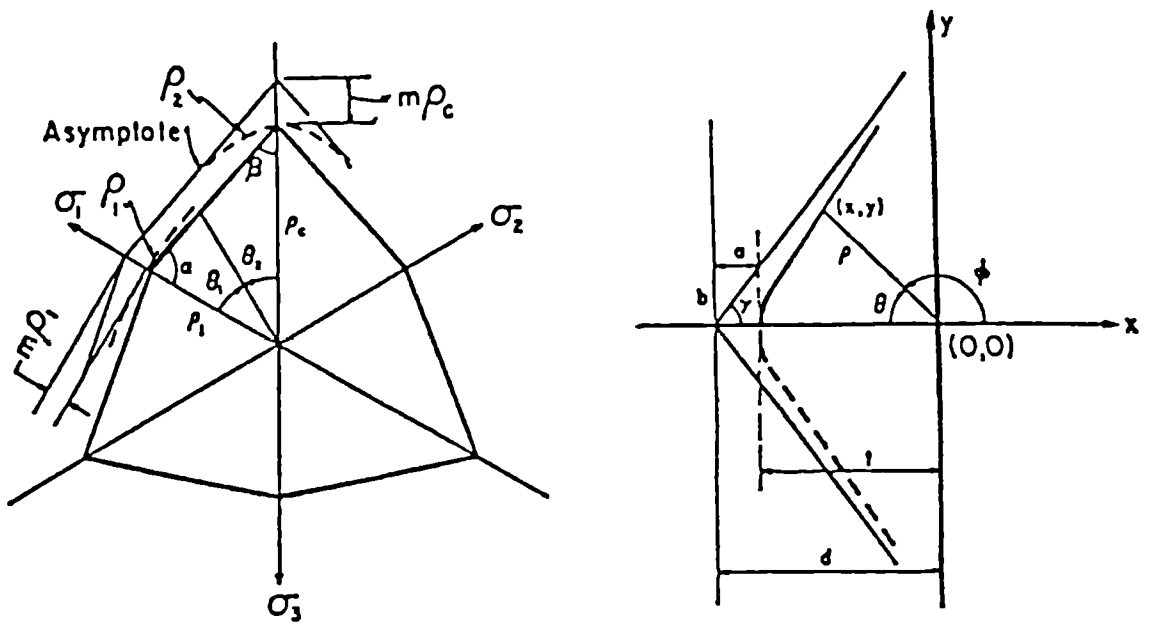
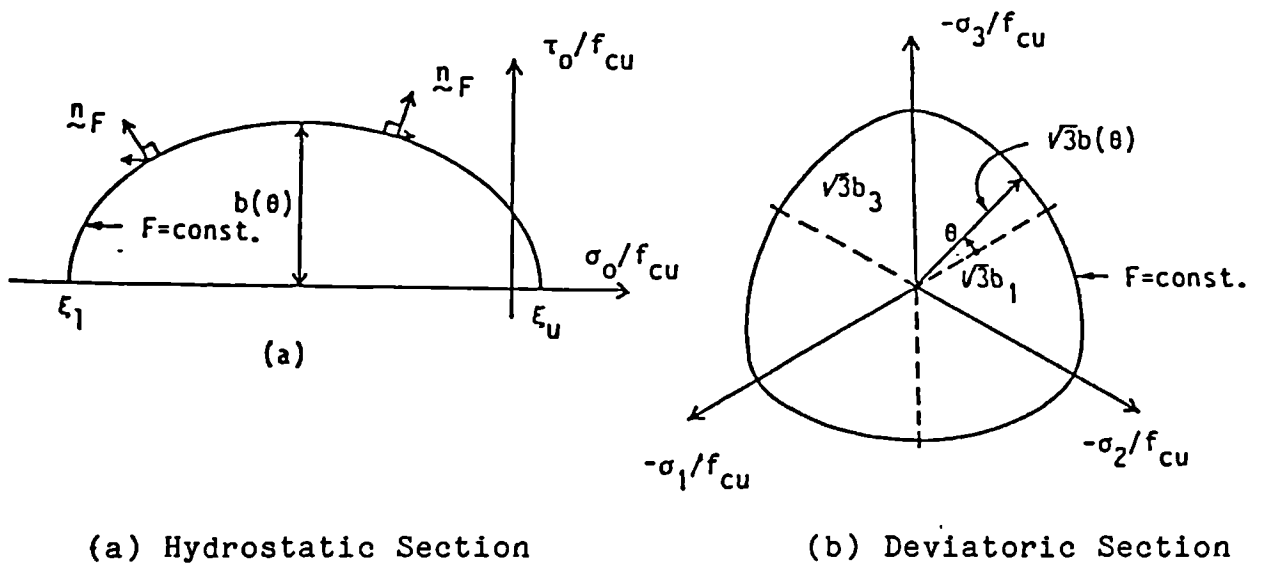


Fig. 2.22 Chen and Schnobrich failure surface: hyperbolic curve fitting to the corners of Mohr-Coulomb failure surface.



(a) Hydrostatic Section

(b) Deviatoric Section

Fig. 2.23 Representation of Nilsson and Glemberg's generalised ellipsoidal failure surface.

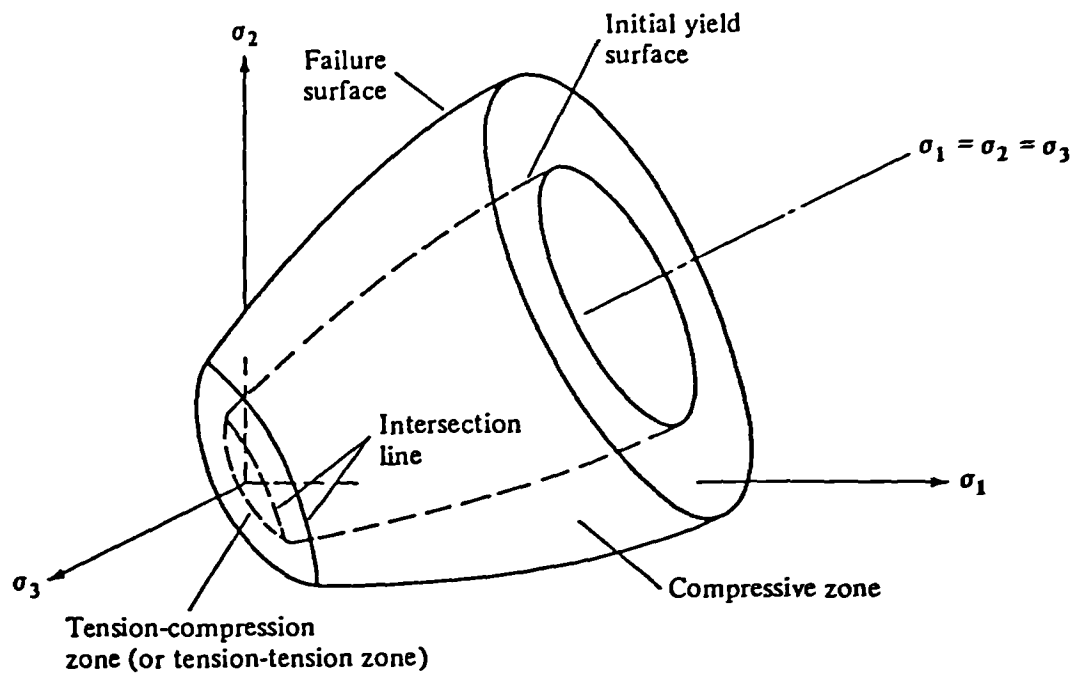
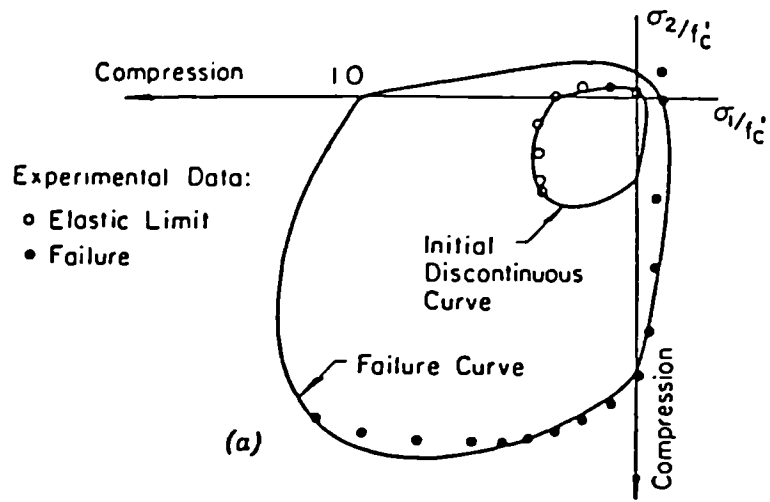
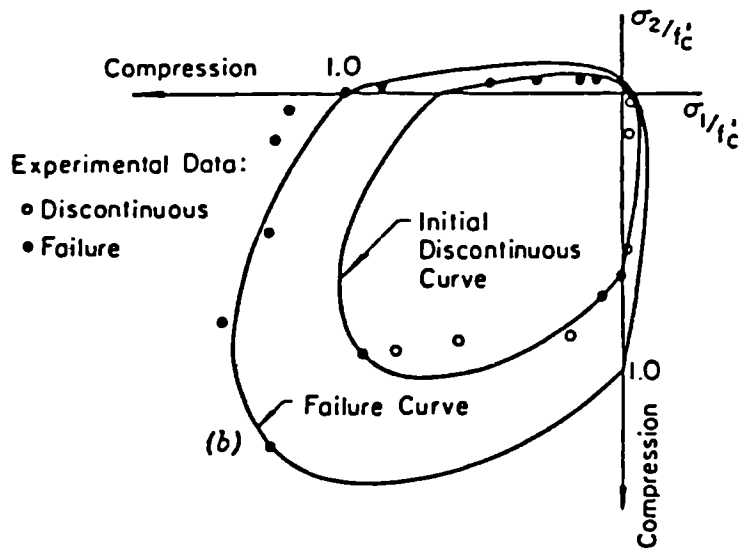


Fig. 2.24 Representation of Chen and Chen's failure and initial loading surfaces.



Experimental Results [44]



Experimental Results [29]

Fig. 2.25 Comparison of Chen and Chen's failure envelopes with experimental results.

CHAPTER THREE

THE MATHEMATICAL MODELLING OF THE STRESS-STRAIN RELATIONSHIP OF CONCRETE

3.1 Introduction

Concrete behaviour depends on the properties of the constituent cement, sand and aggregate as well as the interaction between them. Kotsovos and Newman [41] state that the nonlinear behaviour of concrete is related to mortar-aggregate interaction and is caused by the gradual breakdown of the bond between them through the expansion of the pre-existing microcracks. The observations made by other investigators [42-44] indicate that the deformation behaviour and stiffness of concrete are largely dependent on microcracking in concrete. The experimental evidence of Kotsovos and Newman [45,46], Kotsovos [23], Newman [24], Kuper et al [26] show that the stiffness of concrete under multiaxial compression is totally related to the growth of microcracks, which are initially localised and gradually interconnect into a continuous pattern.

The fact that concrete is composed of different materials and the direction of microcracking is influenced by the state of stress, suggests that concrete should be treated as an inhomogeneous and anisotropic material. Such a representation, however, presents considerable complexities involving experimental information, which is not yet forthcoming. It is reasonable, therefore, to consider concrete material to be homogeneous and isotropic. The micro

effects are, therefore, averaged and continuum mechanics laws are applicable. Such an idealisation is justifiable when considering the randomness of the constituent materials and the localised discontinuities.

In this chapter a mathematical model for the triaxial stress-strain relationship of concrete is developed by the author assuming homogeneous and isotropic material behaviour. The theory of hardening plasticity is used for this purpose. At first, a triaxial failure surface for concrete is developed which has a non-circular base and curved meridians. The work-hardening in concrete is modelled by the isotropic hardening expansion of the surface followed by the contraction (or gradual collapse) of the yield surface to represent the strain softening in concrete after the ultimate strength has been achieved. The incremental stress-strain relationship is derived using a flow rule and the consistency condition. Finally, the analytical results of the proposed constitutive relationship are compared with the published uniaxial, biaxial and triaxial experimental data.

3.2 Work-Hardening Plasticity for Concrete

Plasticity occurs when time independent irreversible straining takes place once a certain stress level known as the yielding limit is reached. The yielding of the material is assumed to take place when the following criterion is satisfied

$$f(\sigma_{ij}) = 0 \quad (3.1)$$

where σ_{ij} = stress tensor

The yield criterion is represented by a surface in stress space, Fig. 3.1. Ideally, plasticity does not cause material degradation and upon unloading the initial material properties, i.e Young's modulus and Poissons's ratio, are restored, Fig. 3.2. The plastic strains are conveniently characterised in terms of the yield surface using a flow rule as follows [47]

$$d\epsilon^P = d\lambda \frac{\partial f}{\partial \sigma_{ij}} \quad (3.2)$$

where $d\lambda$ = the magnitude of $d\epsilon^P$, and

$$\frac{\partial f}{\partial \sigma_{ij}} = \text{the direction of } d\epsilon^P$$

Progressive yielding, such as in the case of work-hardening materials, may be represented by a hardening parameter β , which is introduced into Eq. 3.1 as

$$f(\sigma_{ij}, \beta) = 0 \quad (3.3)$$

This implies that there are an infinite number of yield surfaces between the initial and the ultimate yield surface, Fig. 3.3. In this study the parameter β , represents the isotropic hardening which defines the shape and the size of the initial and the subsequent yield surface.

For each stage of loading, therefore, there is a yield surface which can be reached by elastic behaviour beyond which plasticity takes place. This process continues until the peak stress corresponding to the ultimate yield surface is reached, Fig. 3.4. The concrete material may be liable to crack after its stress level reaches the ultimate yield surface providing the state of stress is in the tensile region. In the compression region, however, concrete exhibits strain-softening and this characteristic cannot be adequately described by the work-hardening concept. In order to account for the strain-softening in concrete, the technique proposed by Argyris et al [39] is adopted in this study. This technique enables the gradual collapse of the ultimate yield surface after the compressive strength has been achieved.

The following are the important stages which have been developed by the author to establish a triaxial concrete constitutive model within the concept of work-hardening plasticity.

- i) A triaxial yield surface is developed,
- ii) A failure criterion is proposed to represent the initial yield limit and the subsequent expansion and contraction of the yield surface,
- iii) An isotropic hardening rule is adopted here and the explicit expressions for the hardening parameter β , are proposed to monitor the variation of the yield surface with plastic flow,

- iv) A flow rule satisfying the normality condition is used to relate the inelastic strains to the current stress level, and
- v) A three dimensional incremental stress-strain relationship for concrete behaviour is developed.

3.3 The Proposed Triaxial Failure Surface

In the subsequent sections of this chapter a failure surface is developed which is able to predict the ultimate strength of concrete subjected to a triaxial state of stress. This surface is derived from the experimental results of previous investigators. It should be noted, that normally experiments are conducted by applying proportional loading under uniform stress or strain conditions which is not necessarily the case in actual structures. It is common practice, however, to predict the ultimate behaviour of the structural components subjected to non-uniform stress or strain conditions by assuming uniform loading condition. There is little justification for this hypothesis.

The general shape of the yield surface that is proposed here is shown in Fig. 3.5. It is basically a conical shaped surface with a non-circular base and curved meridians. This surface is mathematically defined in terms of the hydrostatic and the deviatoric stresses. The meridional planes pass through the equi-sectrix ($\sigma_1 = \sigma_2 = \sigma_3$) and the deviatoric planes are normal to it, Fig. 3.6. It is a requirement to have a three-fold type of symmetry at an equi-pressure cross-

section (deviatoric-section) to satisfy material isotropy. This means that only a sextant of the stress space need be considered. If the yield surface is constructed in principal stress space and $\sigma_1 \geq \sigma_2 \geq \sigma_3$, the region to be considered is bounded by the tensile meridian ρ_t , for $\sigma_1 = \sigma_2 > \sigma_3$, and the compressive meridian ρ_c , for $\sigma_1 > \sigma_2 = \sigma_3$. These meridians correspond to $\theta = 0^\circ$ and $\theta = 60^\circ$, respectively, where θ is the angle of similarity, Fig. 3.6a. The yield surface must be continuous [20] to produce a unique gradient which is used to determine the direction of the inelastic strains, i.e. the normality rule. The yield surface should also be convex [20] to assure material stability according to Drucker's postulate [48,49].

In the following sections explicit mathematical formulations for a yield surface are produced. The mathematical definition of the variables used is given in Appendix A.

3.3.1 Meridional Definition of the Proposed Yield Surface

The following functions are proposed to describe the tensile and compressive meridians of the yield surface, Fig. 3.6b. The stresses are normalised with respect to the uniaxial compressive strength of concrete f_{cu} , as follows

$$\bar{\xi} = m_1 + m_2 \bar{\rho}_t + m_3 \bar{\rho}_t^2 \quad (3.4)$$

$$\bar{\xi} = n_1 + n_2 \bar{\rho}_c + n_3 \bar{\rho}_c^2 \quad (3.5)$$

where $\bar{\xi}$ = hydrostatic component of stress,
 $\bar{\rho}_c$ = deviatoric component of the compressive
meridian,
 $\bar{\rho}_t$ = deviatoric component of the tensile
meridian, and
 $m_1, m_2, m_3, n_1, n_2,$ and n_3 = material parameters

The upper bar notation in Eq's. 3.4 and 3.5 refers to normalisation with respect to concrete uniaxial compressive strength.

Standard test results are used by the author to define the material parameters, e.g. uniaxial tensile and compressive, and equal biaxial compressive strength of concrete. That is to say, that the uniaxial compressive strength lies on the compressive meridian and the uniaxial tensile and biaxial compressive strengths lie on the tensile meridian. In addition to these points, two more values in the high compressive region are used. Finally, both meridians must pass through a common apex i.e

$$\bar{\rho}_c = \bar{\rho}_t = 0 \quad \text{at} \quad \bar{\xi} = 0 \quad (3.6)$$

There is, therefore, enough information to obtain the six material parameters in Eq's. 3.4 and 3.5, Fig. 3.7a. Using the strength ratios α_{tu} and α_{bc} defined as

$$\alpha_{tu} = \frac{f_{tu}}{f_{cu}} \quad \text{and} \quad \alpha_{bc} = \frac{f_{bc}}{f_{cu}} \quad (3.7)$$

where f_{cu} = uniaxial compressive strength of concrete,
 f_{tu} = uniaxial tensile strength of concrete, and
 f_{bc} = biaxial compressive strength of concrete

The applied constraints may be summarised as shown in Table 3.1.

Table 3.1 Boundary conditions used for the yield surface

Type of Test	θ	$\bar{\xi}$	$\bar{\xi}$
U.C	60°	$-1/\sqrt{3}$	$\sqrt{2/3}$
B.C	0°	$-\alpha_{bc}/\sqrt{3}$	$\sqrt{2}\alpha_{bc}/\sqrt{3}$
U.T	0°	$-\alpha_{tu}/\sqrt{3}$	$2\alpha_{tu}/\sqrt{3}$
A.P	60°	$-\bar{\xi}_{c0}$	$\bar{\rho}_{c0}$
A.P	0°	$-\bar{\xi}_{t0}$	$\bar{\rho}_{t0}$

where U.C. = uniaxial compression,
U.T. = uniaxial tension,
B.C. = biaxial compression, and
A.P. = arbitrary point in the high
compression region

Applying the above boundary conditions and rearranging Eq's. 3.4 and 3.5 in terms of $\bar{\rho}_c$ and $\bar{\rho}_t$, the tensile and compressive meridians become

$$\bar{\rho}_t = a_1 + a_2 \sqrt{a_3 + a_4 \bar{\xi}} \quad (3.8)$$

$$\bar{\rho}_c = b_1 + b_2 \sqrt{b_3 + b_4 \bar{\xi}} \quad (3.9)$$

where

$$a_1 = - \frac{2\alpha_{bc} + \alpha_{tu}}{2(\alpha_{bc} - \alpha_{tu})} a_2 + \frac{1}{\sqrt{6}}(\alpha_{bc} + \alpha_{tu})$$

$$a_2 = \frac{2(\alpha_{bc}^2 - \alpha_{tu}^2)(\sqrt{2}\alpha_{bc} - \sqrt{3}\bar{\rho}_{tc}) - \sqrt{2}(\alpha_{bc} - \alpha_{tu})(2\alpha_{bc}^2 - 3\bar{\rho}_{t0}^2)}{2\sqrt{3}[(2\alpha_{bc} + \alpha_{tu})(\sqrt{2}\alpha_{bc} - \sqrt{3}\bar{\rho}_{t0}) - \sqrt{2}(\alpha_{bc} - \alpha_{tu})(2\alpha_{bc} - \sqrt{3}\bar{\xi}_{t0})]}$$

$$a_3 = \left(\frac{a_1}{a_2}\right)^2 - \frac{2\alpha_{bc}}{3a_2} 2\sqrt{3} + \sqrt{6} \frac{a_1}{a_2} - \frac{\alpha_{bc}}{a_2}$$

$$a_4 = - \frac{2}{a_2}$$

$$b_1 = - \frac{1}{\sqrt{2}}(1 - \sqrt{3}\bar{\xi}_T)b_2 + \frac{1}{\sqrt{6}}$$

$$b_2 = \frac{(2\sqrt{3} - 3\sqrt{2}\bar{\rho}_{c0})\bar{\rho}_{c0}}{6[(1 - \sqrt{3}\bar{\xi}_T)\bar{\rho}_{c0} - \sqrt{2}(\bar{\rho}_{c0} + \bar{\xi}_T)]}$$

$$b_3 = \left(\frac{b_1}{b_2}\right)^2 + \frac{2\bar{\xi}_T}{b_2}$$

$$b_4 = - \frac{2}{b_2}$$

$$\bar{\xi}_0 = \frac{a_1^2 - a_3 a_2^2}{a_2^2 a_4}$$

Concrete material dilates at low hydrostatic pressure and compresses at high hydrostatic pressure. This behaviour is typical of granular materials and the associated effects can be modelled using a closed yield surface. Argyris et al [39]

have suggested that the conical failure surface be closed by an elliptic cap, Fig. 3.7b. A similar closed yield surface is used by Nilsson and Glemberg [32]. The conical yield surface is closed by two elliptic caps in the triaxial compression zone, Argyris et al [39]. The minor axes of these ellipses are defined by an additional parameter $\bar{\xi}_C$, along the equi-sectrix and the major axes by two points on the compressive and tensile meridians $\bar{\rho}_{c1}$ and $\bar{\rho}_{t1}$, respectively, which corresponds to $\bar{\xi}_1$ on the equi-sectrix, Fig. 3.7b. Thus the hydrostatic dependence in the cap zone is controlled by

$$\bar{\rho}_t = \bar{\rho}_{t1} \sqrt{1 - \left(\frac{\bar{\xi} - \bar{\xi}_1}{\bar{\xi}_1 - \bar{\xi}_C} \right)^2} \quad (3.10)$$

$$\bar{\rho}_c = \bar{\rho}_{c1} \sqrt{1 - \left(\frac{\bar{\xi} - \bar{\xi}_1}{\bar{\xi}_1 - \bar{\xi}_C} \right)^2} \quad (3.11)$$

The shape and size of the elliptic cap depends on the choice of $\bar{\xi}_1$ and $\bar{\xi}_C$, however, at present there is insufficient experimental evidence in triaxial loading at high compression to define these parameters adequately. The choice of the values of these parameters, therefore, relies somewhat on intuition. It is suggested to use values of 4.4 and 5.5 for $\bar{\xi}_1$ and $\bar{\xi}_C$, respectively.

Results obtained from the proposed Eq's. 3.8 and 3.9 for the meridians of the yield surface are compared with published experimental results of concrete [14,21,29,50,51]. These comparisons are shown in Fig's. 3.8a to 3.8e. It appears that a reasonable correlation may be achieved provided the correct

parameters are selected. The obvious problem is the choice of these parameters. It is, therefore, proposed that the following values to be used

$$\begin{aligned}\alpha_{bc} &= 1.2, \\ \alpha_{tu} &= 0.1, \\ \bar{\xi}_{c0} &= \bar{\xi}_{t0} = 6.0, \\ \bar{\rho}_{c0} &= 4.4, \text{ and} \\ \bar{\rho}_{t0} &= 3.3\end{aligned}$$

These parameters have been obtained from a regression analysis carried out by the author using selected experimental results obtained between the years 1928-1974. The resulting equations for the meridians are as follows

$$\bar{\rho}_t = -6.2441 + 4.2157 \sqrt{2.2790 + 0.4744 \bar{\xi}} \quad (3.12)$$

$$\bar{\rho}_c = -3.0696 + 3.7522 \sqrt{0.7649 + 0.5330 \bar{\xi}} \quad (3.13)$$

The comparison of the results obtained using the above equations and obtained from experimental work [14,19,21, 23,24,27,29,50-54] is given in Fig's. 3.9a to 3.9c.

3.3.2 Deviatoric Definition of the Proposed Yield Surface

The general equation for the deviatoric variation of the yield surface $\bar{\rho}_u$, for an arbitrary value of the angle of similarity θ , between 0° and 60° , is proposed. The equations are obtained by fitting a general elliptic curve between $\bar{\rho}_t$ and $\bar{\rho}_c$ in the deviatoric section of the yield surface.

The geometry of such an elliptic curve, in the X-Y plane, is shown in Fig. 3.10. The condition for convexity ($\bar{\rho}_c > \bar{\rho}_t/2$) is automatically satisfied and to have continuity $\bar{\rho}_t$ must coincide with the Y-axis and the direction of $\bar{\rho}_c$ must be normal to the elliptic curve, Fig. 3.10. The general form of an ellipse is considered to be

$$X^2 + a Y^2 + b XY + c X + d Y + e = 0 \quad (3.14)$$

To define the unknown parameters a, b, c, d and e in the above equation the following boundary conditions must be satisfied:

- i) The ellipse must pass through points A and B, Fig. 3.10
- ii) The tangent at A and B must be perpendicular to the direction of $\bar{\rho}_t$ and $\bar{\rho}_c$, respectively, Fig. 3.10.

The above conditions are used to obtain four of the unknown parameters in terms of the fifth parameter e. This unknown parameter is then obtained by means of a regression analysis to achieve the best fit to the experimental results of Launay and Gachon [21,30,55].

Having established the ellipse in the cartesian coordinate system X-Y, the polar equation of $\bar{\rho}_u$ for the variation of θ can be easily obtained by replacing X by $\bar{\rho}_u \sin\theta$ and Y by $\bar{\rho}_u \cos\theta$. The final result after some algebraic manipulation (see Appendix B) is as follows

$$\bar{\rho}_u = \bar{\rho}_u(\bar{\xi}, \theta) = \bar{\rho}_t \frac{A \cos\theta + B \sin\theta}{A \cos^2\theta + B \sin\theta \cos\theta + \sin^2\theta} \quad (3.15)$$

where $A = \frac{3\bar{\rho}_c(2\bar{\rho}_c - \bar{\rho}_t)}{2(2\bar{\rho}_t - \bar{\rho}_c)^2}$, and

$$B = \frac{\sqrt{3}\bar{\rho}_c(5\bar{\rho}_t - 4\bar{\rho}_c)}{2(2\bar{\rho}_t - \bar{\rho}_c)^2}$$

The comparison between the results of Eq. 3.15 and the experimental strength data of Kupfer et al [26] and Launay and Gachon [21] for the biaxial case ($\sigma_2 = 0$ section) and the triaxial case (deviatoric section) are shown in Fig's. 3.11a, 3.11b and 3.11c, respectively.

3.4 The Proposed Failure Criterion

The failure criterion adopted here compares the deviatoric component ρ , of the stress tensor σ_{ij} , with the corresponding deviatoric component of the yield surface $\bar{\rho}_u$. The failure criterion is satisfied when ρ reaches $\bar{\rho}_u$. This condition is defined as follows

$$f(\sigma_{ij}) = \rho - f_{cu} \bar{\rho}_u = 0 \quad (3.16)$$

where

$$\rho = \sqrt{2J_2},$$

$$\bar{\rho}_u = \frac{\rho_u}{f_{cu}}$$

= deviatoric component of the yield surface given by Eq. 3.15, and

f_{cu} = uniaxial compressive strength of concrete

It has been previously stated that plasticity in concrete occurs at some stress level below the ultimate and failure is achieved by progressive yielding of the material. This phenomenon is incorporated into the yield criterion (Eq. 3.16) by an isotropic hardening approach, which assumes that the initial yield surface (the elastic limit) and thereafter any subsequent yield surface (loading surface) has basically the same geometrical shape as the ultimate yield surface. The intermediate yield surface is defined by the uniform reduction of the ultimate yield surface according to the ratio of the current stress position vector R , to that of the corresponding maximum value R_{\max} , Fig. 3.12. Introducing the hardening parameter β , into Eq. 3.16, the intermediate yield criterion is written as

$$f(\sigma_{ij}, \beta) = \rho - \beta f_{cu} \bar{\rho}_u = 0 \quad (3.17)$$

where $\bar{\rho}_u = \bar{\rho}_u(\bar{\xi}_u, \theta)$,

$$\bar{\xi}_u = \frac{\bar{\xi}}{\beta}, \text{ and}$$

$$\beta = \frac{R}{R_{\max}}$$

The geometrical representation of the intermediate yield surface is illustrated in Fig. 3.13.

In the pre-ultimate state of stress the value of the hardening parameter β , is less than unity and increases to represent the progressive yielding until it reaches the

maximum value of unity, which corresponds to the peak stress level. Thereafter, strain-softening is represented by assuming a progressive reduction of β until some residual value β_r , is achieved. This process implies the gradual collapse of the yield surface rather than the case of ductile material, for which the ultimate yield surface remains unchanged or the case of brittle material, for which the failure surface suddenly collapses and the stress level drops to zero. These extreme cases may be considered as the upper and lower bounds of the proposed strain-softening material. Fig. 3.14 shows the variation of the parameter β with the deformation.

3.5 Mathematical Definition of the Proposed Hardening and Softening Parameter

The hardening and softening parameter β , is developed in this section in order to define the initial and the subsequent yield surfaces.

The experimental results of previous investigators [23,24, 26,51,56,57] indicate that initial yielding corresponds to 30-60 percent of the ultimate strength of concrete. Thereafter, the stress-strain behaviour of concrete is nonlinear upto a peak stress followed by strain-softening. The variation of the parameter β is, therefore, attributed to the development of inelastic strains. Thus, β is expressed as

$$\beta = f(\epsilon_{ij}^p) \quad (3.18)$$

where $f(\epsilon_{ij}^p)$ = a function of inelastic strain

In this study a scalar quantity of the plastic strain, e.g. the effective plastic strain is used to quantify the parameter β as follows

$$\beta = f(\epsilon_p) \quad (3.19)$$

and

$$\begin{aligned} \epsilon_p &= \int d\epsilon_{ij}^p d\epsilon_{ji}^p \\ &\doteq \epsilon_{ij}^p \epsilon_{ji}^p \end{aligned} \quad (3.20)$$

where ϵ_{ij} = tensor of total plastic strain,
 $d\epsilon_{ij}$ = tensor of plastic strain increment, and
 ϵ_p = effective plastic strain

The schematic variation of β with ϵ_p is shown in Fig. 3.15. The following regions are distinguished for the development of Eq. 3.19 (see Fig. 3.15)

i) material hardening exists when:

$$\beta_0 \leq \beta \leq \beta_u \quad \text{and} \quad \epsilon_p \leq \epsilon_{p,u}$$

ii) material softening exists when:

$$\beta_u > \beta \geq \beta_r \quad \text{and} \quad \epsilon_p \geq \epsilon_{p,u}$$

where β_0 = hardening parameter at initial yielding,
 β_u = hardening parameter at peak stress,
 β_r = residual hardening parameter,
 ϵ_p = effective plastic strain, and
 $\epsilon_{p,u}$ = effective plastic strain at peak stress

The experimental results of Kupfer et al [26] and Ahmad [58] are used to determine the mathematical function $f(\epsilon_p)$ for the variation of β . These experimental results are used to calculate R and R_{\max} (Fig. 3.12) at each stress level, hence the ratio

$$\beta = \frac{R}{R_{\max}} \quad (3.21)$$

and the plastic strain tensor ϵ_{ij}^p , is calculated as

$$\epsilon_{ij}^p = \epsilon_{ij} - \epsilon_{ij}^e \quad (3.22)$$

where ϵ_{ij} = total strain tensor,
 ϵ_{ij}^e = total elastic strain tensor, and
 ϵ_{ij}^p = total plastic strain tensor

The effective plastic strain ϵ_p , is obtained by substituting the result of Eq. 3.22 into Eq. 3.20. A series of data are generated in this way and the mathematical formulations of β are obtained by curve fitting techniques (least square and error minimisation) using the experimental data. The result is as follows

$$\beta = c_1 + c_2 X + c_3 X^2 + c_4 X^4 \quad \text{for } 0 \leq X \leq 1.0 \quad (3.23)$$

$$\beta = e^{-c_5 \left(1.0 - \frac{1}{X}\right)^{c_6}} \quad \text{for } X > 1.0 \quad (3.24)$$

where

$$X = \frac{\epsilon_p}{\epsilon_{p,u}}$$

ϵ_p = effective plastic strain,
 $\epsilon_{p,u}$ = effective plastic strain at peak stress,
 $c_1 = 0.35$,
 $c_2 = 1.5208$,
 $c_3 = -1.0916$,
 $c_4 = 0.2208$,
 $c_5 = 1.17$, and
 $c_6 = 3.61$

the value of $\epsilon_{p,u}$ is dependent upon the state of stress at the peak stress level. A relatively simple method is proposed in the following section to evaluate this parameter. From a regression analysis of data the initial and residual values of β are found to be

$$\beta_0 = 0.35 \quad \text{and} \quad \beta_r = 0.45$$

The fit of Eq. 3.20 to the experimental results [26,58] is given in Fig. 3.16.

3.5.1 Determination of the Effective Plastic Strain at Peak Stress

The concept of the effective plastic strain ϵ_p , is discussed in section 3.5. In this section a technique is proposed for the calculation of the effective plastic strain at peak stress $\epsilon_{p,u}$, for the use in Eq's. 3.23 and 3.24. At first, the relationship for the determination of ϵ_p (Eq. 3.20) is

rearranged and is expressed in terms of the octahedral normal and shear strains (see Appendix C). The resulting formulation is as follows

$$\epsilon_p = \sqrt{3(\epsilon_0^p{}^2 + \gamma_0^p{}^2)} \quad (3.25)$$

where ϵ_0^p = plastic octahedral normal strain, and
 γ_0^p = plastic octahedral shear strain

The ultimate effective plastic strain $\epsilon_{p,u}$, is now obtained from Eq. 3.25 by replacing ϵ_0^p and γ_0^p by their corresponding ultimate values $\epsilon_{0,u}^p$ and $\gamma_{0,u}^p$, respectively. At this stage the ultimate plastic octahedral normal and shear strains $\epsilon_{0,u}^p$ and $\gamma_{0,u}^p$, are calculated from the following equations

$$\epsilon_{0,u}^p = \epsilon_{0,u} - \epsilon_{0,u}^e \quad (3.26)$$

$$\gamma_{0,u}^p = \gamma_{0,u} - \gamma_{0,u}^e \quad (3.27)$$

where $\epsilon_{0,u}$ = ultimate octahedral normal strain,
 given by Eq. 3.26

$\gamma_{0,u}$ = ultimate octahedral shear strain,
 given by Eq. 3.27

$\epsilon_{0,u}^e = \frac{\sigma_{0,u}}{3K_0}$ = ultimate elastic octahedral
 normal strain,

$\gamma_{0,u}^e = \frac{\tau_{0,u}}{2G_0}$ = ultimate elastic octahedral
 shear strain,

K_0 = initial bulk modulus, and

G_0 = initial shear modulus

The author proposes the use of Ahmad and Shah's formulations [59] for the calculation of the ultimate octahedral normal and shear strains $\epsilon_{0,u}$ and $\gamma_{0,u}$. They obtained their relationships using the experimental results reported in References [26,51,52,60,61] and given as

$$\epsilon_{0,u} = 0.197877 e^{0.9475 \left(\frac{\sigma_{0,u}}{f_{cu}} \right)} (\epsilon_{0,u})_{uni} \quad (3.28)$$

$$\gamma_{0,u} = -4.8629 + 12.756 \left(\frac{\tau_{0,u}}{f_{cu}} \right) (\gamma_{0,u})_{uni} \quad (3.29)$$

where

$$(\epsilon_{0,u})_{uni} = 0.001648 + 0.000114 f_{cu},$$

$$(\gamma_{0,u})_{uni} = 0.0011775 f_{cu}^{0.12817},$$

$\sigma_{0,u}$ = octahedral normal strength,
 $\tau_{0,u}$ = octahedral shear strength, and
 f_{cu} = concrete uniaxial compressive strength in ksi

Eq's. 3.25 to 3.29 are combined to calculate $\epsilon_{p,u}$ provided the ultimate octahedral stresses $\sigma_{0,u}$ and $\tau_{0,u}$ are known. These quantities are obtained geometrically from a known stress location, e.g. $\bar{\xi}$ and $\bar{\rho}$ (point A in Fig. 3.17). The ultimate values are predicted assuming proportional loading and extending the current stress vector until it intersects the ultimate yield surface at point B, Fig 3.17. The stresses corresponding to this point $\bar{\xi}_u$ and $\bar{\rho}_u$ (Fig.3.17), are used to calculate the ultimate octahedral stresses $\sigma_{0,u}$ and $\tau_{0,u}$, for use in Eq's. 3.26 to 3.29. Therefore,

$$\sigma_{0,u} = \frac{1}{\sqrt{3}} f_{cu} \bar{\epsilon}_u \quad (3.30)$$

$$\tau_{0,u} = \frac{1}{\sqrt{3}} f_{cu} \bar{p}_u \quad (3.31)$$

3.6 Incremental Stress-Strain Relationship for Concrete

In this section an elastic-plastic constitutive relationship for the incremental stress-strain behaviour of concrete is developed. The strain increments are decomposed into elastic and plastic components as

$$d\epsilon_{ij} = d\epsilon_{ij}^e + d\epsilon_{ij}^p \quad (3.32)$$

where $d\epsilon_{ij}$ = increment of strain tensor,
 $d\epsilon_{ij}^e$ = increment of elastic strain tensor, and
 $d\epsilon_{ij}^p$ = increment of plastic strain tensor

The increments of stress are related to the elastic strain increments using Hook's law, Fig. 3.18, as follows

$$d\sigma_{ij} = D_{ijkl}^e d\epsilon_{kl}^e \quad (3.33)$$

where D_{ijkl}^e = elastic modular matrix

Combining Eq. 3.32 and Eq 3.33, results in

$$d\sigma_{ij} = D_{ijkl}^e (d\epsilon_{kl} - d\epsilon_{kl}^p) \quad (3.34)$$

The increments of plastic strain are defined by a 'flow rule' (normality rule) [48,49,62-65]. Such a rule satisfies the

plastic flow requirements that the shape of the plastic potential g , remains unchanged and the stress vector stays on the surface g while the plastic strains continuously increase. Inelastic strains, therefore, make no contribution towards the elastic strain energy. This condition requires the plastic strain increments to be perpendicular to the surface g , Fig 3.19. The flow rule is, therefore, given as

$$d\varepsilon_{ij}^p = d\lambda \frac{\partial g}{\partial \sigma_{ij}} \quad (3.35)$$

where g = plastic potential,

$$\frac{\partial g}{\partial \sigma_{ij}} = \text{direction of the normal, and}$$

$$d\lambda = \text{proportionality parameter}$$

The magnitude of the plastic strain increment depend upon the proportionality parameter $d\lambda$ which must always be positive. This parameter remain to be obtained.

During plastic flow the yield surface must remain unchanged to ensure that the stress path describes a trajectory on the yield surface. This requirement is known as the 'consistency condition' and is written as

$$df(\sigma_{ij}, \beta) = 0 \quad (3.36)$$

or

$$df = \frac{\partial f^T}{\partial \sigma_{ij}} d\sigma_{ij} + \frac{\partial f}{\partial \beta} d\beta = 0 \quad (3.37)$$

where f = current yield surface,

$\frac{\partial f}{\partial \sigma_{ij}}$ = the gradient vector of the yield surface, and

$\frac{\partial f}{\partial \beta}$ = the change of yield surface with the hardening parameter, β

The derivation of $\frac{\partial f}{\partial \sigma_{ij}}$ and $\frac{\partial f}{\partial \beta}$ is given in Appendix D.

The consistency condition Eq. 3.37, may be written as

$$\begin{aligned} \frac{\partial f}{\partial \sigma_{ij}} d\sigma_{ij} &= - \frac{\partial f}{\partial \beta} d\beta \\ &= - \frac{\partial f}{\partial \beta} \frac{\partial \beta}{\partial \epsilon_p} d\epsilon_p \end{aligned} \quad (3.38)$$

where $d\epsilon_p = \sqrt{d\epsilon_{ij}^p d\epsilon_{ji}^p}$

From the flow rule $d\epsilon_p$ can be expressed as

$$d\epsilon_p = d\lambda \sqrt{\frac{\partial g}{\partial \sigma_{ij}} \frac{\partial g^T}{\partial \sigma_{ij}}} \quad (3.39)$$

Combining Eq's. 3.38 and 3.39 yields the following

$$\frac{\partial f}{\partial \sigma_{ij}} d\sigma_{ij} = - \frac{\partial f}{\partial \beta} \frac{\partial \beta}{\partial \epsilon_p} \sqrt{\frac{\partial g}{\partial \sigma_{ij}} \frac{\partial g^T}{\partial \sigma_{ij}}} d\lambda \quad (3.40)$$

Pre-multiplying Eq. 3.34 by $\frac{\partial f^T}{\partial \sigma_{ij}}$ and combining the results

with Eq's. 3.35 and 3.40 to solve for $d\lambda$ results in

$$d\lambda = \frac{\frac{\partial f}{\partial \sigma_{mn}} D_{mnkl}^e}{-\frac{\partial f}{\partial \beta} \frac{\partial \beta}{\partial \epsilon_p} \sqrt{\frac{\partial g}{\partial \sigma_{ij}} \frac{\partial g^T}{\partial \sigma_{ij}}} + \frac{\partial f^T}{\partial \sigma_{mn}} D_{mnkl}^e \frac{\partial g}{\partial \sigma_{kl}}} d\epsilon_{kl} \quad (3.41)$$

The incremental stress-strain relationship of concrete is obtained by substituting Eq. 3.35 into Eq. 3.34 in conjunction with Eq. 3.41. The result is given as

$$d\sigma_{ij} = D_{ijkl}^{ep} d\epsilon_{kl} \quad (3.42)$$

where $D_{ijkl}^{ep} = D_{ijkl}^e - D_{ijkl}^p$

= elastic-plastic modular matrix,

D_{ijkl}^e = elastic modular matrix, and

$$D_{ijkl}^p = \frac{D_{ijmn}^e \frac{\partial g}{\partial \sigma_{mn}} \frac{\partial f^T}{\partial \sigma_{rs}} D_{rskl}^e}{-\frac{\partial f}{\partial \beta} \frac{\partial \beta}{\partial \epsilon_p} \sqrt{\frac{\partial g}{\partial \sigma_{uv}} \frac{\partial g^T}{\partial \sigma_{uv}}} + \frac{\partial f^T}{\partial \sigma_{mn}} D_{mnr s}^e \frac{\partial g}{\partial \sigma_{rs}}}$$

= plastic modular matrix

A general incremental stress-strain relationship for concrete may be written in tensorial form by assuming an associated

flow rule, i.e $g = f$, and by substituting the yield surface gradient $\frac{\partial f}{\partial \sigma}$, and the elastic modular matrix D^e , in Eq. 3.42.

This relationship is given by

$$d\sigma_{ij} = \frac{E}{(1 + \nu)(1 - 2\nu)} (C_{ijkl} - \mu \Phi_{ijkl}) d\epsilon_{kl} \quad (3.43)$$

where $C_{ijkl} = \frac{1}{2}(1-2\nu)(\delta_{ik}\delta_{jl} + \delta_{il}\delta_{jk}) + \nu\delta_{ij}\delta_{kl}$,

$$\Phi_{ijkl} = \kappa_1\delta_{ij}\delta_{kl} + \kappa_2[(\delta_{ij}+1)\delta_{kl}\eta_{ij} + (\delta_{kl}+1)\delta_{ij}\eta_{kl}] + \kappa_3(\delta_{ij}+1)(\delta_{kl}+1)\eta_{ij}\eta_{kl} ,$$

$$\eta_{ij} = \chi s_{ij} + \psi s_{im}s_{mj} ,$$

$$\kappa_1 = \frac{\kappa_2}{1-2\nu} ,$$

$$\kappa_2 = [(1+\nu)\omega + 2\nu\psi J_2](1-2\nu) ,$$

$$\kappa_3 = (1-2\nu)^2 ,$$

$$\omega = \zeta - \frac{2}{3}\psi J_2 ,$$

$$\zeta = \frac{\partial f}{\partial \bar{\rho}_u} \frac{\partial \bar{\rho}_u}{\partial \bar{\xi}} \frac{\partial \bar{\xi}}{\partial I_1} ,$$

$$\chi = \frac{\partial f}{\partial \bar{\rho}} \frac{\partial \bar{\rho}}{\partial J_2} - \beta f_{cu} \frac{\partial \bar{\rho}_u}{\partial J_2} ,$$

$$\psi = \frac{\partial \bar{\rho}_u}{\partial J_3} ,$$

$$\rho = \sqrt{2J_2} ,$$

$$\xi = \frac{I_1}{\sqrt{3}},$$

$$\mu = \frac{E}{\alpha(1+\nu)(1-2\nu)},$$

$$\alpha = h + \frac{[(1+\nu)(3\omega+4\psi J_2)\omega+4(1-\nu)\psi^2 J_2^2+(1-2\nu)J_4]}{(1+\nu)(1-2\nu)} E,$$

$$h = \gamma (3\omega+4\psi J_2)\omega + 4\psi^2 J_2^2 + J_5$$

$$\gamma = - \frac{\partial f}{\partial \beta} \frac{\partial \beta}{\partial \epsilon_p},$$

$$J_4 = \frac{1}{2}(\eta_{12}^2 + \eta_{23}^2 + \eta_{31}^2) - 2(\eta_{11}\eta_{22} + \eta_{22}\eta_{33} + \eta_{33}\eta_{11}),$$

$$J_5 = J_4 + \frac{1}{2}(\eta_{12}^2 + \eta_{23}^2 + \eta_{31}^2)$$

β = the hardening parameter ,

f_{cu} = concrete uniaxial compressive strength ,

E = Young's modulus , and

ν = Poisson's ratio

Explicit expressions for ζ , χ , ψ and γ are given in Appendix D. The derivation of Eq. 3.43 is fully explained in Appendix E.

3.7 Comparison of the Proposed Constitutive Model with Experimental Results

In this section some experimental results found in the literature are compared with the numerical results obtained from the proposed constitutive model. The experimental

results of Kupfer et al [26] , Kotsovos [66], and Kotsovos and Newman [46,67] form the standard against which the proposed material model has been assessed.

In most cases it is extremely difficult to simulate the loading history applied to the specimens in the actual experiments. Comparisons, therefore, have been conducted for certain test cases in which the strain rate is controlled for a given principal stress ratio. Four types of loading have been investigated and these are; the uniaxial compression; the equal biaxial compression; the triaxial compression; and the triaxial extension tests.

Fig's. 3.20a and 3.20b show the fit of uniaxial and equal biaxial compression curves. Some deviation between the mathematical model and the uniaxial test case can be observed. The proposed model does not predict the lateral strains accurately. However, the peak stresses are in very close agreement with the corresponding experimental values.

Fig's. 3.21a, 3.21b and 3.21c show the fit of triaxial compression curves. The hydrostatic pressure was applied by imposing equal strain increments in the principal directions until the prescribed confining pressure σ_h , was achieved. Then, the lateral pressure was fixed and only the axial stress was increased. It is noted that very close correlation exists between the experimental and the analytical results, particularly for high strength concretes.

Fig's. 3.22a, 3.22b and 3.22c show the fit of triaxial extension curves. The hydrostatic pressure was applied in a

similar way to the triaxial compression tests. For this series of tests, however, the lateral pressure was fixed and the axial stresses were gradually removed until the applied stress was reduced to zero. A reasonably good fit is achieved while the prediction of the general trend of the curves is considered to be satisfactory.

Fig's. 3.23a to 3.23e compare the volumetric response of the proposed concrete model with the uniaxial, biaxial and triaxial compression experimental results. The proposed analytical model produces excessive dilation, especially near the ultimate strength. This shortcoming could be improved by using a non-associated flow rule and introducing an independent hardening parameter to control the movement of the cap zone according to the variation of the plastic volumetric strains. However, a lack of experimental results prevents a reasonable theoretical model to be proposed to describe this effect.

3.8 Conclusions

A failure surface containing all three stress invariants has been proposed. This surface is defined by curved meridians and a non-circular base which changes from nearly triangular to a more circular shape with increasing hydrostatic pressure. This surface is closed by an elliptic cap in the compression zone to control the material dilation. The mathematical model of the yield surface is obtained by fitting curves to the available experimental strength data. The resulting yield surface conforms with the generally accepted shape requirements and was found to closely fit

published biaxial and triaxial strength data.

An isotropic hardening and softening model has been developed to control the expansion and contraction of the yield surface during plastic flow and in the strain-softening region. The hardening parameter β , is defined in terms of the effective plastic strain ϵ_p . This parameter monitors the movement of both the conical surface and the elliptic cap.

An incremental stress-strain constitutive relationship has been developed using the proposed yield surface in conjunction with a flow rule. The results of this model are compared with a selection of experimental test results. The proposed model agrees qualitatively, well with all the test cases and the prediction of the peak stresses is favourable. The deviations from the experimental results are observed in relation to the lateral strains and in particular to the volumetric response. The material dilatancy according to the model appears to be too abrupt at the instant of material instability. These discrepancies are attributed to the use of an associated flow rule and lack of an independent volumetric hardening parameter to monitor the movement of the yield surface.

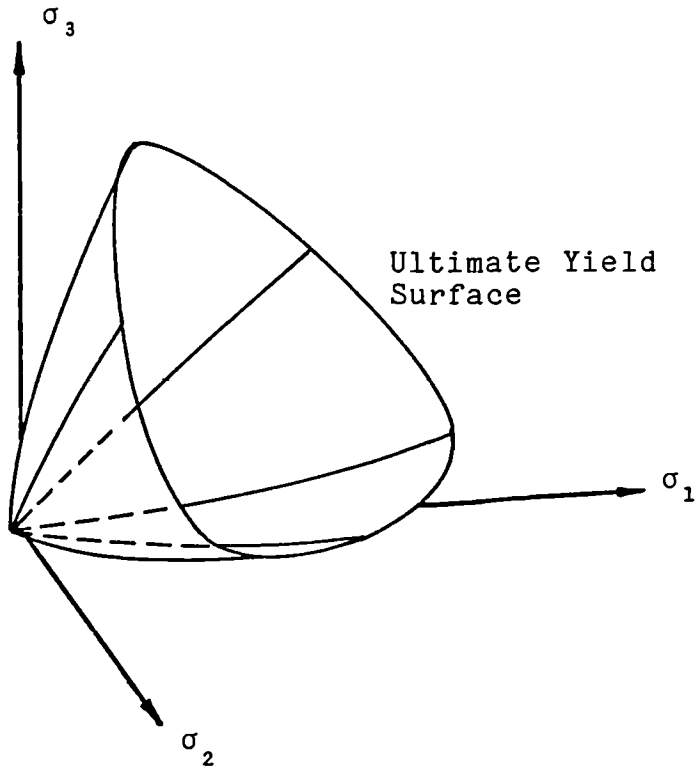


Fig. 3.1 Schematic representation of a yield surface.

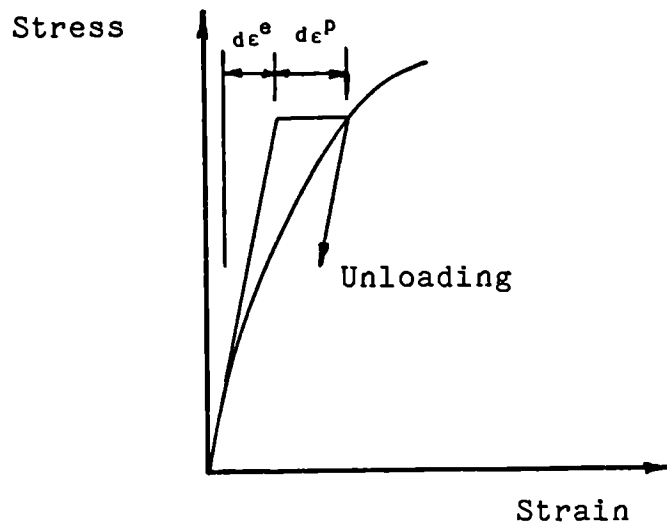
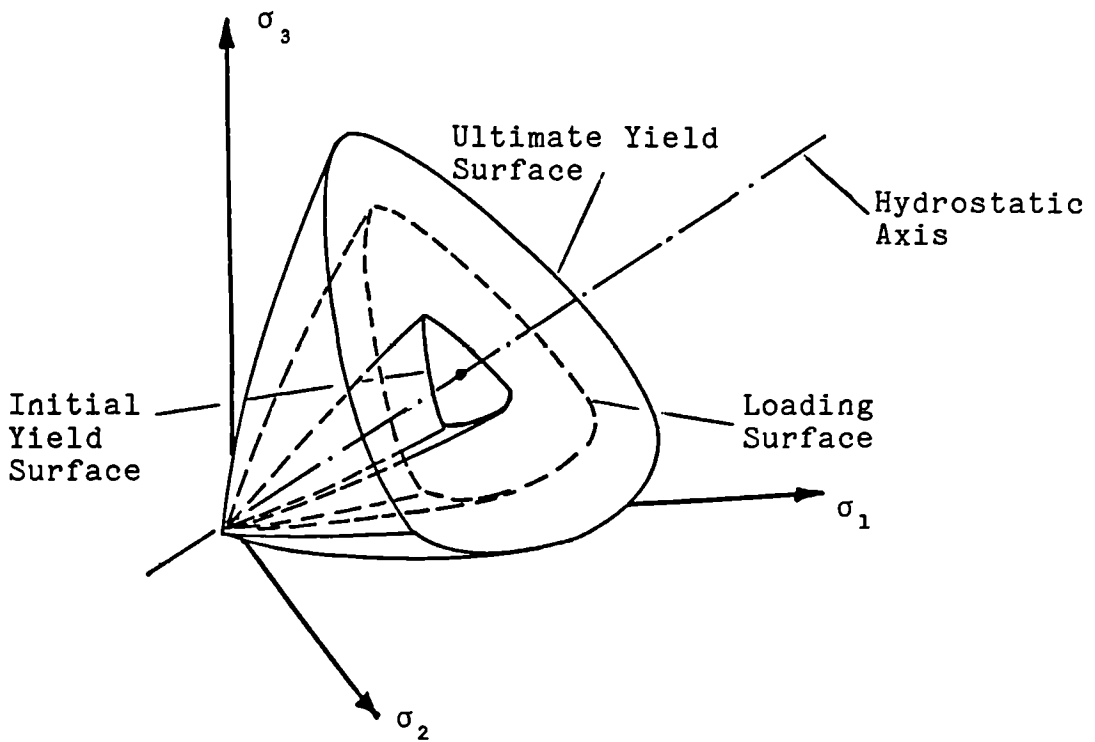
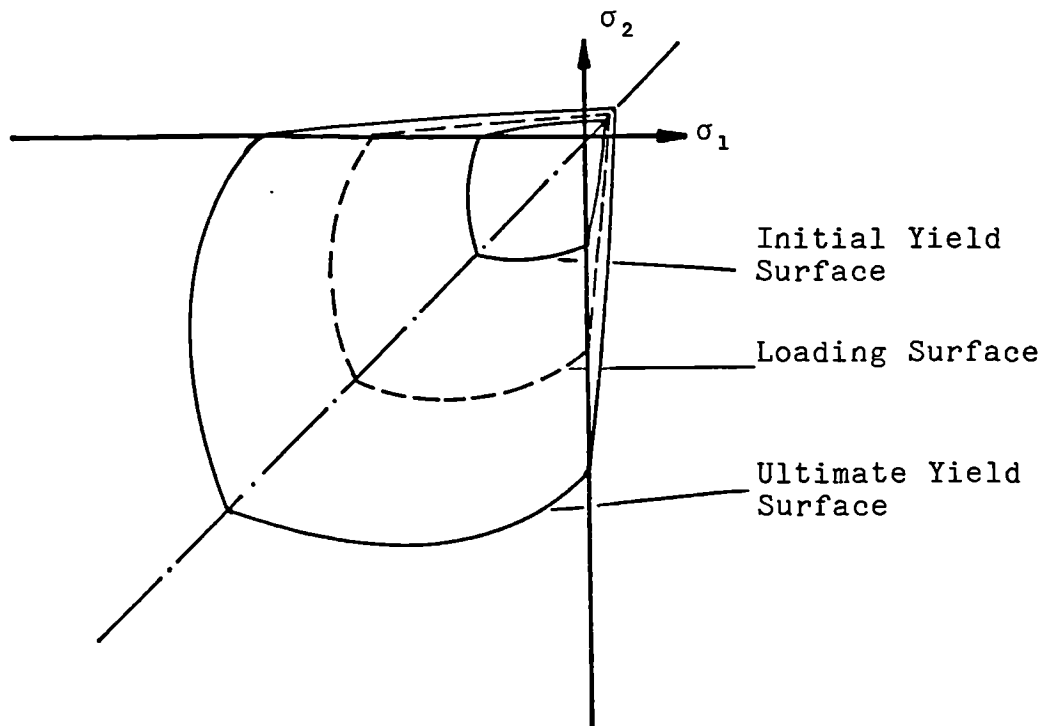


Fig. 3.2 Schematic representation of plastic material behaviour.



(a) Triaxial Representation



(b) Biaxial Representation

Fig. 3.3 Isotropic hardening expansion of the failure surface.

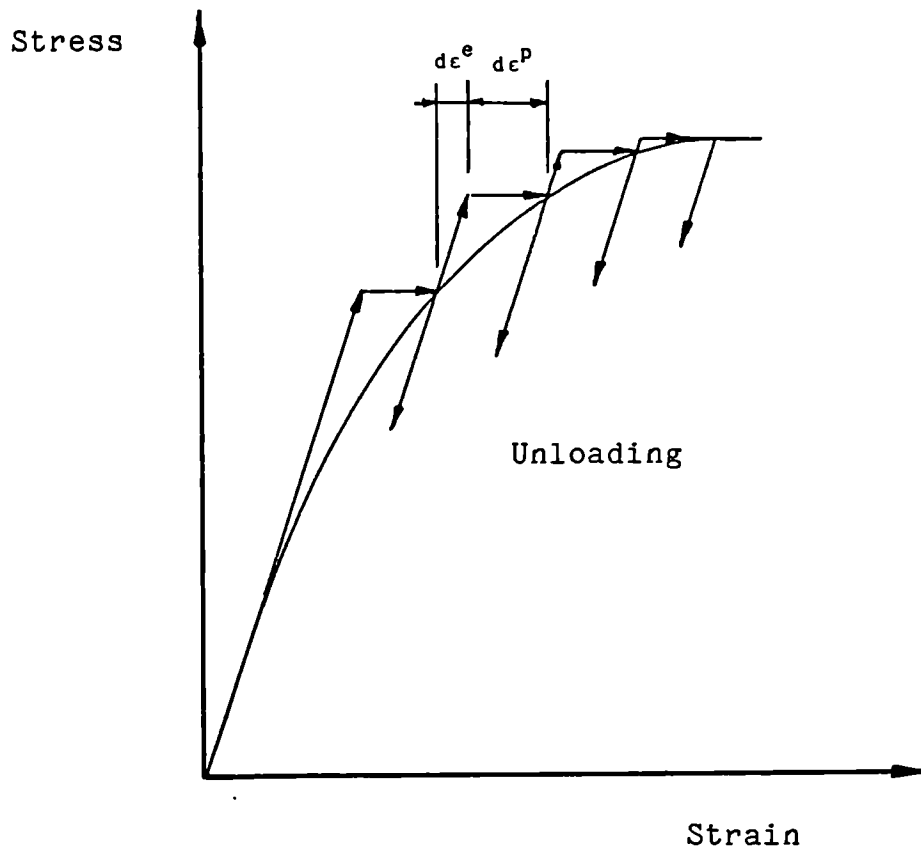


Fig. 3.4 Schematic representation of plastic strain hardening material behaviour.

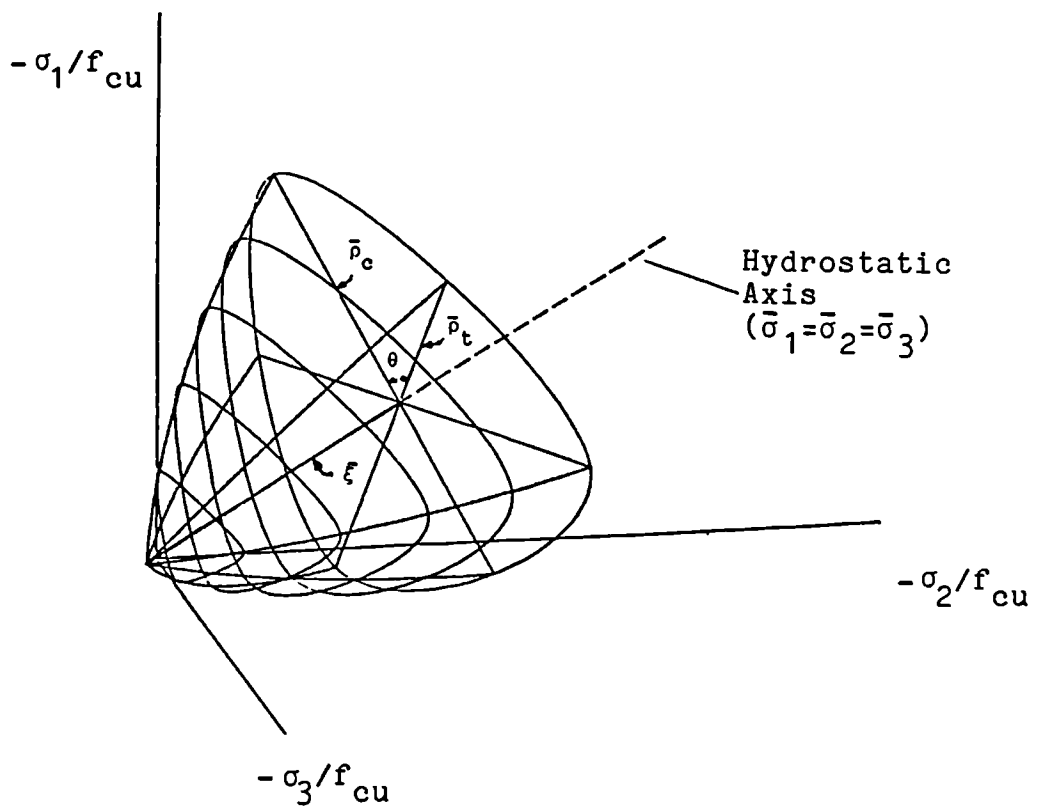
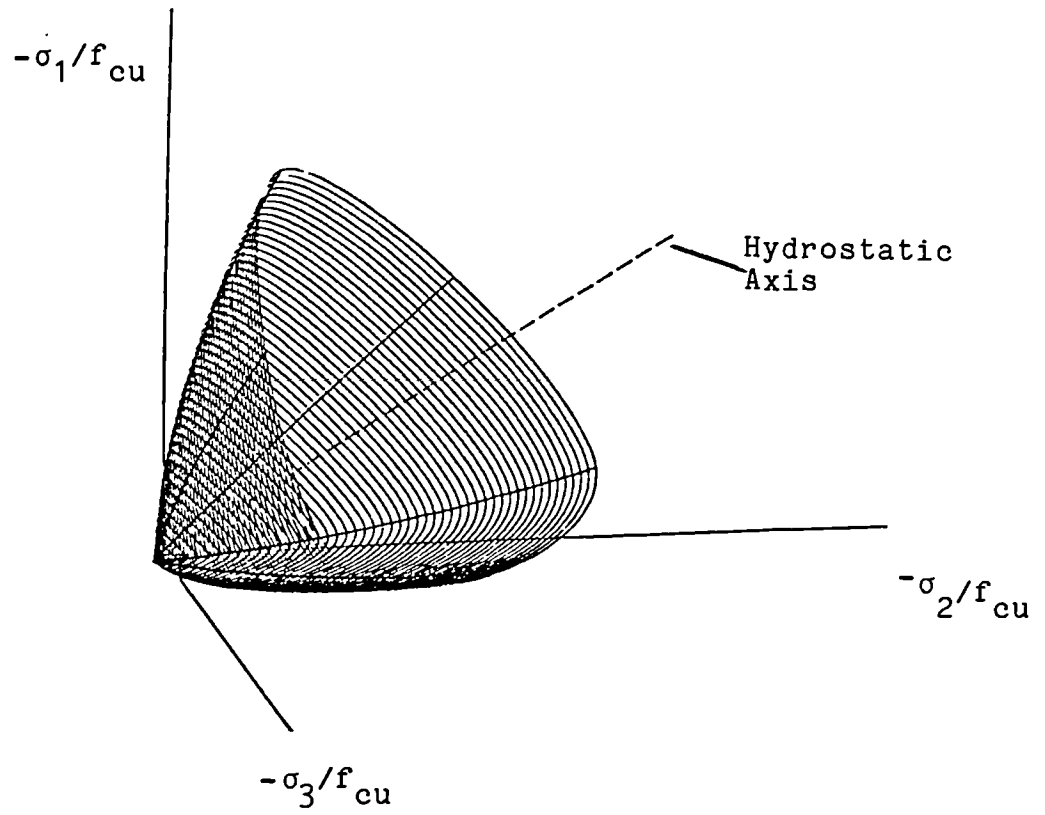


Fig. 3.5 General shape of the proposed failure surface.

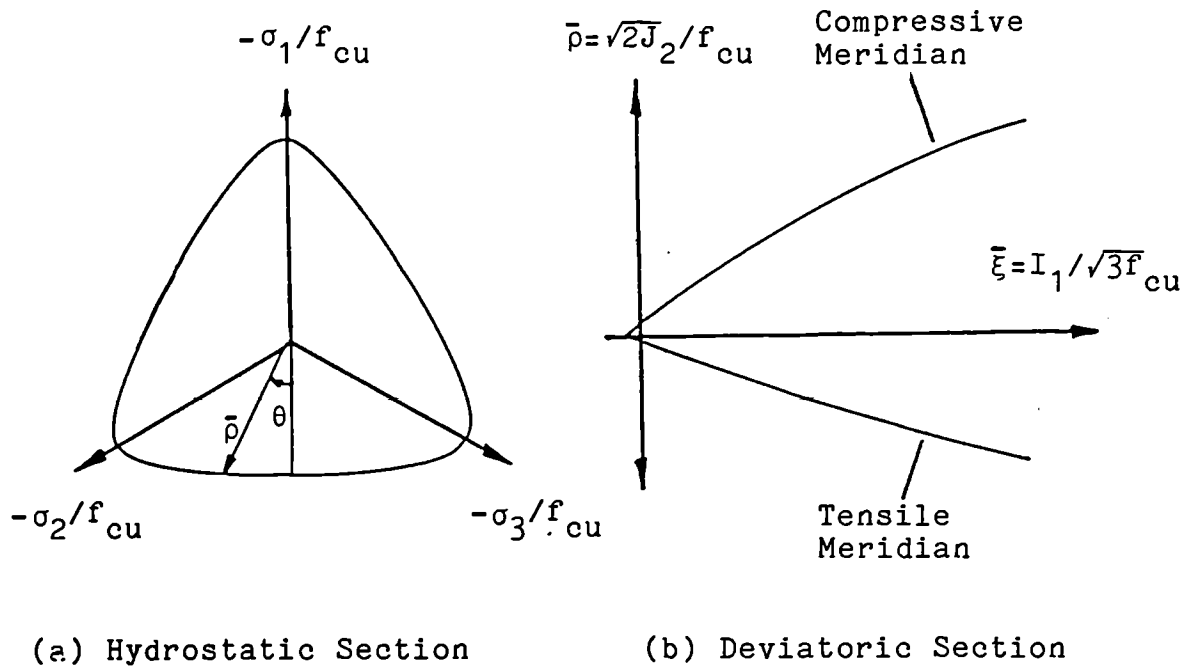


Fig. 3.6 Deviatoric and hydrostatic sections of the proposed failure surface.

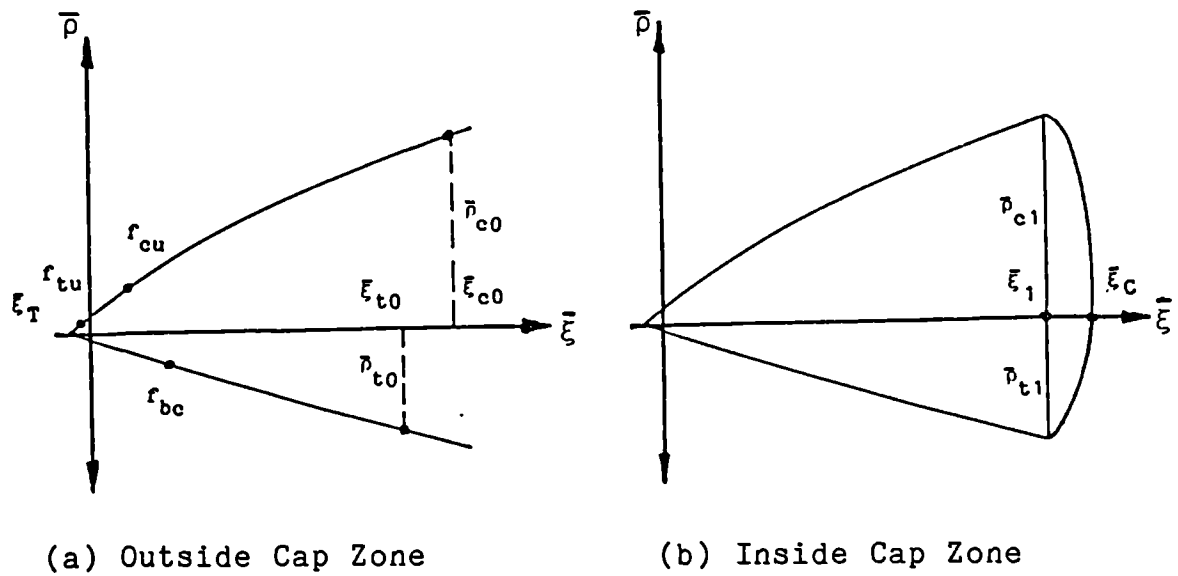
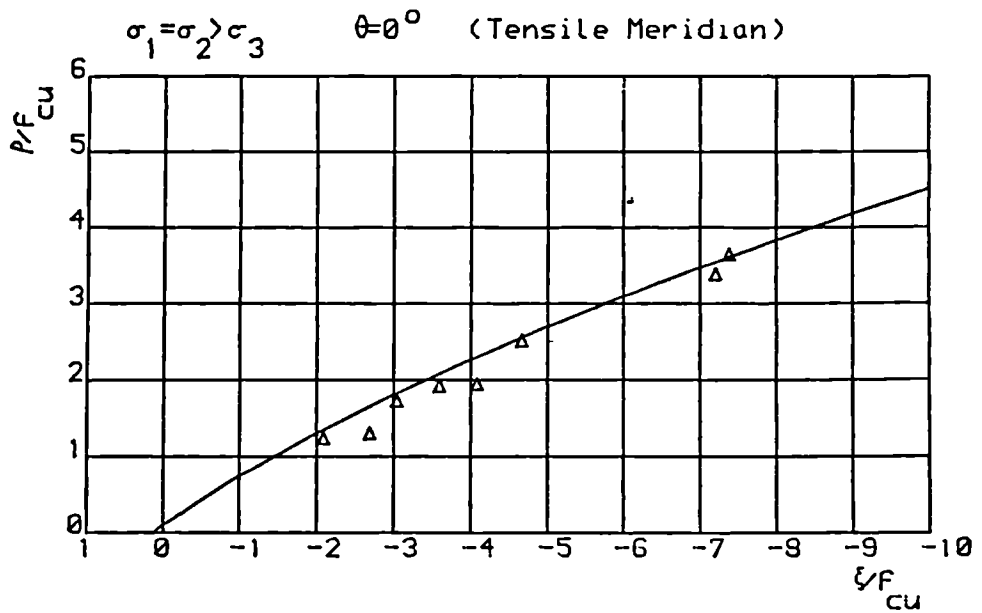
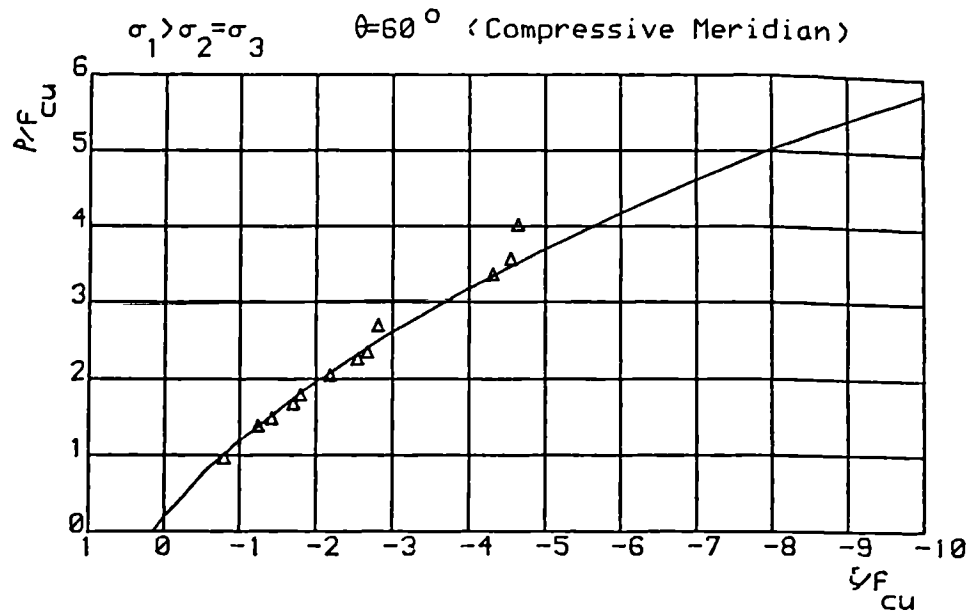


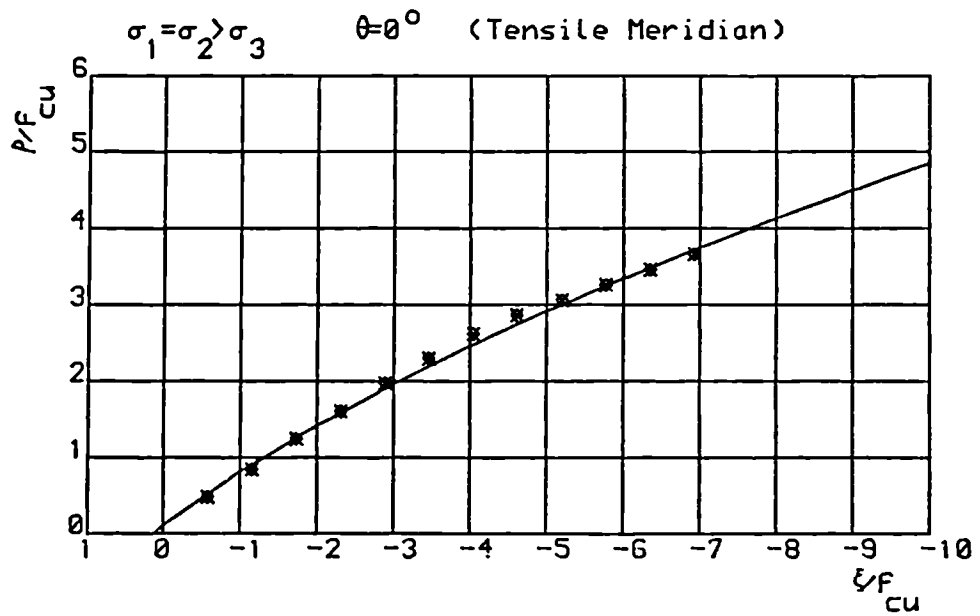
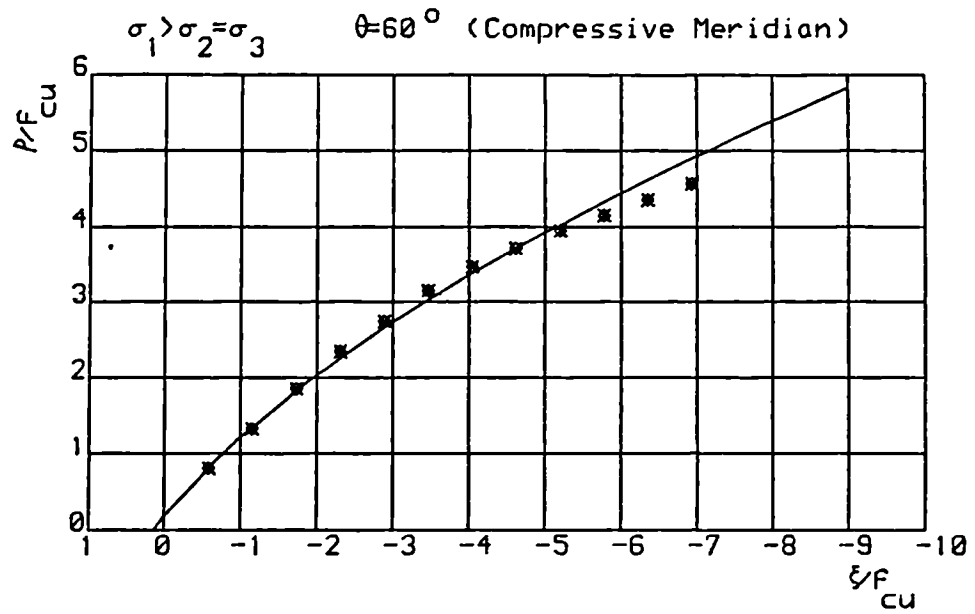
Fig. 3.7 Schematic representation of the boundary conditions for the proposed failure surface.



— Suggested Theory $a_t = .09$
 Δ Richart et al [14] $a_{bc} = 1.16$
 $\bar{\xi}_{co} = 5.00$ $\bar{P}_{co} = 3.70$
 $\bar{\xi}_{to} = 5.00$ $\bar{P}_{to} = 2.70$

(a)

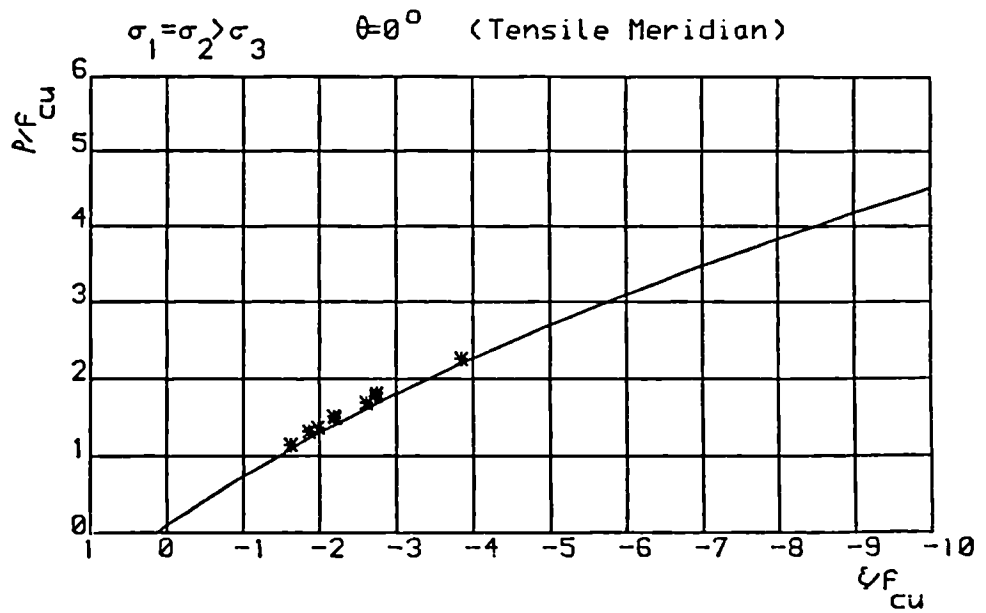
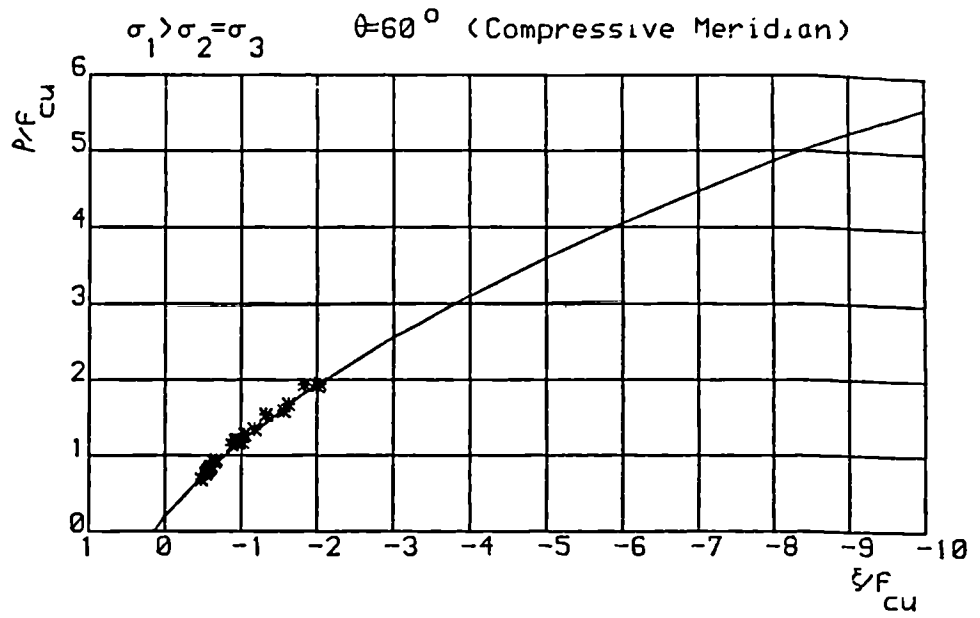
Fig. 3.8 Comparison of the proposed compressive and tensile meridians with experimental results.



— Suggested Theory $\alpha_t = .09$
 * Launay & Gachon [21] $\alpha_{bc} = 1.80$
 $\bar{\xi}_{co} = 6.00$ $\bar{p}_{co} = 4.45$
 $\bar{\xi}_{to} = 6.00$ $\bar{p}_{to} = 3.35$

(b)

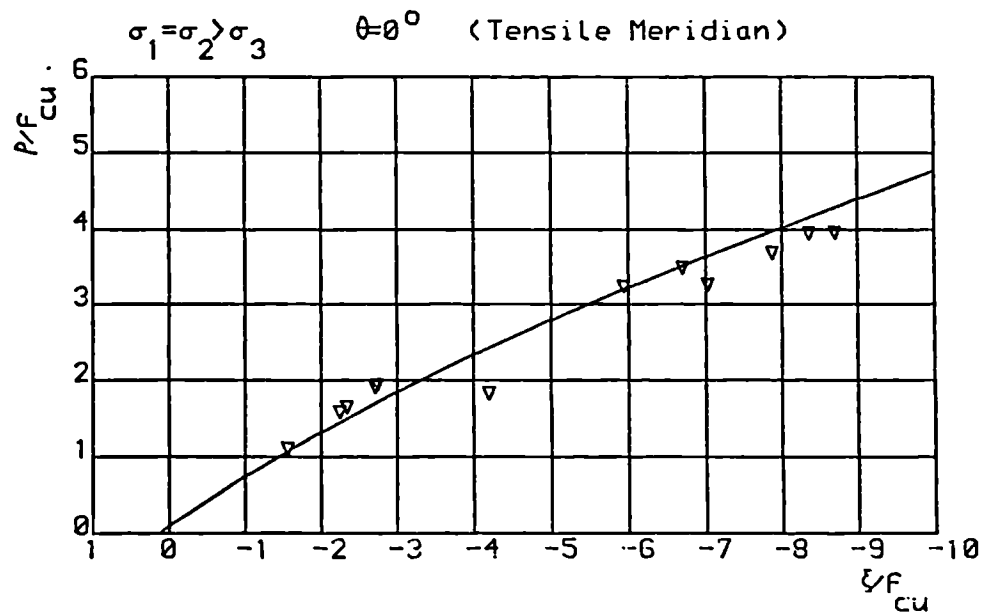
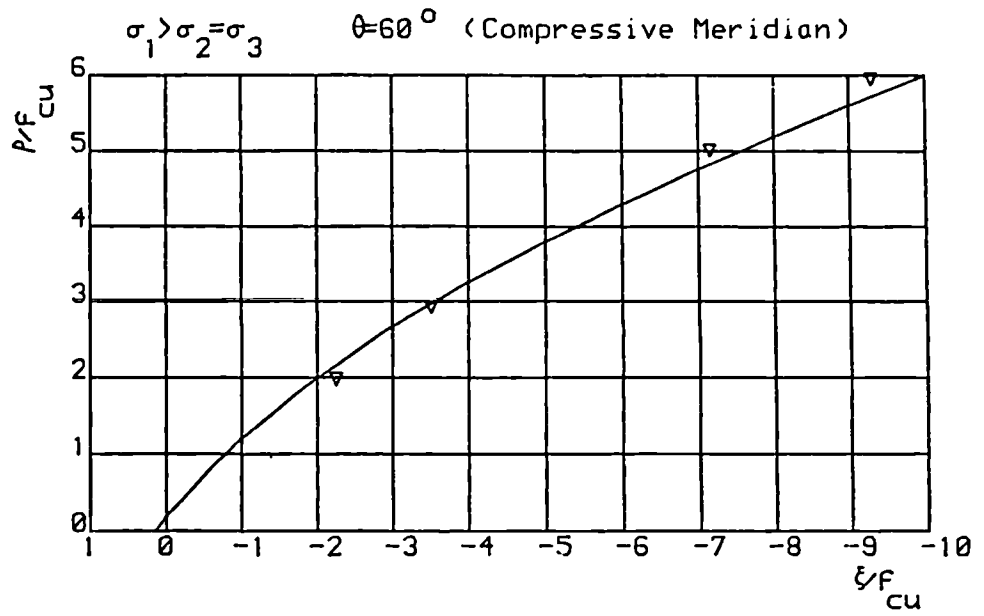
Fig. 3.8 Continued



— Suggested Theory $\alpha_t = .09$
 * Mills & Zimmerman [29] $\alpha_{bc} = 1.16$
 $\bar{\xi}_{co} = 5.00$ $\bar{p}_{co} = 3.60$
 $\bar{\xi}_{to} = 5.00$ $\bar{p}_{to} = 2.70$

(c)

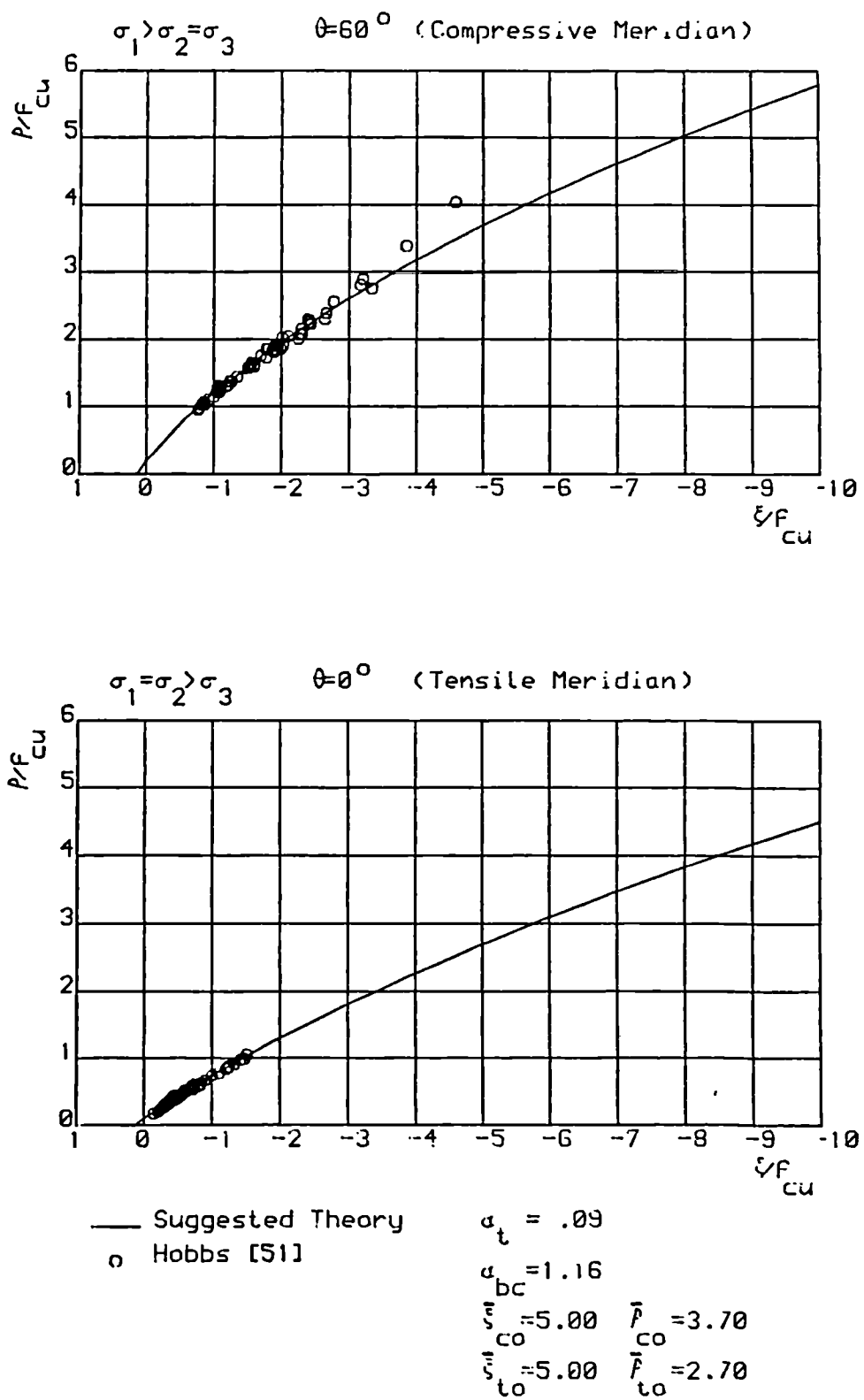
Fig. 3.8 Continued



— Suggested Theory $\alpha_t = .09$
 ▽ Chinn&Zimmerman [50] $\alpha_{bc} = 1.20$
 $\bar{\xi}_{co} = 5.00$ $\bar{P}_{co} = 3.80$
 $\bar{\xi}_{to} = 5.00$ $\bar{P}_{to} = 2.80$

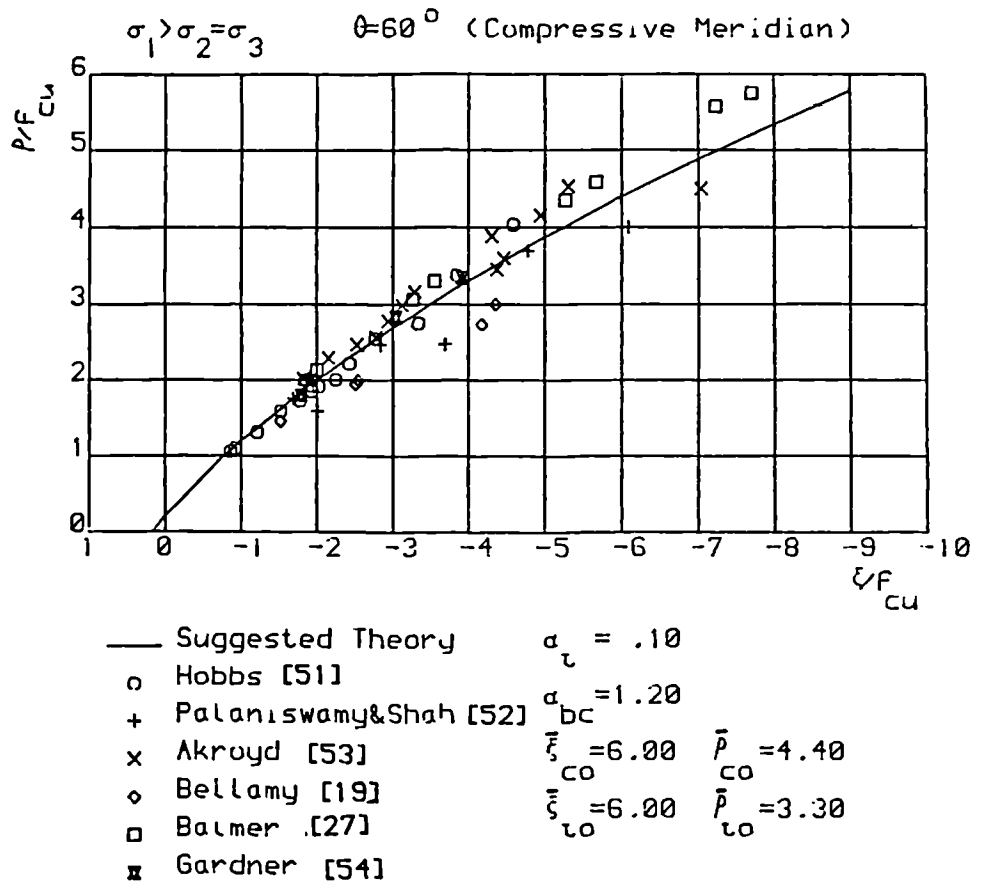
(d)

Fig. 3.8 Continued



(e)

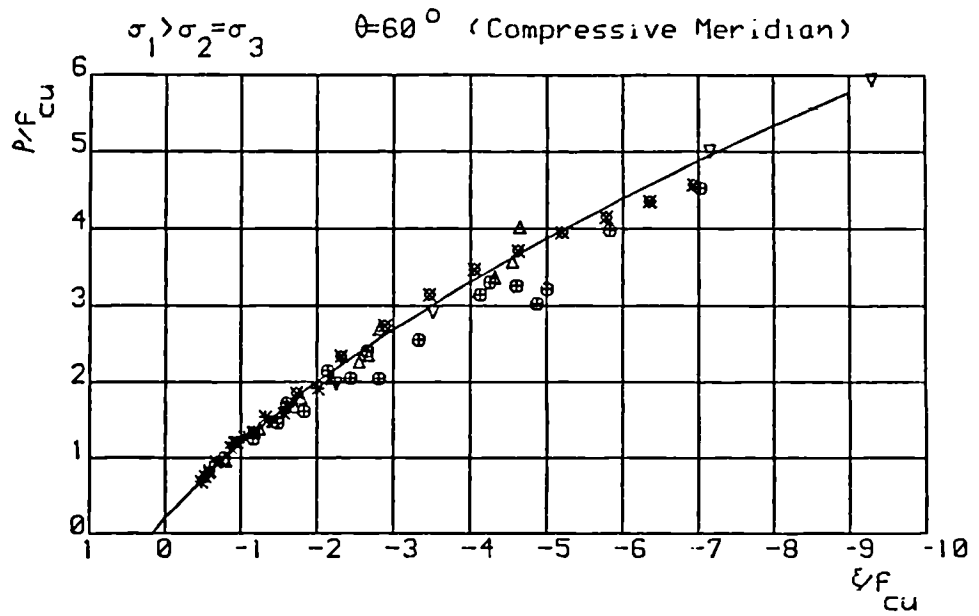
Fig. 3.8 Continued



$$\bar{p}_c = -6.2441 + 4.2157 \sqrt{2.2790 + 0.4744 \bar{\xi}}$$

(a)

Fig. 3.9 Comparison of the recommended compressive and tensile meridians with experimental results.

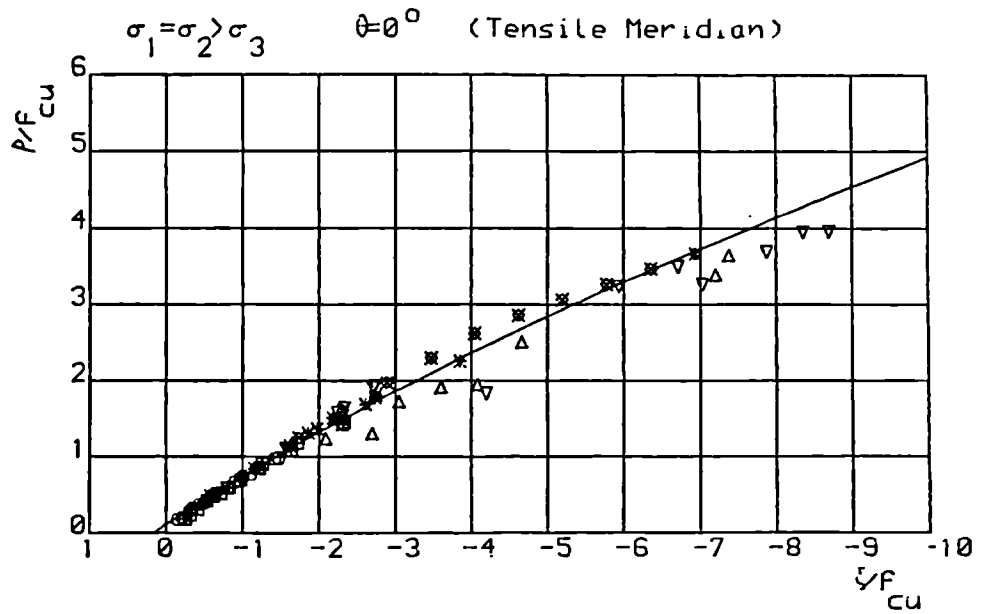


- | | | | |
|---|------------------------|-------------------------|-----------------------|
| — | Suggested Theory | $a_\tau = .10$ | |
| * | Mills & Zimmerman [29] | $a_{bc} = 1.20$ | |
| × | Launay & Gachon [21] | $\bar{\xi}_{co} = 6.00$ | $\bar{p}_{co} = 4.40$ |
| ▽ | Chinn & Zimmerman [50] | $\bar{\xi}_{co} = 6.00$ | $\bar{p}_{co} = 3.30$ |
| △ | Richard et al [14] | $\bar{\xi}_{co} = 6.00$ | |
| ⊙ | Newman [24] | $\bar{\xi}_{co} = 6.00$ | |

$$\bar{p}_c = -6.2441 + 4.2157 \sqrt{2.2790 + 0.4744 \bar{\xi}}$$

(b)

Fig. 3.9 Continued



- | | | | |
|---|------------------------|-----------------------|-----------------------|
| — | Suggested Theory | $\alpha_t = .10$ | |
| * | Mills & Zimmerman [29] | $\alpha_{bc} = 1.20$ | |
| × | Launay & Gachon [21] | $\bar{s}_{co} = 6.00$ | $\bar{p}_{co} = 4.40$ |
| ▽ | Chinn & Zimmerman [50] | $\bar{s}_{to} = 6.00$ | $\bar{p}_{to} = 3.30$ |
| △ | Richart et al [14] | | |
| ■ | Kotsovos [23] | | |
| ○ | Hobbs [51] | | |

$$\bar{p}_t = -3.0696 + 3.7522 \sqrt{0.7649 + 0.5330 \bar{\xi}}$$

(c)

Fig. 3.9 Continued

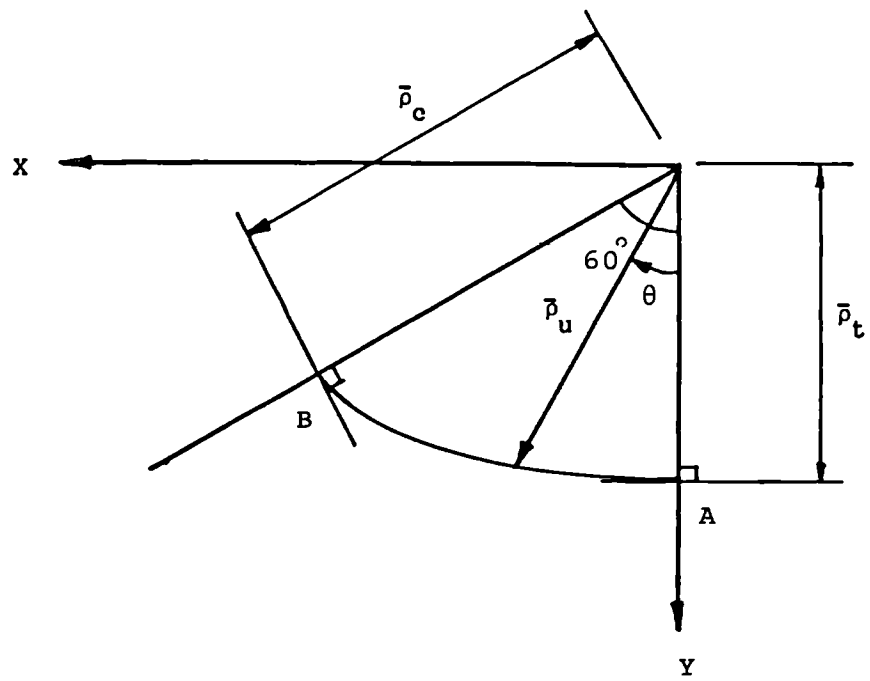
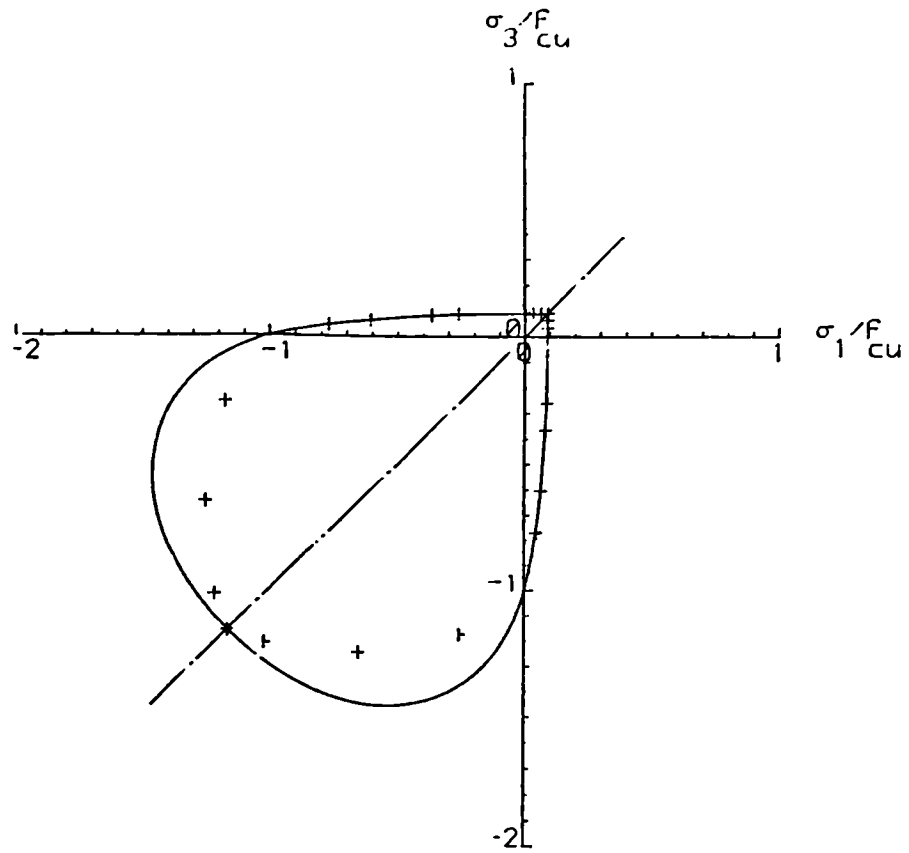


Fig. 3.10 Geometry of the proposed failure surface at the deviatoric section.

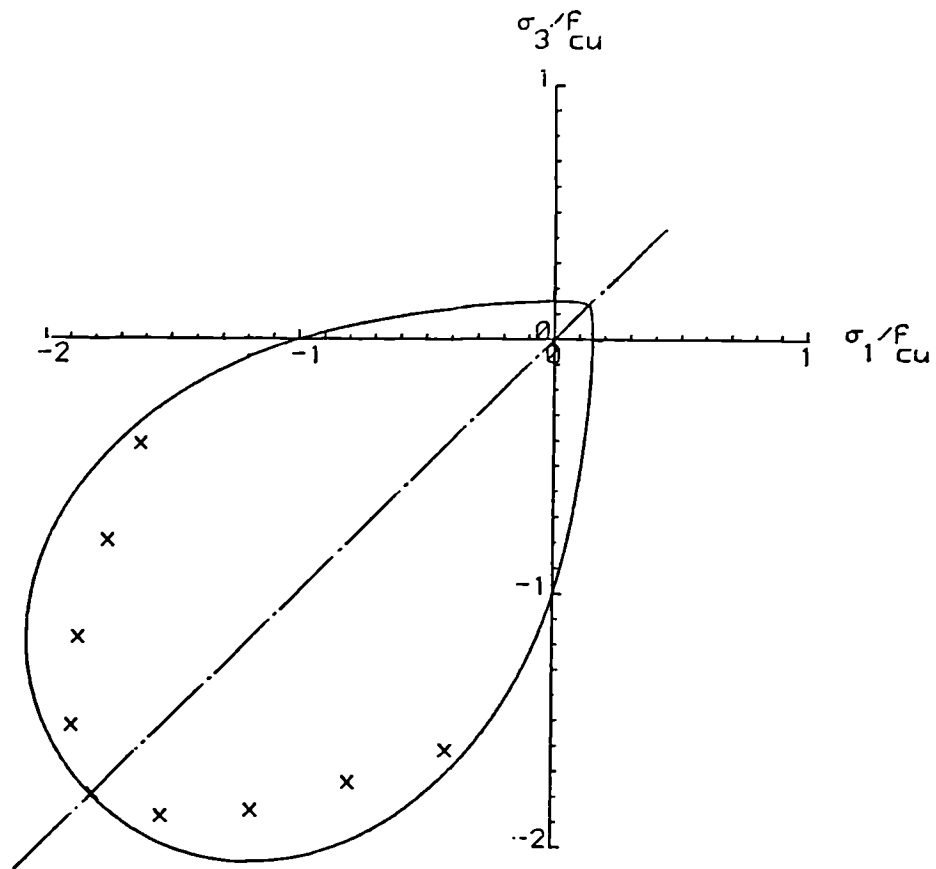


— Suggested Theory
 + Kupfer et al [26]

$$\begin{aligned}
 \alpha_{\tau} &= .09 \\
 \alpha_{bc} &= 1.16 \\
 \bar{\xi}_{co} &= 1.00 & \bar{p}_{co} &= 1.20 \\
 \bar{\xi}_{\tau o} &= 1.00 & \bar{f}_{\tau o} &= .75
 \end{aligned}$$

(a) Biaxial

Fig. 3.11 Fit of the proposed failure surface to biaxial and triaxial experimental results.

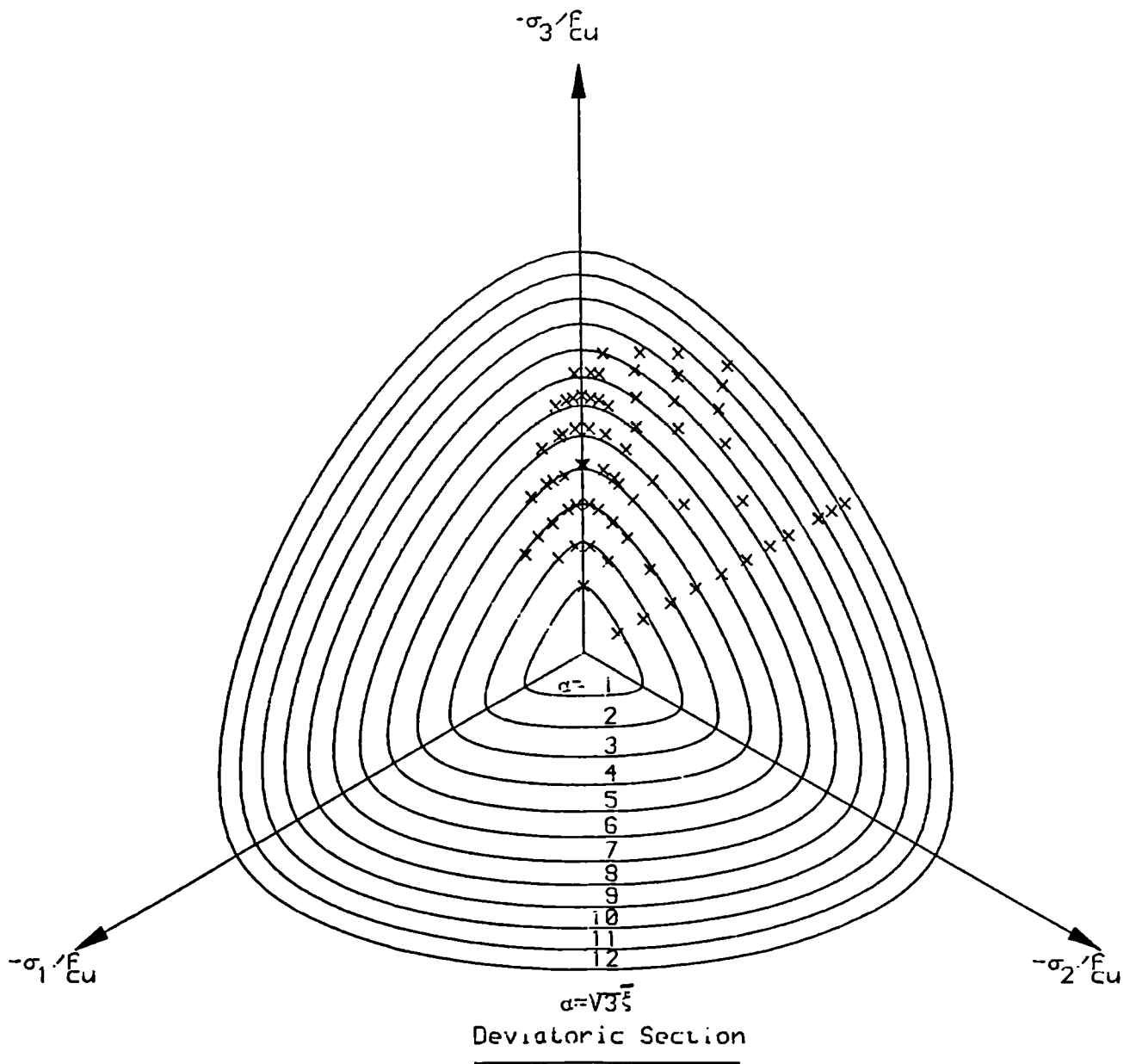


— Suggested Theory
 x Launay&Gachon [21]

$\alpha_t = .15$
 $\alpha_{bc} = 1.80$
 $\bar{\xi}_{co} = 4.00$ $\bar{P}_{co} = 3.50$
 $\bar{\xi}_{to} = 4.00$ $\bar{P}_{to} = 2.50$

(b) Biaxial

Fig. 3.11 Continued



— Suggested Theory
 x Launay & Gachon [21]

$\alpha_t = .09$	
$\alpha_{bc} = 1.80$	
$\bar{\xi}_{co} = 6.00$	$\bar{p}_{co} = 4.45$
$\bar{\xi}_{to} = 6.00$	$\bar{p}_{to} = 3.45$

(c) Triaxial

Fig. 3.11 Continued

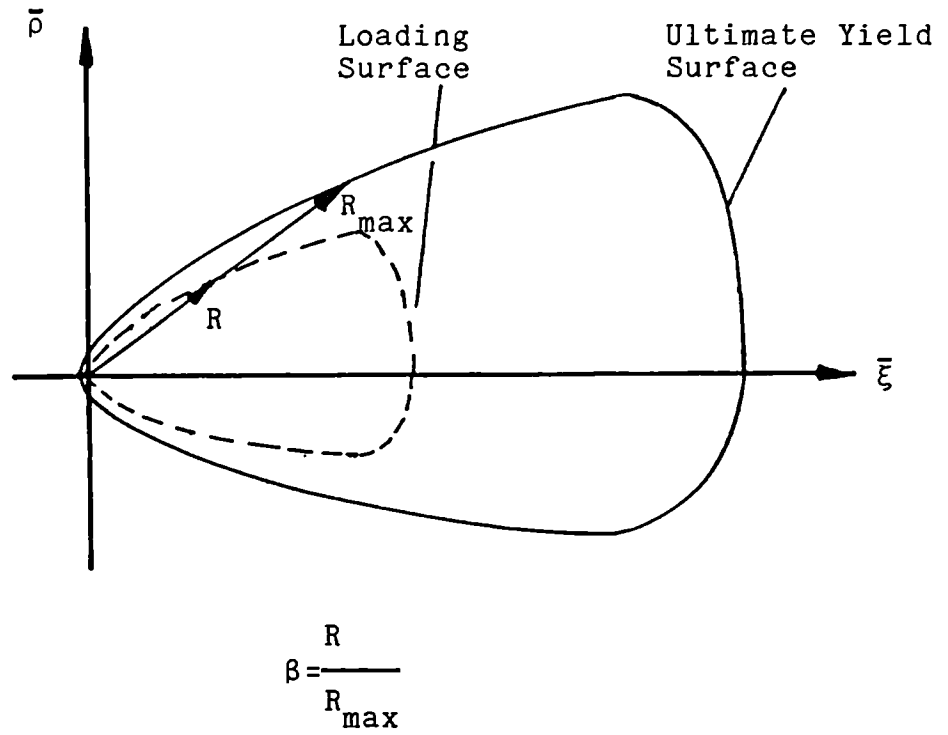


Fig. 3.12 Definition of the hardening parameter β .

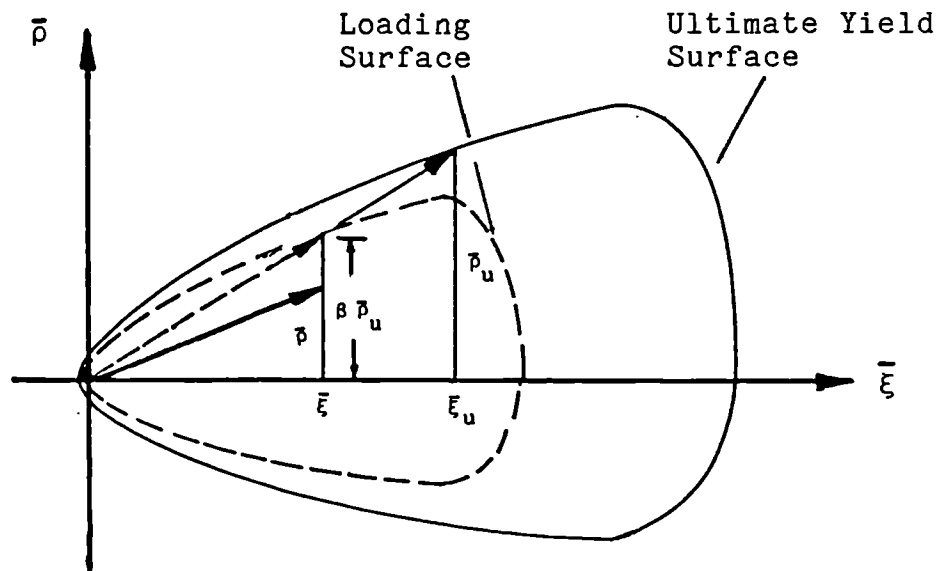


Fig. 3.13 Geometrical relationship between the intermediate failure surface and the ultimate yield surface.

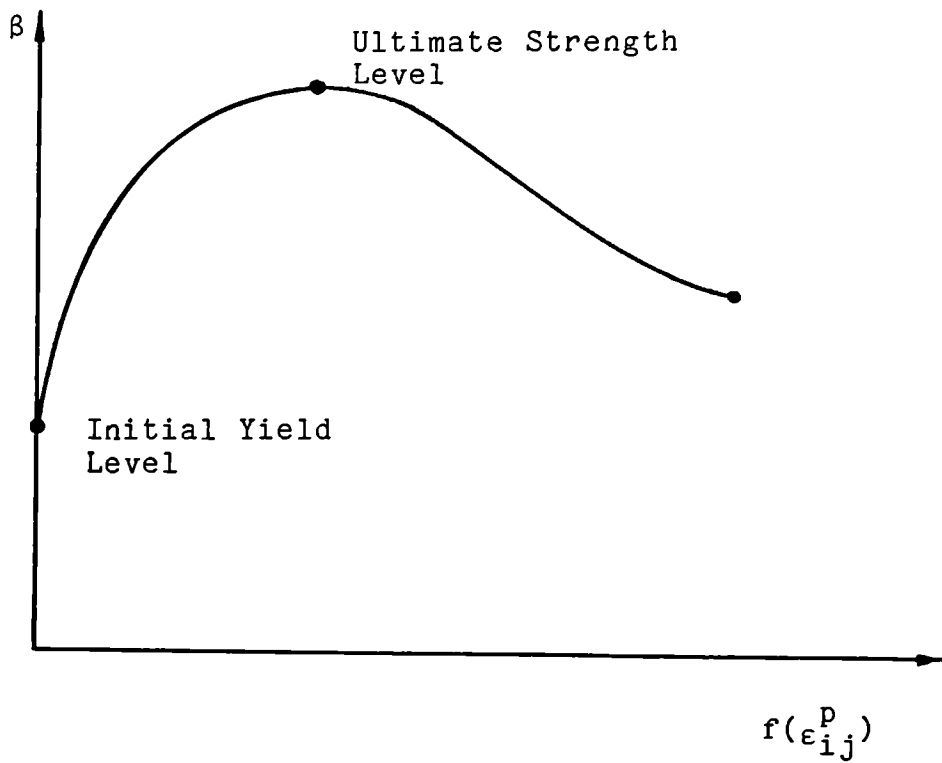


Fig. 3.14 Variation of the hardening parameter β , with plastic strain.

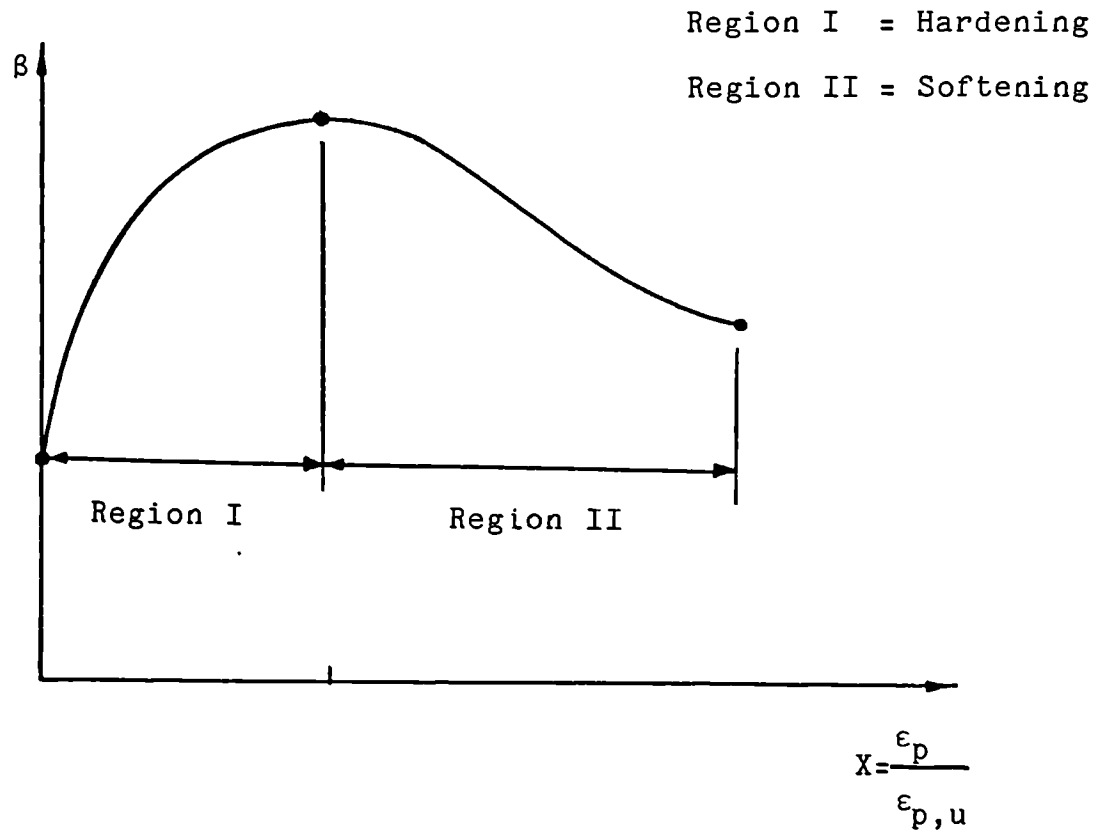


Fig. 3.15 Variation of β with non-dimensional parameter X .

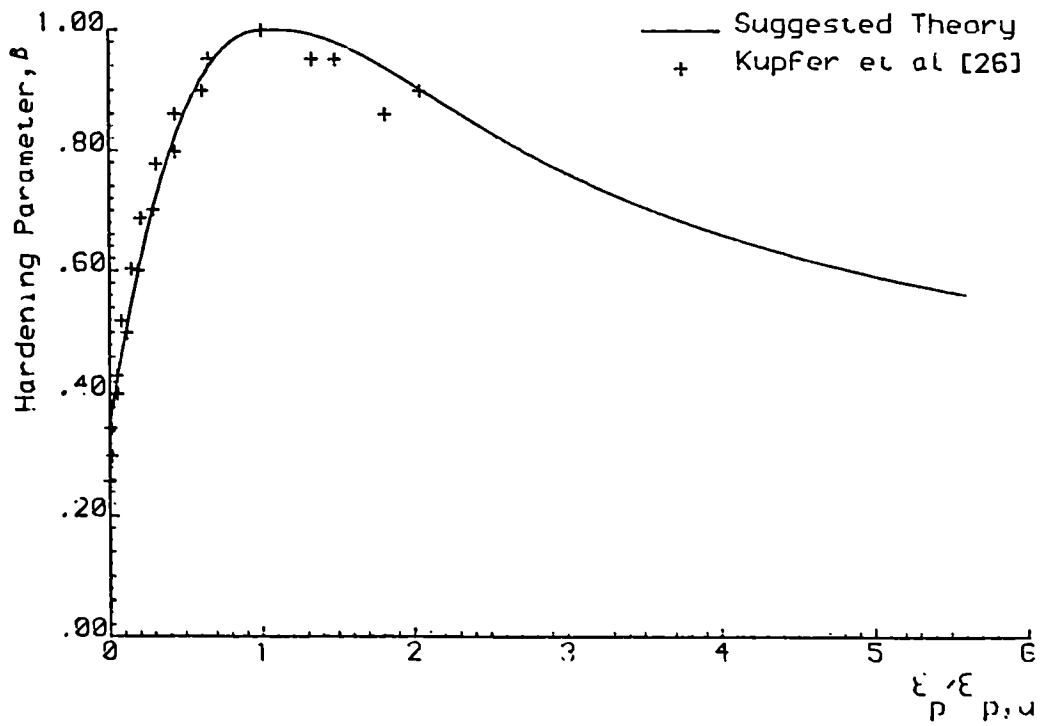
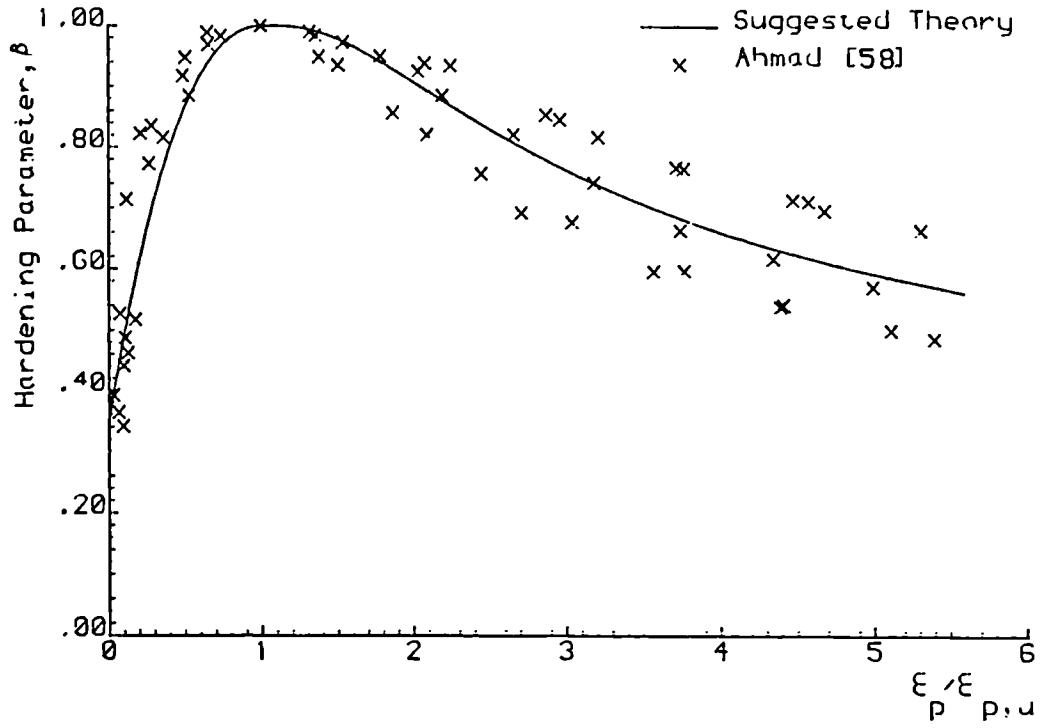


Fig. 3.16 Comparison of the hardening model with experimental results.

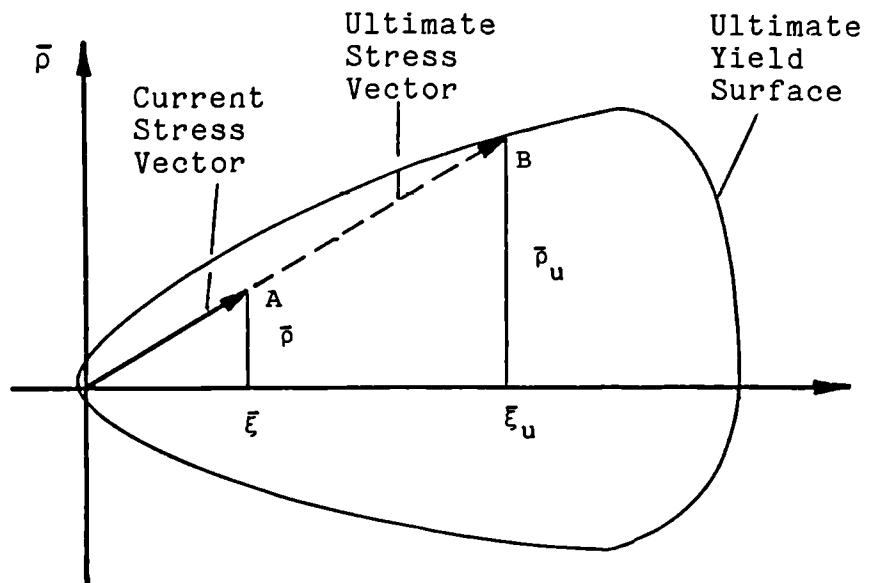


Fig. 3.17 Geometrical definition of the ultimate stress vector from the current stress vector.

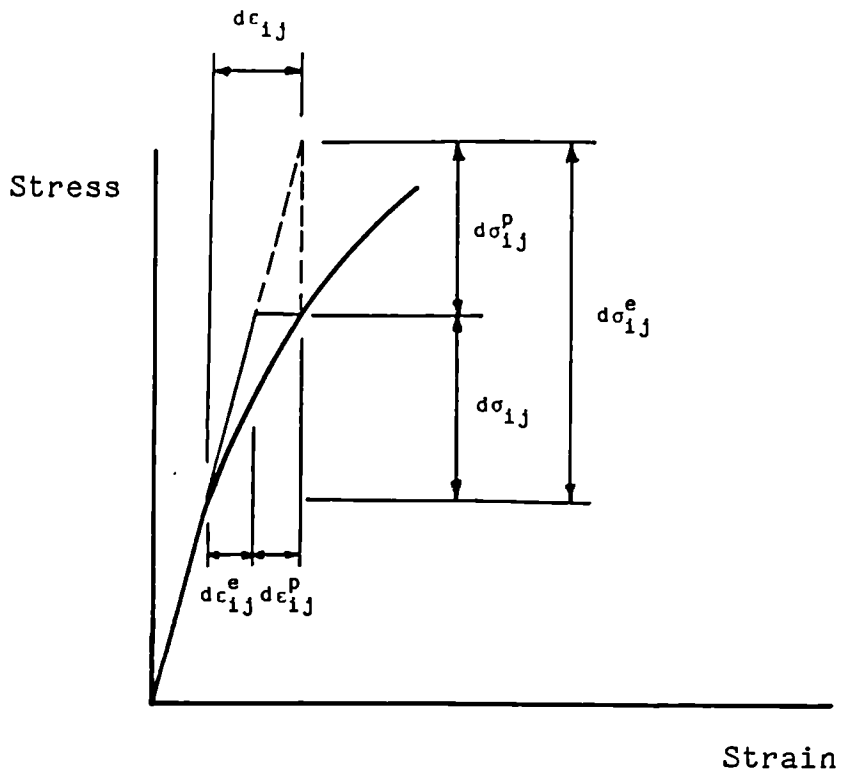


Fig. 3.18 Schematic representation of plastic flow.

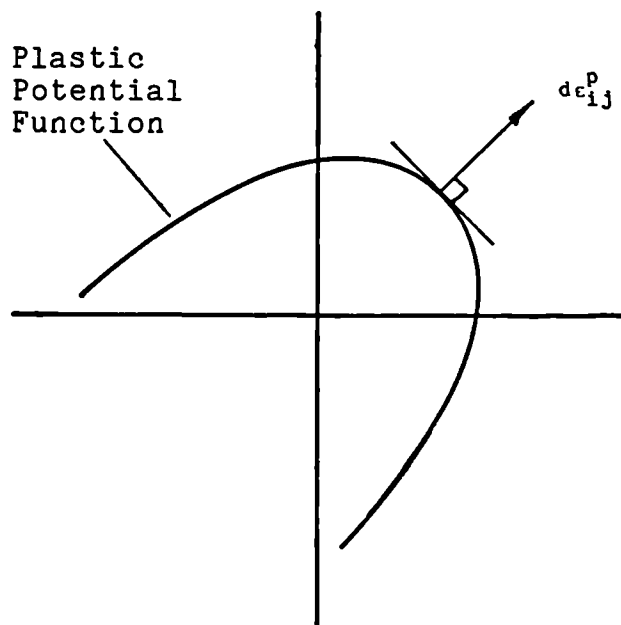
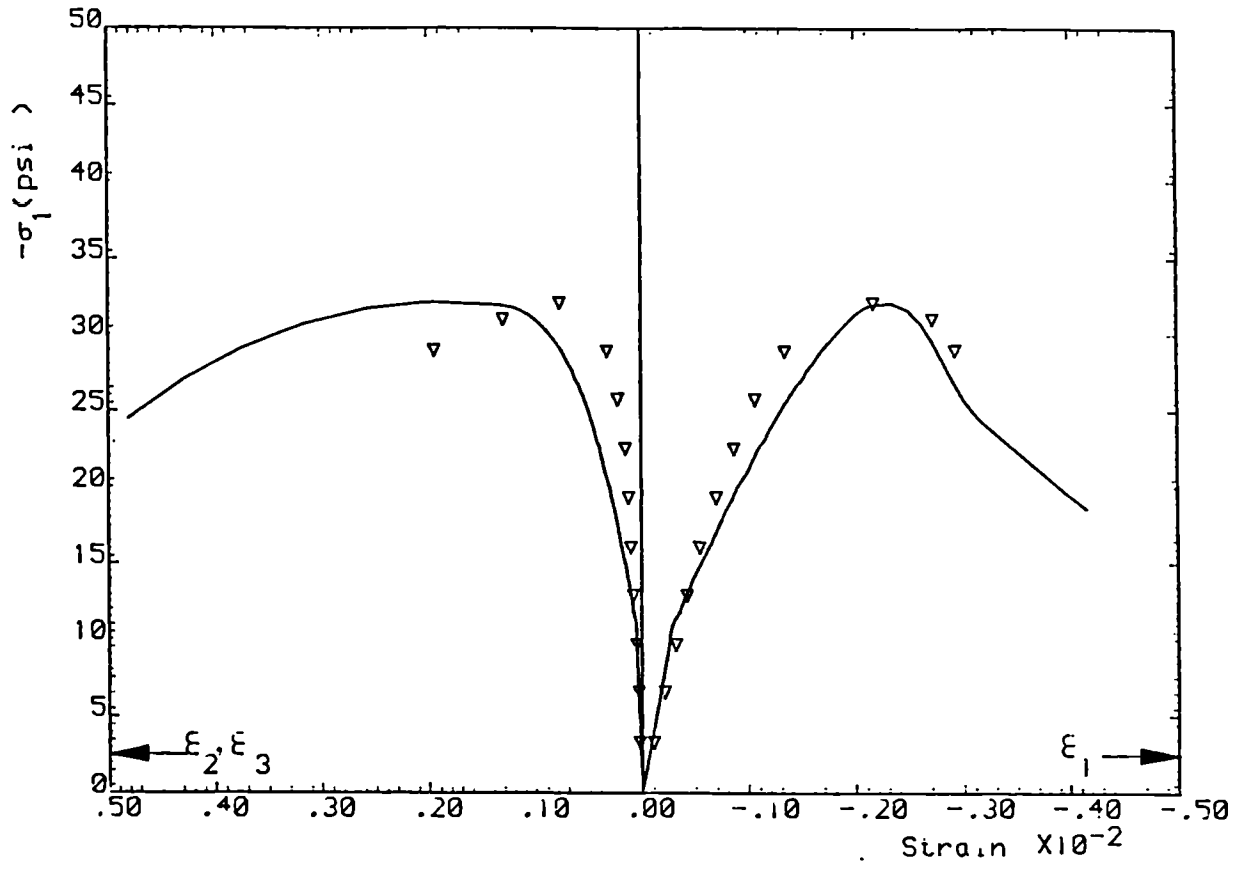
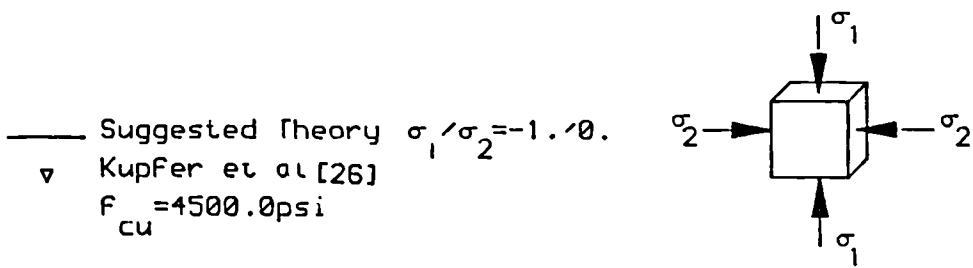


Fig. 3.19 Representation of normality rule.

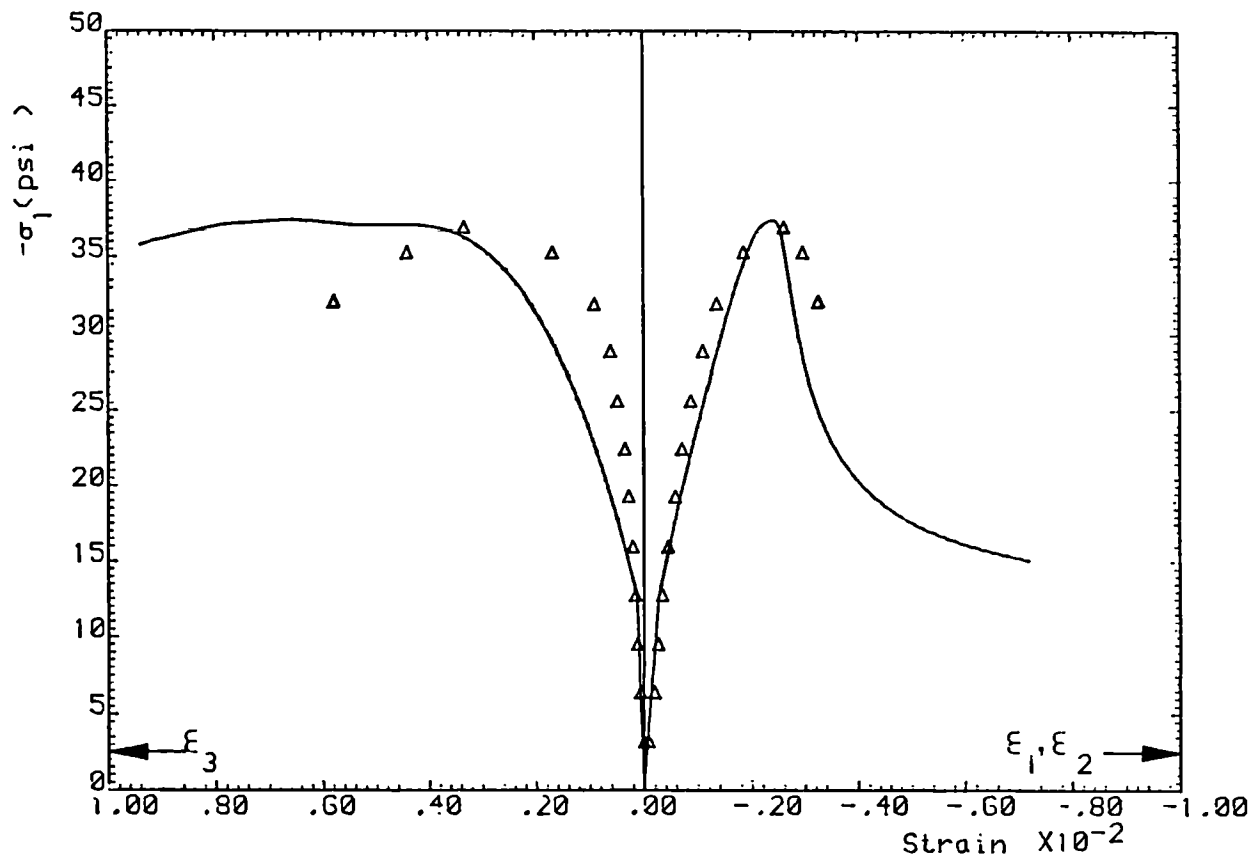


Uniaxial Test



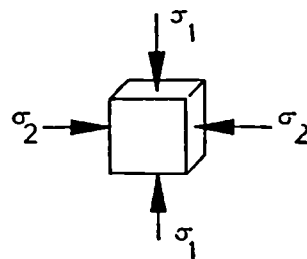
(a)

Fig. 3.20 Comparison of the performance of the proposed concrete constitutive model with uniaxial and biaxial experimental results.



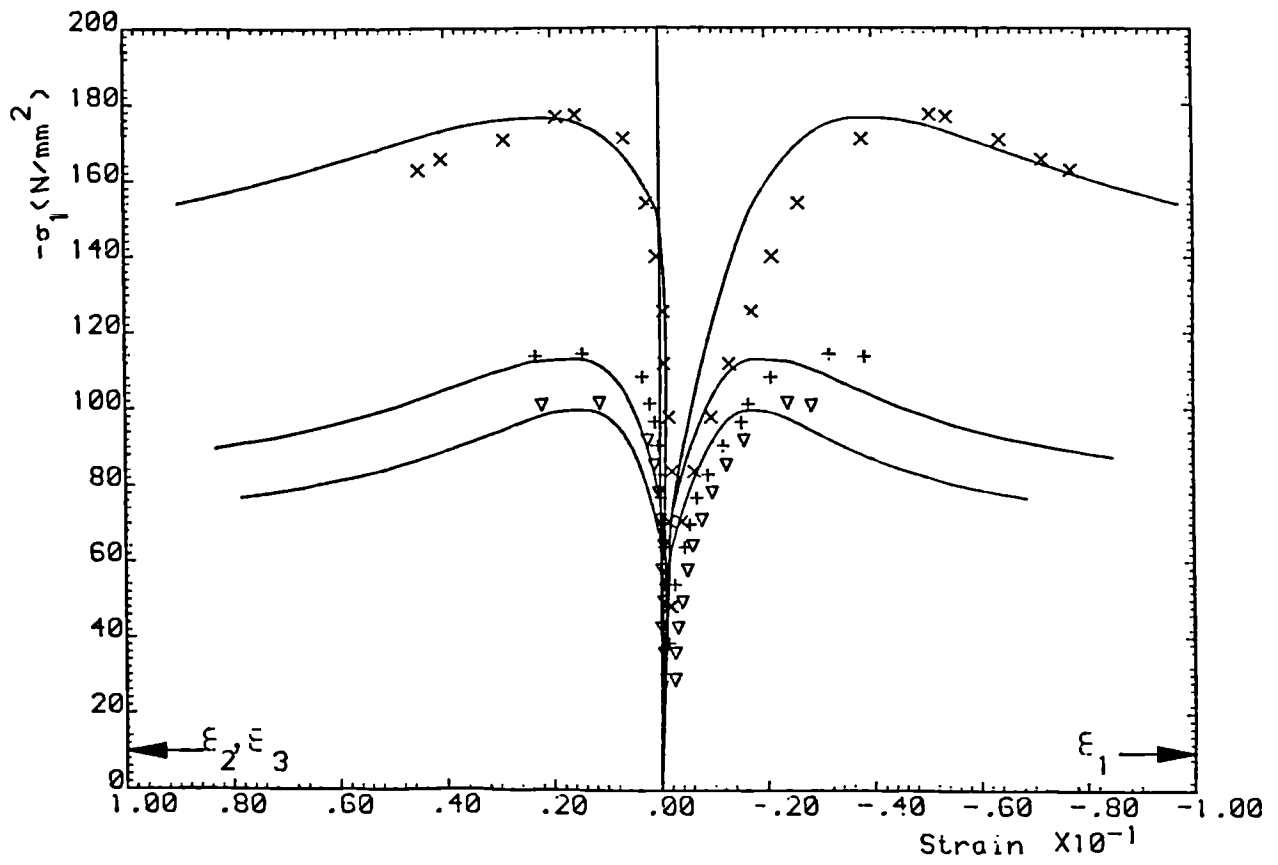
Biaxial Test

— Suggested Theory $\sigma_1/\sigma_2 = -1, -1$
 Δ Kupfer et al [26]
 $F_{cu} = 32.7 \text{ psi}$

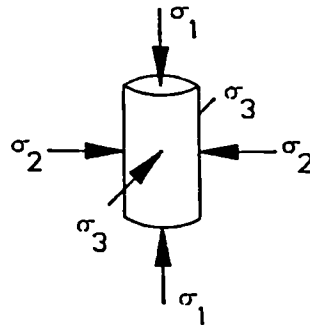
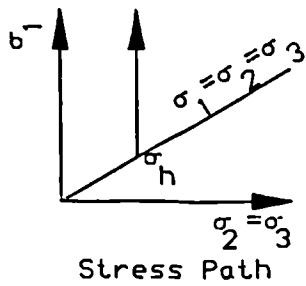


(b)

Fig. 3.20 Continued



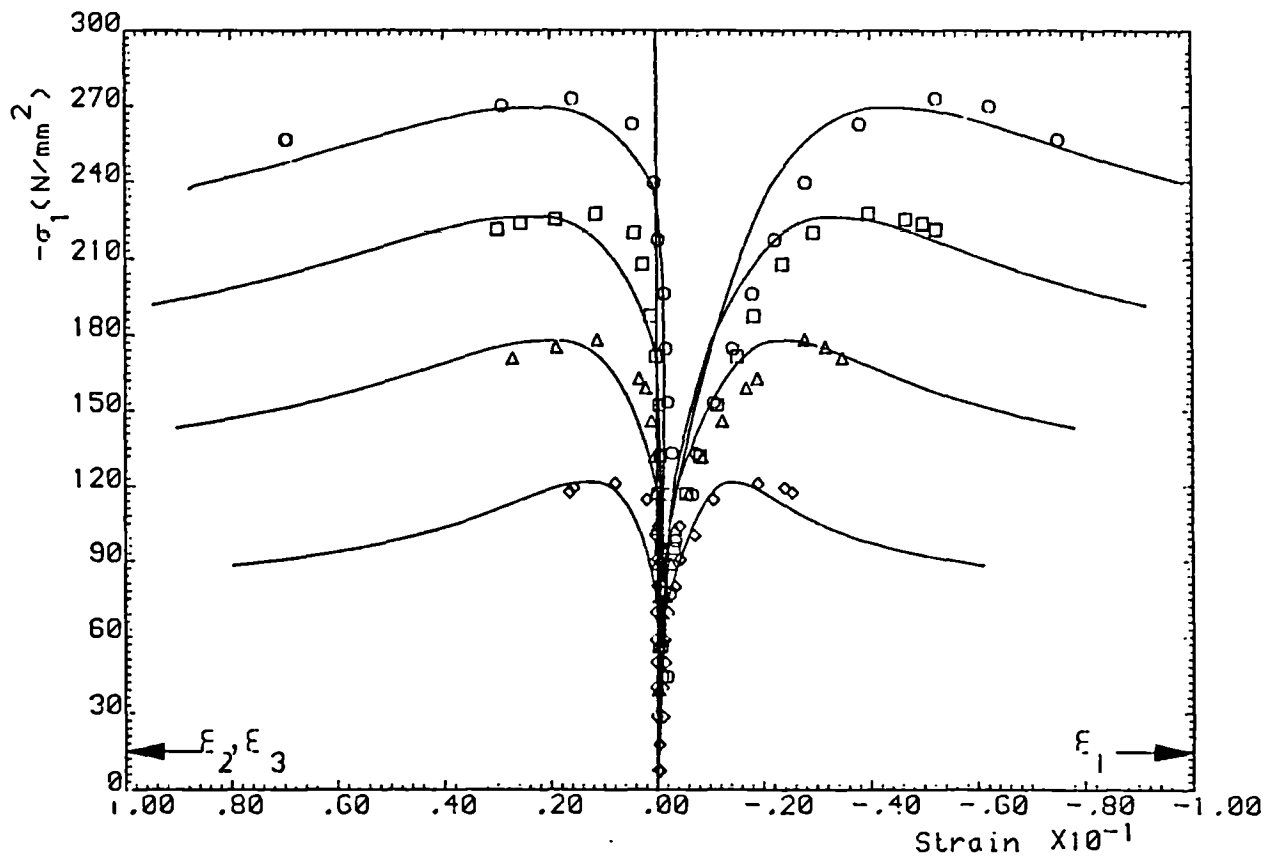
Triaxial Test



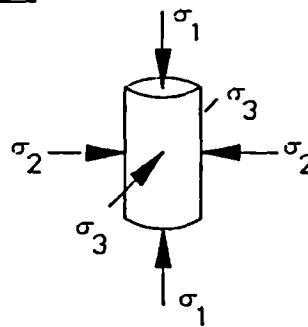
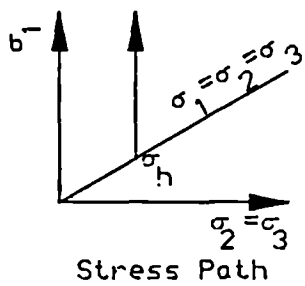
—	Suggested Theory	$\sigma_h =$
	Kotsovos & Newman [67]	$\nabla -19.0 \text{ N/mm}^2$
	$F_{cu} = 31.7 \text{ N/mm}^2$	$+ -24.0 \text{ N/mm}^2$
		$x -44.0 \text{ N/mm}^2$

(a)

Fig. 3.21 Comparison of the performance of the proposed concrete constitutive model with triaxial compression experimental results.



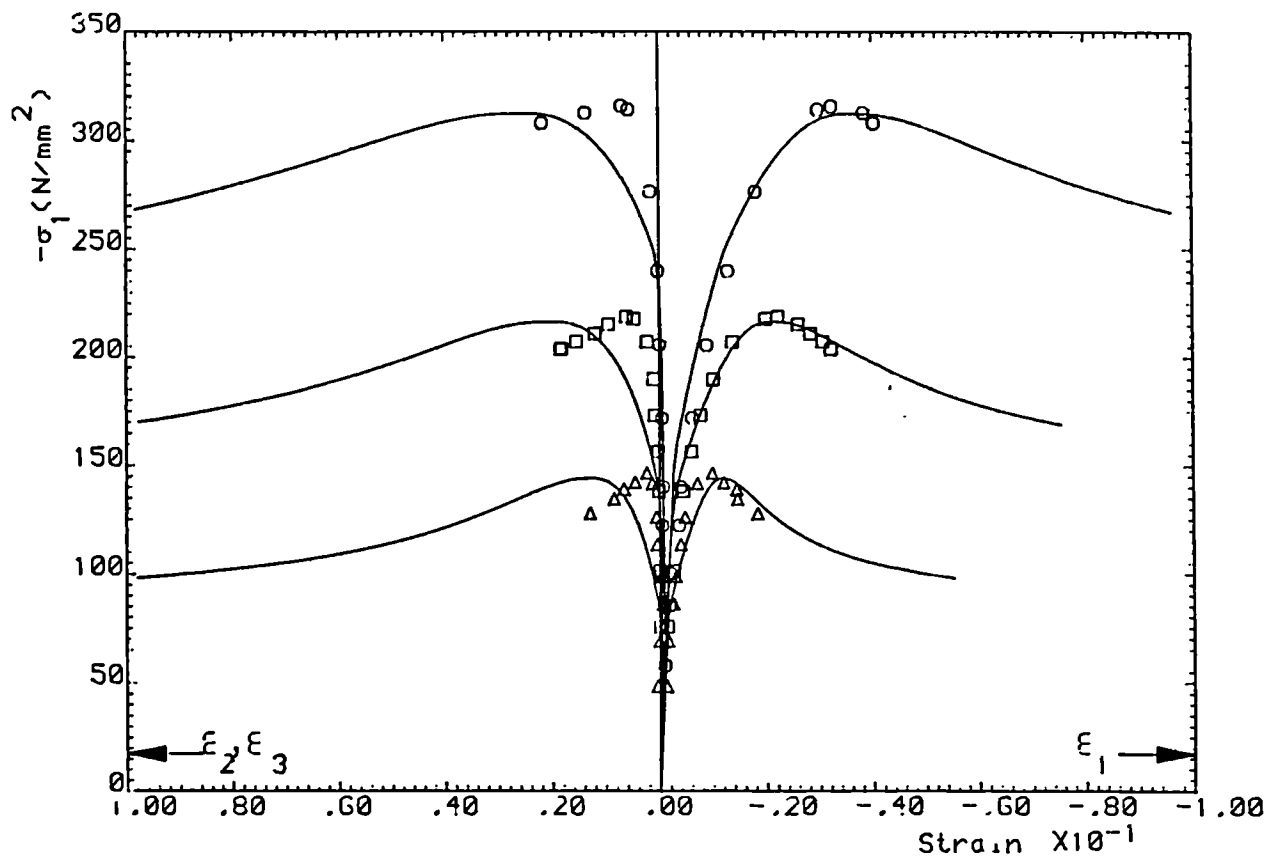
Triaxial Test



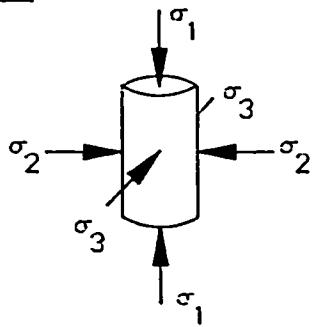
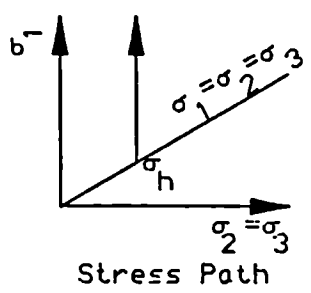
— Suggested Theory	$\sigma_h =$
Kotsovos & Newman [67]	$\diamond -18.0 \text{ N/mm}^2$
$F_{CI} = 46.9 \text{ N/mm}^2$	$\triangle -35.0 \text{ N/mm}^2$
	$\square -51.0 \text{ N/mm}^2$
	$\circ -70.0 \text{ N/mm}^2$

(b)

Fig. 3.21 Continued



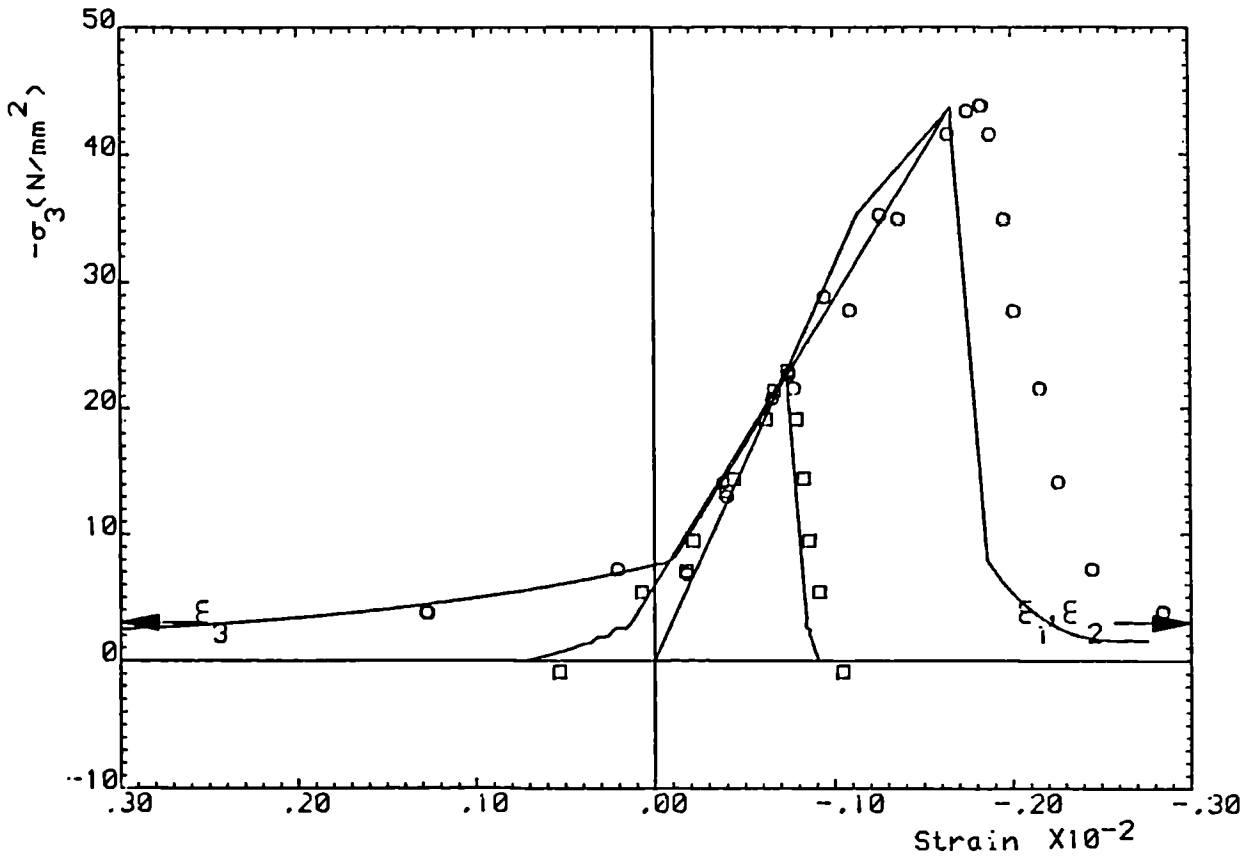
Triaxial Test



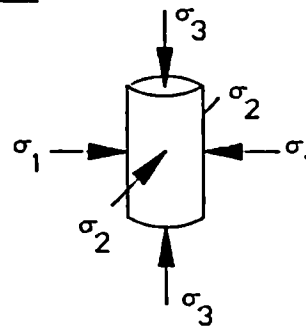
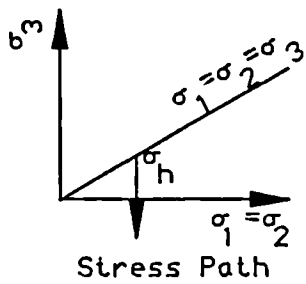
— Suggested Theory
 Kotsovos & Newman [67] Δ $\sigma_h = 14.0 \text{ N/mm}^2$
 $F_{cu} = 62.1 \text{ N/mm}^2$ \square $\sigma_h = 35.0 \text{ N/mm}^2$
 \circ $\sigma_h = 69.0 \text{ N/mm}^2$

(c)

Fig. 3.21 Continued



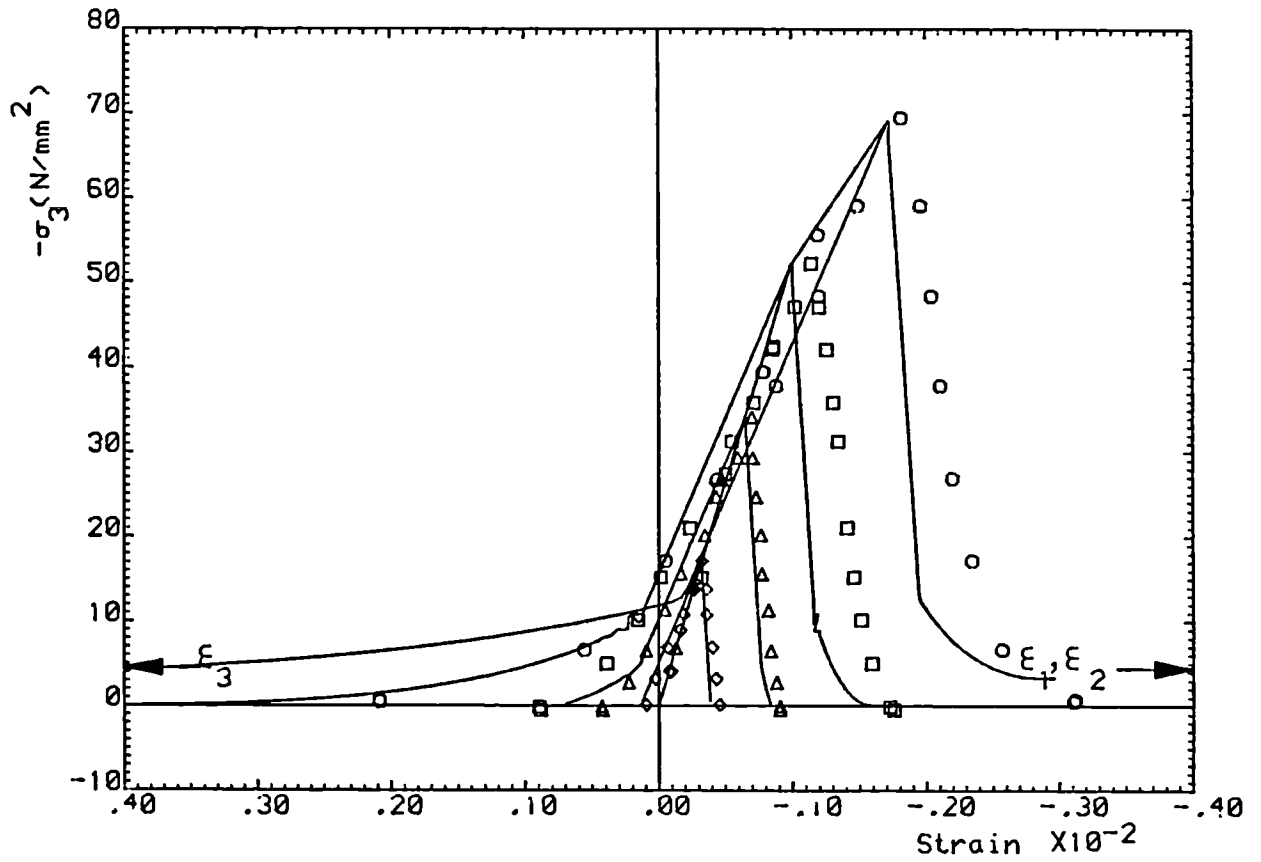
Triaxial Test



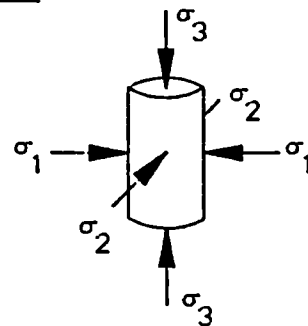
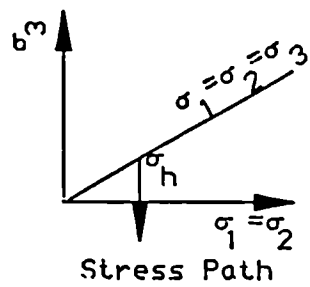
— Suggested Theory
 Kotsovos & Newman [46] □ $\sigma_h = -22.8 \text{ N/mm}^2$
 $F_{cu} = 31.7 \text{ N/mm}^2$ ○ -43.5 N/mm^2

(a)

Fig. 3.22 Comparison of the performance of the proposed concrete constitutive model with triaxial extension experimental results.



Triaxial Test

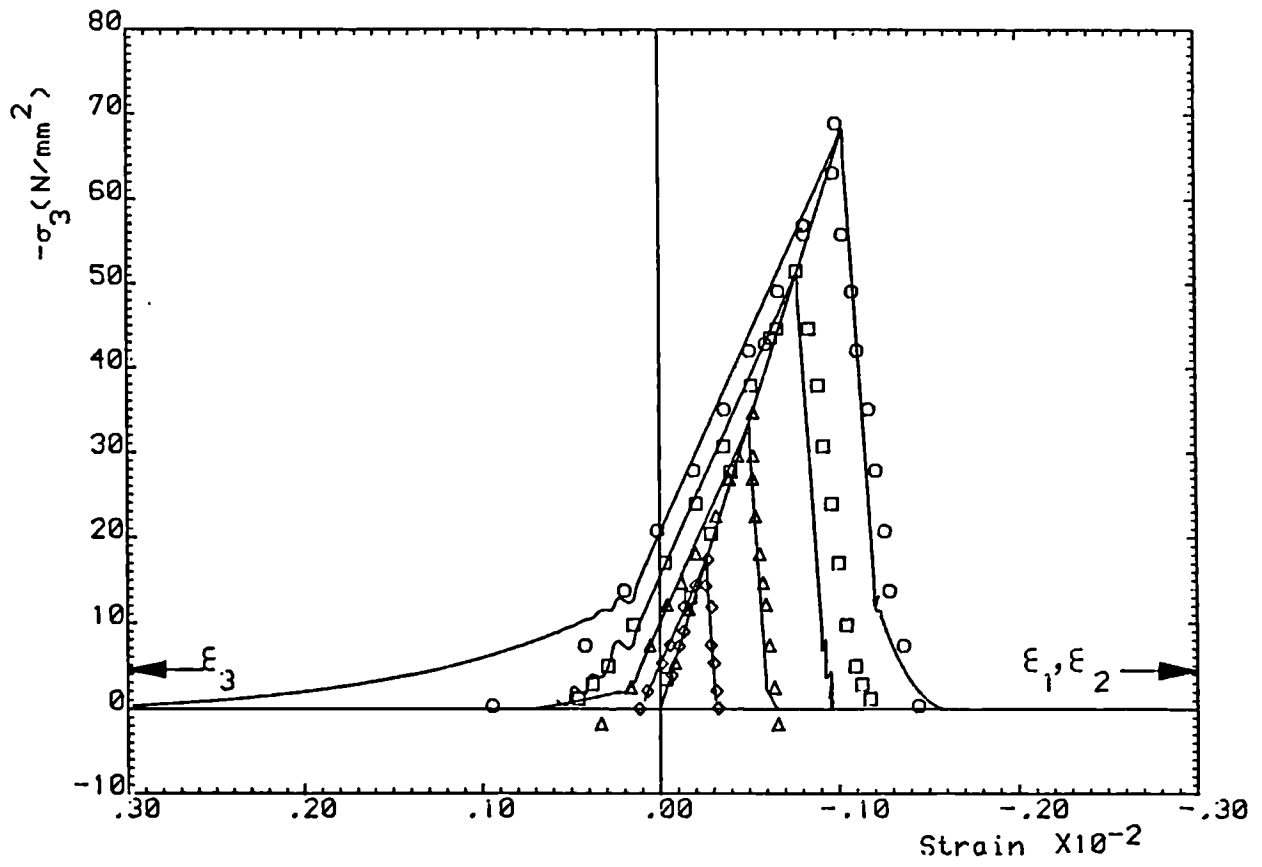


— Suggested Theory
 Kotsovos & Newman [46]
 $F_{cu} = 46.9 \text{ N/mm}^2$

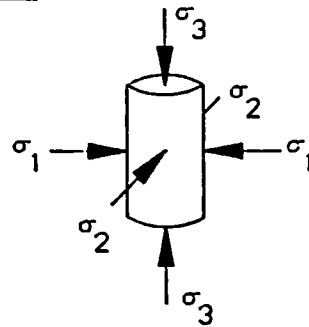
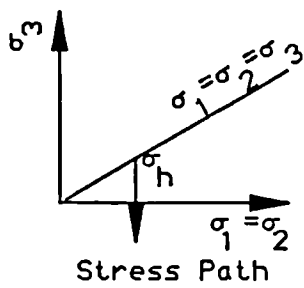
$\sigma_h =$	
\diamond	-17.0 N/mm^2
Δ	-34.0 N/mm^2
\square	-52.0 N/mm^2
\circ	-69.0 N/mm^2

(b)

Fig. 3.22 Continued



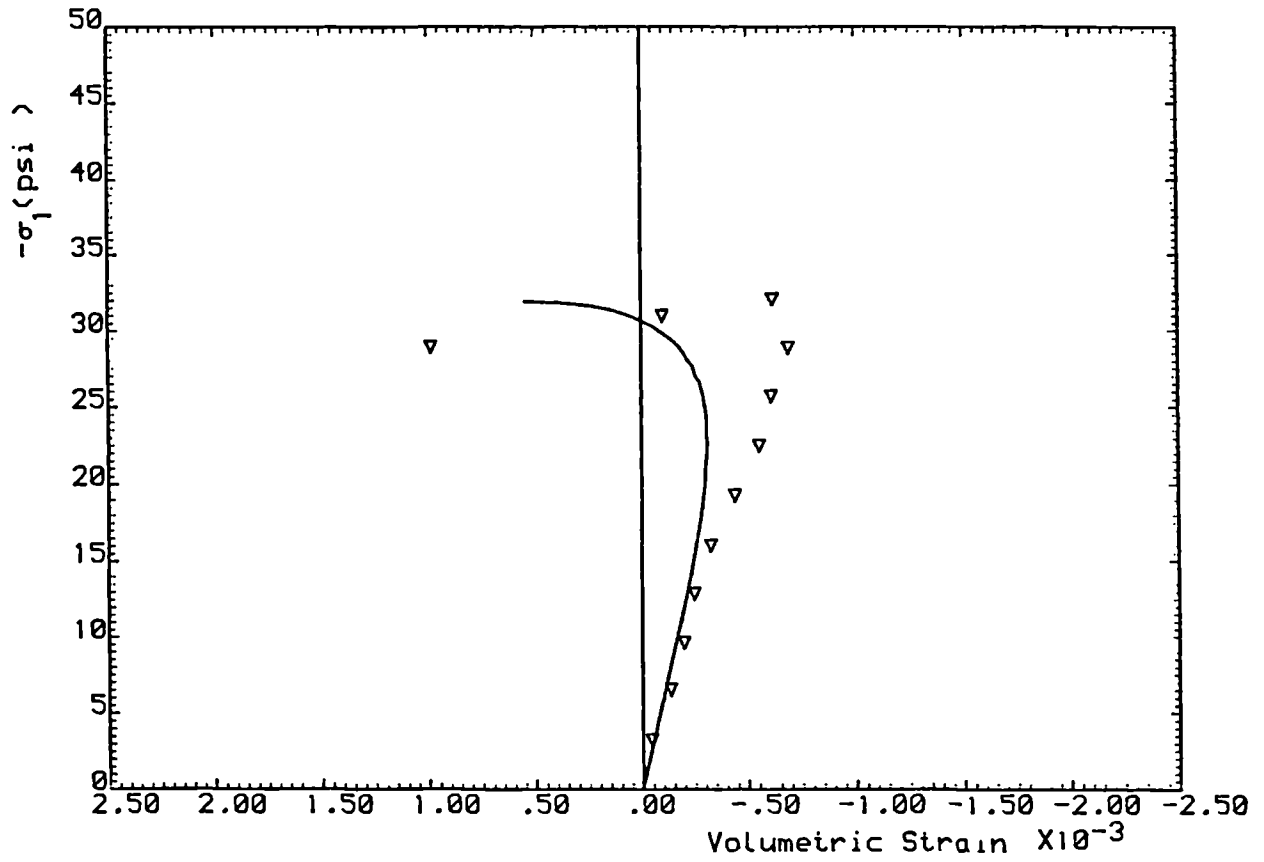
Triaxial Test



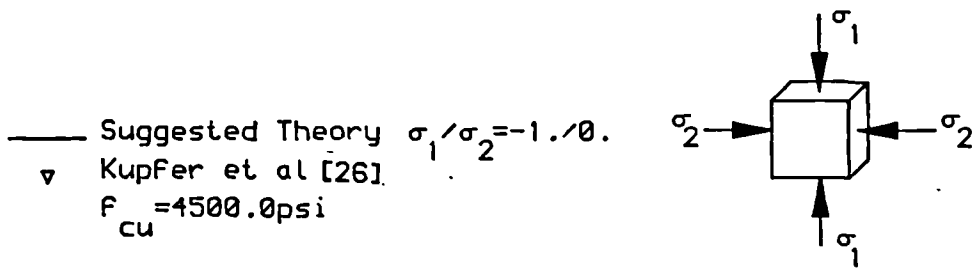
—	Suggested Theory	
	Kotsovos & Newman [46]	
	$F_{cu} = 62.1 \text{ N/mm}^2$	
◇	$\sigma_h = -17.0 \text{ N/mm}^2$	
△	$\sigma_h = -33.0 \text{ N/mm}^2$	
□	$\sigma_h = -51.0 \text{ N/mm}^2$	
○	$\sigma_h = -68.0 \text{ N/mm}^2$	

(c)

Fig. 3.22 Continued

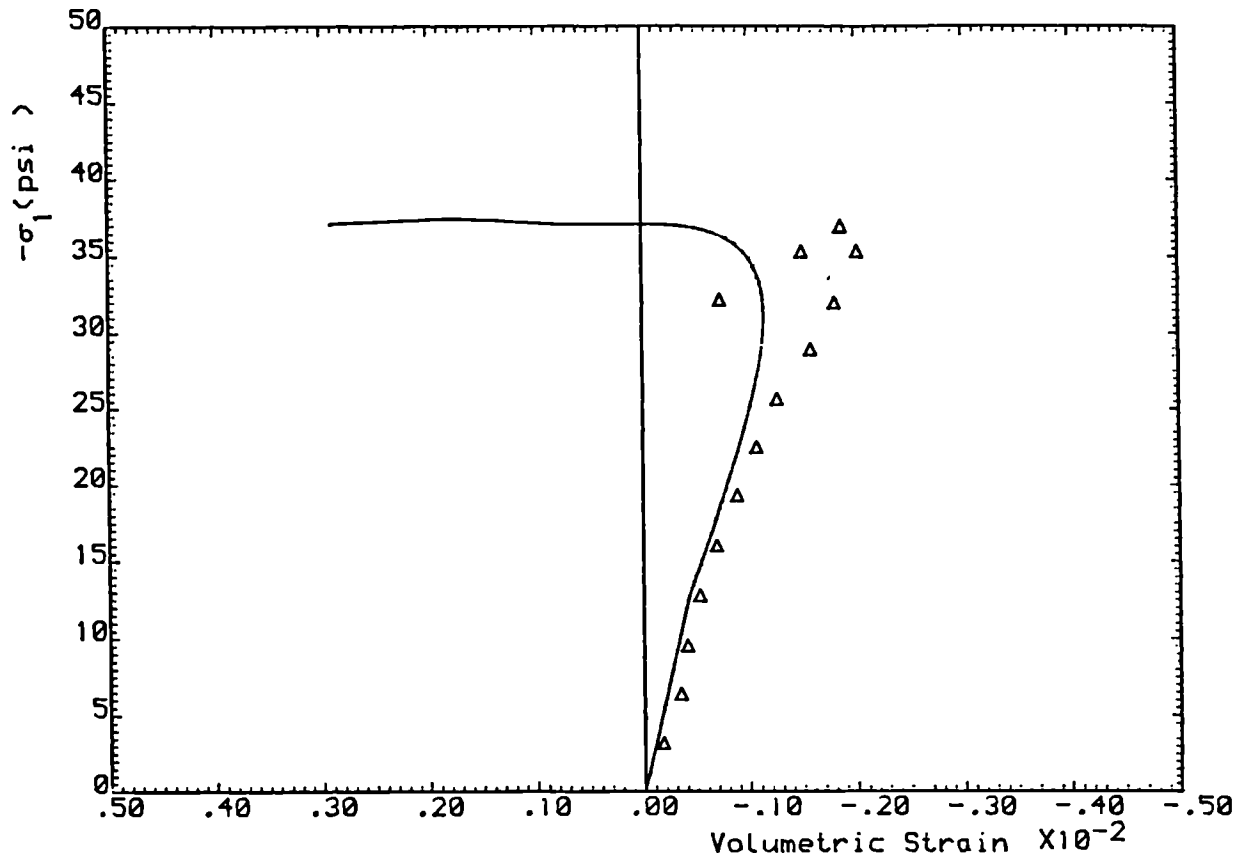


Uniaxial Test

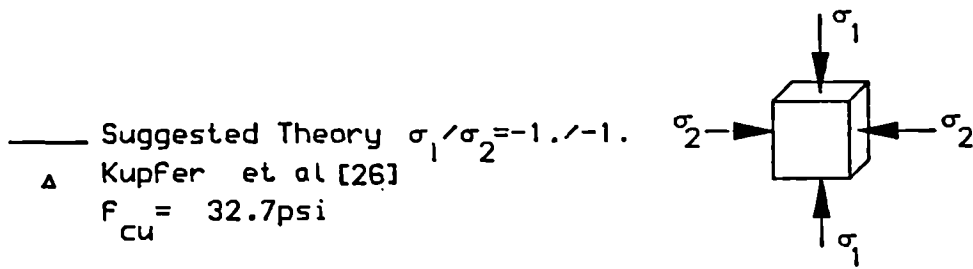


(a)

Fig. 3.23 Comparison of volumetric response of the proposed concrete constitutive model with experimental results.

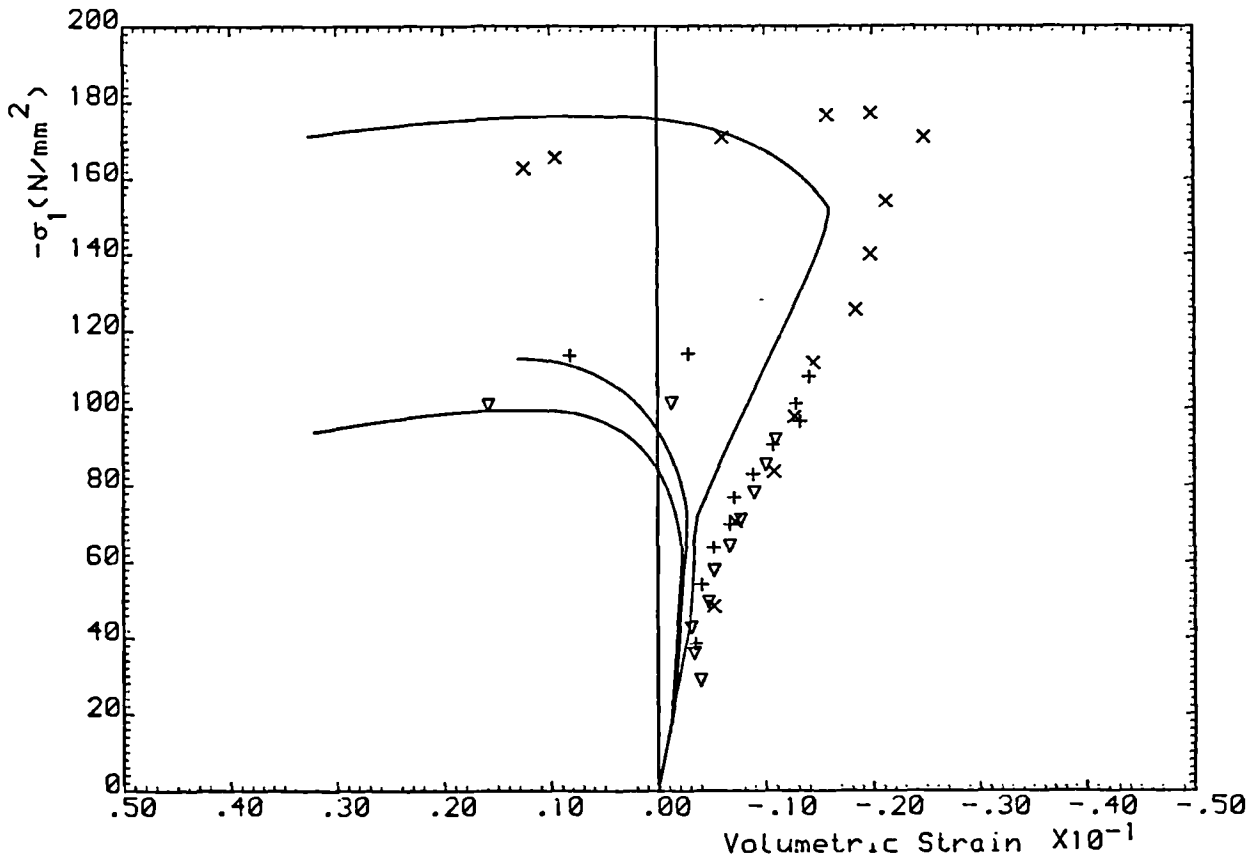


Biaxial Test

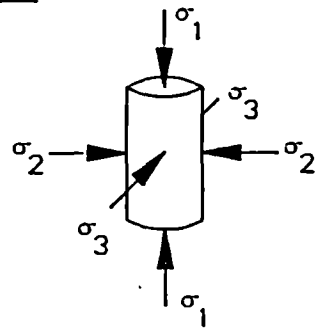
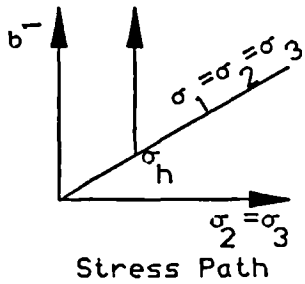


(b)

Fig. 3.23 Continued



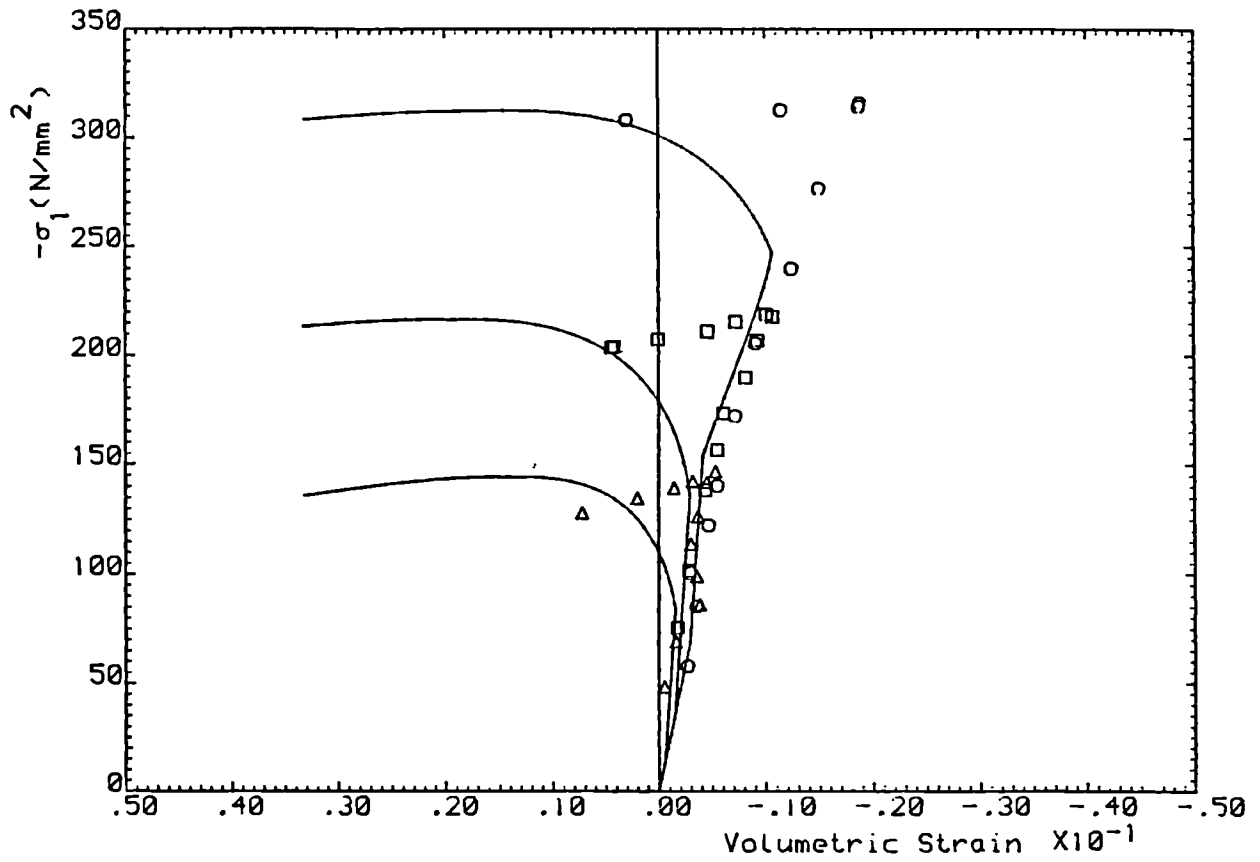
Triaxial Test



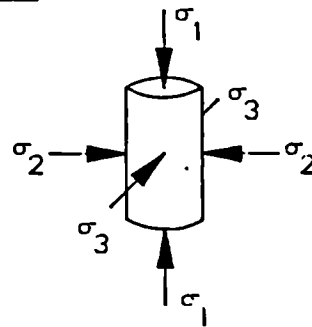
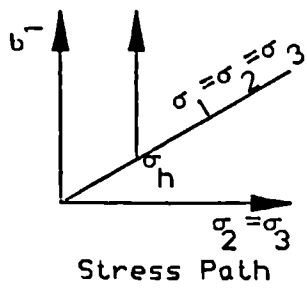
— Suggested Theory	$\sigma_h =$
Kotsovos & Newman [67]	$\nabla -19.0 \text{ N/mm}^2$
$F_{cu} = 31.7 \text{ N/mm}^2$	$+ -24.0 \text{ N/mm}^2$
	$x -44.0 \text{ N/mm}^2$

(c)

Fig. 3.23 Continued



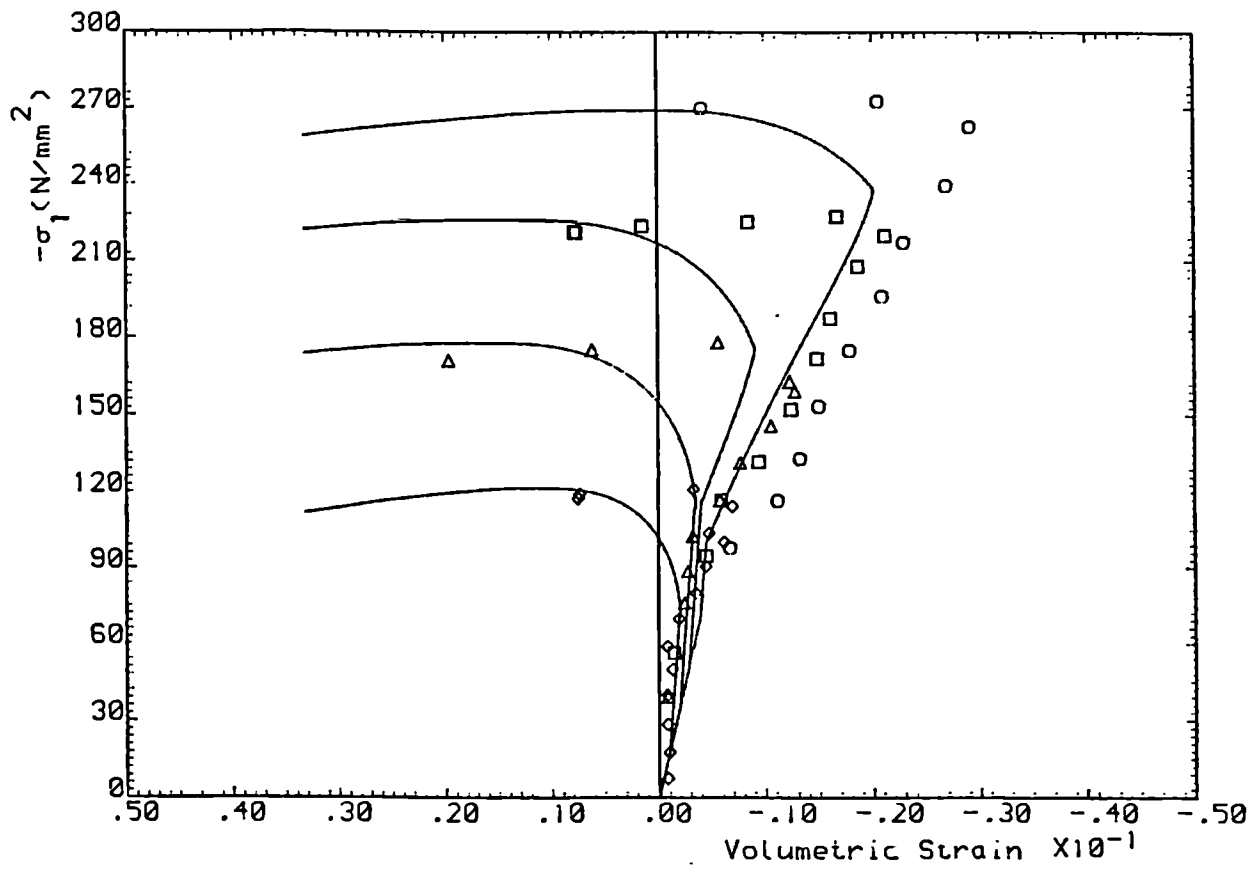
Triaxial Test



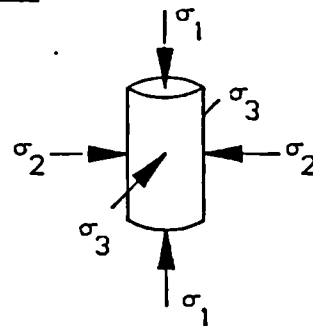
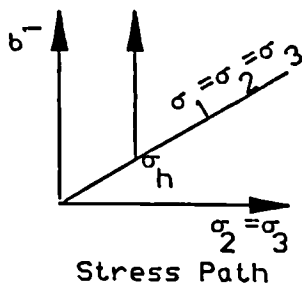
— Suggested Theory	$\sigma_h =$
Kotsovos & Newman [67]	Δ -14.0 N/mm ²
$F_{cu} = 62.1$ N/mm ²	\square -35.0 N/mm ²
	\circ -69.0 N/mm ²

(d)

Fig. 3.23 Continued



Triaxial Test



— Suggested Theory	$\sigma_h =$
Kotsovos & Newman [67]	$\circ -18.0 \text{ N/mm}^2$
$F_{cu} = 46.9 \text{ N/mm}^2$	$\Delta -35.0 \text{ N/mm}^2$
	$\square -51.0 \text{ N/mm}^2$
	$\circ -70.0 \text{ N/mm}^2$

(e)

Fig. 3.23 Continued

C H A P T E R F O U R

FRACTURE MODELLING OF CONCRETE AND EFFECT OF DOWEL ACTION AND TENSION-STIFFENING

4.1 Introduction

Cracking contributes towards the nonlinear behaviour of concrete. In order to represent more closely the behaviour of concrete, the effects of cracking must be accounted for in the constitutive equations.

Plain concrete is assumed to fail by fracturing when a limiting stress or strain criterion is satisfied. Fracture in concrete is defined as 'cracking', when the limiting stress or strain is tensile or defined as 'crushing', when the limiting stress or strain is compressive. Crack planes are, in general, formed perpendicular to the direction of maximum principal stress or strain depending on the fracture criterion used. Once cracking has taken place and the crack surfaces move relative to each other, some forces normal and parallel to the direction of the crack would be transmitted to the adjacent concrete. This phenomenon is due to the irregularities and roughness of the crack planes. Force transmission is partially related to the 'friction' between the two surfaces of a crack and the wedging action of the aggregates and is known as the 'aggregate interlock'. It is very unlikely that cracks form through aggregate since the harden cement matrix is lower in strength than the aggregate. Usually, cracks form in the cement and along the edges of the aggregate particles. Shear displacements are resisted by the

aggregate particles bearing against the opposite crack surfaces when lateral movement of the opposite crack planes occur, Fig. 4.1a.

Crack planes may be crossed by reinforcement bars in reinforced concrete, which could in general be at any arbitrary angle to the crack direction. Such reinforcement provides further resistance against the relative displacements of the crack planes by a phenomenon called 'dowel action', Fig. 4.1b. The other mechanism that influence the force transmission across the crack planes is the bonding action between concrete and reinforcement. Tensile forces may be transmitted to adjacent concrete due to bar-to-concrete bond which is counteracted by the compressive forces in concrete. That is, concrete provides confinement which limits the steel deformation or makes it stiffer. This phenomenon is known as 'tension-stiffening', Fig 4.1c.

In the case of crushing, unlike cracking, concrete loses its stiffness and is no longer capable of transmitting any force upon further loading and total material disintegration is assumed.

In this chapter the fracture behaviour of concrete is studied. First, a general criterion for the fracture of concrete is proposed using the ultimate strength surface proposed in Chapter Three. The cracking process has been studied and it is suggested that the strain normal to the crack direction to be used to monitor the opening and closure of the cracks. The smeared crack approach is adopted here and combined with the rough crack concept to model the behaviour

of a cracked concrete element. The problem of shear transfer has been studied and the constitutive equations relating the crack forces to the crack displacements are developed. These equations are obtained by curve fitting techniques using some experimental data published in the literature. A mathematical model is proposed for the effects of dowel action which relates the dowel forces to the crack displacements. The tension-stiffening effect is considered by introducing a factor to modify the material properties of steel reinforcement. Such a factor is obtained by considering the mechanism of the forces acting on a bar due to the presence of concrete bond stresses. Finally, the equations governing the behaviour of a crack and the reinforcement crossing the crack are combined with the equations of the solid concrete between the cracks to develop the cracked concrete stiffness matrix. Such matrices are developed for a plain concrete element and a concrete element with uniformly distributed steel reinforcement.

4.2 The Proposed Fracture Criteria

It has already been stated that fracturing takes place when the state of stress or strain reaches a critical value. In this study a stress criterion is proposed to determine the fracture of concrete subjected multi-axial loading. The failure criterion proposed in Chapter Three is used to define fracture. Fracture, therefore, is assumed to occur when the following condition is satisfied.

$$\rho - f_{cu} \bar{\rho}_u = 0 \quad (4.1)$$

where $\rho = \sqrt{2J_2}$
 $\bar{\rho}_u =$ ultimate strength given by Eq 3.15, and
 $f_{cu} =$ concrete uniaxial strength

Two possibilities may arise after the criterion for fracturing has been satisfied, fracture may be caused by 'cracking' or it may be caused by 'crushing' depending upon the state of stress. It is, therefore, required to make a distinction between the states of stress on the yield surface. The criteria for distinction of the states of stress are developed in Appendix F. It is assumed that concrete would crack, when the yield surface is reached and one of the principal stresses is tensile or the concrete crushes, when all the principal stresses are compressive and either the residual yield surface defined by β_r is reached or the most compressive principal strain has exceeded a prescribed limit. These two conditions may be represented in the following way

i) Cracking

$$\text{if } \sqrt{2J_2} \geq f_{cu} \bar{\rho}_u \text{ and } \left\{ \begin{array}{l} \bar{\xi} > \bar{\xi}_{C2} \\ \text{or} \\ \bar{\xi}_{C1} < \bar{\xi} \leq \bar{\xi}_{C2} \\ \text{and } \sigma_1 > 0 \end{array} \right.$$

ii) Crushing

$$\text{if } \sqrt{2J_2} \geq f_{cu} \bar{\rho}_u \text{ and } \left\{ \begin{array}{l} \bar{\xi} \leq \bar{\xi}_{C1} \\ \text{or} \\ \bar{\xi}_{C1} < \bar{\xi} \leq \bar{\xi}_{C2} \\ \text{and } \sigma_1 \leq 0 \end{array} \right. \text{ and } \left\{ \begin{array}{l} \beta < \beta_r \\ \text{or} \\ \epsilon_3 < 2\epsilon_{pu} \end{array} \right.$$

where $\bar{\xi}_{C1}$ = a limiting hydrostatic stress in compression zone (see Appendix F),
 $\bar{\xi}_{C2}$ = a limiting hydrostatic stress in compression zone (see Appendix F),
 σ_1 = maximum principal stress,
 ϵ_3 = minimum principal strain,
 β_r = residual value of hardening parameter, and
 ϵ_{pu} = peak uniaxial strain of concrete

4.3 The Adopted Procedures for Cracking

A crack is proposed to form normal to the direction of the maximum principal tensile stress, when the cracking criteria are satisfied. It is assumed that upon cracking partial failure occurs. The cracked concrete can still deform without overall collapse after the formation of the first set of cracks. It is possible, therefore, that the critical cracking criteria are met in other directions when subsequent cracking occurs. The second cracks are usually assumed to be normal to the direction of the first cracks. This is an assumption which may not necessarily hold for concrete since the direction of the principal stresses may change during loading of a structure. Non-orthogonal cracking is, therefore, used in this study. It is possible that due to the capability of cracked concrete to withstand further loading, the cracks may close or reopen. A crack is assumed to close when the strain normal to the crack direction ϵ_{nn} , is compressive or reopen when ϵ_{nn} is tensile. It is, therefore, proposed that new sets of cracks can form provided the cracking criteria are satisfied and at the instant of cracking not more than two

sets of crack are open. Possible crack formations for non-orthogonal cracks are shown in Fig. 4.2.

4.4 Crack Idealisation in Concrete

There are two main approaches used in the finite element method for the treatment of cracked concrete structures and these are the 'smeared' and 'discrete' crack idealisations.

The smeared crack approach assumes that cracks are uniformly distributed over the area of a finite element and considers an average effect of the crack properties over that element, Fig. 4.3a. The cracked concrete is considered to be anisotropic with the crack directions as the axes of anisotropy (local material coordinates). The properties of the cracked concrete are modified in the material coordinate system and transformed to the global axes in order to assemble the overall stiffness of the structure.

The discrete crack approach treats each crack individually by changing the element topology in order to embody the crack formation. A change of direction of the nodal coordinates may also be necessary if the direction of a crack changes, Fig. 4.3b. The application of the discrete crack approach, therefore, causes complications and requires considerable computational time.

The smeared crack approach has been used in this study for its simplicity and practical application. Such a method has been successful when used in the finite element analysis of

structures [68-72].

4.5 Fracture Treatment in Concrete

There are two approaches in characterising the behaviour of cracked concrete within the smeared crack concept and these are the 'smooth' and the 'rough' crack techniques. The former technique neglects the effect of friction due to aggregate interlock and surface roughness. It assumes that upon cracking only shear displacement takes place and crack surfaces behave smoothly without any shear stresses transmitted. Gervenka [73] and Loov [74] applied this technique to concrete by reducing the shear modulus G , to zero after cracking takes place, Fig. 4.4b. Disregarding friction was thought to be on the safe side for the limit state design. Later, shear transfer across cracks was introduced by Franklin [75], Zienkiewicz et al [76] and Mueller [77] in the finite element analysis of concrete structures by maintaining the full shear modulus after cracking, Fig 4.4c. A more realistic method, however, which is still used is to reduce the shear capacity of the cracked concrete by a shear retention factor α [69,71,78], Fig. 4.4d. Later, Cedolin and Dei Poli [72] suggested the use of a variable shear retention factor α , whose variation was dependent upon the change in the strain normal to the crack direction.

By ignoring friction on the crack surfaces or considering the shear transfer in the cracked concrete by the reduction of the shear capacity of cracked concrete may result in an unsafe design [79]. These approaches ignore the normal forces

which act on the crack planes as a result of shear displacement. These forces impose additional tensile stresses in the crossing reinforcement bars, which if ignored may result in the design of insufficient steel reinforcement. A more realistic approach would be to consider the effects of shear dilatancy in the cracked concrete and to model the shear and normal stresses on the crack in terms of the corresponding displacements, Fig 4.5. Some empirical formulations have been proposed for the calculation of these stresses [80-82]. Walraven [83,84] in particular has proposed a theoretical approach to define the fundamentals of the cracked concrete mechanism. His formulations fit the experimental results well. Such a good correlation was achieved, however, at the cost of a great deal of mathematical complexity, which make these equations unfavourable for practical use.

The general behaviour of cracked concrete is studied in the following sections. An attempt is made to determine the stress-displacement relationship of a crack by fitting curves to the results obtained from published experiments conducted on small specimens. These stresses are then combined with the stresses from the solid concrete between the cracks to determine the overall behaviour of cracked concrete.

Unlike cracking, where concrete is considered partially collapsed, the crushing type of failure causes total disintegration of the material resulting in the sudden loss of stiffness. It is, therefore, proposed that the stresses are reduced to zero upon crushing and no further resistance

may be offered by concrete towards any deformation. Fig's. 4.6a and 4.6b show an intact concrete specimen and a crushed specimen.

4.6 The Proposed Models for a Cracked Concrete Element

In this section the three phenomena related to cracked reinforced concrete are considered. These are the aggregate shear transfer, the dowel action, and the tension-stiffening effect. In each case the mechanism of failure of cracked concrete with reinforcement crossing the crack is considered and a mathematical formulation is proposed to describe the corresponding behaviour. The experimental results of previous investigators have been used whenever applicable to obtain the material parameters and to verify the performance of the proposed models.

4.6.1 Aggregate Shear Transfer

Consider a single crack, Fig. 4.7, with local axes defined by the normal direction n , and the tangential directions s and t , respectively. The surface roughness is attributed to the aggregate asperities, which are assumed to be more significant than the crack plane undulation. Thus the crack planes are assumed to be flat. It is further assumed that the aggregate particles are randomly situated on the crack surface so that no preferred direction exists. It is, therefore, justifiable to use the same relationships for shear stresses in both the t and s directions. Hence, a two-dimensional crack is studied, Fig. 4.8. It is assumed that the normal and shear stresses σ_{nn}^{cr} and σ_{nt}^{cr} , on the crack are

developed only when the two crack surfaces are displaced an amount δ_n and δ_t , relative to each other and the crack asperities have made contact with each other. The proposed formulations must, therefore, satisfy the following conditions.

- i) When $\delta_n = 0$ the concrete is in a solid state and no crack exists,
- ii) δ_n should always be positive for a crack to exist,
- iii) The contact points can be developed between the two cracks provided δ_t is positive. Therefore, for $\delta_n > 0$ and $\delta_t = 0$, $\sigma_{nt}^{cr} = \sigma_{nn}^{cr} = 0$,
- iv) For $\delta_t = \text{constant}$ and δ_n increasing, the number of contact points decreases resulting in a reduction of σ_{nt}^{cr} and σ_{nn}^{cr} ,
- v) For $\delta_n = \text{constant}$ and δ_t increasing, the number of contact points increases resulting in an increase of σ_{nt}^{cr} and σ_{nn}^{cr} , and
- vi) The asperities may break down as a result of a large shear displacement which reduces the rate of increase of σ_{nt}^{cr} and σ_{nn}^{cr} . Finally, some stresses remain which is due to pure friction between the two crack surfaces.

In addition, the proposed formulations must be continuous since there are an infinite number of contact points.

4.6.1.1 The Proposed Cross Crack Stress-Displacement Mathematical Model

Prior to the development of the mathematical models, it is worth considering some experimentally obtained characteristics of crack behaviour. The results of Loeber[85] and Paulay and Loeber [86] show that at constant normal displacement δ_n , the shear stress σ_{nt}^{cr} , increases as the shear displacement δ_t , is increased. At early stages the slope of σ_{nt}^{cr} versus δ_t is fairly small but becomes steeper as δ_t increases, before finally reducing to zero, Fig 4.9. This kind of behaviour was also observed in the experimental results of other investigators such as Walraven et al [87]. This behaviour may be explained in the following way. During the early stages of the crack displacement, contact points have not fully developed, therefore, small stresses exist on the crack. Higher shear stresses are expected as the shear displacement is increased and more contacts are made. It can also be seen that as the normal displacement δ_n , decreases steeper curves occur which reflect the higher crack stiffness due to increased contact area between the two cracks. The ultimate shear stress capacity $\sigma_{nt,u}^{cr}$, is reached when a large shear displacement has been taken place. A gradual decrease in $\sigma_{nt,u}^{cr}$ is attributed to the variation of δ_n and is considered to be independent of δ_t . Walraven showed theoretically that the maximum shear stress $\sigma_{nt,u}^{cr}$, at constant crack width δ_n , increases as the maximum aggregate particle size D_{max} , is increased [84,87]. Similar behaviour was observed by Walraven for normal crack stresses σ_{nn}^{cr} , [84,87].

The following mathematical models are proposed for the variation of normal and shear stresses σ_{nn}^{cr} and σ_{nt}^{cr} , with the crack displacements δ_n and δ_t . These relationships are obtained by a regression analysis of the experimental results reported in Ref's. [84,87] and are proposed in the following form

$$\sigma_{nt}^{cr} = \sigma_{nt,u}^{cr} \left(1 - \frac{1}{1 + m_1 \delta_t^{m_2}} \right) \quad (4.2a)$$

$$\sigma_{nn}^{cr} = \sigma_{nn,u}^{cr} \left(1 - \frac{1}{1 + n_1 \delta_t^{n_2}} \right) \quad (4.2b)$$

where

$$\sigma_{nt,u}^{cr} = \frac{\sigma_{nt,0}^{cr}}{1 + m_3 \delta_n^{m_4}}$$

= ultimate shear stress,

$$\sigma_{nn,u}^{cr} = \frac{\sigma_{nn,0}^{cr}}{1 + n_3 \delta_n^{n_4}}$$

= ultimate normal stress,

$$\sigma_{nt,0}^{cr} = m_5 f_{cu}^{m_6}$$

= limiting value of $\sigma_{nt,u}^{cr}$ when $\delta_n \rightarrow 0$,

$$\sigma_{nn,0}^{cr} = n_5 f_{cu}^{n_6}$$

= limiting value of $\sigma_{nn,u}^{cr}$ when $\delta_n \rightarrow 0$,

$$\begin{aligned}
m_1 &= m_7 \delta_n^{m_8}, \\
m_2 &= m_9 + m_{10} \delta_n, \\
m_3 &= 2.9335 - 61.6351 \times 10^{-3} D_{\max}, \\
m_4 &= 1.2830 + 6.6224 \times 10^{-3} D_{\max}, \\
m_5 &= 2.05, \\
m_6 &= 0.56, \\
m_7 &= 1.2272 - 14.1339 \times 10^{-3} D_{\max}, \\
m_8 &= -2.0375 + 7.8263 \times 10^{-3} D_{\max}, \\
m_9 &= 2.2455 - 17.3866 \times 10^{-3} D_{\max}, \\
m_{10} &= 1.6305 - 13.4943 \times 10^{-3} D_{\max}, \\
n_1 &= n_7 \delta_n^{n_8}, \\
n_2 &= n_9 + n_{10} \delta_n, \\
n_3 &= 2.3588 - 35.6138 \times 10^{-3} D_{\max}, \\
n_4 &= 2.5056 - 34.0107 \times 10^{-3} D_{\max}, \\
n_5 &= 2.00, \\
n_6 &= 0.56, \\
n_7 &= 0.3217 - 2.8436 \times 10^{-3} D_{\max}, \\
n_8 &= -1.3415 - 12.1207 \times 10^{-3} D_{\max}, \\
n_9 &= 1.2840 + 12.5100 \times 10^{-3} D_{\max}, \\
n_{10} &= 3.0162 - 25.9231 \times 10^{-3} D_{\max}, \\
f_{cu} &= \text{concrete uniaxial compressive} \\
&\quad \text{strength, and} \\
D_{\max} &= \text{maximum aggregate particle size}
\end{aligned}$$

Fig's. 4.10a to 4.10d show the comparison between the experimental results of Walraven [84,87] and the proposed theoretical model for different concrete grades, crack widths and maximum aggregate size. The fit of the experimental values is satisfactory. Fig. 4.11 shows the fit of the proposed model to the experimental results of Loeber [85]

together with the suggested bilinear equations of Loeber [85]. It appears that a better correlation exists at low crack widths. The proposed theory provides a reasonably accurate model, considering the scatter of the experimental results and the variation of upto ± 45 percent for the shear stress values obtained on either side of the test specimen [85].

4.6.1.2 The Crack Stiffness Matrix due to Aggregate Interlock

The shear and normal stresses on a crack σ_{nt}^{cr} and σ_{nn}^{cr} are functions of the normal and shear displacements δ_n and δ_t , given by Eq's. 4.2a and 4.2b. These equations can be written in a general form as

$$\sigma_{nt}^{cr} = f_t(\delta_t, \delta_n) \quad (4.3)$$

$$\sigma_{nn}^{cr} = f_n(\delta_t, \delta_n) \quad (4.4)$$

The incremental crack stresses can be related to the increments of displacements in a manner similar to that for uncracked concrete as follows

$$\begin{Bmatrix} d\sigma_{nn}^{cr} \\ d\sigma_{nt}^{cr} \end{Bmatrix} = \begin{bmatrix} K_{nn} & K_{nt} \\ K_{tn} & K_{tt} \end{bmatrix} \begin{Bmatrix} d\delta_n \\ d\delta_t \end{Bmatrix} \quad (4.5)$$

where

$$K_{nn} = \frac{\partial f_n}{\partial \delta_n},$$

$$K_{nt} = \frac{\partial f_n}{\partial \delta_t},$$

$$K_{tt} = \frac{\partial f_t}{\partial \delta_t}, \text{ and}$$

$$K_{tn} = \frac{\partial f_t}{\partial \delta_n}$$

The parameters K_{nn} , K_{nt} , K_{tt} and K_{tn} are known as the crack 'stiffness coefficients' which are dependent on δ_n and δ_t . The explicit expressions for these coefficients are obtained by differentiation of Eq's. 4.2a and 4.2b with respect to δ_n and δ_t . These expressions are given in Appendix G.

4.6.2 Dowel Action

If cracks are crossed by reinforcement bars and the crack planes are subjected to shear displacement, the shear forces are partly counteracted by the surface roughness and irregularities and partly by the steel bars by flexure. This counteraction of the bars is called 'dowel action', Fig. 4.1b. The dowel force F_d , is assumed to act normal to the bar direction. It is possible to simulate the dowel action by considering a block of concrete with a single reinforcement bar casted in the block, Fig. 4.12a. The dowel force may be idealised by the application of a force F_d , normal to the bar which results in a bar deflection of Δ . This deflection is equivalent to the crack shear

displacement. The stress distribution in concrete, Fig. 4.12a, indicates that the concrete immediately below the bar crushes which in turn causes an increase in the bar deflection at constant dowel force. This type of behaviour suggests that an elasto-plastic behaviour may be assumed for the variation of F_d with Δ , Fig. 4.12b.

4.6.2.1 The Proposed Dowel Force-Displacement Mathematical Model

Several investigators have attempted to obtain the relationship between force and dowel deflection [83,84,88-92]. In this study the model proposed by Dulacscka [92] is used to predict the dowel force F_d . Some modifications are made, however, to the original form of the equations. The original dowel force-displacement relationships were given as follows

$$\Delta = \frac{k A}{\phi \sqrt{f_{cu}}} F_{d,u} \quad (4.6)$$

where

$$A = \frac{F_d}{F_{d,u}} \sqrt{\tan\left(\frac{F_d}{F_{d,u}} \frac{\pi}{2}\right)},$$

Δ = dowel displacement,

F_d = dowel force,

$F_{d,u}$ = ultimate dowel force,

ϕ = bar diameter,

f_{cu} = concrete uniaxial compressive strength, and

$k = 1.1423 \times 10^{-3}$

The modifications proposed here involve a rearrangement of the expression for the nondimensional dowel force $\frac{F_d}{F_{d,u}}$, and introduction of the reduction coefficient R_w used by Walraven [83,84] and Walraven and Reinhardt [89] to include the effects of the crack width on the dowel force. It is proposed to use the following expression for the nondimensional dowel force, Fig. 4.13

$$\frac{F_d}{F_{d,u}} = \frac{a A^b}{1 + a A^b} \quad (4.7)$$

where $a = 2.2915$, and
 $b = 1.1963$

combining Eq's. 4.6 and 4.7 and introducing the reduction coefficient R_w , results in the following

$$F_d = \frac{R_w t \delta_t^b}{1 + t \delta_t^b} F_{d,u} \quad (4.8)$$

where F_d = dowel force,

$$t = a \left(\frac{\phi \sqrt{f_{cu}}}{k F_{d,u}} \right)^b,$$

$$R_w = \frac{0.2}{\delta_n + 0.2}$$

= reduction factor [83,84,89],

$$F_{d,u} = 0.2 \phi^2 f_y \left[\sqrt{\sin^2 \theta_{bc} + \frac{f_{cu}}{0.03 f_y}} - \sin \theta_{bc} \right]$$

= ultimate dowel force [92],

θ_{bc} = angle between reinforcement bar and the
normal to the crack direction,
 δ_n = crack normal displacement,
 δ_t = crack shear displacement,
 ϕ = bar diameter,
 f_{cu} = concrete uniaxial compressive strength,
 f_y = steel yield stress, and
a, b and k = constants (see above)

A comparison between the theoretical dowel stress proposed by Eq. 4.8 and the experimental results of Paulay et al [93] for different bar sizes has been made, Fig 4.14. A reasonable correlation is achieved particularly for the smaller bar sizes and the comparison is considered satisfactory.

A comparison between the contribution of the dowel shear stress τ_d (Eq. 4.8), and the total shear stress τ_i on the crack surface of specimens with embedded bars (after Walraven et al [87]) is shown in Table 4.1. It can be seen that in all the cases the dowel force contribution is less than 10 percent of the total shear stress and thus of minor importance. A similar conclusion was made by Walraven [84]. Eleiott [94] conducted tests on specimens with dowel action alone and specimens which combined the effects of aggregate interlock and dowel action. The investigation showed that about 12 percent of the stiffness was provided by dowel action and about 88 percent by aggregate interlock. The results obtained from the proposed model, therefore, are consistent with the experimental results of Eleiott.

Table 4.1 A comparison of the contribution of shear stress due to dowel force with shear stress due to aggregate interlock. (Experimental results of Walraven et al [87] versus Eq. 4.8)

No. of bars	δ_t (mm)	δ_n (mm)	τ_d (N/mm ²)	τ_i (N/mm ²)	% $\frac{\tau_d}{\tau_i}$
2	0.10	0.131	0.152	5.35	2.84
2	0.30	0.320	0.162	6.75	2.37
2	0.50	0.493	0.134	6.87	1.95
4	0.10	0.127	0.308	6.36	1.96
4	0.30	0.136	0.322	8.27	3.89
4	0.50	0.486	0.271	8.71	3.11
6	0.10	0.124	0.468	7.38	6.34
6	0.30	0.313	0.485	9.29	5.22
6	0.50	0.479	0.411	9.55	4.30
8	0.10	0.121	0.628	8.27	7.59
8	0.30	0.310	0.651	10.00	6.51
8	0.50	0.472	0.554	—	—

Detail of the test specimen

(Mix No.5 of Walraven et al [89]) :

$$\theta_{bc} = 0^\circ,$$

$$f_{cu} = 38.2 \text{ N/mm}^2,$$

$$f_y = 460.0 \text{ N/mm}^2,$$

$$\phi = 8 \text{ mm},$$

$$A_{sh} = 36000 \text{ mm}^2$$

= shear area, and

$$D_{max} = 32 \text{ mm}$$

4.6.2.2 Dowel Stiffness

The geometry of a cracked reinforced concrete element and the associated dowel forces are shown in Fig. 4.15a. The dowel force F_d , is resolved into normal and shear components acting on the crack surface when the reinforcement bar is inclined to the crack direction at an angle θ_{bc} . These components are transformed into the corresponding stresses using the cross-sectional area of concrete A_c , Fig. 4.15b. It should be noted, however, that Eq. 4.8 gives the component of the dowel force parallel to the crack direction. The dowel stresses are, therefore, given as

$$\sigma_{nt}^d = \frac{F_d}{A_c} \quad (4.9)$$

$$\sigma_{nn}^d = \frac{F_d}{A_c} \tan\theta_{bc} \quad (4.10)$$

alternatively

$$\sigma_{nt}^d = \frac{p F_d}{A_b} \quad (4.11)$$

$$\sigma_{nn}^d = \frac{p F_d}{A_b} \tan\theta_{bc} \quad (4.12)$$

where $p = \frac{A_s}{A_c}$

= steel ratio,

A_s = area of steel,

A_c = area of concrete, and

A_b = area of one bar

The dowel stress increments are related to the displacement increments using the dowel stiffness matrix as

$$\begin{Bmatrix} d\sigma_{nn}^d \\ d\sigma_{nt}^d \end{Bmatrix} = \begin{bmatrix} H_{nn} & H_{nt} \\ H_{tn} & H_{tt} \end{bmatrix} \begin{Bmatrix} d\delta_n \\ d\delta_t \end{Bmatrix} \quad (4.13)$$

where

$$H_{nn} = \frac{\partial \sigma_{nn}^d}{\partial \delta_n},$$

$$H_{nt} = \frac{\partial \sigma_{nn}^d}{\partial \delta_t},$$

$$H_{tt} = \frac{\partial \sigma_{nt}^d}{\partial \delta_t}, \text{ and}$$

$$H_{tn} = \frac{\partial \sigma_{nt}^d}{\partial \delta_n}$$

The parameters H_{nn} , H_{nt} , H_{tt} and H_{tn} are known as dowel 'stiffness coefficients. The explicit expressions for these coefficients are obtained by differentiation of Eq's. 4.11 and 4.12 with respect to δ_t and δ_n . These expressions are given in Appendix H.

4.6.3 Tension Stiffening

Prior to the development of cracks there is a full continuity between the reinforcement bars and the surrounding concrete, which is provided by the steel to concrete bond. The concrete in the vicinity of a crack is no longer capable of carrying

any tensile stress as a result of cracking and the full load is taken by steel. The concrete between the cracks, however, is still able to carry some tensile stress. The tensile stiffness of concrete reduces gradually as the bond slip between reinforcement bars and the surrounding concrete takes place [95]. In general, concrete between the two adjacent cracks partially resists the tensile stress which otherwise would be imposed on steel bars. Concrete, therefore, prevents some of the steel deformation. This effect would be enhanced if compressive stresses were present in the concrete close to the reinforcement bars. This phenomenon is known as 'tension-stiffening'. In summary, although tension-stiffening is related to concrete it may be included in the properties of steel reinforcement bars.

Previous investigators have introduced tension-stiffening effects by modifying concrete properties [78,96] or by changing the steel properties [97-99]. More recently, Bazant and Oh [100] used fracture mechanics laws to characterise the tension-stiffening in terms of an equivalent cross-sectional area of steel bars. Such an area represents an equivalent 'bond free' steel bar which produces the same axial extension as the actual bar with the bond stresses present.

4.6.3.1 The Proposed Tension-Stiffening Factor

Consider a block of concrete with an embedded bar which is subjected to an increasing pull-out force, Fig. 4.16a. Bond slip δ_b , takes place over a certain length of the bar upon increasing the pull-out force. The steel bar becomes separated from the surrounding concrete, as a result of this

slip over the bond slip length L_s . The bond over the bond slip length is assured by friction and interlock between the concrete and the reinforcing bar ribs. The variation of bond stress τ_b , over this length is non-uniform, Fig. 4.16b. To obtain a simple and approximate solution, however, the bond stress is assumed to be uniform and of magnitude of τ_b , over the bond slip length, Fig. 4.16c.

The bond slip length is obtained in accordance with the equation proposed by Bazant and Cedolin [101]. This length is, therefore, given as

$$L_s = \frac{A_b \sigma_s}{U_b (1 + n p)} \quad (4.14)$$

where

- L_s = bond slip length,
- σ_s = steel stress at the crack,
- A_b = cross-sectional area of a bar,
- $U_b = \pi \cdot \phi \cdot \tau_b$
= bond force per unit length of a bar,
- τ_b = bond stress,
- ϕ = bar diameter,
- $n = \frac{E_s}{E_c}$
= ratio of the steel Young's modulus to that of concrete, and
- p = percentage of steel reinforcement

The equilibrium of forces is then considered for a bar crossing a crack in accordance with the technique used by

Gambarova [81]. The average steel strain for the length of a bar bounded between two adjacent cracks can be described in terms of the steel stress and bond slip length. From such a consideration, the tension-stiffening parameter α_t , is deduced as follows

$$\alpha_t = \frac{s' U_b (1 + n p)^2}{2A_b s + s' U_b n p (1 + n p)} \quad (4.15)$$

where

$$s' = \frac{s}{\cos \theta_{bc}},$$

s = crack spacing,

θ_{bc} = the angle between the normal to the crack and the bar,

U_b = bond force per unit length,

A_b = cross-sectional area of a bar,

$$n = \frac{E_s}{E_c}, \text{ and}$$

p = percentage of reinforcement

The derivation of α_t is given in Appendix I and is used to modify the steel properties as follows

$$E_s^* = \alpha_t E_s \quad (4.16)$$

where

E_s = initial steel Young's modulus,

E_s^* = steel Young's modulus with tension-stiffening effect, and

α_t = tension-stiffening parameter

The evaluation of the tension-stiffening factor α_t , for the experimental results of Walraven [84] and Walraven et al [87] is given in Fig. 4.17. It can be seen that the effective Young's modulus of steel E_s^* , may be many times larger than the initial value E_s .

It is concluded that when high bond characteristics exists, i.e. for a smaller steel ratio, a higher tension-stiffening factor α_t , is achieved. The value of α_t tends to unity as the bond slip length L_s , approaches its limiting value $s/2$, i.e. the one half of the crack spacing. This limit indicates that the bar between the two cracks is completely separated from the surrounding concrete.

4.7 The Proposed Crack Concrete Stiffness Matrices

In this section, the theoretical developments proposed in the previous sections for the different features of a cracked concrete element are combined with the properties of solid concrete to form the stiffness matrices, which represent the response of an element of concrete with cracking. The implementation of the developments is presented in two parts. The first part deals with plain concrete elements in which the reinforcement bars are idealised at the boundaries of a concrete finite element, e.g. using bar elements. In this case the properties of the solid concrete between the cracks are only combined with crack properties caused by aggregate shear transfer. In the second part, a reinforced concrete element is considered in which the reinforcement bars are uniformly distributed over the area of concrete. In this case

the effects of dowel forces and tension-stiffening as well as the effects of aggregate interlock are introduced.

4.7.1 The Stiffness Matrix of a Cracked Plain Concrete

Fig. 4.18a shows a finite element mesh for plain concrete which includes a cracked zone. Consider an element of plain concrete within the cracked zone where a system of parallel cracks is running at an angle θ_{cr} through the element, Fig. 4.18b. Using the concept of a smeared crack, it is possible that the effect of the sharp cracks is distributed uniformly over the tributary area of a gauss point. The relative displacements in the crack could be, therefore, transformed into equivalent crack strains as

$$\epsilon_{nn}^{cr} = \frac{\delta_n}{s} \quad (4.17)$$

$$\gamma_{nt}^{cr} = 2\epsilon_{nt}^{cr} = \frac{\delta_t}{s} \quad (4.18)$$

where ϵ_{nn}^{cr} = crack normal strains,
 γ_{nt}^{cr} = crack shear strains,
 δ_n = crack normal displacement,
 δ_t = crack shear displacement, and
 s = the average crack spacing

In the absence of reinforcement bars the stresses in the uncracked concrete σ^{sc} , are the same as the stresses in the crack σ^{cr} , and equal to the normal stresses σ . The increments of stress are also equal, therefore

$$d\sigma^{sc} = d\sigma^{cr} = d\sigma \quad (4.19)$$

The average strains in concrete are the sum of strains in the uncracked concrete ϵ^{sc} , and strains due to the cracks ϵ^{cr} , therefore

$$d\epsilon = d\epsilon^{sc} + d\epsilon^{cr} \quad (4.20)$$

At this stage the constitutive equations developed for a crack are used, i.e. Eq. 4.5. If this relationship is inverted the crack flexibility matrix is obtained as

$$\begin{Bmatrix} d\delta_n \\ d\delta_t \end{Bmatrix} = \begin{Bmatrix} F_{nn} & F_{nt} \\ F_{tn} & F_{tt} \end{Bmatrix} \begin{Bmatrix} d\sigma_{nn}^{cr} \\ d\sigma_{nt}^{cr} \end{Bmatrix} \quad (4.21)$$

where $F = K^{-1}$
 $=$ crack flexibility matrix, and
 $K =$ crack stiffness matrix from Eq. 4.5

Combining Eq's. 4.17, 4.18 and 4.21, yields

$$\begin{Bmatrix} d\epsilon_{nn}^{cr} \\ d\epsilon_{tt}^{cr} \\ d\gamma_{nt}^{cr} \end{Bmatrix} = \begin{Bmatrix} F_{nn} s^{-1} & 0 & F_{nt} s^{-1} \\ 0 & 0 & 0 \\ F_{tn} s^{-1} & 0 & F_{tt} s^{-1} \end{Bmatrix} \begin{Bmatrix} d\sigma_{nn}^{cr} \\ d\sigma_{tt}^{cr} \\ d\tau_{nt}^{cr} \end{Bmatrix} \quad (4.22)$$

or simply

$$d\epsilon^{cr} = C^{cr} d\sigma^{cr} \quad (4.23)$$

where $C^{cr} = F s^{-1}$
= crack flexibility matrix

Combining Eq's. 4.19 and 4.23, gives

$$d\epsilon^{cr} = C^{cr} d\sigma \quad (4.24)$$

By using the Hook's law the uncracked concrete strains may be written as

$$d\epsilon^{sc} = C^{sc} d\sigma^{sc} \quad (4.25)$$

where $C^{sc} = D^{sc-1}$
= solid concrete flexibility matrix

Combining Eq's. 4.19 and 4.25, gives

$$d\epsilon^{sc} = C^{sc} d\sigma \quad (4.26)$$

D^{sc} may be obtained from the elasto-plastic relationship developed in Chapter Three (Eq. 3.43) if the stresses and strains are large, otherwise it is acceptable to use the linear elastic modular matrix D^e . Combining Eq. 4.20, 4.24 and 4.26, the flexibility matrix for cracked concrete C^{cc} , is obtained as

$$d\varepsilon = C^{cc} d\sigma \quad (4.27)$$

where $C^{cc} = C^{sc} + C^{cr}$

From Eq. 4.27 the constitutive law for cracked concrete is given by

$$d\sigma = D^{cc} d\varepsilon \quad (4.28)$$

where $D^{cc} = C^{cc^{-1}}$

The matrix D^{cc} is the incremental stiffness matrix of a cracked plain concrete element in the local crack coordinates n and t . It should be, therefore, transformed to the element coordinate system by means of a transformation matrix T , for use in a finite element method, as

$$D_{elem}^{cc} = T^T D^{cc} T \quad (4.29)$$

The transformation matrix is given as

$$T = \begin{pmatrix} c^2 & s^2 & sc \\ s^2 & c^2 & -sc \\ -2sc & 2sc & c^2 - s^2 \end{pmatrix} \quad (4.30)$$

where $C = \cos\theta_{cr}$

$S = \sin\theta_{cr}$, and

$\theta_{cr} =$ crack angle (see Fig. 4.18)

In Eq's. 4.17-4.30, the superscripts refer to crack (cr), solid concrete (sc) and cracked concrete (cc).

4.7.2 The Stiffness Matrix of Cracked Reinforced Concrete

The relationships which have been used between stresses and displacements in cracked reinforced concrete are those proposed by Bazant and Gambarova [80]. A modification for the dowel stresses and tension-stiffening effect has been incorporated, however, in accordance with the suggested methods by Bazant and Oh [100] and Walraven [84] and Walraven and Reinhardt [89], respectively.

Consider a panel of reinforced concrete where reinforcement bars are uniformly and densely distributed, Fig. 4.19b. In the uncracked zone, the separate stiffnesses of the concrete and steel can be combined into an equivalent stiffness for a reinforced concrete element. Since the stresses and strains in the concrete and the bars are the same, therefore

$$d\sigma = D^{rc} d\epsilon \quad (4.31)$$

where $D^{rc} = D^{sc} + D^s$
 $=$ reinforced concrete modular matrix,
 $D^{sc} =$ solid concrete modular matrix, and
 $D^s =$ steel bars modular matrix

D^{sc} may be obtained from Eq. 3.43 and D^s is given as follows

$$D^S = \sum_{i=1}^n T^T D_i^S T \quad (4.32)$$

where

$$D_i^S = \begin{pmatrix} p_i E_{s,i} & 0 & 0 \\ 0 & 0 & 0 \\ 0 & 0 & 0 \end{pmatrix}$$

= modular matrix of the i^{th} system
of reinforcements,

$i = 1, 2, \dots, n$

= number of reinforcement systems,

$E_{s,i}$ = Young's modulus of the i^{th} reinforcement
system,

p_i = percentage of steel of the i^{th}
reinforcement system,

T = transformation matrix for angle ω_i
(see Eq.4.30), and

ω_i = angle of the i^{th} reinforcement system,
(see Fig. 4.19)

The cracked reinforced concrete stiffness matrix is obtained in a similar way to the plain concrete stiffness matrix but account is now taken of the effects of dowel action and tension-stiffening. Consider an element of reinforced concrete with a set of reinforced bars at angles of θ_{bc1} and θ_{bc2} to the direction of normal to the crack, and a set of parallel cracks running at angle of θ_{cr} to the x-element axis, Fig 4.19b. The average strains are the sum of the strains in the solid concrete and in the cracks and are given as

$$d\varepsilon = d\varepsilon^{cr} + d\varepsilon^{sc} \quad (4.33)$$

where $d\varepsilon^{sc} = C^{sc} d\sigma^{sc}$ (4.34)

$$d\varepsilon^{cr} = C^{cr} d\sigma^{cr} \quad (4.35)$$

Unlike plain concrete the stresses in the uncracked concrete σ^{sc} , must equal the sum of stresses in the cracks σ^{cr} , and the stresses due to the dowel action σ^d . Therefore,

$$d\sigma^{sc} = d\sigma^{cr} + d\sigma^d \quad (4.36)$$

From Eq's. 4.13, 4.17 and 4.18, the dowel stresses for a bar system is given as

$$\begin{Bmatrix} d\sigma_{nn}^d \\ d\sigma_{tt}^d \\ d\tau_{nt}^d \end{Bmatrix} = \begin{bmatrix} H_{nn} s^{-1} & 0 & H_{nt} s^{-1} \\ 0 & 0 & 0 \\ H_{tn} s^{-1} & 0 & H_{tt} s^{-1} \end{bmatrix} \begin{Bmatrix} d\varepsilon_{nn}^{cr} \\ d\varepsilon_{tt}^{cr} \\ d\gamma_{nt}^{cr} \end{Bmatrix} \quad (4.37)$$

The summation of the dowel stresses due to all the bars is

$$d\sigma^d = D^d d\varepsilon^{cr} \quad (4.38)$$

where $D^d = \sum_{i=1}^n H_i$,
 H_i = dowel stiffness matrix for the i^{th}
 reinforcement system (see Eq. 4.37), and
 $i = 1, 2, \dots, n$
 = number of reinforcement systems

Substituting Eq. 4.35 in Eq. 4.38 gives

$$d\sigma^d = D^d C^{cr} d\sigma^{cr} \quad (4.39)$$

and combining Eq. 4.34 and Eq. 4.37 yields

$$d\sigma^{sc} = [I + D^d C^{cr}] d\sigma^{cr} \quad (4.40)$$

where I = unit matrix

Inverting Eq. 4.40 and substituting the result in into Eq. 4.35 gives

$$d\epsilon^{cr} = C^{cr} [I + D^d C^{cr}]^{-1} d\sigma^{sc} \quad (4.41)$$

Combining Eq's. 4.33, 4.34 and 4.41, produces

$$d\epsilon = \left\{ C^{sc} + C^{cr} [I + D^d C^{cr}]^{-1} \right\} d\sigma^{sc} \quad (4.42)$$

alternatively

$$d\epsilon = C^{ccd} d\sigma^{sc} \quad (4.43)$$

where C^{ccd} = cracked concrete flexibility matrix
with dowel force effect included

It should be noted that if the effect of dowel action is neglected Eq. 4.42 reduces to

$$d\epsilon = [C^{sc} + C^{cr}] d\sigma^{sc} \quad (4.44)$$

The effect of reinforcement bars can now be introduced by assuming that the total stresses σ , are equal to the summation of the stresses in the solid concrete σ^{sc} , and stresses in the steel reinforcement bars σ^S . The increments of stress are, therefore, given as follows

$$d\sigma = d\sigma^{sc} + d\sigma^S \quad (4.45)$$

From Eq. 4.43 it is concluded that

$$d\sigma^{sc} = C^{ccd^{-1}} d\epsilon \quad (4.46)$$

and the steel stresses are

$$d\sigma^S = D^S d\epsilon \quad (4.47)$$

D^S is obtained in a similar way to Eq. 4.32, but the Young's modulus of steel bars E_s , is replaced by E_s^* from Eq. 4.16 to include the tension-stiffening effect. Also, D^S must be transformed to the crack coordinate system by the transformation matrix T , Eq. 4.30. The stiffness of the cracked reinforced concrete is obtained by combining Eq's. 4.45 to 4.47, as follows

$$d\sigma = [D^S + C^{ccd^{-1}}] d\epsilon \quad (4.48)$$

alternatively

$$d\sigma = D^{rccd} d\varepsilon \quad (4.49)$$

where D^{rccd} = cracked reinforced concrete stiffness matrix including dowel action and tension-stiffening effects

The matrix D^{rccd} must be transformed to the element coordinate system by means of a transformation matrix T , for use in a finite element method, as

$$D_{elem}^{rccd} = T^T D^{rccd} T \quad (4.50)$$

In Eq's. 4.31 to 4.50, the superscripts refer to reinforced concrete (rc), solid concrete (sc), steel (s), crack (cr), dowel (d), cracked concrete with dowel effect (ccd), cracked concrete (cc) and cracked reinforced concrete with dowel effect (rccd).

4.8 Conclusions

The following points are concluded from this chapter

- i) Fracture in concrete occurs when the fracturing criteria are satisfied. Fracture is by cracking in the tensile region, where concrete is partially failed, or by crushing, where total failure of concrete takes place. A stress criterion is proposed for the definition of fracture based on the proposed yield surface developed in Chapter Three.

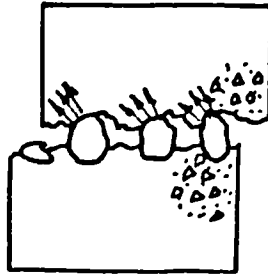
- ii) A smeared crack approach is more favourable for use in the finite element method in comparison with the discrete crack approach. This is due to computational simplicity and relatively easy computer programming.

- iii) The shear transfer due to the aggregate interlock has an important effect on the behaviour of cracked concrete and is best modelled by considering normal and shear stresses on the crack surfaces. Suitable mathematical models are proposed to represent the aggregate interlock effect. Close correlation of the resulting equations with the published experimental results confirm their validity.

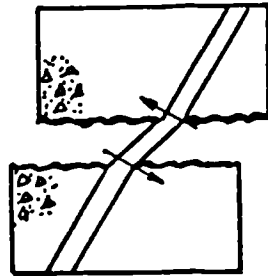
- iv) Dowel action makes some contribution towards resisting the shear stresses in cracked reinforced concrete. Its contribution, however, is small compared with aggregate interlock. Some existing models have been modified to enable a reasonable representation of dowel stresses in cracked reinforced concrete. The comparison between the results of the proposed model and the experimental evidence is considered satisfactory.

- v) The effect of bar-to-concrete bond is introduced within the concept of tension stiffening which involves the modification of the steel properties. It was found that the modified steel Young's modulus may be several times greater than the initial value before cracks were formed

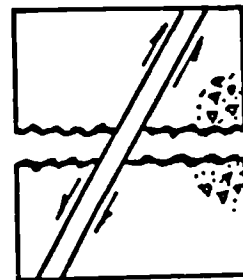
vi) Cracked stiffness matrices of cracked plain and reinforced concrete were obtained by combining the stiffness of the solid concrete between the cracks and the stiffness of cracks. In the case of the cracked reinforced concrete, dowel stiffness and tension-stiffening effects were also introduced. These matrices were assembled in a form suitable for use in the finite element method.



(a) Aggregate Interlock

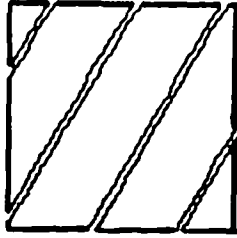


(b) Dowel Action

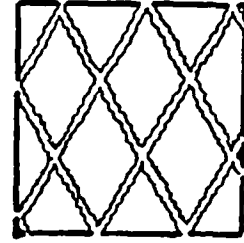


(c) Bond Action

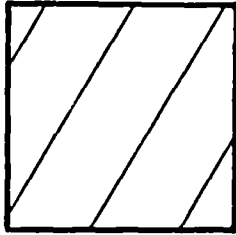
Fig. 4.1 Representation of different mechanisms for cracked reinforced concrete.



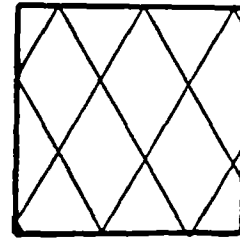
(a) First Crack Formed



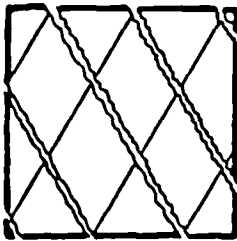
(b) First Crack Open and Second Crack Formed



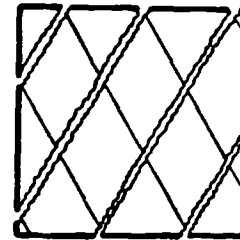
(c) First Crack Closed



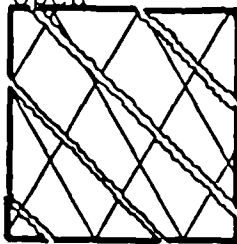
(d) First and Second Cracks Closed



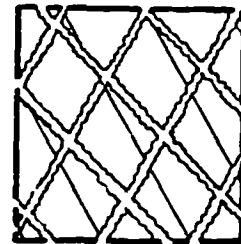
(e) First Crack Closed and Second Crack Open



(f) Second Crack Closed and Second Crack Open

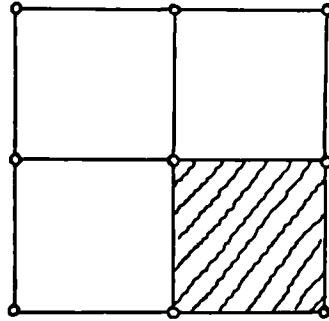


(g) First and Second Cracks Closed and Third Crack Formed

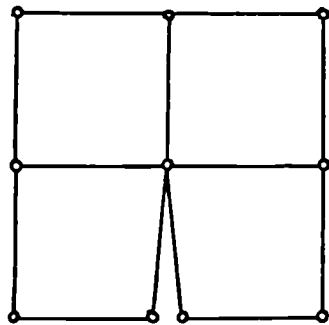


(h) First Crack Closed, Second Crack Open and Third Crack Formed

Fig. 4.2 Possible crack formations and crack opening and closure.



(a) Smearred Crack



(b) Discrete Crack

Fig. 4.3 Crack idealisation in the finite element method.

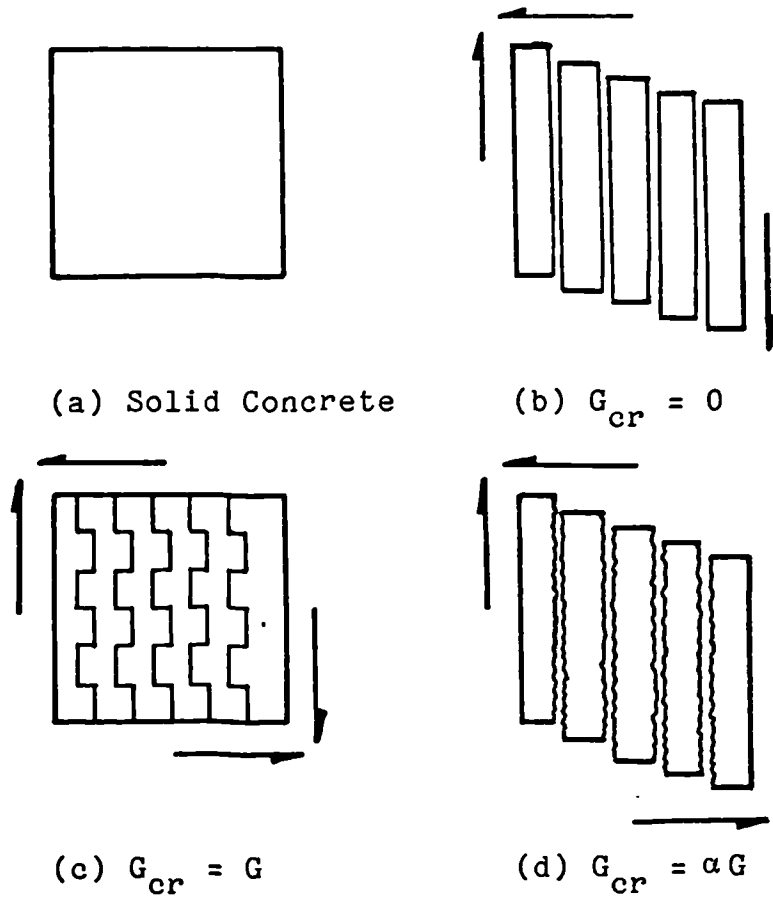


Fig. 4.4 Schematic representation of different crack models.

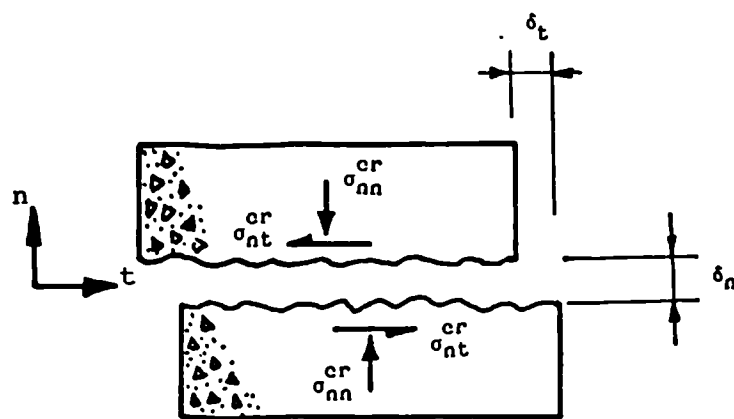
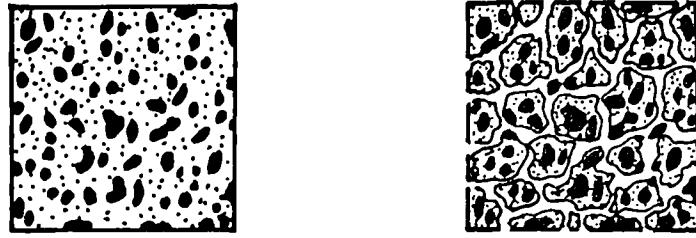


Fig. 4.5 Rough crack representation.



(a) Solid Concrete (b) Crushed Concrete

Fig. 4.6 Crushed concrete representation.

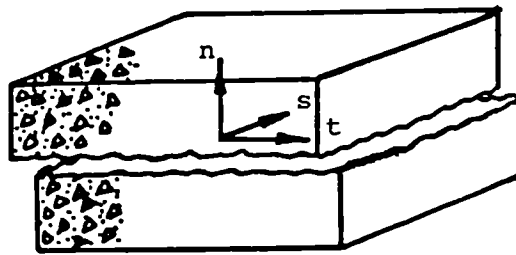


Fig. 4.7 Three-dimensional representation of a single crack.

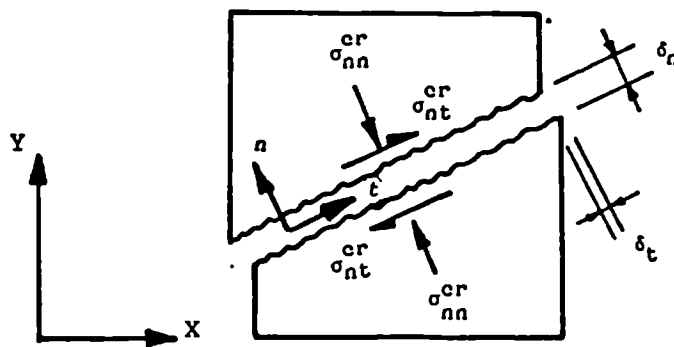


Fig. 4.8 Two-dimensional representation of a single crack and associated crack stresses and displacements.

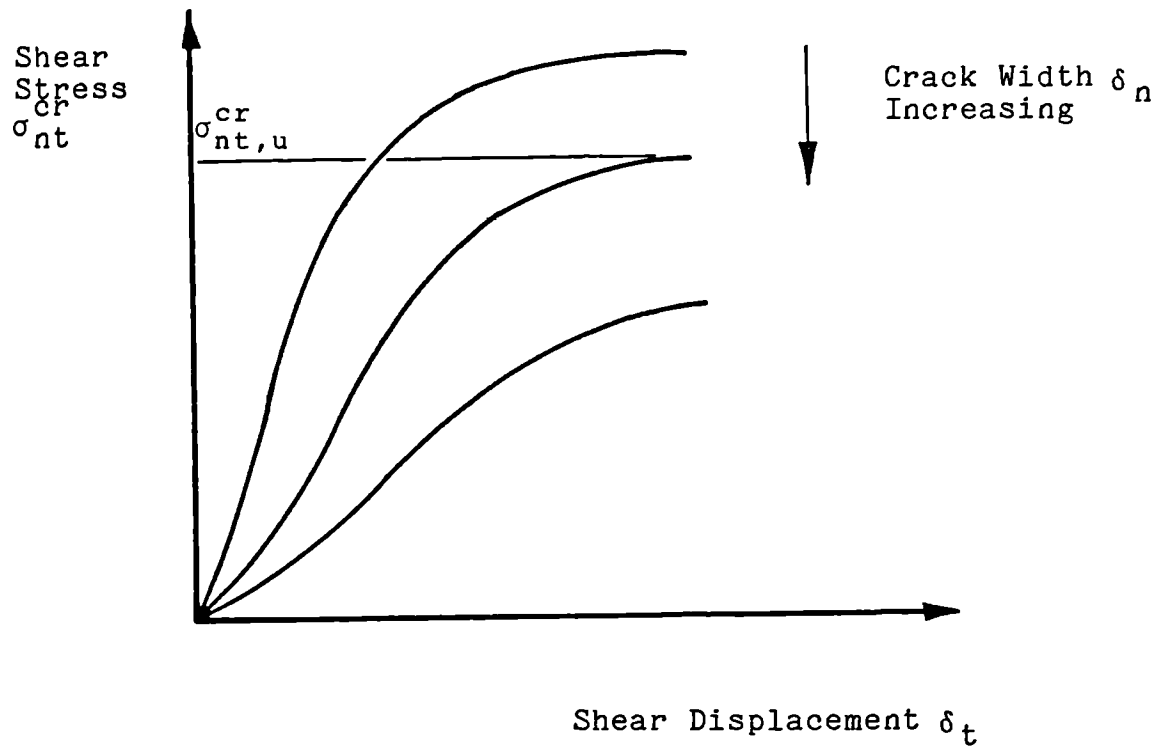
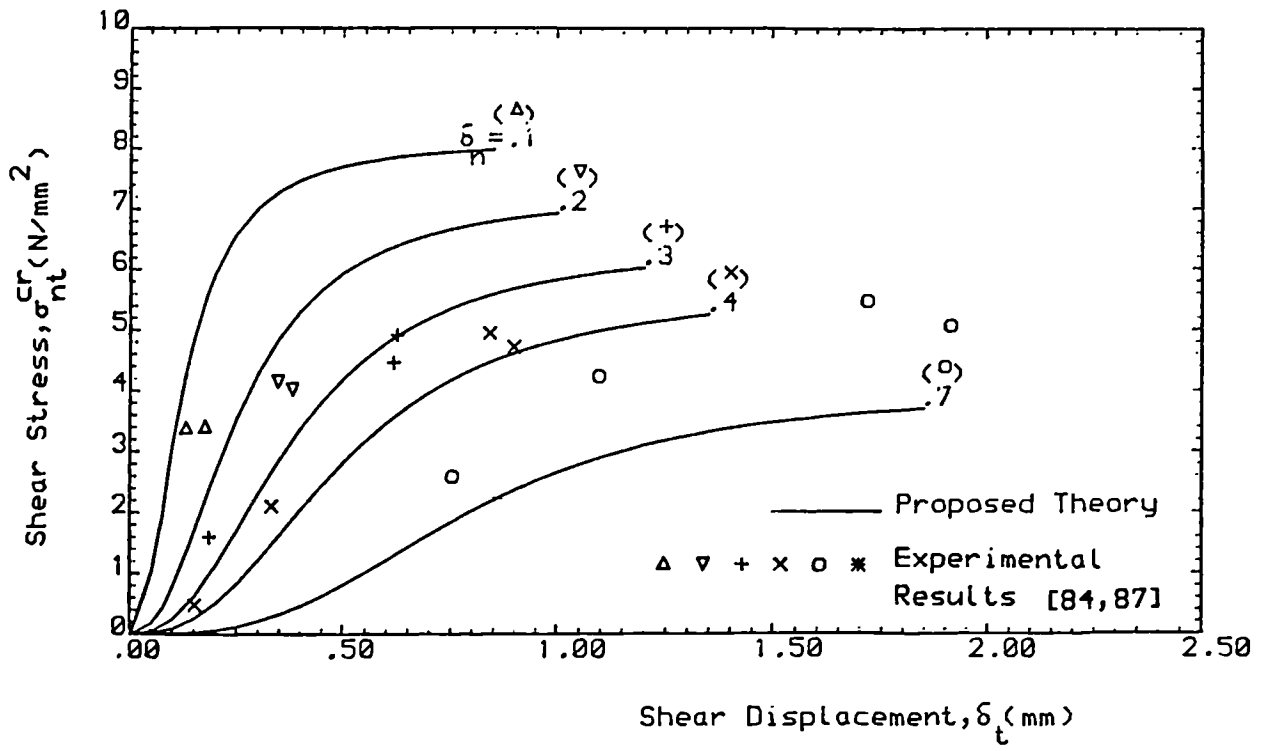
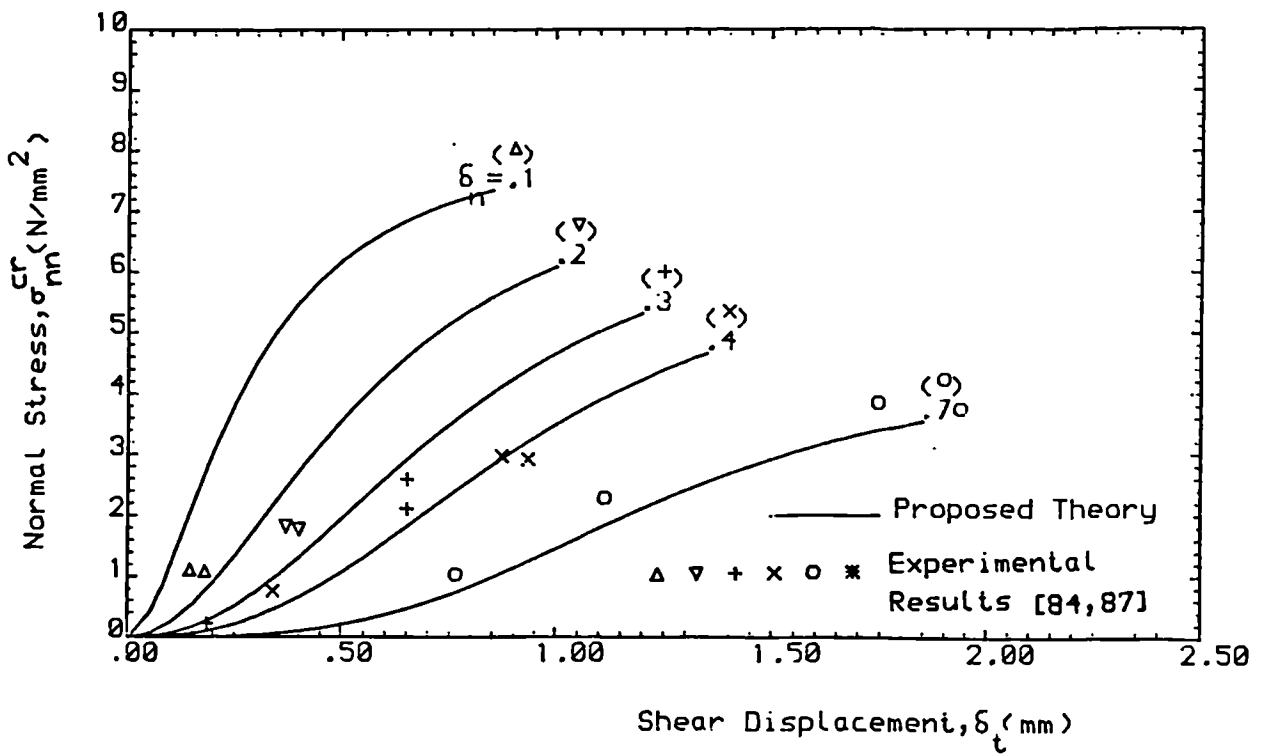


Fig. 4.9 General shear stress-displacement behaviour of cracked concrete.

$D_{max} = 16\text{mm}$ $F_{cu} = 13.4\text{N/mm}^2$



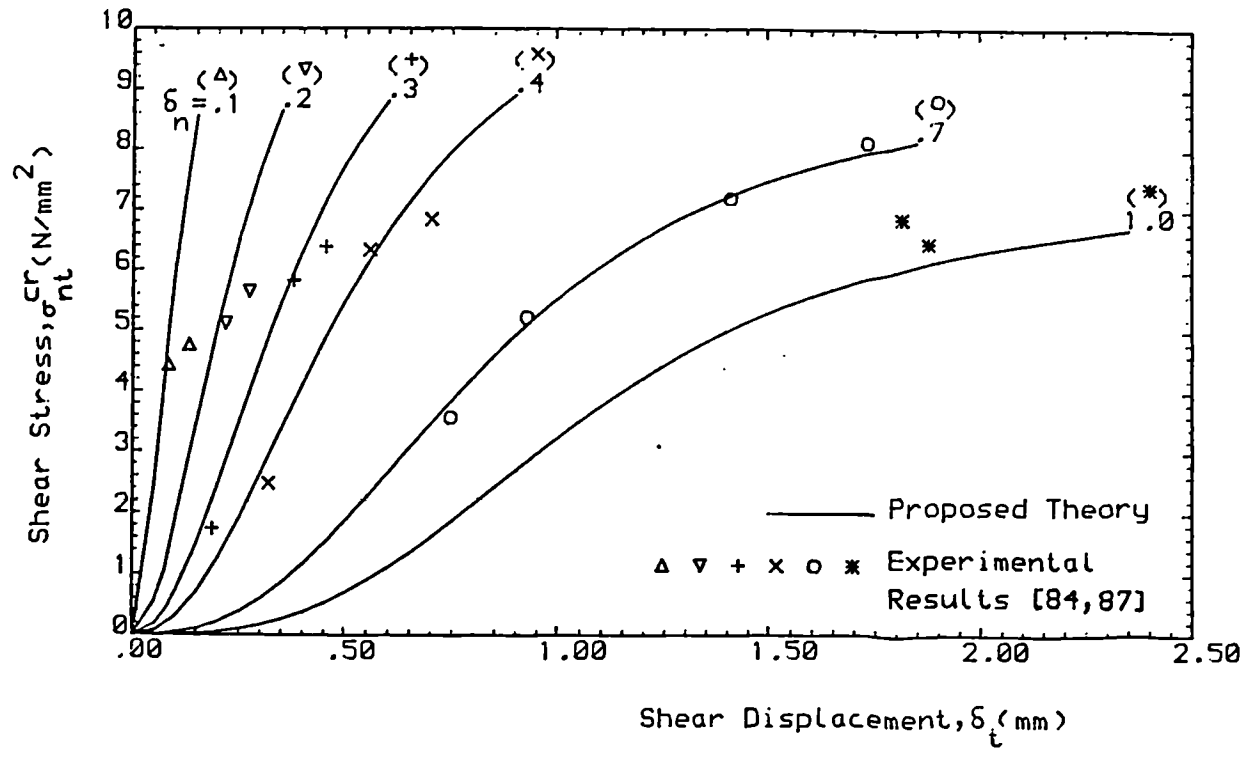
$D_{max} = 16\text{mm}$ $F_{cu} = 13.4\text{N/mm}^2$



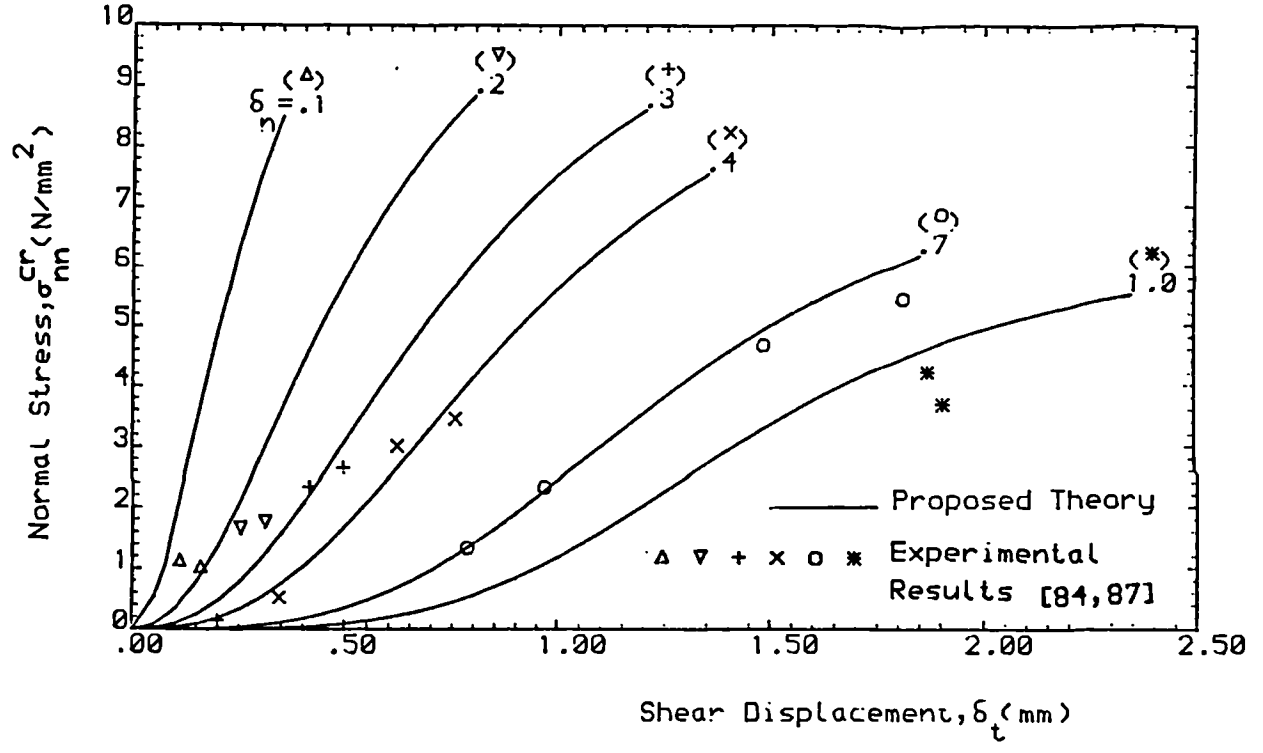
(a)

Fig. 4.10 Comparison of the proposed aggregate interlock model with experimental results.

$D_{max} = 32\text{mm}$ $F_{cu} = 33.2\text{N/mm}^2$



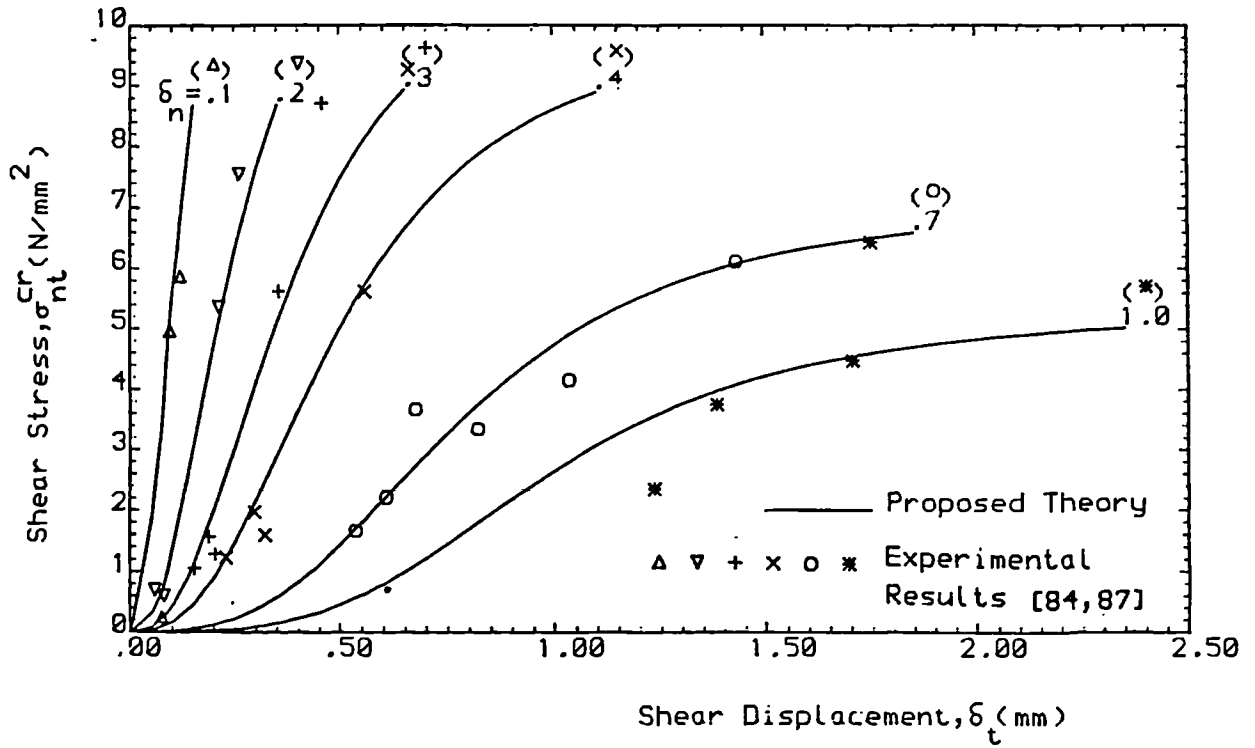
$D_{max} = 32\text{mm}$ $F_{cu} = 33.2\text{N/mm}^2$



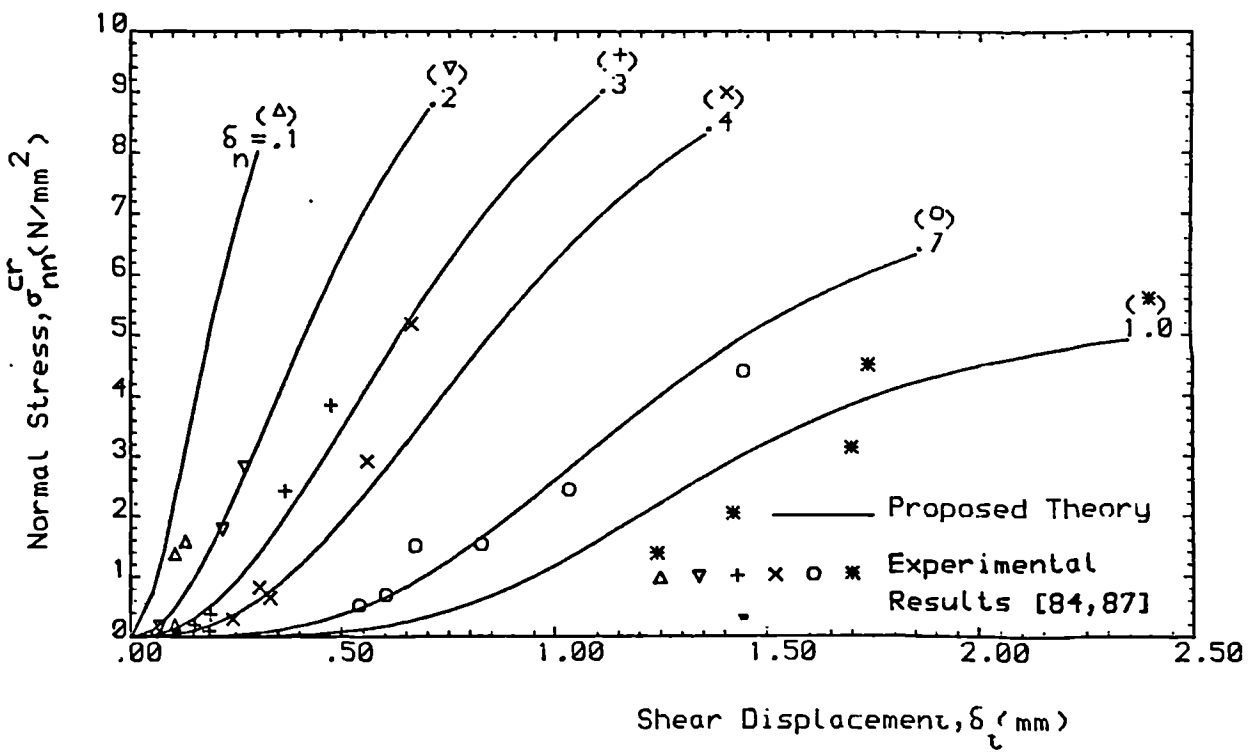
(b)

Fig. 4.10 Continued

$D_{max} = 16\text{mm}$ $F_{cu} = 37.6\text{N/mm}^2$



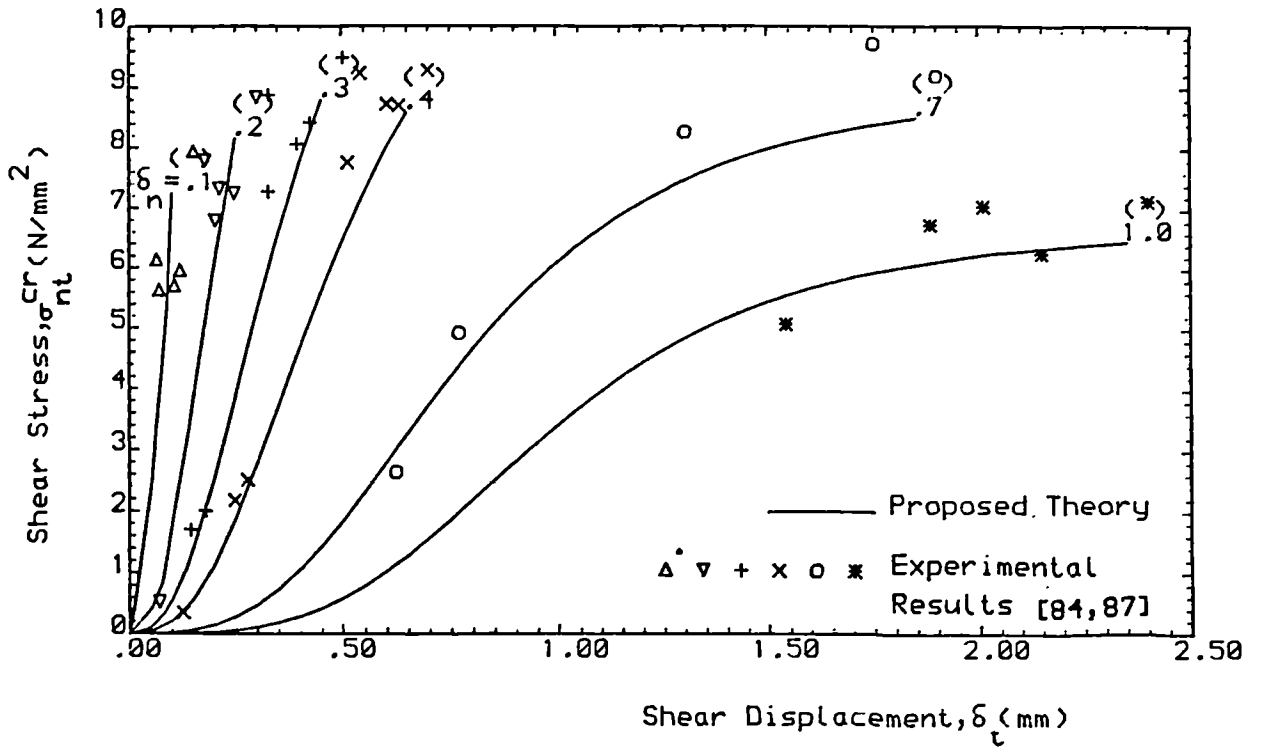
$D_{max} = 16\text{mm}$ $F_{cu} = 37.6\text{N/mm}^2$



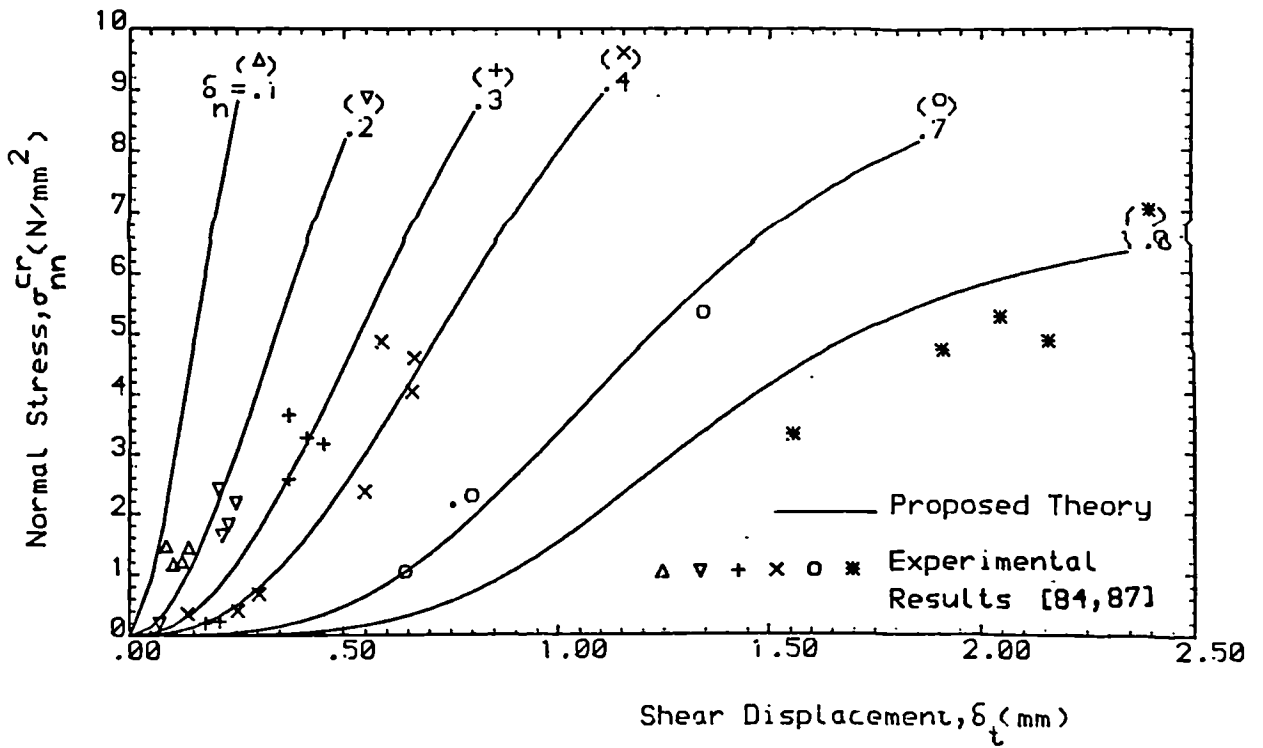
(c)

Fig. 4.10 Continued

$D_{max} = 16\text{mm}$ $F_{cu} = 59.1\text{N/mm}^2$

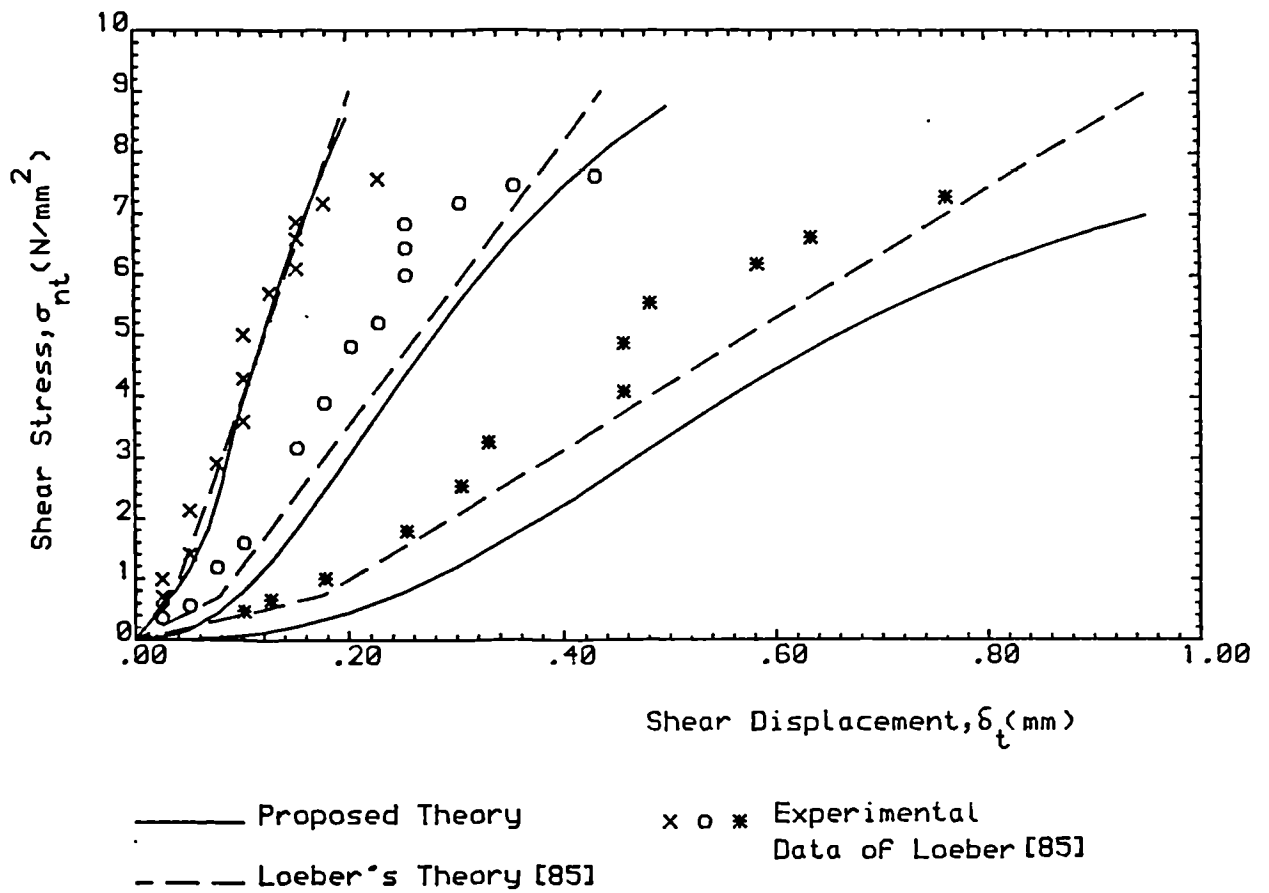


$D_{max} = 16\text{mm}$ $F_{cu} = 59.1\text{N/mm}^2$



(d)

Fig. 4.10 Continued



Symbol	δ_n (mm)	F_{cu} (N/mm ²)
x	.127	35.5
o	.254	35.9
*	.508	37.7

Fig. 4.11 Comparison of the proposed aggregate interlock model with theoretical and experimental results of Loeber.

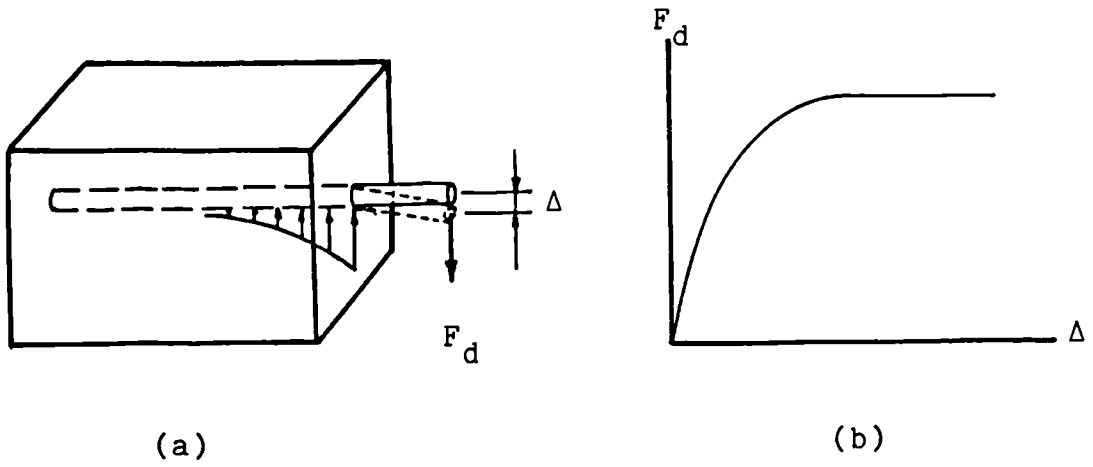


Fig. 4.12 Model representation of dowel force-displacement relationship.

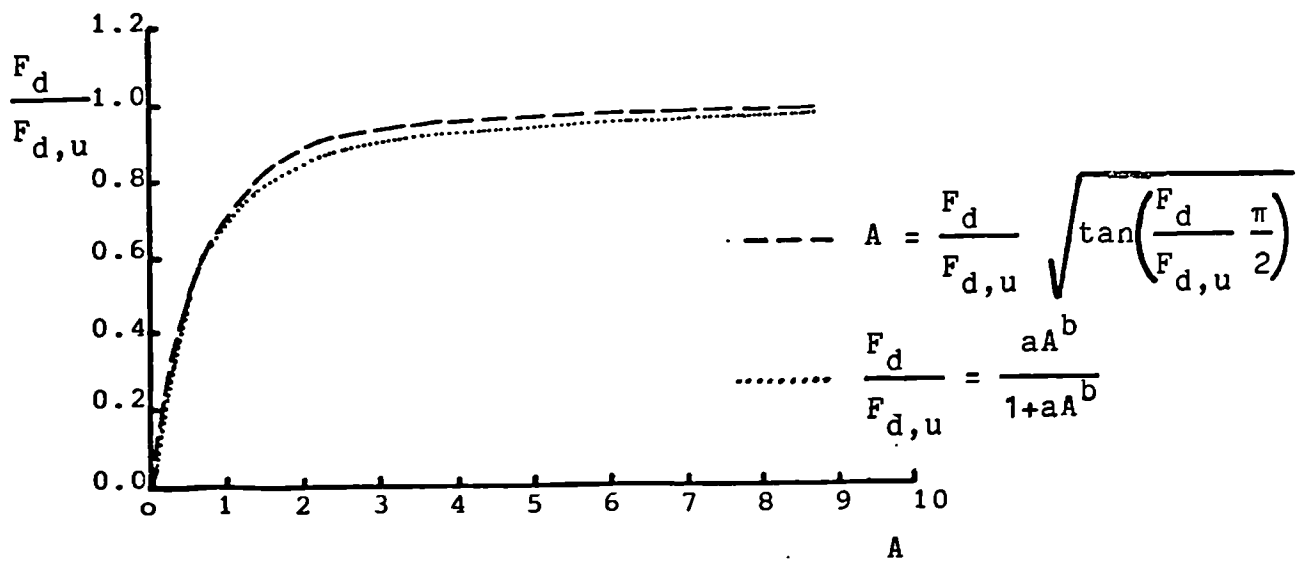
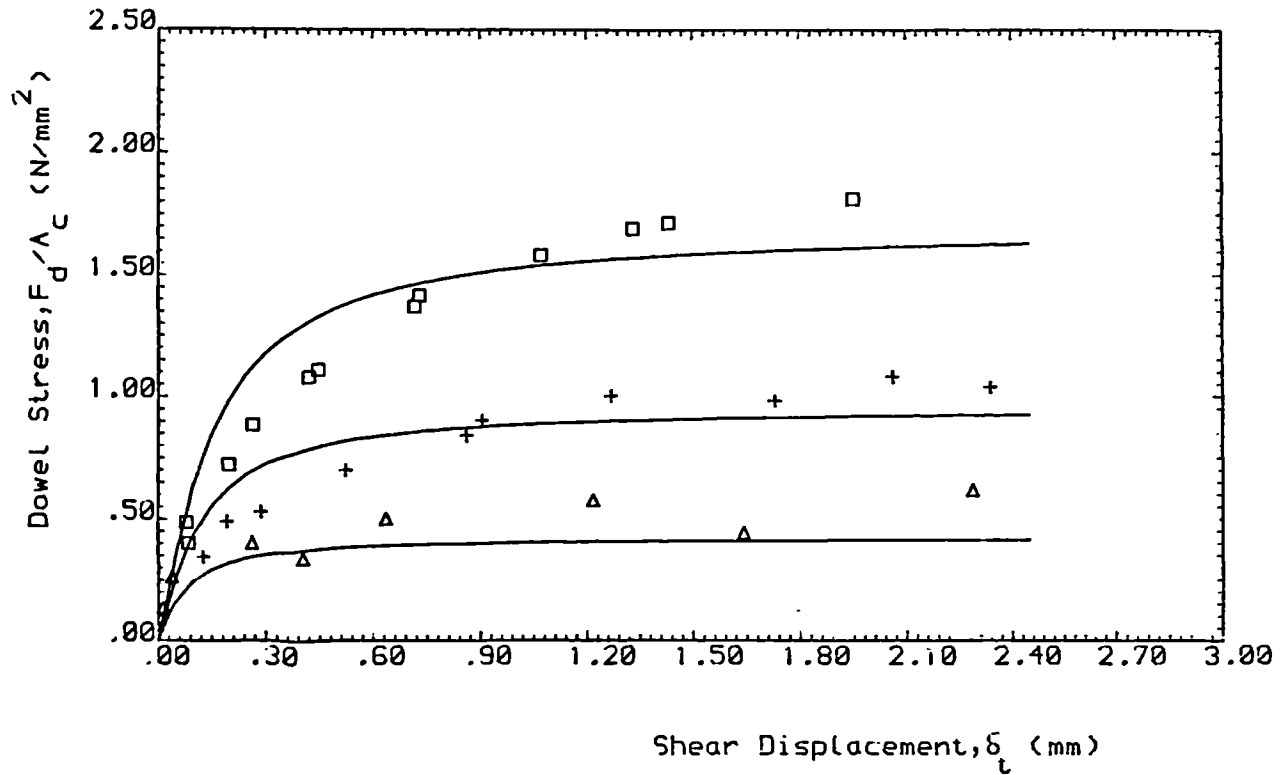


Fig. 4.13 Non-dimensional dowel force curve.

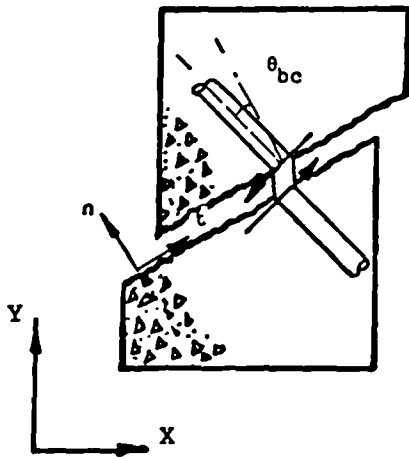


———— Proposed Theory

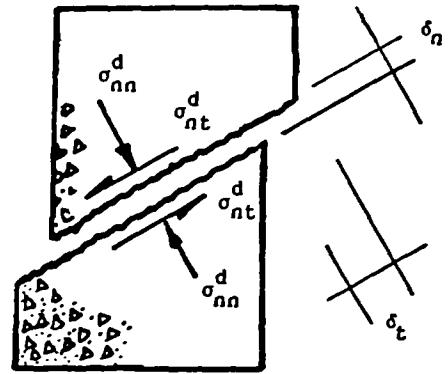
△ + □ Experimental Results of Paulay et al [93]

Symbol	No. of Bars	Dim. (mm)	F_{y2} (N/mm ²)	F_{cu2} (N/mm ²)	Λ_c (mm ²)
△	6	6.350	320	28	62000
+	6	9.525	320	28	62000
□	6	12.700	320	28	62000

Fig. 4.14 Comparison of the proposed dowel force model with experimental results.

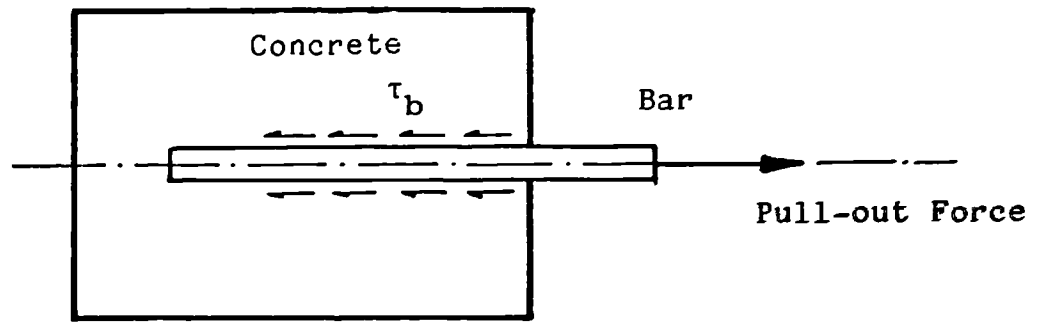


(a) Dowel Force

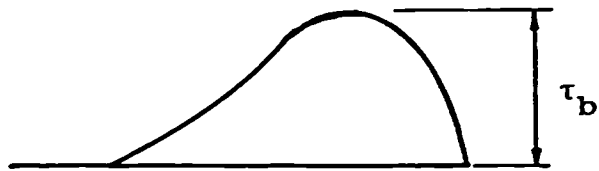


(b) Dowel Stress

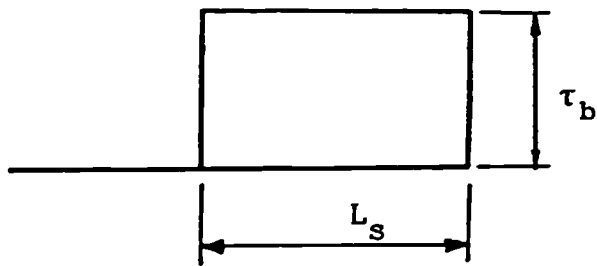
Fig. 4.15 Schematic representation of dowel force and stresses on a cracked concrete element.



(a) Bar Subjected to Pull-Out Force



(b) Actual Bond Stress Distribution



(c) Idealised Bond Stress Distribution

Fig. 4.16 Actual and idealised bond stress distribution for an embedded bar subjected to pull-out force.

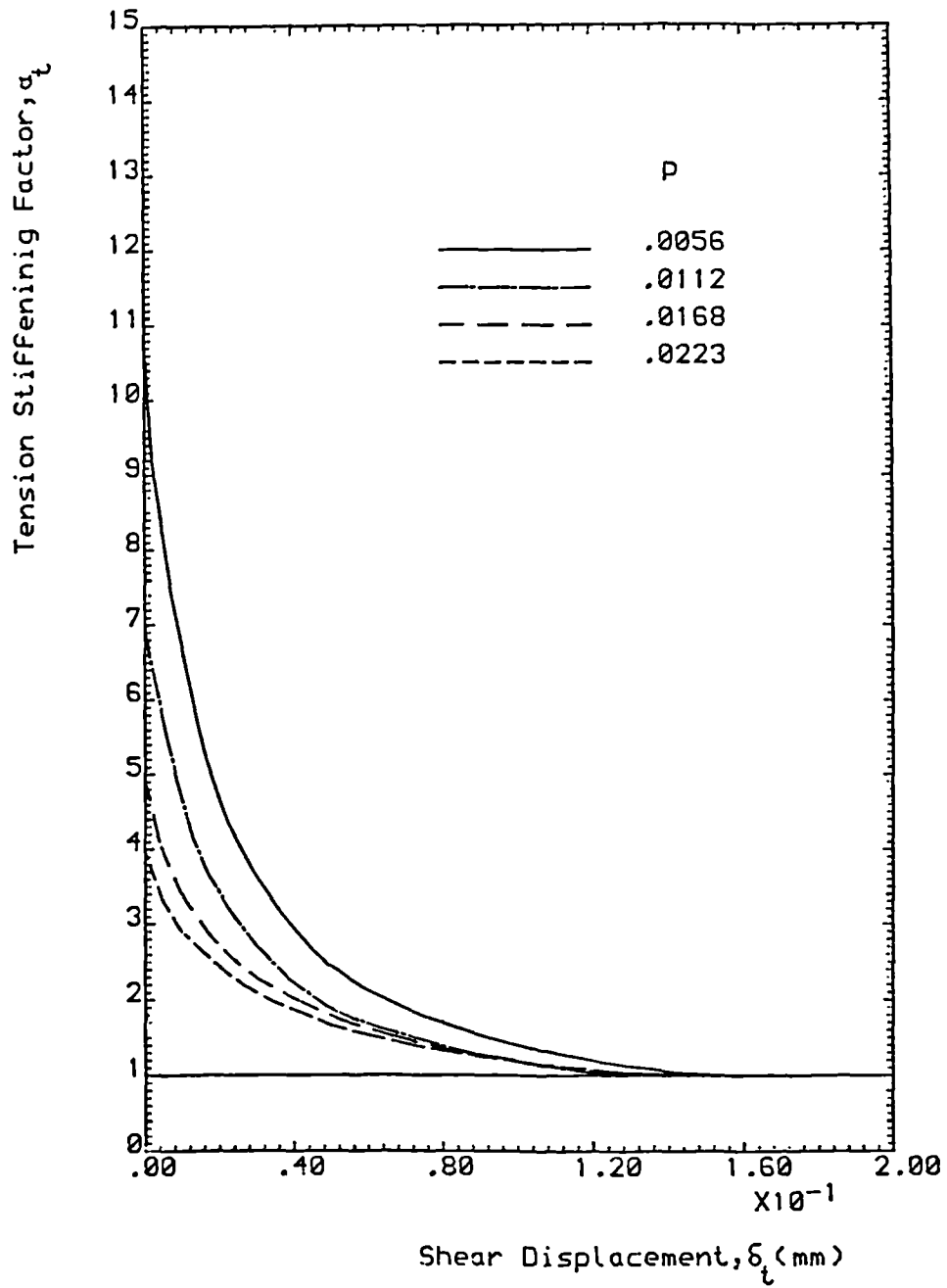


Fig. 4.17 Proposed tension-stiffening model for different steel ratio.

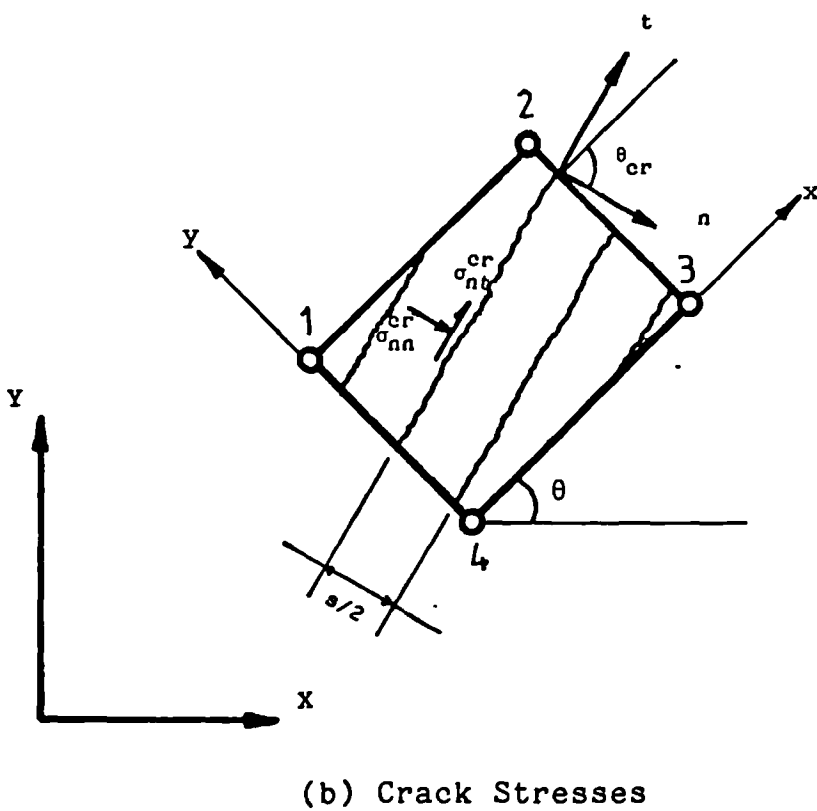
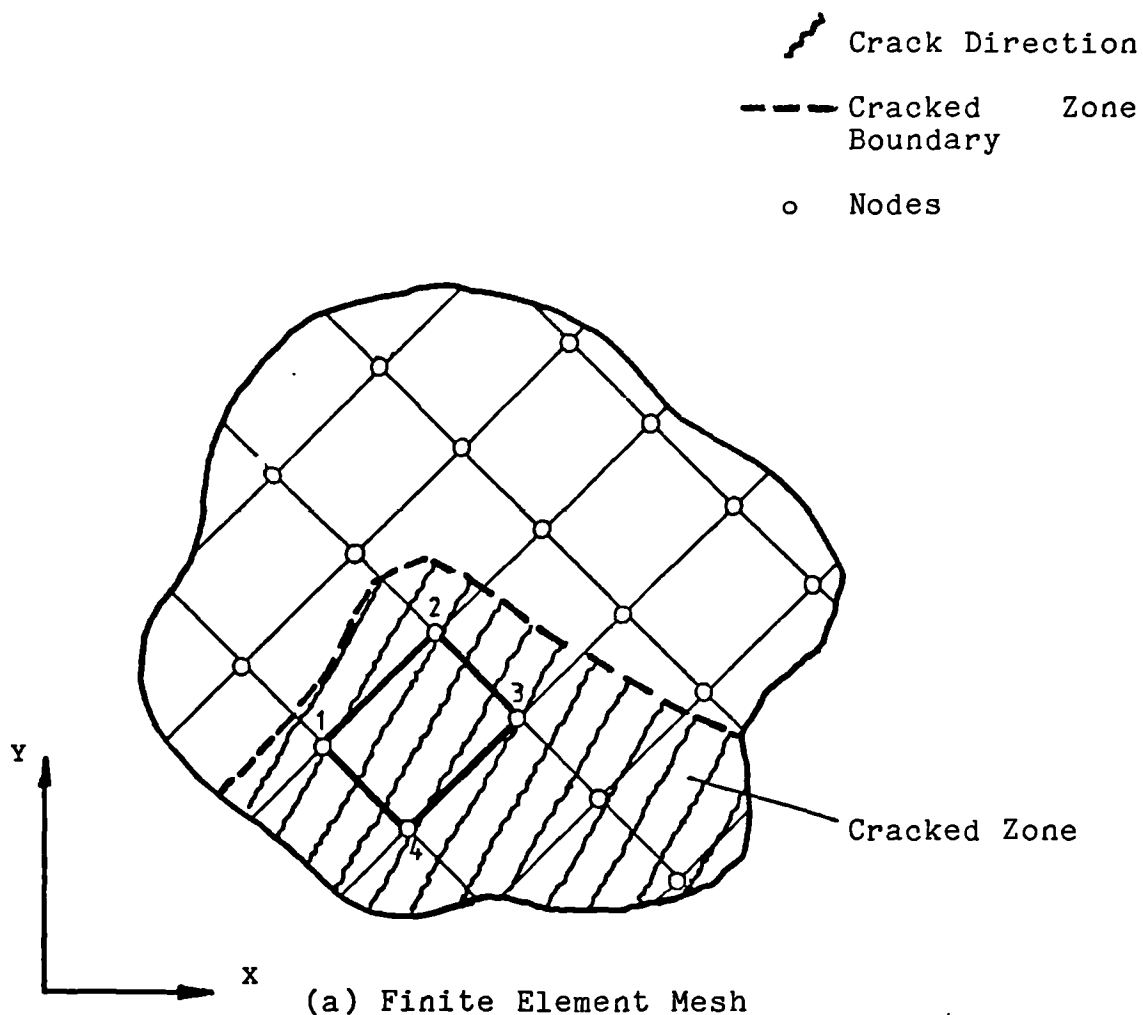


Fig. 4.18 Cracked plain concrete with smeared cracking.

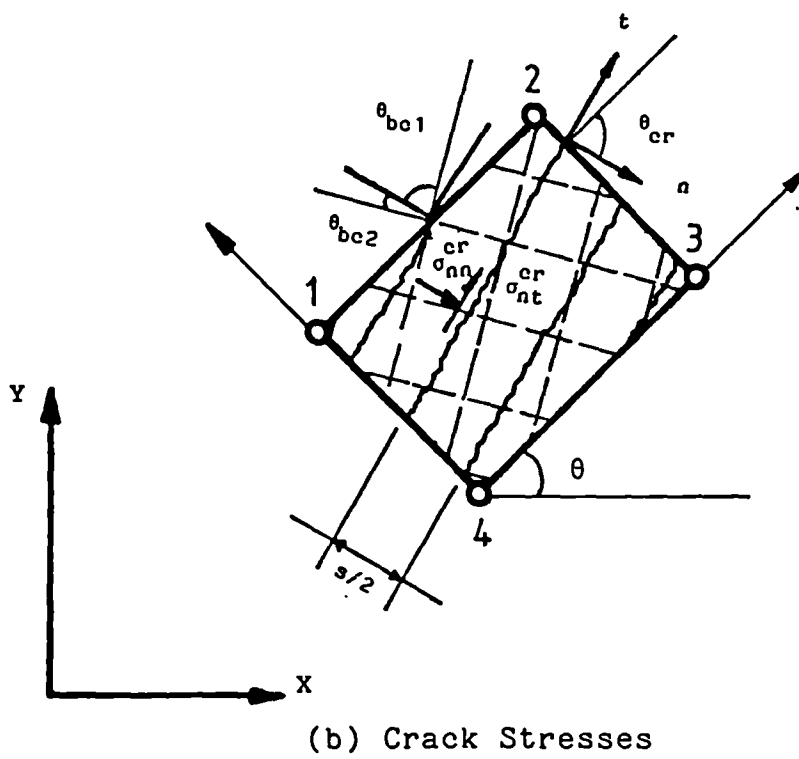
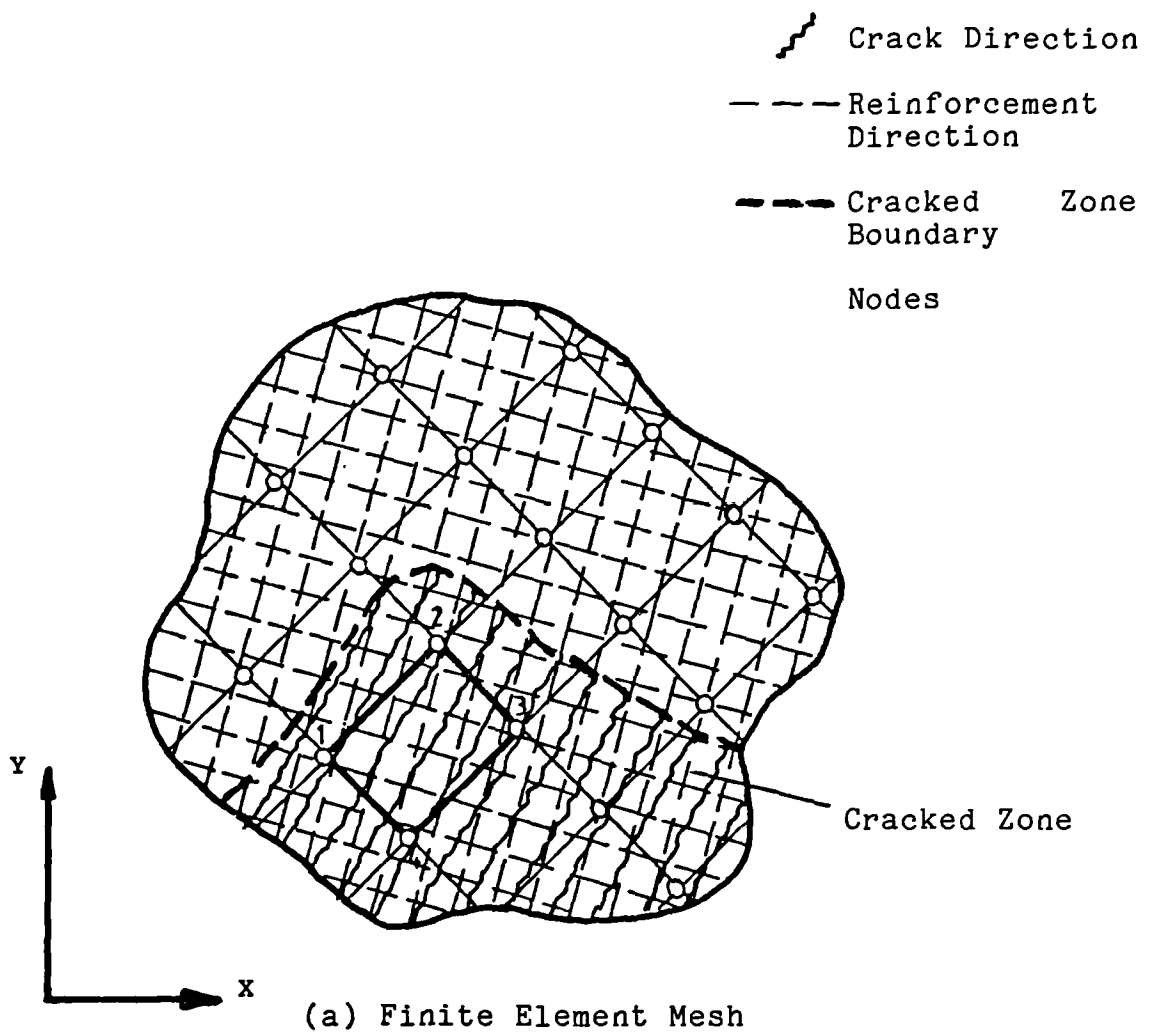


Fig. 4.19 Cracked reinforced concrete with smeared cracking.

CHAPTER FIVE

IMPLEMENTATION OF THE PROPOSED CONCRETE CONSTITUTIVE AND FRACTURE MODELS AND ASSOCIATED ANALYTICAL RESULTS

5.1 Introduction

The development of the constitutive equations and fracture models of concrete have been discussed in the previous chapters. These models are proposed to represent the multi-axial stress-strain relationship of concrete in the pre and post ultimate load levels and simulate different fractured concrete mechanisms for the concrete material which has exceeded its permissible strength. The validity of these equations has been investigated in comparison with the experimental results of previous investigators which have been carried out on small concrete specimens and subjected to idealised loading under laboratory conditions. This chapter is aimed at verifying the performance and capability of the proposed concrete models in relation to experimental results of large scale concrete structures.

The proposed constitutive equations presented in Chapter Three and the fracturing model produced in Chapter Four have been implemented into a general purpose finite element program called LUSAS. The LUSAS system is used for the analysis of the plane stress and the axisymmetric solid stress reinforced and prestressed concrete structures. The analytical results are compared with the experimental results whenever applicable.

Two typical examples have been chosen for the analytical verification of the proposed models. These are a reinforced concrete beam subjected to a central point load and a prestressed concrete reactor vessel subjected to internal pressure. The two test cases are considered sufficient to examine the capability of the models in the plane and axisymmetric solid states of stress. In solving these problems, it is of interest to predict accurately the displacement and the ultimate load carrying capacity of the structure as well as crack initiation and propagation throughout the loading. The prediction of failure mechanisms is also important.

5.2 The Finite Element System Used - LUSAS

LUSAS is a general purpose finite element system which incorporates facilities for linear and nonlinear static, dynamic and transient field analysis. The LUSAS system contains a comprehensive range of elements, solution procedures and a wide range of both linear and nonlinear material models [102]. The method adopted in the LUSAS system for solving the load-deflection equations is the 'frontal method' [103]. This method is regarded as the most efficient solution technique for a large number of equations with a large front width. One of the main features of the LUSAS system is its structured modular system designed to allow modification and update to be carried out with the minimum complexity. In addition to that, the system offers a wide range of easily accessible utility routines which simplifies the implementation of new features into the system.

5.2.1 Nonlinear Analysis in LUSAS

The LUSAS system has the capability of dealing with two types of nonlinearities encountered in the structural analysis :-

- (i) geometrical nonlinearity, when the strain-displacement relationships are nonlinear, and
- (ii) material nonlinearity, when the stress-strain relationships are nonlinear.

The latter type of nonlinearity requires an incremental and iterative solution procedure. There are three incremental procedures in the LUSAS system :-

- (i) pure incremental solution,
- (ii) incremental with the Newton-Raphson iteration, and
- (iii) incremental with the modified Newton-Raphsan iteration.

There are also facilities to combine these techniques with the 'line-search' and 'arc-length' methods for a particular problem solved.

5.2.2 LUSAS Element Library

There are many different types of elements available in the LUSAS element library. Most of these elements can have isotropic, anisotropic and nonlinear material properties as

well as varying geometric properties. Most elements are numerically integrated. Different type of elements can be mixed to simulate a structure as long as they have the same degrees of freedom. In the following the elements that have been used in this study are briefly described

(i) Bar Element - BAR2 and BAR3

This type of element is used to model the reinforcement bars. BAR2 and BAR3 are two and three noded curved isoparametric elements in two-dimensions which can accommodate varying cross-sectional area at each node, Fig. 5.1. Each node has two degrees of freedom and the node coordinates are defined with respect to X-Y axes. The material properties for this element can be defined by a linear elastic or Von Mises elasto-plastic constitutive model. The loading can be applied as concentrated load, constant body force, and body force potential at each nodes or as initial stresses at gauss points.

(ii) Plane Membrane Element - QPM8

This type of element is used to model concrete in the state of plane stress, such as beams and panels. QPM8 is a two-dimensional isoparametric element with higher order models capable of modelling curved boundaries, Fig 5.2. This element has eight nodes with two degrees of freedom at each node. The thickness at each node can be defined independently. The element can

therefore have a varying thickness if required. The node coordinates are defined with respect to X-Y axes. There are several linear and nonlinear material models available to this type of element such as orthotropic, orthotropic plane strain, anisotropic, Von Mises elasto-plastic and a nonlinear concrete model. The proposed concrete model is used to define the material properties of the plane stress concrete elements. QPM8 element is capable of adopting concentrated load, constant body force and body force potential at each node and face load at each side of the element.

(iii) Axisymmetric Membrane Element - BXM3

This type of element is used to model circumferential cables as axisymmetric membranes with equivalent thickness in the axisymmetric problems. BXM3 is a straight or curved axisymmetric element which can accommodate varying thickness. The Y-axis is considered as the axis of symmetry, Fig 5.3. This type of element has three nodes with two degrees of freedom at each node. The node coordinates are defined with respect to X-Y axes. A linear elastic or Von Mises elasto-plastic material model may be used with this type of element. The loading can be applied as concentrated load, constant body force, and body force potential at each nodes.

(iv) Axisymmetric Solid Element - QAX8

This type of element is used to model solid concrete structures subjected to axisymmetric state of stress, such as cylindrical structures. QAX8 is an isoparametric element with the higher order models capable of modelling curved boundaries. The element formulations apply to a one radian segment of the structure with the Y-axis as the axis of symmetry, Fig 5.4. QAX8 has eight nodes with two degrees of freedom at each node. The node coordinates are defined with respect to X-Y axes. There are several linear and nonlinear material models available for the use with this type of element such as orthotropic, isotropic and Von Mises elasto-plastic models. The proposed concrete model is used to define the material properties of axisymmetric concrete elements. The loading can be applied as concentrated load, constant body force and body force potential at each nodes and as face load at each side of the element.

5.3 The Finite Element Implementation of the Proposed Concrete Model

The proposed constitutive equations developed in Chapter Three are incorporated into the LUSAS system for the finite element analysis of reinforced and prestressed concrete structures. The concrete model has been implemented in the

LUSAS system for the use in conjunction with plane stress and axisymmetric solid elements. The implementation of the concrete model was carried out in two stages :-

- (i) The development of routines to calculate the modular matrix D , for a given state of stress σ , in the pre-solution and
- (ii) The development of routines to calculate the stresses σ , for a given set of strain increments $d\epsilon$ in the post-solution.

The routines developed in stage (i) are used to calculate the element stiffness matrix k , in the pre-solution and the routines developed in stage (ii) are used in the post-solution to calculate the element stresses σ .

The constitutive equations developed in Chapter Three are used to assemble the modular matrix D , and the incremental stress-strain relationship of concrete

$$d\sigma_{ij} = D_{ijkl} d\epsilon_{kl} \quad (5.1)$$

where

$$D_{ijkl} = \frac{E}{(1 + \nu)(1 - 2\nu)} (C_{ijkl} - \mu \phi_{ijkl}) \quad (5.2)$$

(see Chapter Three, Eq 3.43 for parameters definition)

A symmetrical modular matrix is directly obtained from Eq. 5.2 for the use in the pre-solution of the finite element

analysis. In the post-solution, however, two possibilities may arise during a finite change of strain $\Delta\varepsilon$, and these are :-

- (i) stress level is below the current yield surface, i.e. $f(\sigma, \beta) < 0$ (elastic state), or
- (ii) stresses violate the yield criteria and exceed the current yield surface, i.e. $f(\sigma, \beta) \geq 0$ (plastic state).

These two cases must be treated separately. A simple elastic modular matrix D^e , may be used to obtain the stress increments corresponding to an strain increment in the elastic state. In the plastic state, however, an elasto-plastic modular matrix D^{ep} must be used. In the case of plastic yielding, attention must be paid to the problem of transition from the elastic to plastic zone [20,47,104]. The problem may be examined by considering a concrete material which is loaded such that the stresses have reached point A inside the current yield surface (elastic zone), Fig. 5.5. Upon further elastic loading a new stress level is attained which violates the yielding criterion, point B, Fig. 5.5. In this case, part of the strain increment $\Delta\varepsilon$, should be treated elastically and the remaining part of it elasto-plastically. The transition problem can be solved geometrically by intersecting line \overline{AB} with the current yield surface at point C, Fig. 5.5. The solution results in a percentage of the strain increment r , which is sufficient to promote the stresses from point A to point C on the yield surface. The elastic stress increment $\Delta\sigma_e$, is therefore given as

$$\Delta\sigma_e = \int_0^{r\Delta\varepsilon} D^e d\varepsilon \equiv r D^e \Delta\varepsilon \quad (5.3)$$

The remaining strain increment $(1-r)\Delta\varepsilon$, would contribute towards the elasto-plastic stress increment $\Delta\sigma_{ep}$, given as

$$\Delta\sigma_{ep} = \int_r^{\Delta\varepsilon} D^{ep} d\varepsilon \equiv (1-r) D^{ep} \Delta\varepsilon \quad (5.4)$$

The total change of the stress increment is given as

$$\Delta\sigma = \Delta\sigma_e + \Delta\sigma_{ep} \quad (5.5)$$

Such approximation is admissible if infinitesimal strain increments are used. The use of Eq. 5.4 for relatively large strain increments, however, produces a stress change such that

$$f(\sigma+\Delta\sigma, \beta) \neq 0 \quad (5.6)$$

This implies a departure from the current yield surface which results in an over-stiffening of the structure, Fig. 5.6a. It is very important to preserve the yield criterion during the plastic flow. An alternative solution is the sub-incremental technique where the elasto-plastic strain increment $(1-r)\Delta\varepsilon$, is subdivided into a number of smaller increments so that the final stress position would be much closer to the yield surface [104], Fig. 5.6b. The number of sub-increments may be

calculated as follows

$$m = \frac{\Delta f(\sigma)}{v \cdot f(\sigma)} + 1 \quad (5.7)$$

where m = number of sub-increments,
 $\Delta f(\sigma)$ = excess stress corresponding to stress at point B,
 $f(\sigma)$ = yield stress corresponding to point B, and
 v = a percentage of the yield stress used as the tolerance limit (1 percent has been used in this study)

After m number of iterations a stress level corresponding to point D' is achieved, Fig 5.6b. The drift away from the yield surface at point D' is corrected by applying a stress adjustment decrement $\Delta\sigma_{adj}$, to the stresses at point D'. Such a correction is achieved by assuming that the stress changes in the direction of normal to the yield surface [104] as

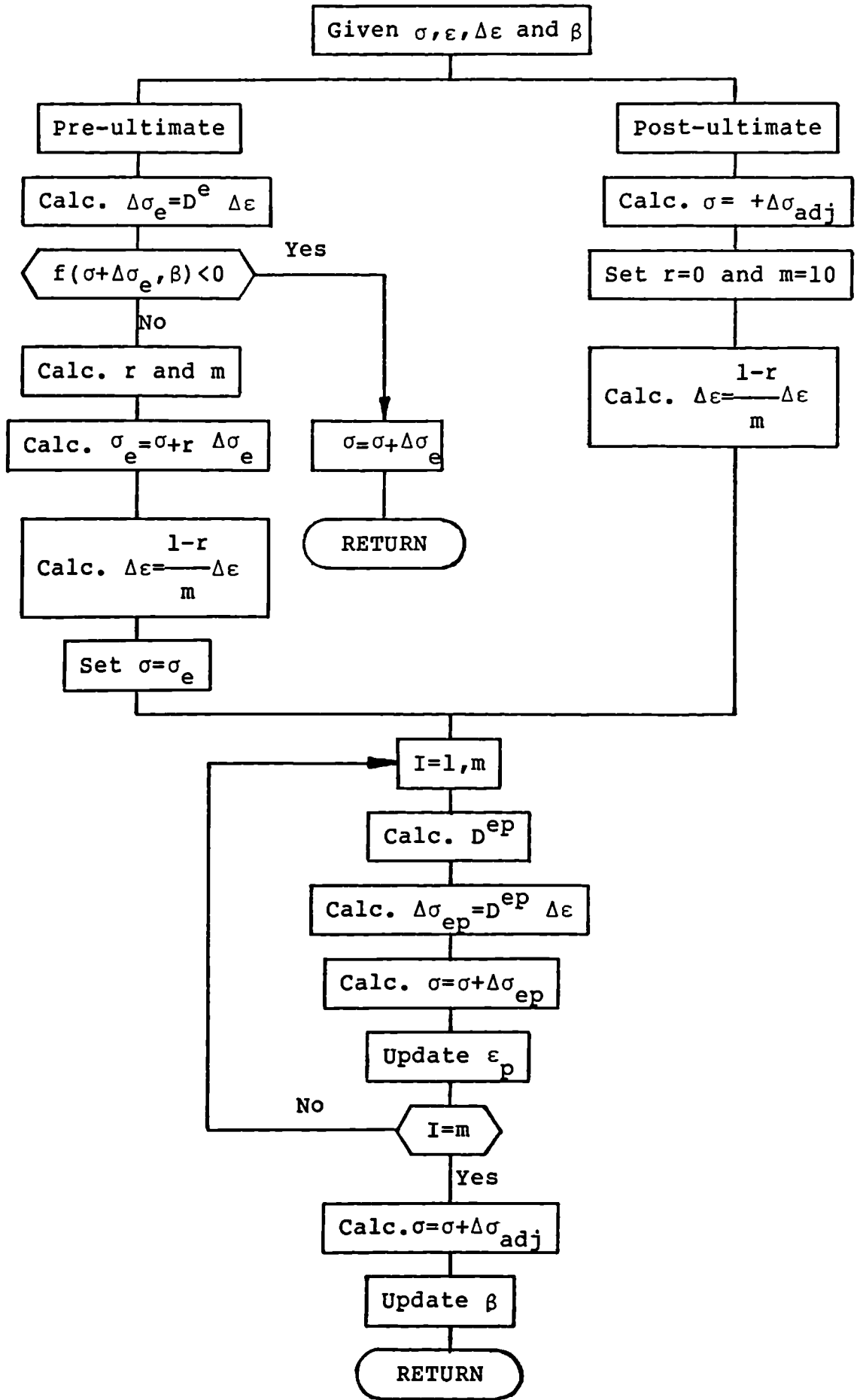
$$\Delta\sigma_{adj} = - \left(\frac{\Delta F}{\frac{\partial f^T}{\partial \sigma} \frac{\partial f}{\partial \sigma}} \right) \frac{\partial f}{\partial \sigma} \quad (5.8)$$

where ΔF = excess stress at point D' (Fig. 5.6b), and
 $\frac{\partial f}{\partial \sigma}$ = direction of the normal to the yield surface at point D'

The adjustment of the stress level may be carried out at the end of iteration to bring the stresses back to the yield

surface. An additional refinement may be achieved by introducing the stress adjustment at each cycle of the sub-incremental iteration.

The computational procedure described above is suitable for the pre-ultimate state of stress when the material hardening is assumed to be governed by the isotropic hardening rule. In the post-ultimate state of stress, however, the concrete material exhibits strain-softening which is modelled by assuming a progressive collapse of the yield surface. The numerical technique adopted for the strain-softening state of stress involves a reduction of the stress level until the stresses reach the current or collapsed yield surface. The stresses are reduced such that the stress decrements remain in the direction of the normal to the yield surface in accordance with Eq. 5.8. Once the state of stress has reached the collapsed yield surface the strain increment $\Delta\epsilon$, is applied using the elasto-plastic modular matrix and the sub-incremental technique. A flow chart showing the numerical procedure adopted here is given below



Flow Chart Representing the Numerical Procedure Adopted

5.4 Material Modelling of the Fractured Concrete

The fracture in concrete is classified into 'crushing' type of failure in the compressive state of stress and 'cracking' type of failure in the tensile state of stress. The fracture criteria developed in section 4.2 are used to identify the nature of fracturing in concrete.

5.4.1 Compressive Failure

A gauss point is assumed to fail by crushing when the compressive failure criterion (Section 4.2) is satisfied or the least principal strain has reached the limiting value of $2\epsilon_{pu}$ where ϵ_{pu} is the ultimate uniaxial compressive strain of concrete. A crushed gauss point is assumed to lose its stiffness completely and unable to sustain any further load. The Young's modulus of a crushed gauss point is set to zero to represent total failure of concrete.

5.4.2 Tensile Failure and Crack Formation

A gauss point is assumed to fail by cracking when the tensile failure criterion (Section 4.2) is satisfied and at least one of the principal stresses has exceeded the limiting uniaxial tensile strength of concrete f_t . A cracked gauss point loses its stiffness partially and is assumed to be in the orthotropic state of stress with the crack directions as the axes of orthotropy.

Cracks are allowed to form normal to the direction of the offending principal stress. A further violation of the

cracking criterion results in the formation of subsequent cracks. The subsequent cracks form a non-orthogonal set of cracks with the initial crack owing to the rotation of the principal stress directions resulting from the continuous stress redistribution (see Fig. 4.2, Chapter Four). A set of orthogonal cracks may only form if the principal stresses violate the cracking criteria simultaneously. A minimum angle of thirty degrees between the initial and the subsequent crack planes is used as the threshold angle of rotation of principal stress direction before a new crack is allowed to form. This requirement prevents the formation of unrealistic cracks which may initiate as a result of small rotation of the principal stress direction. It should be noted that such policy may, however, result in excessive tensile stresses in the vicinity of an existing crack until a valid crack is allowed to form.

Each gauss point of an element is allowed to embed upto two in-plane cracks in the case of plane stress elements, Fig. 5.7, or two in-plane (circumferential) and one out-of-plane (radial) cracks in the case of axisymmetric elements, Fig. 5.8.

5.4.2.1 Cracked Concrete Properties

The tensile cracks are represented by the smeared crack approach (see Chapter Four). The smeared cracks are uniformly distributed over the area of the cracked gauss point, hence the averaged smeared strains may reasonably be interpreted as a measure of the discrete crack displacements.

The material properties of a cracked gauss point is assumed to be the combination of the stiffness properties of the cracks, as a media, and the solid concrete between them. It is further assumed that the stiffness of a gauss point, containing the maximum allowable number of cracks (two for plane stress and three for axisymmetric elements), reduces to the contibution of the crack stiffnesses alone.

The solid concrete between the cracks is assumed to behave elastically and the crack stiffness is obtained from Eq. 4.5. Such an approach results in the gradual release of the normal stress perpendicular to the crack plane and the shear stress parallel to the crack direction, while the other stresses remain unchanged. It follows that the stress states of the solid concrete between the cracks are reduced to :-

- (a) the uniaxial stress states parallel to the crack direction for a singly cracked plane stress element, Fig. 5.9a, and
- (b) the biaxial stress states parallel to the crack and circumferential or radial directions for a singly cracked axisymmetric solid element, Fig. 5.9b, or
- (c) the uniaxial stress states parallel to the circumferential or radial directions for a doubly cracked axisymmetric solid element, Fig. 5.9c.

The use of Eq. 4.5 produces an unsymmetrical stiffness matrix which requires a non-symmetrical solver in the solution stage of the finite element method. The lack of such facilities in

the LUSAS system leads to the simplification of Eq. 4.5 by ignoring the off-diagonal terms, namely K_{nt} and K_{tn} , resulting in

$$\begin{Bmatrix} d\sigma_{nn}^{cr} \\ d\sigma_{nt}^{cr} \end{Bmatrix} = \begin{bmatrix} K_{nn} & 0 \\ 0 & K_{tt} \end{bmatrix} \begin{Bmatrix} d\delta_n \\ d\delta_t \end{Bmatrix} \quad (5.9)$$

The stiffness matrix of a cracked gauss point is obtained by ignoring the dowel action and the tension stiffening effects of the reinforcing bars and in accordance with the procedure proposed in Section 4.7.1 (see Eq. 4.28). It should be noted that Eq. 4.28 is valid for cracked concrete with only a single crack layer present. The stiffness of a cracked concrete with several crack layers may be obtained by transforming the crack stiffnesses to a common coordinate system (using Eq. 4.29) and combining them with the stiffness of the solid concrete.

5.4.2.2 Crack Opening and Closing

The stresses and strains normal to an existing crack change during the course of the loading history owing to stress redistribution and stress release in the adjacent concrete which may in turn result in loading, unloading and reloading of the cracks. The increment of strain normal to the crack plane $d\varepsilon_{nn}$, is used to determine whether a crack is opening or closing.

The loading of a crack (opening) is governed by the normal component of the crack stiffness matrix K_{nn} , Fig. 5.10. A

crack is assumed to be fully opened when the K_{nn} retains a very small value. It is assumed that a crack unloads (closing) such that the crack normal stress σ_{nn} return towards the zero stress state and reloads (re-opening) along the same path until the crack normal stress reaches the stress level prior to the crack closing, Fig. 5.10. A fully closed crack is achieved when the zero stress state has reached.

It is assumed that a gauss point loses its stiffness when the maximum allowable number of cracks has reached and all the cracks are fully opened. Furthermore, The stiffness properties of a gauss point containing a fully closed crack is assumed to reverse back to its properties prior to the existance of that crack with a reduced shear capacity defined by the shear retention factor α .

5.4.2.3 Cracking Verification

To verify the analytical cracking predicted by the proposed fracture model, four test cases were devised which included a single concrete element subjected to prescribed deformation such that known crack patterns can be anticipated. These test case are

- (a) Test 1, a single concrete element is subjected to an increasing uniform uniaxial stretching until all the gauss points are cracked simultaneously normal to the direction of stretching, Fig. 5.11a,
- (b) Test 2, a single concrete element is subjected to an increasing uniform equal biaxial stretching until all

the gauss points are cracked simultaneously normal to the directions of stretching and such that all the cracks are orthogonal, Fig. 5.11b,

- (c) Test 3, a single concrete element is subjected to shear deformation until a symmetrical inclined single crack pattern is formed, Fig. 5.11c, and
- (d) Test 4, a single concrete element is subjected to a non-uniform stretching in opposite directions followed by a uniform stretching in the orthogonal direction until a symmetrical crack pattern comprising of single cracks, and double orthogonal cracks are formed, Fig. 5.11d.

The crack patterns appear to be consistent with the applied deformations and the fracture model is believed to predict concrete cracking accurately.

5.5 Modelling of the Reinforcement Bars

5.5.1 The Material Behaviour of Steel Bars

The nonlinear stress-strain relationships of steel reinforcement bars is modelled by the Model 62 in the LUSAS finite element system [102]. The material model uses the Von Mises yield surface and an isotropic work-hardening to represent the elasto-plastic material behaviour. The material behaviour is defined by the initial stress, Young's modulus, and the Poisson's ratio of steel and a series of linear sections to model the material behaviour in the work-hardening zone, Fig. 5.12a. The actual stress-strain curve of steel is mapped into a uniaxial yield stress versus effective

plastic strain curve. Each hardening section is defined by its slope and the effective plastic strain at that point, Fig. 5.12b. These quantities are defined as follows

$$C_i = \frac{E_P}{1 - \frac{E_P}{E_S}} \quad (5.10)$$

$$L_i = \epsilon_i - \frac{\sigma_i}{E_S} \quad (5.11)$$

where C_i = slope of the i^{th} hardening section,
 L_i = effective plastic strain at the i^{th} hardening section,

$$E_P = \frac{\sigma_i - \sigma_{i-1}}{\epsilon_i - \epsilon_{i-1}},$$

σ_i = the actual stress of the i^{th} point,
 ϵ_i = the actual strain of the i^{th} point, and
 E_S = initial Young's modulus of steel

5.5.2 Finite Element Idealisation of Steel Bars

The reinforcement bars are assumed to be isotropic material capable of resisting normal stresses along the axial direction of the bar. The reinforcement bars are, therefore, modelled by isolated bar elements (see section 5.2.2) which are assumed to be rigidly connected to the concrete elements at the nodal points. The rigid connection is an approximation to the actual bond between steel and concrete. Further

refinement is required to model the bar-to-concrete bond and the possible slip between them.

5.6 Numerical Analysis and Examples

In this section an attempt is made to investigate the capability of the proposed concrete model in predicting the behaviour of reinforced and prestressed concrete structures and to verify the analytical performance of the proposed constitutive equations. Two problems are selected from the published experimental results for this purpose which comprise of a reinforced concrete beam subjected to a central point load and a prestressed pressure vessel subjected to internal pressure. These examples provide sufficient information to assess the plane stress and axisymmetric solid stress capability of the proposed models in predicting the deformational behaviour and the load carrying capacity of the structures as well as the crack formation and propagation upto the failure load.

The structures have been discretised by the elements which have previously been described. A 3 X 3 gauss point integration rule has been used in the finite element analyses to avoid zero energy rotations of the gauss point inherent with the 2 X 2 integration scheme. The material properties of the concrete and steel reinforcement bar elements have been defined by the proposed concrete models and the Von Mises elasto-plastic model respectively. The steel reinforcement bar elements are assumed to be rigidly connected to the adjacent concrete elements. The Arc-Length method has been used for the automatic load incrementation to avoid the

critical points where small increase in load is matched by a large increase in displacement leading to solution divergence. Such critical situation may arise following substantial crack formation in the structure leading to major loss of structure stiffness. Both structures have been analysed using one Newton-Raphson iteration followed by ten Modified Newton-Raphson iterations combined with the Line-Search method to improve on possible poor solution convergence in the presence of considerable material nonlinearities.

5.6.1 Plane Stress Flexural Beam

The behaviour of reinforced concrete beams in bending has been studied by many researchers for the ultimate load carrying capacity and crack pattern [105-107]. As a result, there is an ample experimental evidence on load-deflection, cracking, and failure load of simply supported reinforced concrete beams which provide a very useful background for analytical work.

The experimental results reported by Bresler and Scordelis [107] are used to investigate the material nonlinearities in concrete beams which are mainly caused by cracking. Beam No. OB-1 has been selected amongst many beams of different size and material strength [107] for the finite element analysis. This beam has a rectangular cross-section and reinforced with four No. 9 bars (diameter 1.128 in) and no web reinforcement. The beam was simply supported and central concentrated point loads were applied until failure was

achieved, Fig. 5.13. A finite element mesh is prepared to discretise one half of the beam due to symmetry of the structure. Concrete has been modelled by 36 QPM8 elements and the reinforcement bars by two layers of BAR3 elements consisting of 6 elements per layer. The size of the elements was varied to achieve a finer mesh near the centre of the beam where the crack distribution is denser, Fig. 5.14. The loading was applied by concentrated loads at the top left hand node upto failure. The details of this beam which have been used in the analysis are given in Table 5.1.

Table 5.1 Details of the Flexure Beam OB-1 used in the Finite Element Analysis.

Breadth of the beam, b	9 in
Cross-sectional area of the reinforcement bar, A_s	4.0 in ²
Young's modulus of concrete, E_c	3.35x10 ⁶ psi
Poisson's ratio of concrete, ν_c	0.18
Concrete uniaxial compressive strength, f_{cu}	3,500 psi
Concrete uniaxial tensile strength, f_{tu}	348 psi
Shear retention factor, α	0.5
Ultimate uniaxial compressive strain of concrete, ϵ_{pu}	0.0022
Young's modulus of steel, E_s	28x10 ⁶ psi
Poisson's ratio of steel, ν_s	0.3
Yield stress of steel, f_y	60,000 psi

The load versus central deflection obtained from the finite element analysis is given in Fig. 5.15. The analytical results indicate an initial linear response corresponding to the uncracked beam behaviour followed by some losses in the beam stiffness due to crack formation. The slope of the curve remain almost unchanged up to the maximum load of 55.0 kips followed by a sharp increase in deformation upon application of further loads where it is assumed that the beam has reached its failure load. A definite transition exists between the uncracked and cracked beam behaviour marked by a kink in the load-deflection curve. The crack initiation corresponds to a load of 15 kips followed by gradual crack propagation towards the support point. The development of cracks and crack growth is shown in Fig. 5.16. It can be seen that as the loading increases the cracks spread along the length of the beam and the depth of the existing cracks increases. The crack propagation ceased to continue at load of 50 kips while the cracks grew deeper inclining towards the point of application of the load. The experimental and analytical crack pattern prior to the failure of the beam is given in Fig. 5.17. The depth of the analytical cracks agrees closely with the depth of the actual cracks at this high load level. The overall deformational behaviour and the ultimate load carrying capacity of the beam compare accurately with the experimental results indicating satisfactory response from the proposed concrete and fracture models. The analytical results suggest that the beam has failed by the formation of flexural cracks which agrees with the experimental evidence.

5.6.2 Axisymmetric Solid Stress Reactor Vessel

An extensive research has been carried out at the research laboratory of the University of Illinois to investigate the response and modes of failure of prestressed concrete reactor vessels subjected to internal pressure [108,109]. A total number of 16 small scale cylindrical vessels with both circumferential and longitudinal prestress were pressurised internally to failure. The main variables were the end-slab thickness and the magnitude of the prestressing forces.

The reactor vessel PV9 [109] has been selected for the finite element analysis. This vessel consists of a slab of 9 in thickness and wall of 5 in thickness. The pressure vessel has been prestressed both longitudinally and laterally. The longitudinal prestress was provided by 30 number of 0.5 in diameter strands anchored at each end of the wall and the circumferential prestress by 0.192 in diameter wire wound around the cylinder at a spacing of 0.33 in. A total force of 750 kips was applied to the strands and the prestress force in the circumferential wires was measured at 4.1 kips per wire, Fig. 5.18. A finite element mesh has been prepared to simulate one half of the vessel with the axis of symmetry along the centre line of the cylinder. A total number of 28 QAX8 elements have been used to model the concrete. The longitudinal prestress tendons were modelled by a single BAR2 element of equivalent cross-section and the circumferential prestressing wires were modelled by 8 BXM3 membrane elements of an equivalent thickness. The prestressing forces were simulated by initial stresses of 127.3 ksi applied longitudinally and 116.5 ksi applied laterally and the

internal pressure was applied as face loads to the edges of the inner elements, Fig. 5.19. The details of the vessel used in the finite element analysis are given in Table 5.4.

Table 5.2 Details of the Pressure Vessel PV9 used in the Finite Element Analysis.

External diameter of the vessel, r	40 in
Height of the vessel, H_w	80 in
Thickness of the end-slab, t_s	9 in
Thickness of the wall, t_w	5 in
Equivalent cross-sectional area of the longitudinal membrane, A_1	0.9375 in ²
Equivalent thickness of the hoop membrane, t_h	0.087 in
Young's modulus of concrete, E_c	4.3x10 ⁶ psi
Poisson's ratio of concrete, ν_c	0.15
Concrete uniaxial compressive strength, f_{cu}	7,300 psi
Concrete uniaxial tensile strength, f_{tu}	446 psi
Shear retention factor, α	0.5
Ultimate uniaxial compressive strain of concrete, ϵ_{pu}	0.0022
Young's modulus of steel, E_s	28x10 ⁶ psi
Poisson's ratio of steel, ν_s	0.3
Yield stress of steel, f_y	225 ksi
Initial longitudinal prestressing stress, P_1	127.3 ksi
Initial hoop prestressing stress, P_h	116.5 ksi

The analytical load-deflection curve for the mid-point of the end-slab of the vessel is illustrated in Fig. 5.20. The defelections are measured from the prestressed configuration. The analytical response indicates a linear behaviour before the crack formation, leading to a highly nonlinear region between 450 to 650 psi where major radial cracking occurs. The finite element results show a large increase in displacement upon application of a small pressure beyond 650 psi. The general trend of the analytical load-deflection curve appears to be in agreement with the experimental results although the ultimate load carrying capacity fall below the predicted experimental value of 887 psi [109]. The initial crack formation occurs at a pressure of 350 psi. The crack formation and growth is illustrated in Fig. 5.21. It can be observed that the radial cracks initially form at the centre of the end-slab and spread towards the wall of the pressure vessel as the internal pressure is increased while the circumferential cracks grow deeper into the slab. The proposed analytical radial cracks propagate up to the inside face of wall of the vessel at pressure of 682.3psi while, the lumped-mass analytical results presented in [109] shows full penetration of the crack to the outside face of the wall of the vessel at a pressure of 666 psi. These crack patterns are compared with the experimental evidence [109] in Fig. 5.22. The comparison confirms that a more realistic cracking is obtained from the proposed analysis. The analytical results indicate the presence of extensive radial cracking in the vessel which suggests flexural type of failure. A similar type of failure was concluded from the experimental results of vessel PV9 [109], which verifies the validity of the

proposed analytical approach.

5.7 Conclusions

The proposed concrete constitutive equations and fracture models have been implemented into the LUSAS finite element system. In implementing these models the effects of dowel action and tension-stiffening have been ignored. The aggregate interlock model developed in Chapter Four was not fully implemented owing to the limitations in the solution facilities in the LUSAS system. The simplified fracture model, however, offers a realistic approach in representing crack tensile softening in concrete.

The concrete models have been tested for plane stress and axisymmetric solid stress problems and in most cases the structures deformational behaviour, load carrying capacity and crack formation are in good agreement with the experimental results.

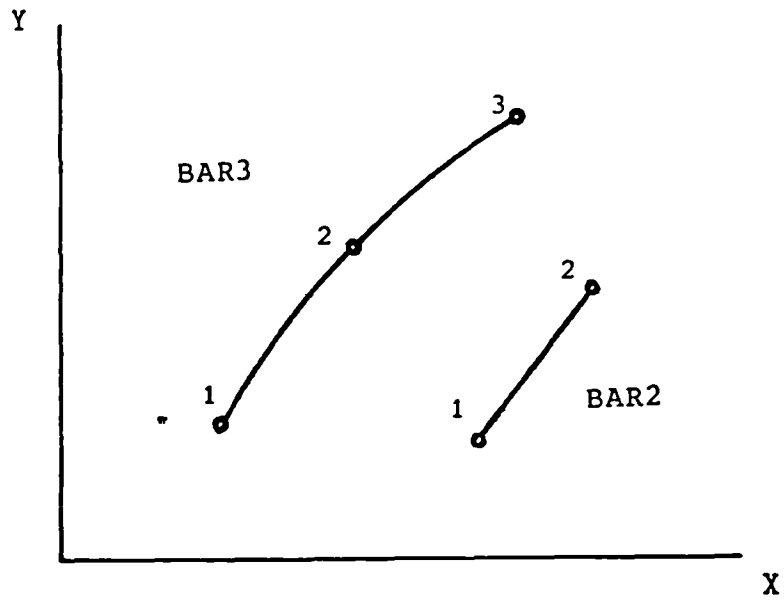


Fig. 5.1 Two-dimensional two and three noded bar elements.

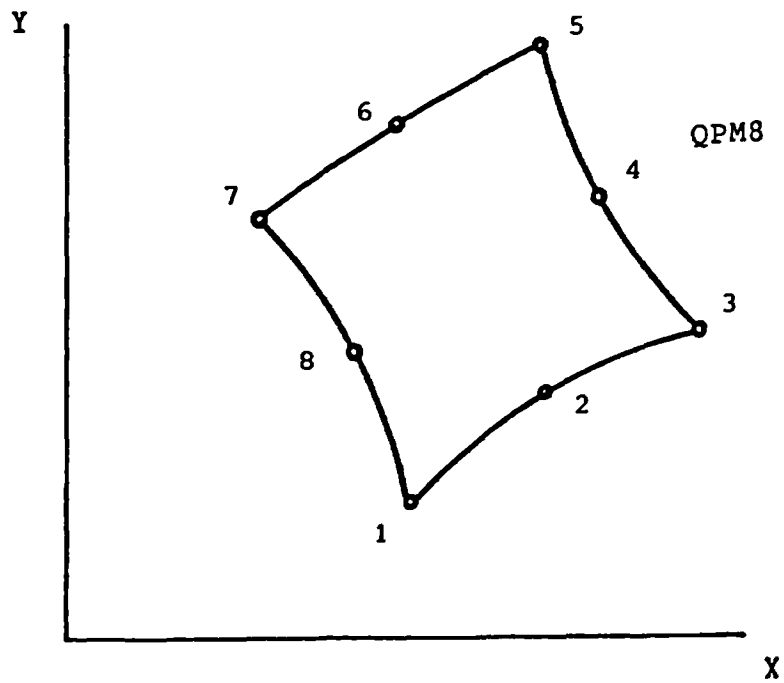


Fig. 5.2 A two-dimensional eight noded plane stress element.

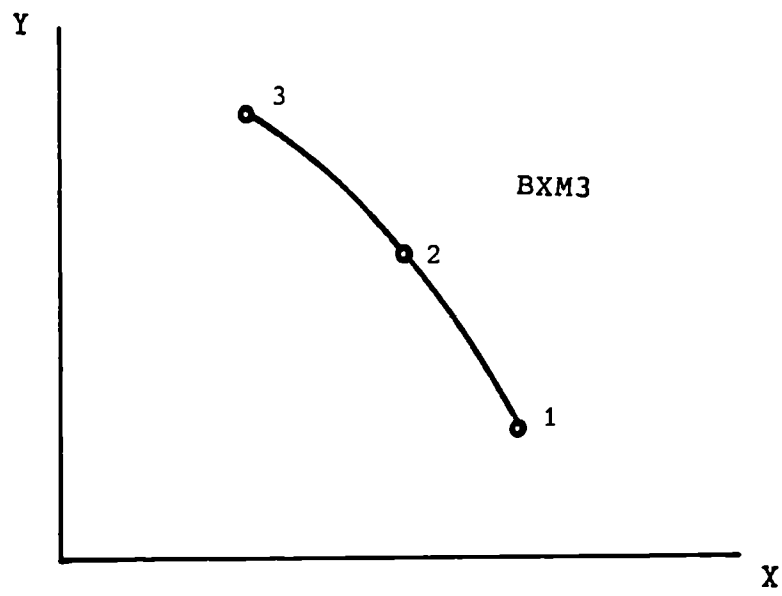


Fig. 5.3 A three noded axisymmetric membrane element.

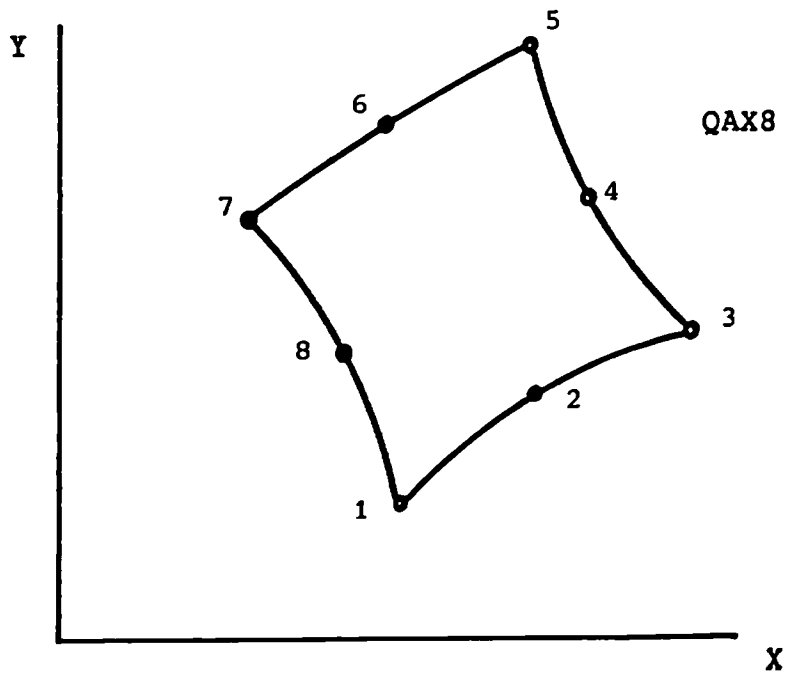


Fig. 5.4 An eight noded axisymmetric solid element.

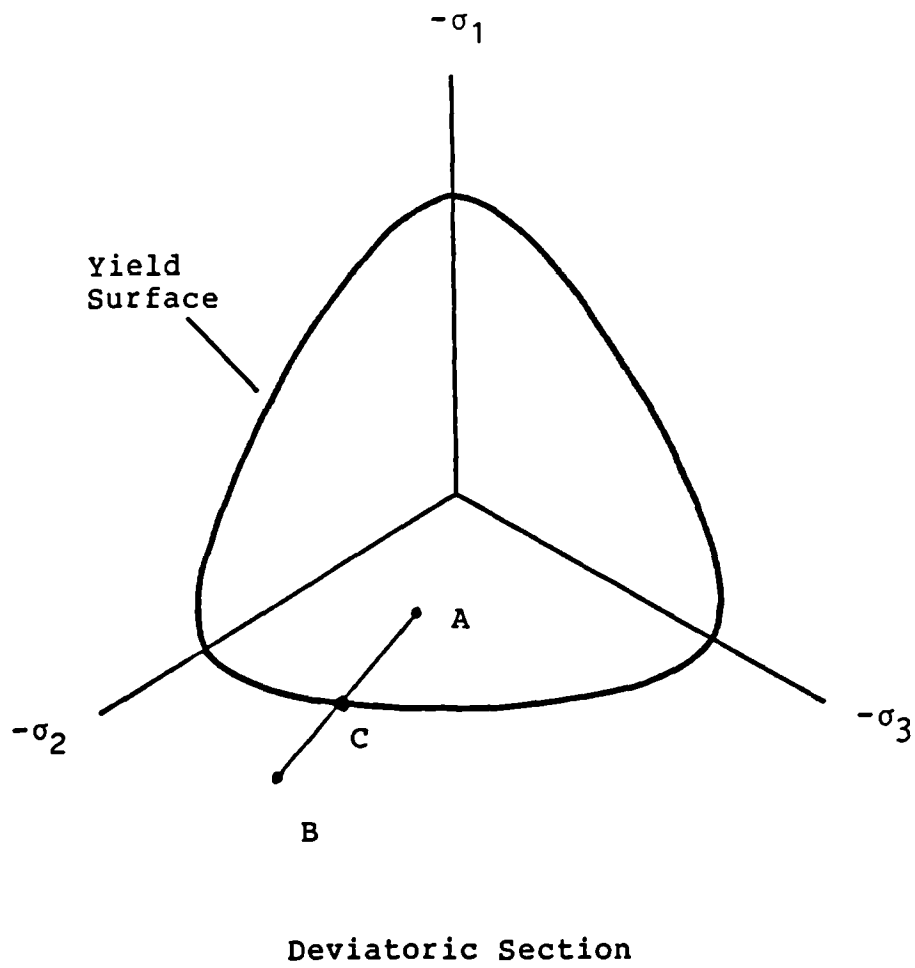
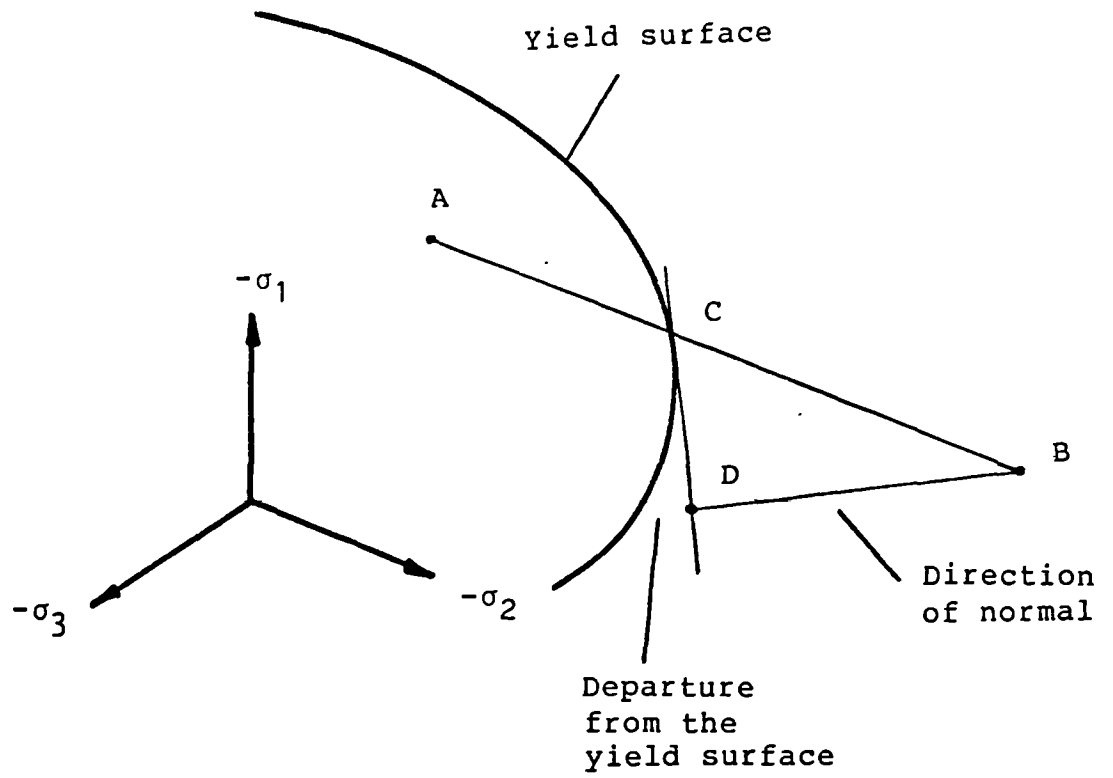
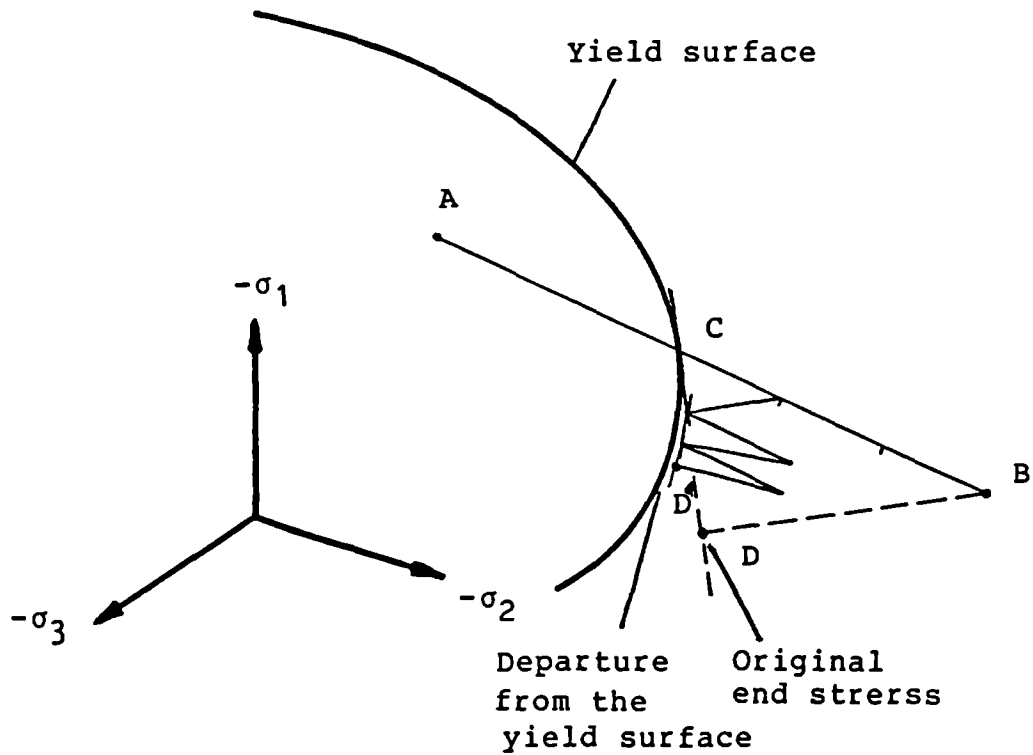


Fig. 5.5 Deviatoric representation of transition from elastic zone to plastic zone.

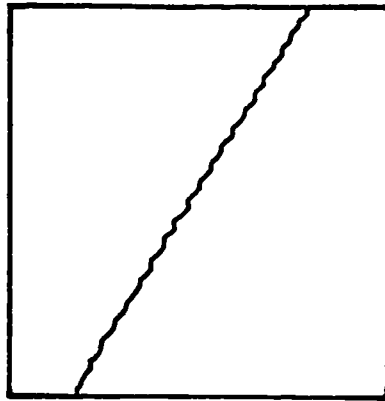


(a) Incremental Technique

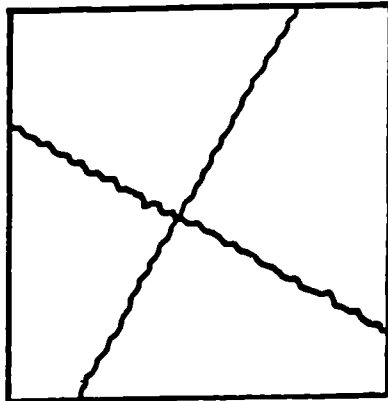


(b) Sub-incremental Technique

Fig. 5.6 Schematic representation of the stresses returned to the yield surface.

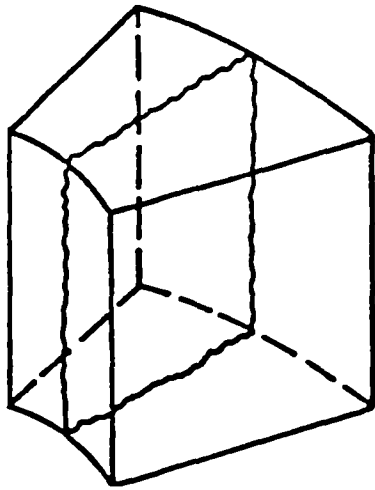


(a) Single Crack

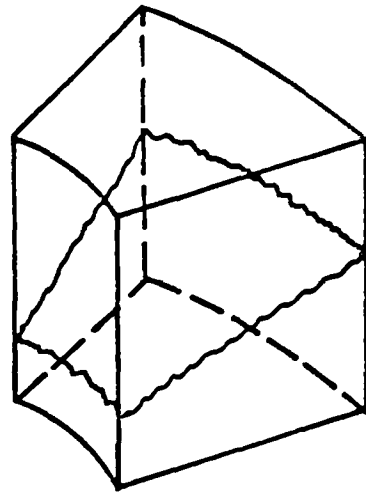


(b) Double Cracks

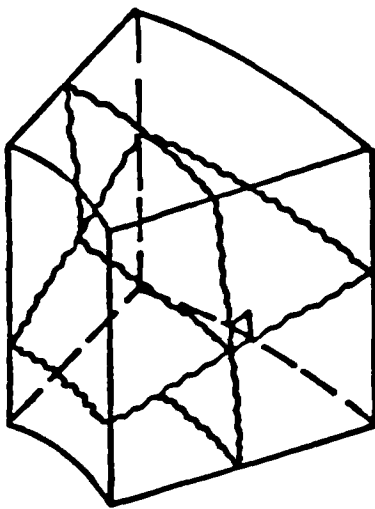
Fig. 5.7 Crack representation for plane stress elements.



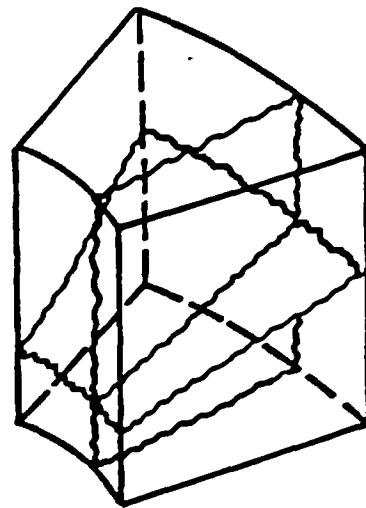
(a) Single Radial Crack



(b) Single Circumferential Crack

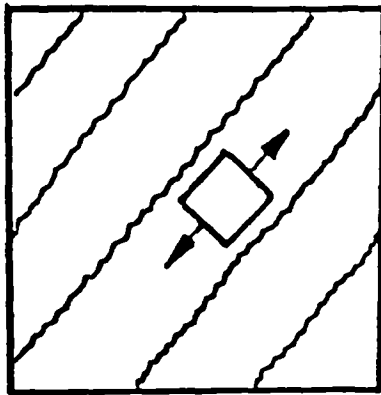


(c) Double Circumferential Cracks

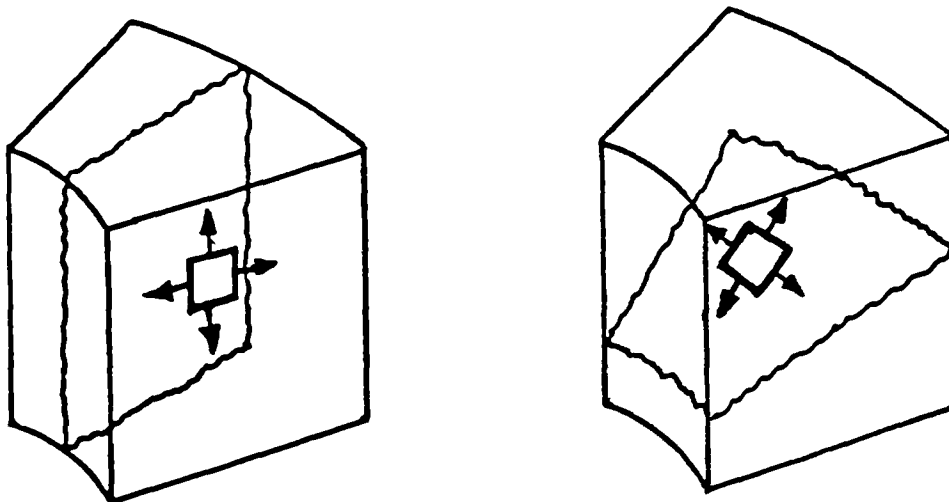


(d) Radial and Circumferential Cracks

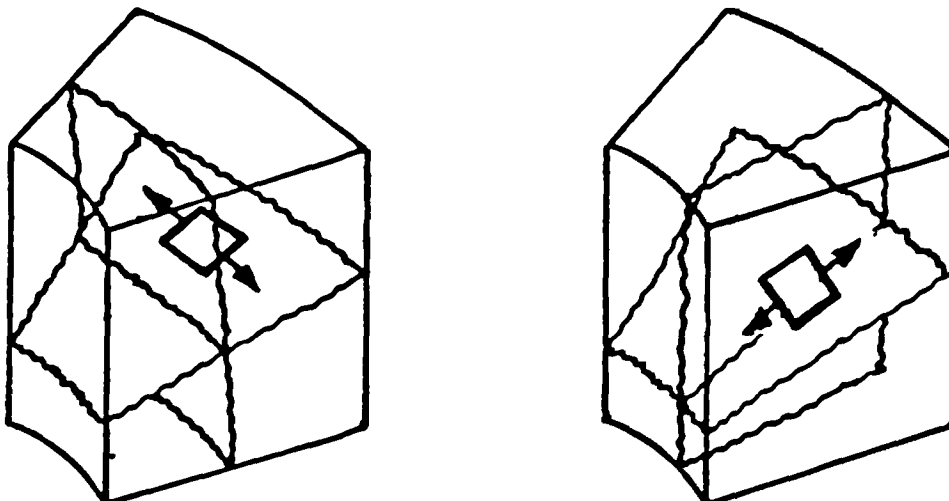
Fig. 5.8 Crack representation for axisymmetric solid stress elements.



(a) Reduction of Plane Stress State to Uniaxial Stress State



(b) Reduction of Axisymmetric Stress State to Biaxial Stress State



(c) Reduction of Axisymmetric Stress State to Uniaxial Stress State

Fig. 5.9 Stress states of the solid concrete between cracks.

Crack Normal
Stress, σ_{nn}

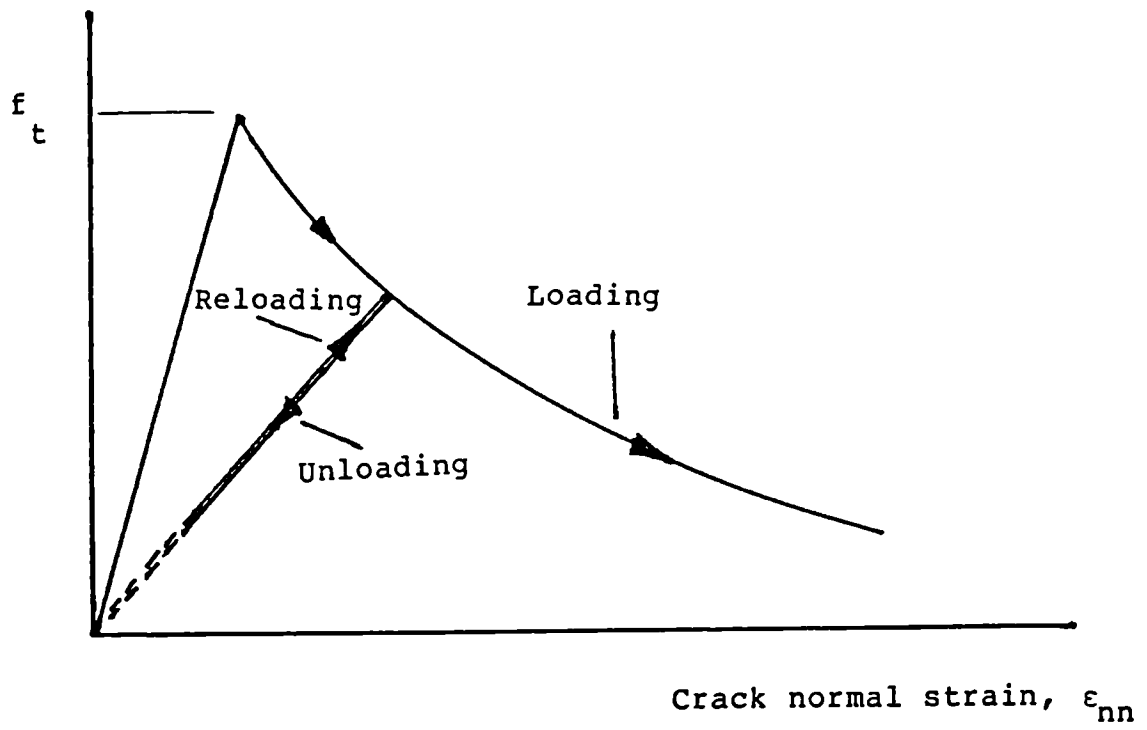
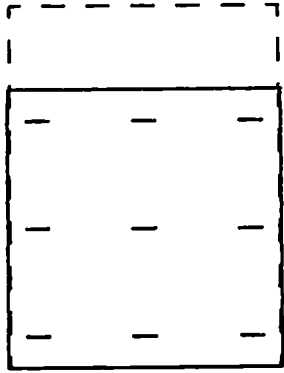
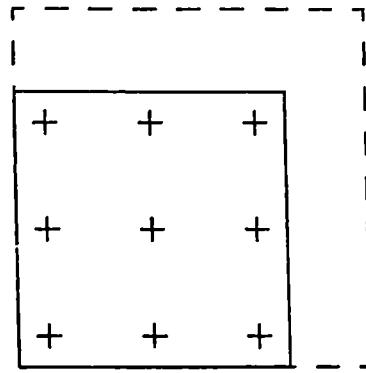


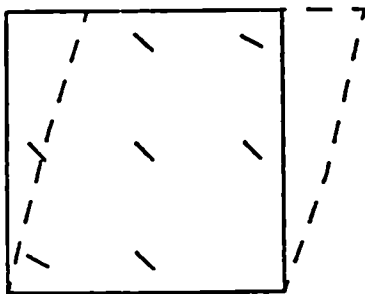
Fig. 5.10 Crack loading and unloading.



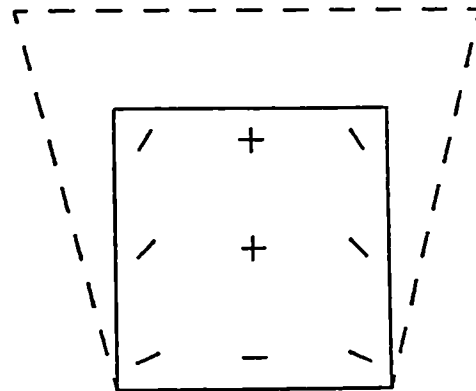
(a) Test Case 1



(b) Test Case 2



(c) Test Case 3



(d) Test Case 4

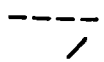
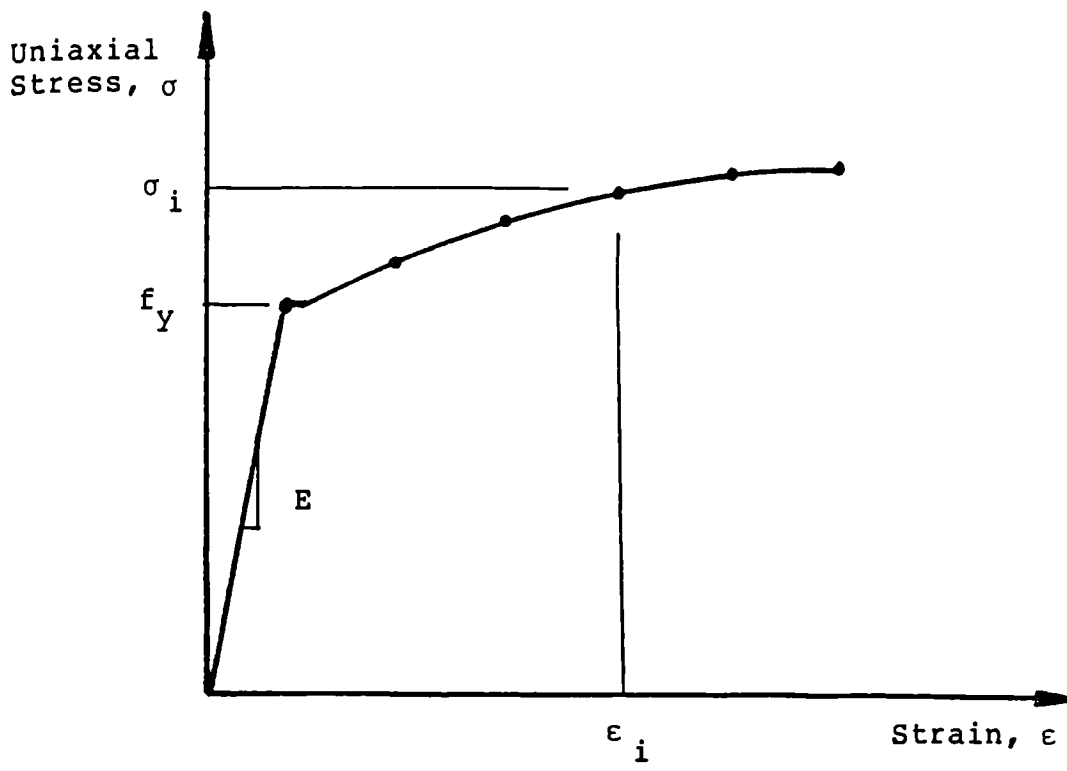
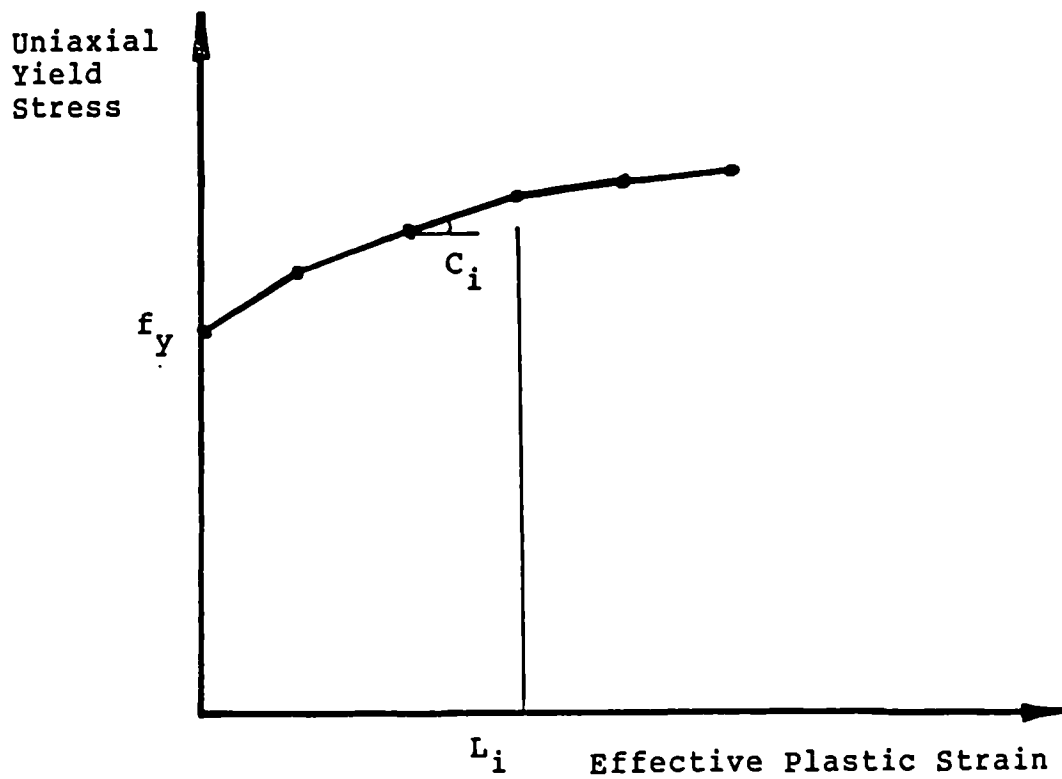

 Deformed Shape
 Crack Direction

Fig. 5.11 Single element tests for crack formation.



(a) Actual Stress-Strain Curve



(b) Yield Stress Versus Effective Plastic Strain Curve

Fig. 5.12 Schematic representation of the steel elasto-plastic model 62 in LUSAS.

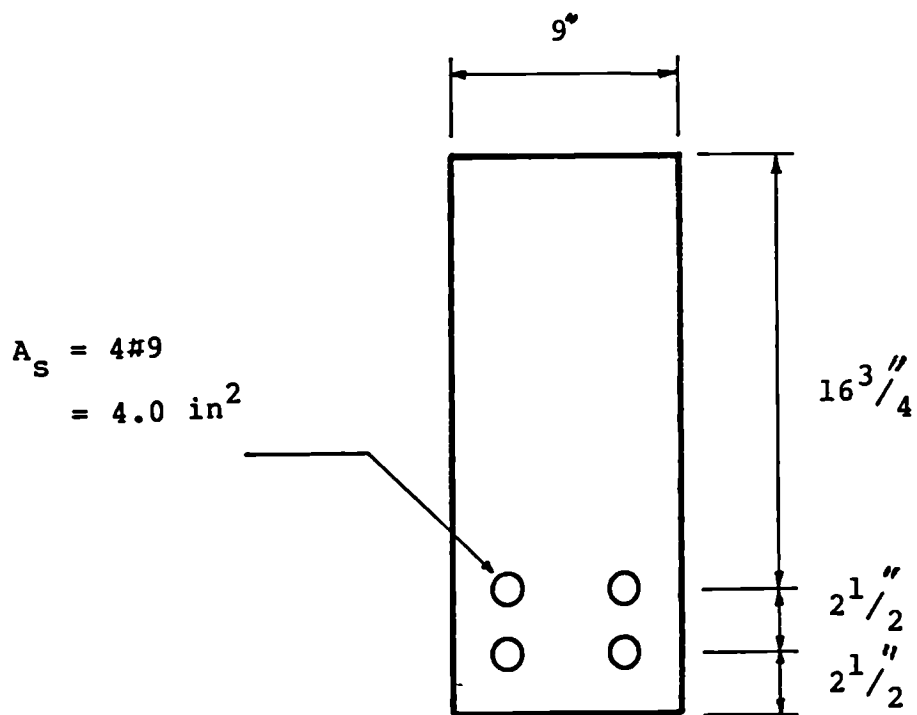
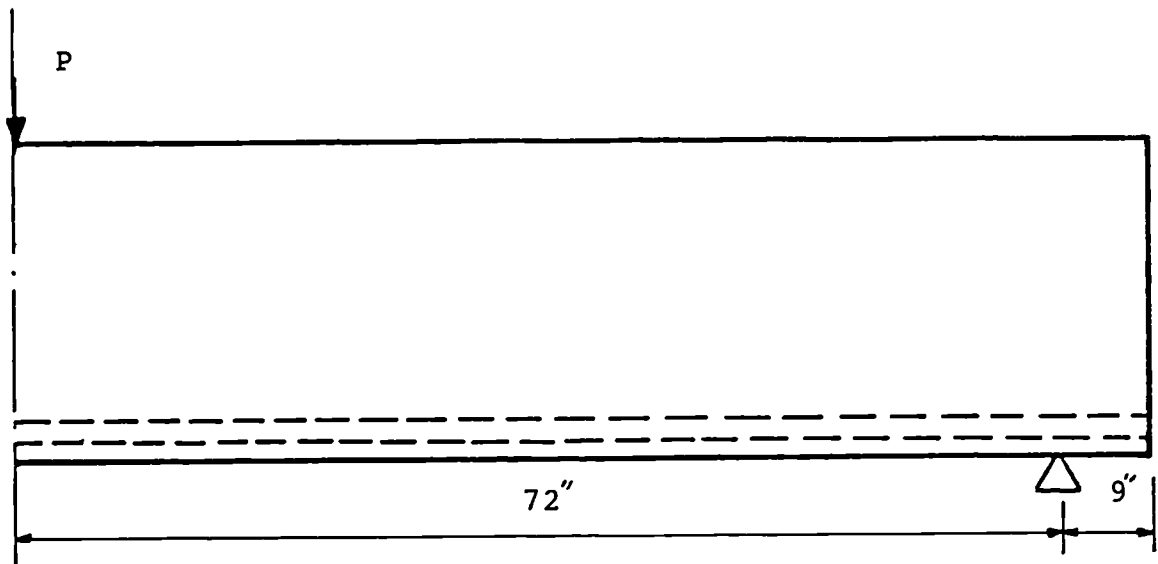
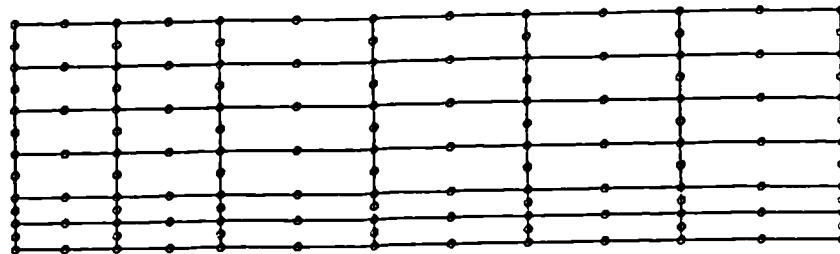
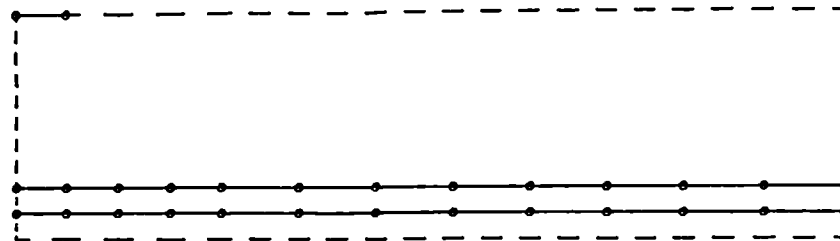


Fig. 5.13 Geometry and the general layout of the flexural beam.

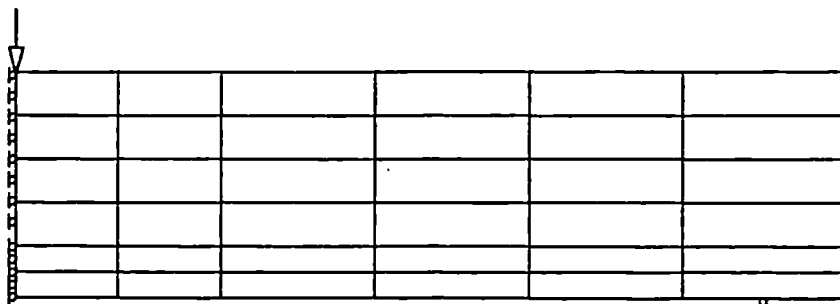


36 QPM8 Elements Used for Concrete



12 BAR3 Elements Used for Reinforcement
1 BAR2 Element Used for Base Plate

Point Load
Applied
Along the
Centre Line



Loading and Support Conditions

Fig. 5.14 Finite element mesh of the flexural beam.

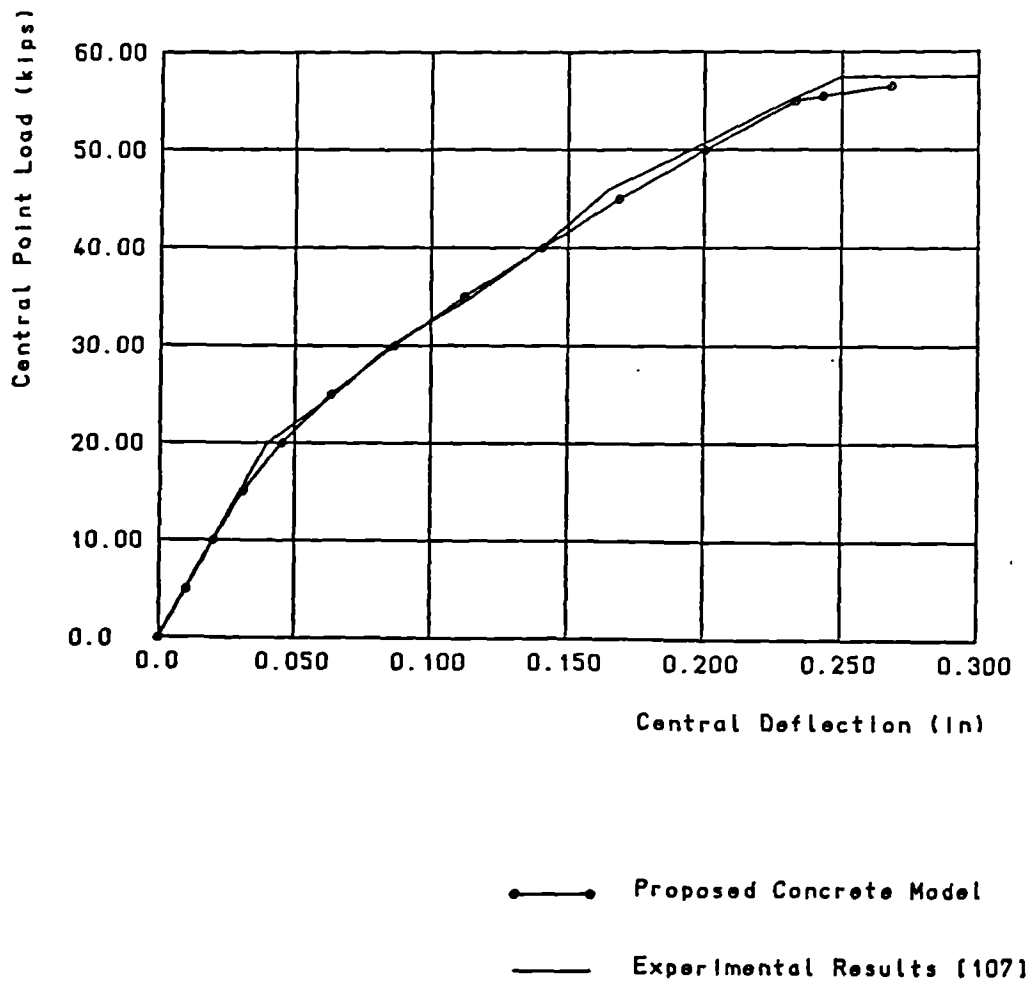


Fig. 5.15 Comparison between the analytical and experimental mid-span load-deflection curves of the flexural beam.

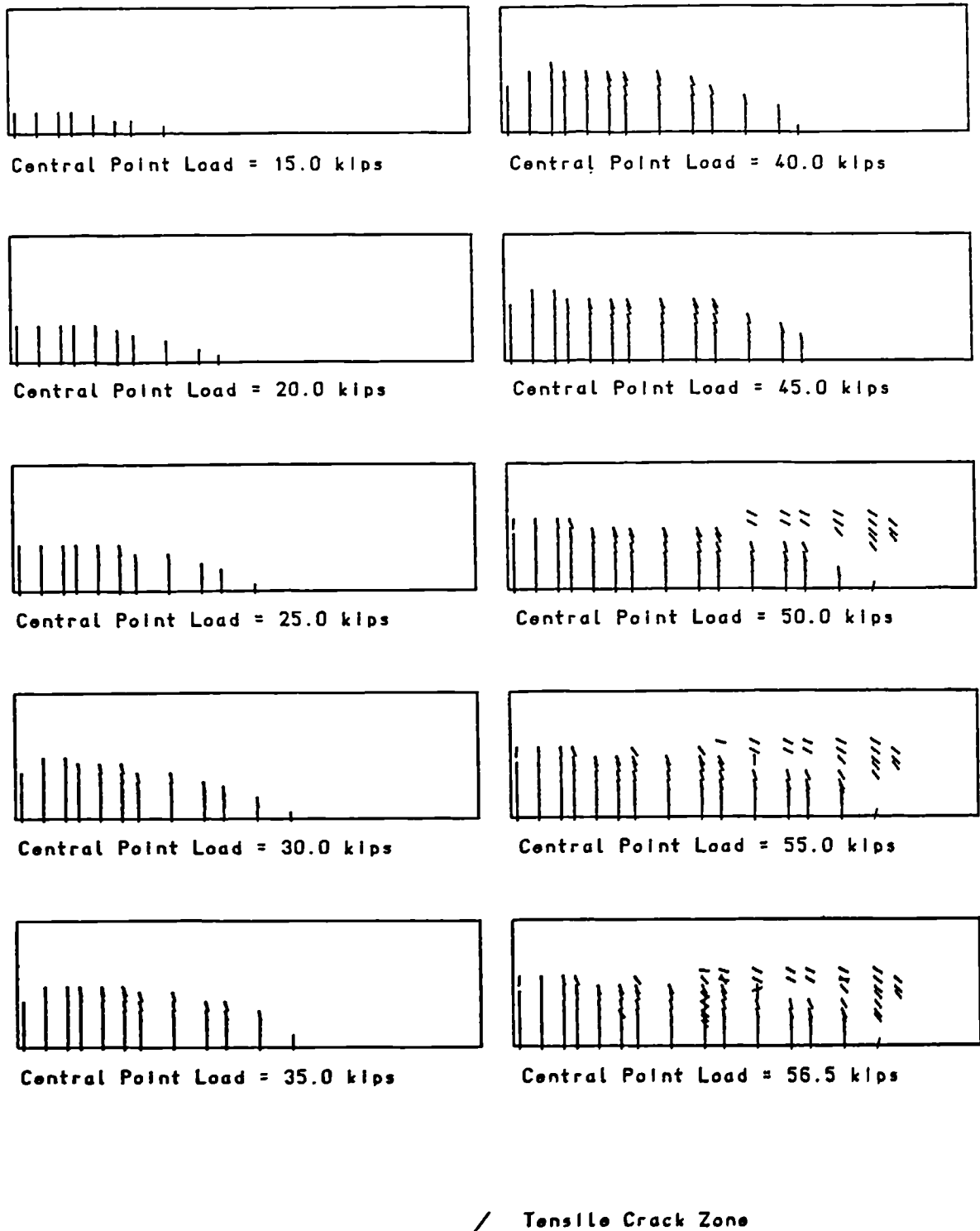
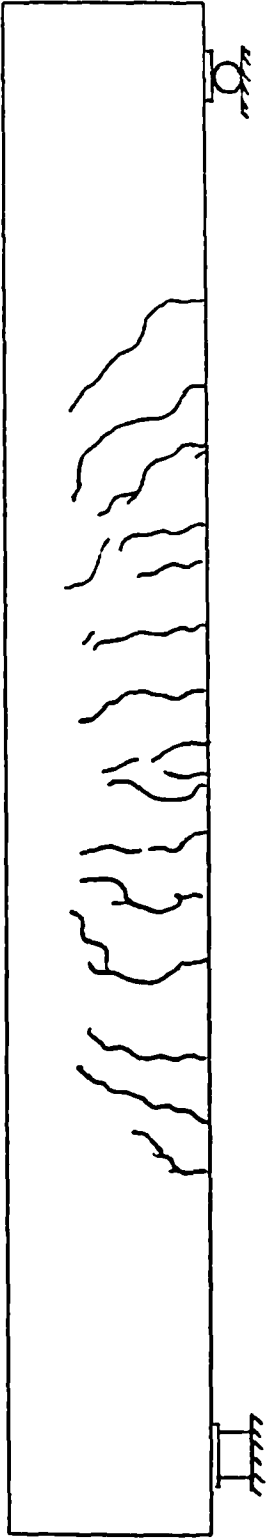
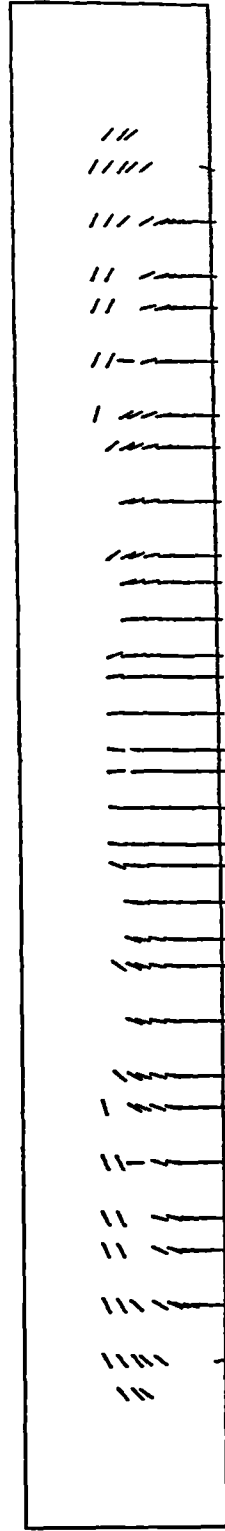


Fig. 5.16 Analytical zones of tensile failure of the flexural beam.



Experimental Crack Pattern at Load = 55.0 kips [107]



Analytical Crack Pattern at Load = 55.0 kips

Fig. 5.17 Comparison between the analytical and experimental crack pattern of the flexural beam at failure.

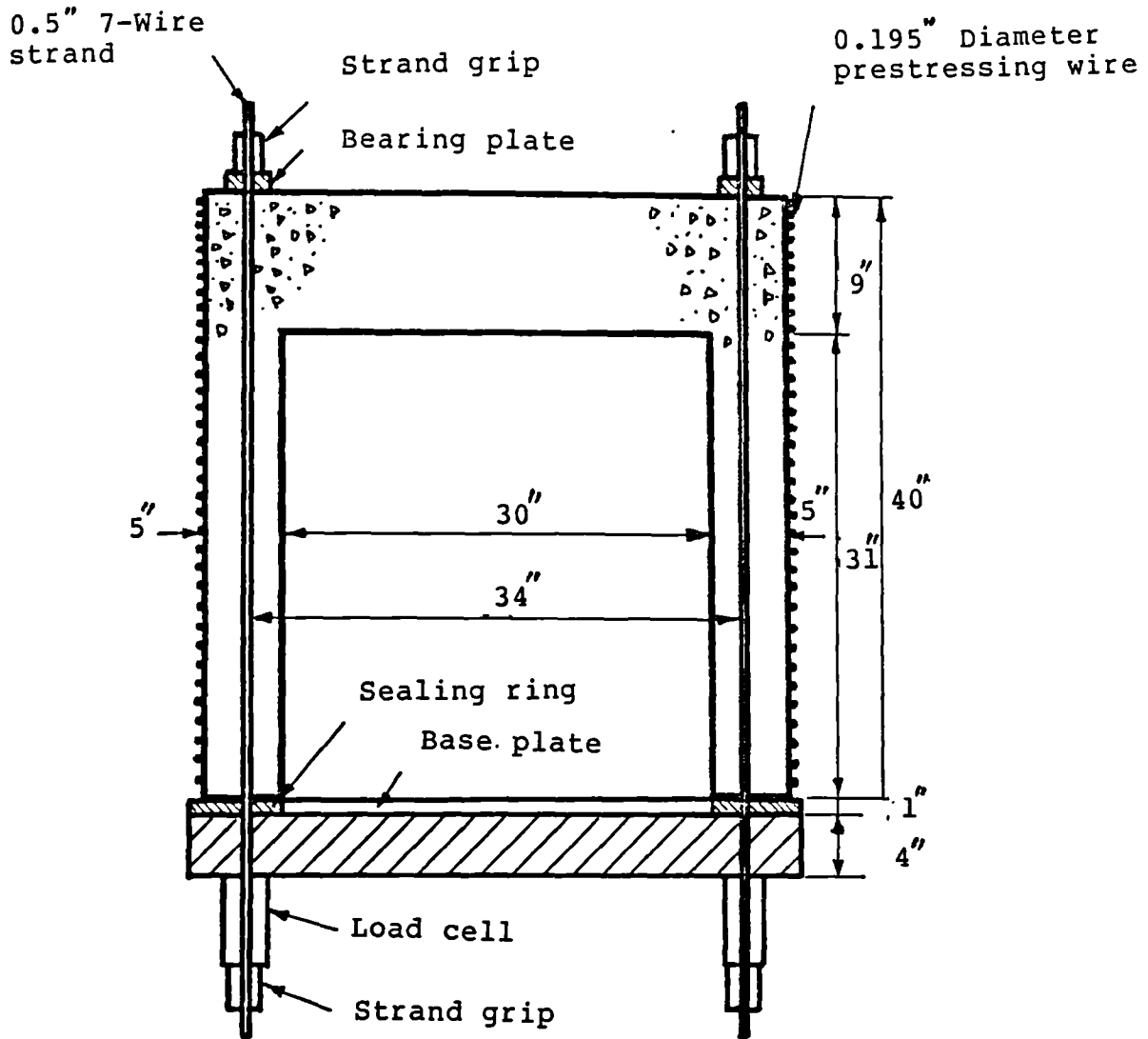
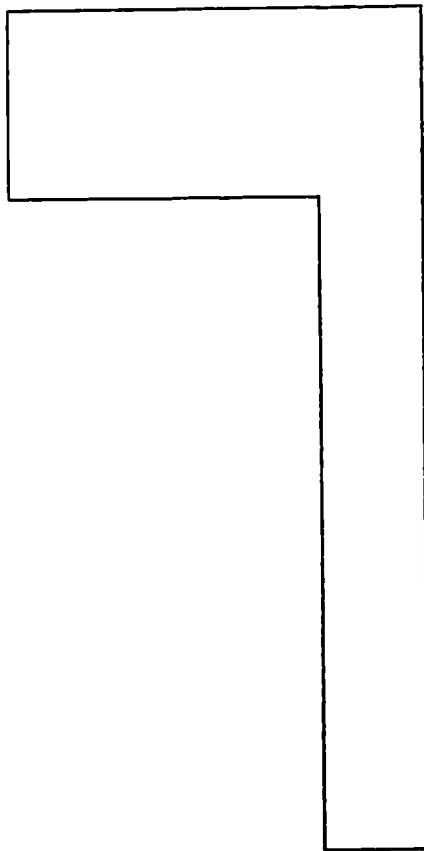
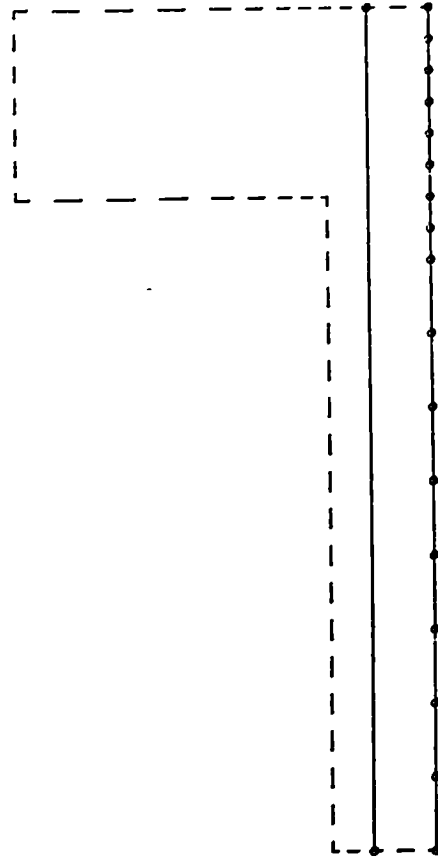


Fig. 5.18 Details of the section and the prestressing arrangement of the reactor vessel.



28 QAX8 Elements Used for Concrete



8 BXM3 Elements Used for Circumferential Prestressing

1 BAR2 Element Used for Longitudinal Prestressing

Fig. 5.19 Finite element mesh of the reactor vessel.

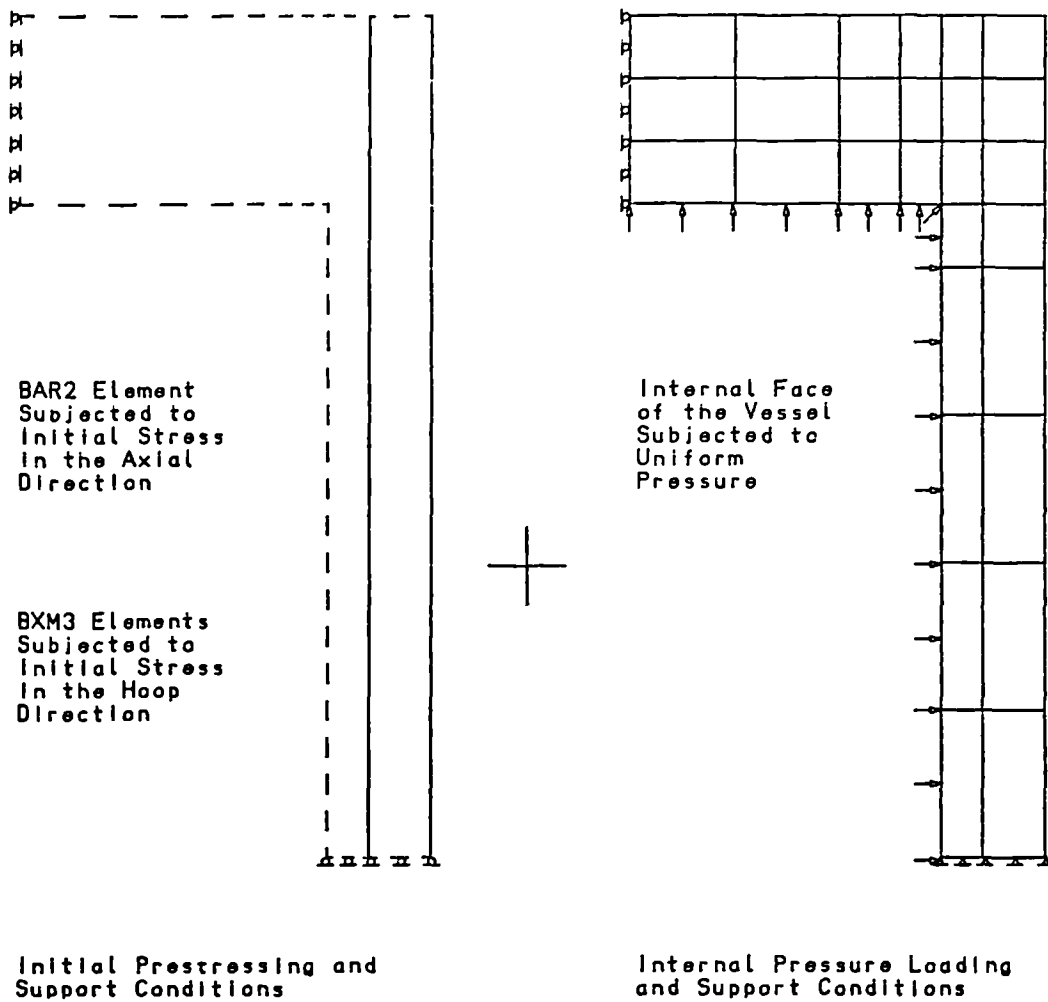
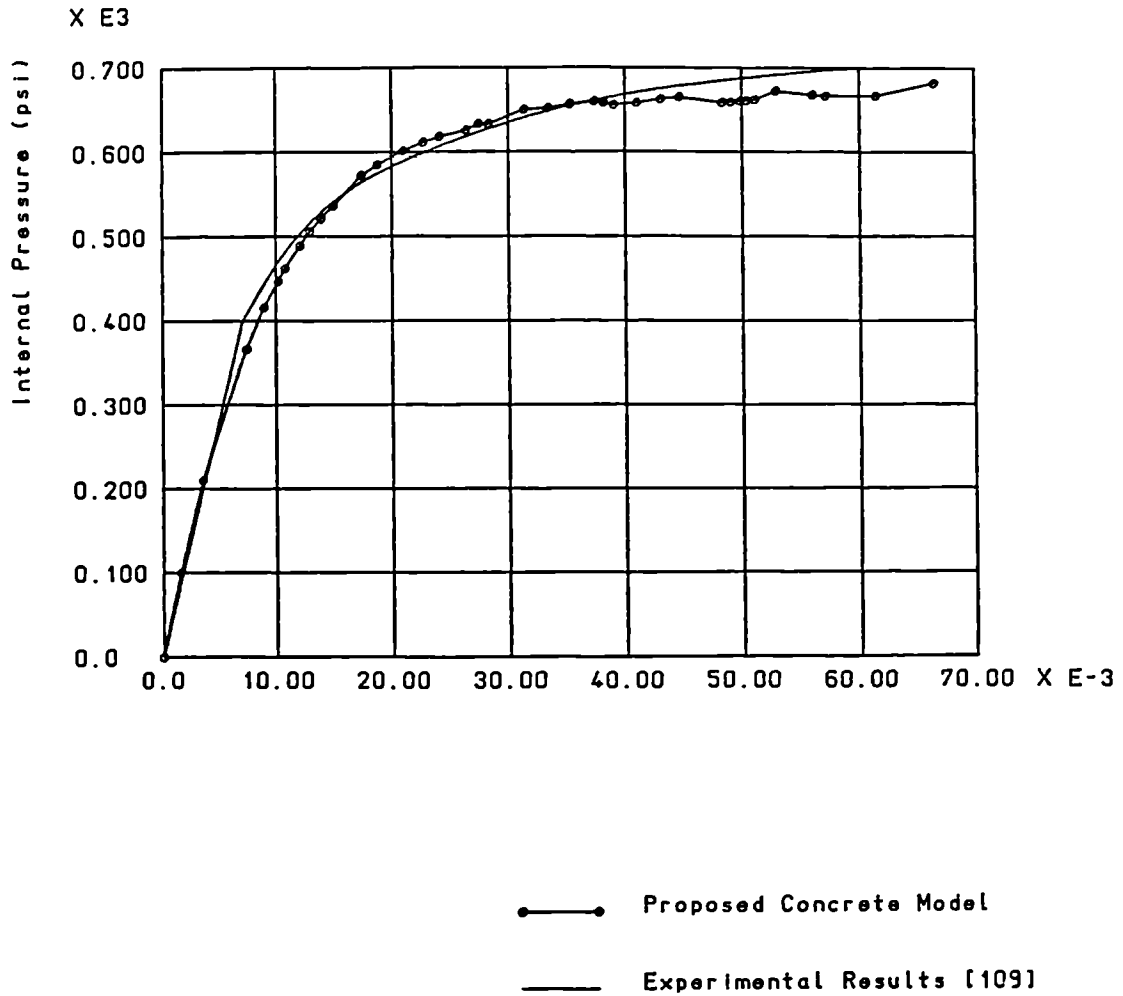
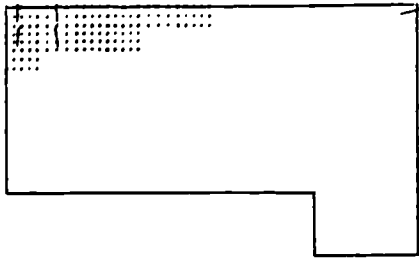


Fig. 5.19 Continued

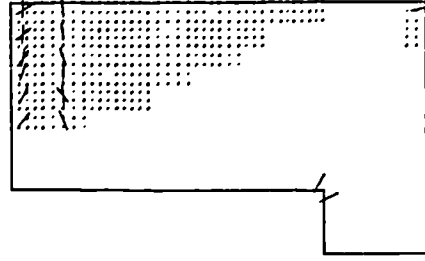


(Deflections measured from the prestressed configuration)

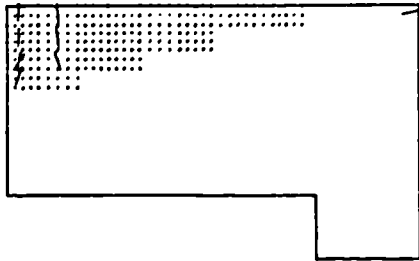
Fig. 5.20 Comparison between the analytical and experimental central load-deflection curves of the reactor vessel.



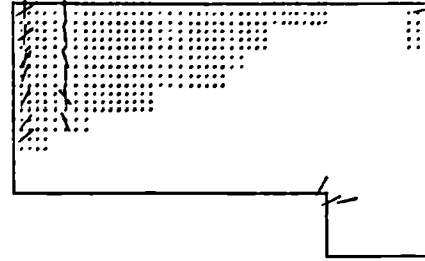
Internal Pressure = 365.7 psi



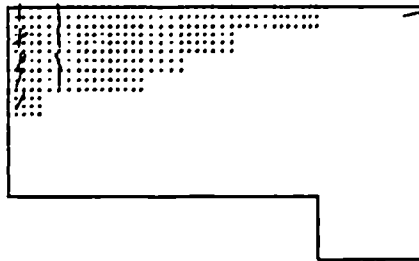
Internal Pressure = 626.0 psi



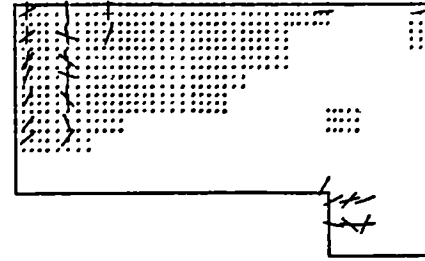
Internal Pressure = 447.1 psi



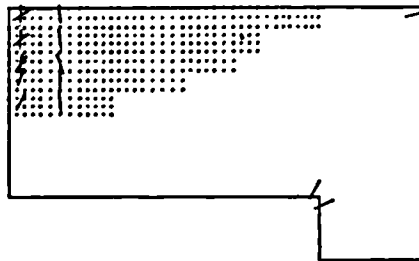
Internal Pressure = 650.0 psi



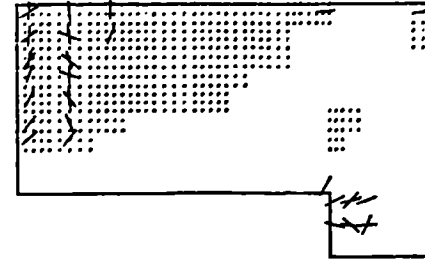
Internal Pressure = 505.6 psi



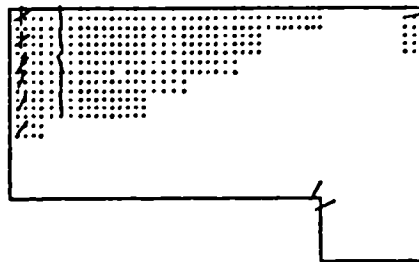
Internal Pressure = 662.0 psi



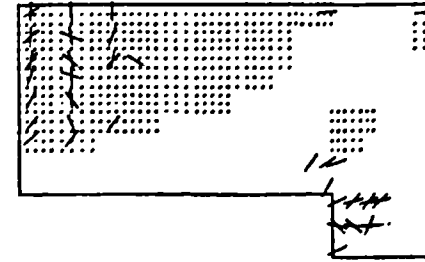
Internal Pressure = 572.5 psi



Internal Pressure = 672.6 psi



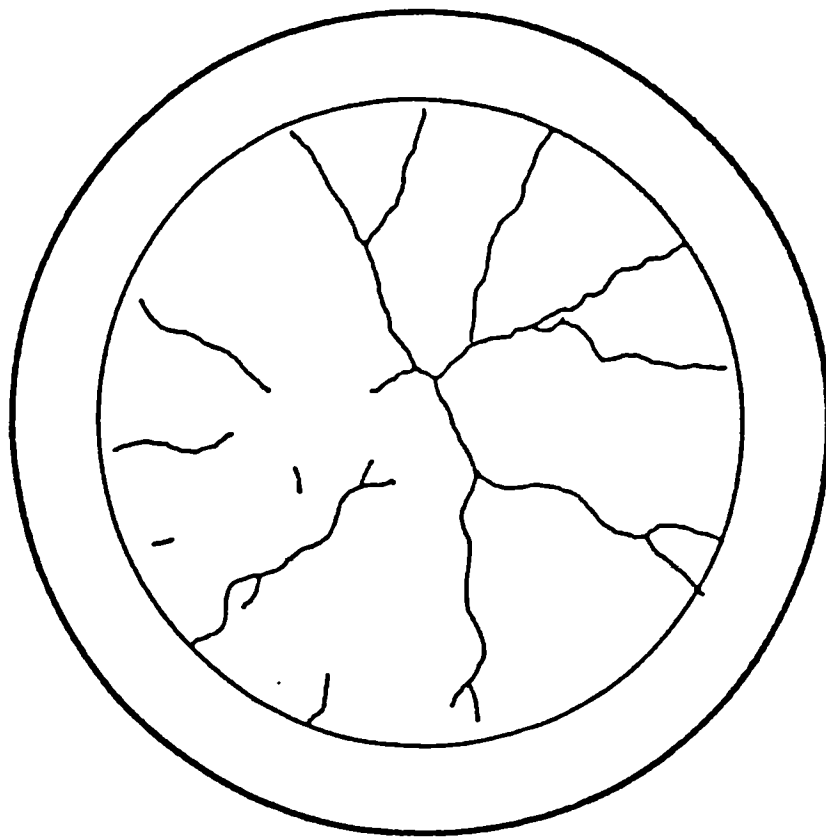
Internal Pressure = 601.6 psi



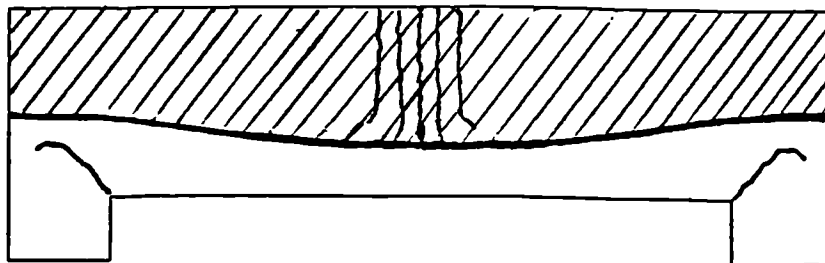
Internal Pressure = 682.3 psi

 Radial Crack Zone
 Circumferential Crack zone

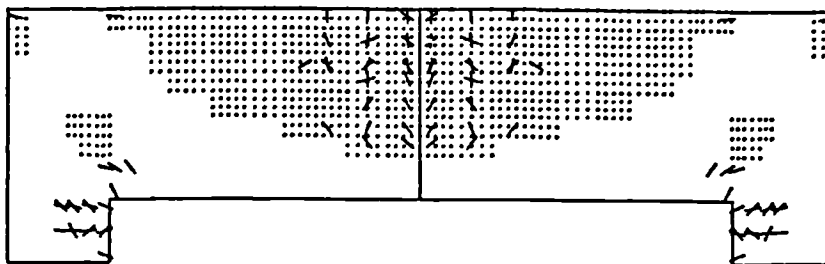
Fig. 5.21 Analytical zones of tensile failure of the reactor vessel.



EXPERIMENTAL CRACK PATTERN
AT INTERNAL PRESSURE = 700.0 PSI [109]



LUMPED-MASS ANALYTICAL CRACK PATTERN
AT INTERNAL PRESSURE = 666.0 PSI [109]



PROPOSED ANALYTICAL CRACK PATTERN
AT INTERNAL PRESSURE = 682.3 PSI

Fig. 5.22 Comparison between the analytical and experimental crack pattern of the reactor vessel.

CHAPTER SIX

CONCLUSIONS AND RECOMMENDATIONS

6.1 Conclusions

A review of the methods available in the mathematical modelling of concrete constitutive relationships has been carried out and their relative advantages and weaknesses have been identified. The outcome of this investigation indicates the need for a concrete model which encompasses the most prominent features associated with a predominantly geological material. The nonlinear features are due to microcracking, stress path dependency, volumetric dilatancy and strain-softening. The development of a realistic concrete model must, however, succumb to the restrictions imposed by the scarcity of the experimental results as well as practical aspects required for the application of the model in a numerical analysis. The available experimental results are often obtained under idealised laboratory conditions and in general do not provide a sound basis for understanding the concrete behaviour subjected to non-proportional loading, high hydrostatic pressure and true triaxial loading conditions. The preliminary review of the literature reveals that the theory of plasticity together with a yield surface suitable for concrete, combined with a realistic hardening rule embraces the most recognised material characteristics of concrete without sacrificing the overall objectivity required for the numerical application.

The present research has concentrated on developing a

concrete model using theory of the hardening plasticity and an associated flow rule. This is despite the fact that a realistic representation of the shear dilatancy in concrete requires the adoption of a non-associated flow rule. In view of the lack of experimental evidence to fully characterise the shear dilatancy in concrete as well as the numerical complexity associated with the use of a non-associated flow rule, namely an unsymmetrical modular matrix, the simple approach adopted here is justified. The current development has been conducted mainly in the same direction as that of previous investigators. There has been a particular emphasis, however, on correlation with experimental results to obtain explicit definitions for the material parameters without losing the flexibility of the proposed model.

A failure surface has been developed which relies on the three stress invariants and contains all the basic features generally recognised by other investigators and validated by experimental results. These features include curved meridians, non-circular deviatoric section and hydrostatic pressure dependency. The general shape of the surface has been formed by applying boundary conditions defining the concrete properties and a unified relationship is obtained by finding the best fit to a wide range of the experimental results.

The hardening and softening in concrete has been modelled by an isotropic hardening rule using the concept of the effective plastic strain. The variation of the hardening parameter with

the effective plastic strain is obtained from the biaxial and triaxial experimental data. The hardening parameter is used to monitor the expansion and contraction of the yield surface in the pre and post ultimate stress levels.

An incremental constitutive model has been developed using the proposed failure surface, isotropic hardening/softening rule and an associated flow rule. The validity of the model has been compared with published experimental results. The overall performance of the proposed model agrees favourably with the experimental results although some discrepancy observed in the volumetric response of the model. The volumetric deviation of the results obtained from the proposed model and the experimental data is attributed to the inadequacy of the hardening rule in modelling volumetric dilatation as well as the need for a non-associated flow rule.

The problem of tensile and compressive failure in concrete has been investigated and a stress base failure criterion has been developed. It is recognised that the prime cause of nonlinearity in most concrete structures is the cracking and its propagation. Three main phenomena have been identified with crack formation in concrete and these are shear transfer across the crack interface due to aggregate interlock, dowel action and the effect of bar-to-concrete bond. These features have been investigated in detail and particular attention is paid to the aggregate interlock and interface shear transfer. The stresses across a crack are obtained in terms of the relative displacements of crack surfaces and explicit relationships of these stresses have been derived from the

experimental evidence. The effects of dowel action and tension stiffening are included by developing suitable mathematical models representing the mechanism of the forces acting on a block of cracked concrete with embedded reinforcement bars. The contribution of the dowel action and aggregate interlock in resisting shear are compared. This comparison indicates that shear is mainly resisted by aggregate interlock and the dowel action has a negligible effect. The crack related models have been verified by comparing them with experimental result.

The concept of a smeared crack has been used in implementing the crack properties in the material behaviour of concrete instead of the discrete crack approach. The latter concept requires the change of element topology to incorporate the crack formation along the element edges. This may lead to numerical difficulties and will increase the computer run time. The development of cracked concrete properties has been carried out for two types of analyses, where concrete and steel reinforcement bars are discretised separately and where, due to uniformity of steel distribution, they are combined into a composite element. The former case combines the effect of aggregate interlock with the solid concrete properties while in the latter steel properties are introduced and combined with the effects of dowel action and tension-stiffening to obtain the plain and reinforced cracked concrete stiffness matrices respectively.

The proposed constitutive relationships and the fracture models have been implemented into the LUSAS finite element

system for the plane stress and axisymmetric solid stress analysis of concrete structures. In the analysis of the concrete structures concrete and steel have been discretised as independent elements which are assumed to be rigidly connected to each other. A more realistic approach, however, requires the interface between steel and concrete to be modelled by joint elements representing the bond between two materials. The exact modelling of the interface has been overlooked owing to the lack of information on the actual bond between concrete and steel.

The properties of solid concrete has been modelled by the proposed constitutive relationships and the cracked concrete has been represented as an orthotropic material comprising of smeared cracks and solid concrete between them. The resulting cracked concrete property is an unsymmetrical stiffness matrix which was made symmetrical by ignoring the coupling effects of the normal and shear crack displacements. The cracked concrete model is capable of simulating the gradual release of tensile stresses (tension softening) as well as allowing for crack opening and closure, which may occur due to stress redistribution. The cracks are allowed to form in non-orthogonal directions at a specified threshold angle to allow for the rotation of principal stress directions.

The proposed models have been applied in the analysis of a reinforced concrete beam and a reactor pressure vessel. The two examples have been used in assessing the overall performance of the concrete models in predicting the deformational behaviour, load carrying capacity and the crack formation in plane stress and axisymmetric solid problems.

The results agree very well with the experimental data.

The proposed research work can be summarised as follows

- (a) A nonlinear constitutive relationship has been developed for concrete. The salient features of this model are stress path dependency, modelling of stress hardening as well as strain-softening and capability to represent uniaxial, biaxial and triaxial stress states.
- (b) The shear aggregate interlock in cracked concrete has been modelled in terms of relative crack displacements and the effects of dowel action due to bar kinking and deformation is related to crack movements. A tension-stiffening parameter representing the bond between steel bar and cracked concrete has been derived.
- (c) The proposed concrete and fracture models have been implemented into a finite element system and the models have been verified for plane stress and axisymmetric solid stress problems.

6.2 Recommendations for Further Research

The following recommendations are suggested for future work

- (a) Improvement of the constitutive equations by introducing a non-associated flow rule for a better representation of volumetric dilatancy in concrete.

- (b) Introduction of a kinematic hardening rule and extension of the proposed concrete model for application in dynamic analysis.
- (c) Modification of the material dependent parameters to include the effect of rate of loading for impact analysis.
- (d) Investigation of the performance of the non-orthogonal crack model against the rotating crack model.
- (e) Implementation of reinforced concrete composite element in the finite element method for the analysis of shell structures.
- (f) Implementation of a non-symmetrical solution technique for complete representation of aggregate interlock.
- (g) A parametric study of the effects of dowel action and tension-stiffening on the overall analytical solution.

**DESCRIPTION OF THE MATHEMATICAL RELATIONS USED
FOR THEORETICAL DEVELOPMENT IN CHAPTER THREE**

A.1 Mathematical Definitions

The state of stress at a point can be defined by the stress tensor as

$$\sigma_{ij} = \begin{bmatrix} \sigma_{11} & \sigma_{12} & \sigma_{13} \\ \sigma_{21} & \sigma_{22} & \sigma_{23} \\ \sigma_{31} & \sigma_{32} & \sigma_{33} \end{bmatrix} \quad (\text{A.1})$$

from which the invariants of stresses are

$$I_1 = \sigma_{ij} \quad (\text{A.2})$$

$$I_2 = \frac{1}{3}(I_1^2 - \sigma_{ij}\sigma_{ij}) \quad (\text{A.2})$$

$$I_3 = \frac{1}{6}(2\sigma_{ij}\sigma_{jk}\sigma_{ki} - 3I_1\sigma_{ij}\sigma_{ji} - I_1^3) \quad (\text{A.3})$$

The deviatoric stress tensor is widely used in the stress-strain relationships of material and is defined as

$$s_{ij} = \sigma_{ij} - \delta_{ij}\sigma_{kk}/3 \quad (\text{A.5})$$

where δ_{ij} = Kronecker delta

Invariants of the deviatoric stress tensor are defined as

$$J_1 = s_{ii} = 0 \quad (\text{A.6})$$

$$J_2 = \frac{1}{2} s_{ij} s_{ji} \quad (\text{A.7})$$

$$J_3 = \frac{1}{3} s_{ij} s_{jk} s_{ki} \quad (\text{A.8})$$

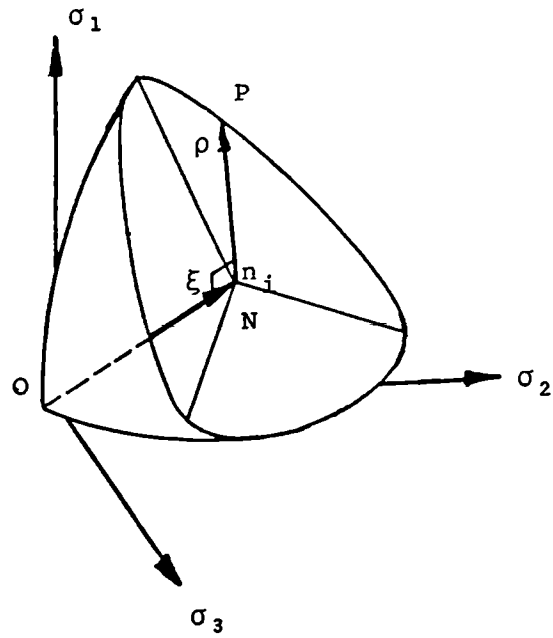
To describe a point in stress space the Haigh-Westegard coordinate system is used Fig. A.1. The following relationships can be obtained from Fig. A.1

$$\xi = |\overline{ON}| = \frac{I_1}{\sqrt{3}} \quad (\text{A.9})$$

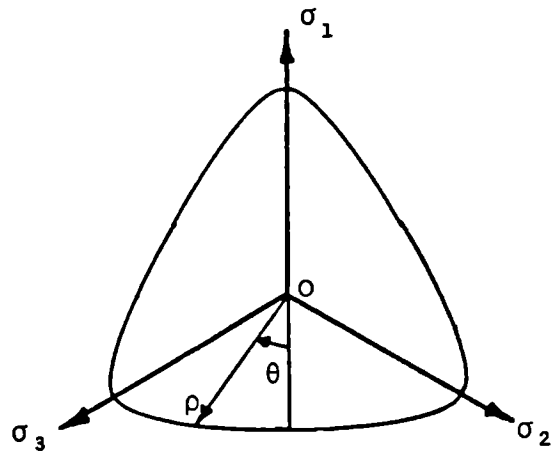
$$\rho = |\overline{NP}| = \sqrt{2} J_2 \quad (\text{A.10})$$

$$\theta = \frac{1}{3} \cos^{-1} \left(\frac{3\sqrt{3}}{2} \frac{J_3}{J_2^{3/2}} \right) \quad (\text{A.11})$$

The hydrostatic axis, $n_i = \langle 1/3 \ 1/3 \ 1/3 \rangle$, is represented by ξ and the deviatoric axis is defined by ρ which is always perpendicular to ξ . The deviatoric plane is generated by varying θ normal to the direction of ξ and intersects the stress axes at equal inclinations. The sign convention used in this study is tension positive and compression negative.



(a) Three-dimensional View



(b) Deviatoric View

Fig. A.1 Haigh-Westergaard coordinate system.

ELLIPTIC TRACE OF THE YIELD SURFACE

B.1 Derivation of the Elliptic Trace

The geometrical representation of the elliptic yield surface is shown in Fig. B.1 with regard to X-Y axes. The general form of such an ellipse is

$$f = X^2 + aY^2 + bXY + cX + dY + e \quad (B.1)$$

Taking derivatives with respect to X and Y

$$\frac{\partial f}{\partial X} = 2X + bY + c \quad (B.2)$$

$$\frac{\partial f}{\partial Y} = 2aY + bX + d \quad (B.3)$$

The direction cosine at a point P on the curve is given as

$$\bar{N}_{P,X} = (2X + bY + c)/R \quad (B.4)$$

$$\bar{N}_{P,Y} = (2aY + bX + d)/R \quad (B.5)$$

where

$$R = \sqrt{\left(\frac{\partial f}{\partial X}\right)^2 + \left(\frac{\partial f}{\partial Y}\right)^2} \quad (B.6)$$

At point A; $\bar{N}_{A,X} = 0$, $\bar{N}_{A,Y} = 1.0$, $X = 0$ and $Y = \bar{\rho}_t$.
Substituting these values in Eq's. B.4 and B.5 gives

$$\bar{\rho}_t b + c = 0 \quad (\text{B.7a})$$

$$2\bar{\rho}_t a + d = R \quad (\text{B.7b})$$

At point B; $N_{B,X} = \sqrt{3}/2$, $N_{B,Y} = 0.5$, $X = \sqrt{3}\bar{\rho}_c/2$ and $Y = \bar{\rho}_c/2$. Substituting these values in Eq's. B.4 and B.5 gives

$$\bar{\rho}_c b + 2c + = \sqrt{3}R - 2\sqrt{3}\bar{\rho}_c \quad (\text{B.8})$$

$$2\bar{\rho}_c a + \sqrt{3}\bar{\rho}_c b + 2d = R \quad (\text{B.9})$$

Eliminating R from Eq's. B.8 and B.9 yields

$$\sqrt{3}\bar{\rho}_c a + \bar{\rho}_c b - c + \sqrt{3}d = \sqrt{3}\bar{\rho}_c \quad (\text{B.10})$$

At point A; $X = 0$ and $Y = \bar{\rho}_t$. Substituting these values in Eq. B.1 gives

$$\bar{\rho}_t^2 a + \bar{\rho}_t d = -e \quad (\text{B.11})$$

At point B; $X = \sqrt{3}\bar{\rho}_c/2$ and $Y = \bar{\rho}_c/2$. Substituting these values in Eq. B.1 gives

$$\bar{\rho}_c a + \sqrt{3}\bar{\rho}_c^2 b + 2\sqrt{3}\bar{\rho}_c c + 2\bar{\rho}_c d = -(4e + 3\bar{\rho}_c^2) \quad (\text{B.12})$$

Parameters a, b, c and d may now be expressed in terms of the fifth parameter e by solving Eq's. B.6, B.10, B.11 and B.12 simultaneously. These parameters are expressed as follows

$$a = \frac{1}{2\bar{\rho}_c \bar{\rho}_t} e + \frac{3\bar{\rho}_c (2\bar{\rho}_c - \bar{\rho}_t)}{2(2\bar{\rho}_t - \bar{\rho}_c)^2} \quad (\text{B.13})$$

$$b = \frac{\sqrt{3}}{2\bar{\rho}_c \bar{\rho}_t} e + \frac{3\bar{\rho}_c (5\bar{\rho}_t - 4\bar{\rho}_c)}{2(2\bar{\rho}_t - \bar{\rho}_c)^2} \quad (\text{B.14})$$

$$c = -\frac{\sqrt{3}}{2\bar{\rho}_c} e - \frac{3\bar{\rho}_c \bar{\rho}_t (5\bar{\rho}_t - 4\bar{\rho}_c)}{2(2\bar{\rho}_t - \bar{\rho}_c)^2} \quad \text{and} \quad (\text{B.15})$$

$$d = -\frac{(\bar{\rho}_t + 2\bar{\rho}_c)}{2\bar{\rho}_c \bar{\rho}_t} e - \frac{3\bar{\rho}_c \bar{\rho}_t (2\bar{\rho}_c - \bar{\rho}_t)}{2(2\bar{\rho}_t - \bar{\rho}_c)^2} \quad (\text{B.16})$$

Experimental results of Launay and Gachon [21,30,55] are used to find a suitable value for the parameter e by means of regression analysis. It is found that $e = 0$ produces the best fit for these data. Substituting for e in Eq's. B.13 to B.16 results in the following parameters

$$a = \frac{3\bar{\rho}_c (2\bar{\rho}_c - \bar{\rho}_t)}{2(2\bar{\rho}_t - \bar{\rho}_c)^2} \quad (\text{B.17})$$

$$b = \frac{\sqrt{3}\bar{\rho}_c (5\bar{\rho}_t - 4\bar{\rho}_c)}{2(2\bar{\rho}_t - \bar{\rho}_c)^2} \quad (\text{B.18})$$

$$c = -\bar{\rho}_t b \quad (\text{B.19})$$

$$d = -\bar{\rho}_c a \quad \text{and} \quad (\text{B.20})$$

$$e = 0 \quad (\text{B.21})$$

The polar equation of the ellipse is obtained by substituting Eq's. B.17 and B.18 in Eq. B.1 and replacing X and Y by $\bar{\rho}_u \sin \theta$ and $\bar{\rho}_u \cos \theta$ respectively. This yields the polar equation as follows

$$\bar{p}_u = \bar{p}_t \frac{A \cos\theta + B \sin\theta}{A \cos^2\theta + B \sin\theta \cos\theta + \sin^2\theta} \quad (\text{B.22})$$

where $A = a$, and

$B = b$

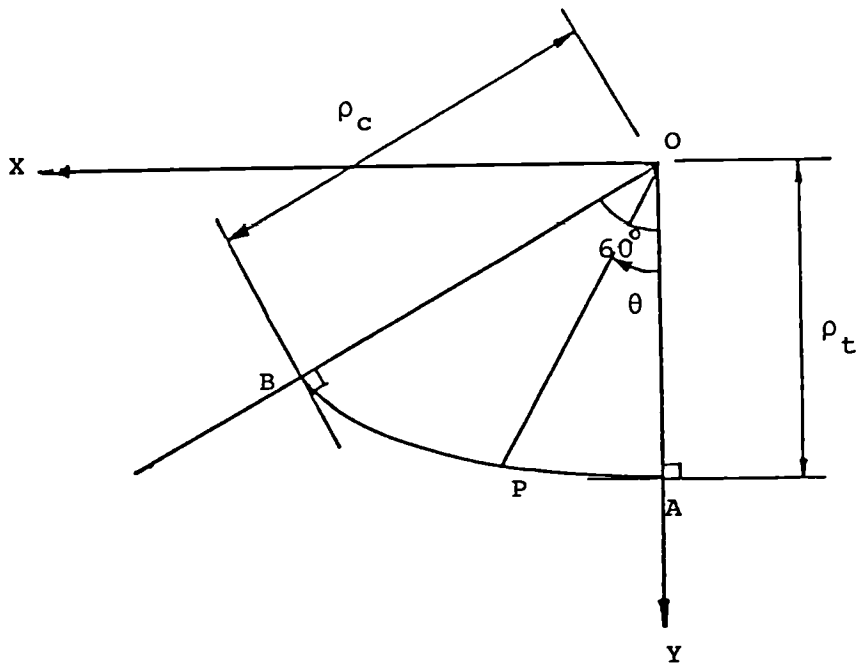


Fig. B.1 Geometry of the proposed elliptic yield surface.

DERIVATION OF ϵ_p IN TERMS OF OCTAHEDRAL STRAINS

C.1 Derivation of ϵ_p

The expression for the effective plastic strain, ϵ_p , could be written as

$$\begin{aligned} \epsilon_p &= \sqrt{\epsilon_{ij}^p \epsilon_{ij}^p} \\ &= \sqrt{\epsilon_1^{p2} + \epsilon_2^{p2} + \epsilon_3^{p2}} \end{aligned} \quad (C.1)$$

where $\epsilon_1^p, \epsilon_2^p, \epsilon_3^p$ = plastic principal strains

Plastic octahedral normal and shear strains are defined as

$$\epsilon_0^p = \frac{\epsilon_1^p + \epsilon_2^p + \epsilon_3^p}{3} \quad (C.2)$$

$$\gamma_0^p = \frac{1}{3} \sqrt{(\epsilon_1^p - \epsilon_2^p)^2 + (\epsilon_2^p - \epsilon_3^p)^2 + (\epsilon_3^p - \epsilon_1^p)^2} \quad (C.3)$$

Eq's. C.2 and C.3 can be written as

$$\epsilon_0^{p2} = [\epsilon_1^{p2} + \epsilon_2^{p2} + \epsilon_3^{p2} + 2(\epsilon_1^p \epsilon_2^p + \epsilon_2^p \epsilon_3^p + \epsilon_3^p \epsilon_1^p)]/9 \quad (C.4)$$

$$\gamma_0^{p2} = 2[\epsilon_1^{p2} + \epsilon_2^{p2} + \epsilon_3^{p2} - (\epsilon_1^p \epsilon_2^p + \epsilon_2^p \epsilon_3^p + \epsilon_3^p \epsilon_1^p)]/9 \quad (C.5)$$

Adding Eq's. C.4 and C.5 and using Eq. C.1 yields

$$\epsilon_p = \sqrt{3(\epsilon_0^p{}^2 + \epsilon_0^p{}^2)} \quad (\text{C.6})$$

A P P E N D I X D

DERIVATIVES OF YIELD SURFACE AND EXPRESSIONS FOR , , AND

D.1 Derivatives of Yield Surface

Equation of the yield surface is expressed as

$$f(\sigma_{ij}, \beta) = \rho - \beta f_{cu} \bar{\rho}_u = 0 \quad (D.1)$$

where $\bar{\rho}_u = \bar{\rho}_u(\bar{\xi}_u, \theta)$,

$$\bar{\xi}_u = \frac{\bar{\xi}}{\beta}, \text{ and}$$

alternatively

$$f(\sigma_{ij}, \beta) = 2J_2 - \beta f_{cu} \bar{\rho}_u(I_1, J_2, J_3, \beta) \quad (D.2)$$

The expression for $\bar{\rho}_u$ is given as

$$\bar{\rho}_u = \bar{\rho}_u(\bar{\xi}_u, \theta) = \bar{\rho}_t \frac{A \cos\theta + B \sin\theta}{A \cos^2\theta + B \sin\theta \cos\theta + \sin^2\theta} \quad (D.3)$$

where $A = \frac{3\bar{\rho}_c(2\bar{\rho}_c - \bar{\rho}_t)}{2(2\bar{\rho}_t - \bar{\rho}_c)^2}$,

$$B = \frac{\sqrt{3}\bar{\rho}_c(5\bar{\rho}_t - 4\bar{\rho}_c)}{2(2\bar{\rho}_t - \bar{\rho}_c)^2},$$

$$\left. \begin{aligned} \bar{\rho}_t &= a_1 + a_2 \sqrt{a_3 + a_4 \bar{\xi}_u} \\ \bar{\rho}_c &= b_1 + b_2 \sqrt{b_3 + b_4 \bar{\xi}_u} \end{aligned} \right\} \text{for } \bar{\xi}_T \geq \bar{\xi}_u > \bar{\xi}_1,$$

$$\left. \begin{aligned} \bar{\rho}_t &= \bar{\rho}_{t1} \sqrt{1 - \left(\frac{\bar{\xi}_u - \bar{\xi}_1}{\bar{\xi}_1 - \bar{\xi}_C} \right)^2} \\ \bar{\rho}_c &= \bar{\rho}_{c1} \sqrt{1 - \left(\frac{\bar{\xi}_u - \bar{\xi}_1}{\bar{\xi}_1 - \bar{\xi}_C} \right)^2} \end{aligned} \right\} \text{for } \bar{\xi}_1 \geq \bar{\xi}_u > \bar{\xi}_C,$$

$a_1, a_2, a_3, a_4, b_1, b_2, b_3$ and b_4 = material constants ,

$$\bar{\xi} = \frac{I_1}{\sqrt{3} f_{cu}},$$

$$\bar{\rho} = \sqrt{2J_2},$$

$$\theta = \frac{1}{3} \cos^{-1} \left(\frac{3\sqrt{3}}{2} \frac{J_3}{J_2^{3/2}} \right),$$

$$I_1 = \sigma_{kk},$$

$$J_2 = \frac{1}{2} s_{ij} s_{ji},$$

$$J_3 = \frac{1}{3} s_{ij} s_{jk} s_{ki},$$

$$s_{ij} = \sigma_{ij} - \delta_{ij} \sigma_{kk} / 3, \text{ and}$$

$$\delta_{ij} = \text{Kronecker delta}$$

Eq. D.3 could be written as

$$\bar{\rho}_u = \frac{M}{N} \quad (D.4)$$

where $M = (A \cos\theta + B \sin\theta)\bar{\rho}_t$, and
 $N = A \cos^2\theta + B \sin\theta \cos\theta + \sin^2\theta$

Taking derivatives of the yield surface, Eq. D.2, with respect to σ_{ij} , yields

$$\frac{\partial f}{\partial \sigma_{ij}} = \frac{\partial f}{\partial I_1} \frac{\partial I_1}{\partial \sigma_{ij}} + \frac{\partial f}{\partial J_2} \frac{\partial J_2}{\partial \sigma_{ij}} + \frac{\partial f}{\partial J_3} \frac{\partial J_3}{\partial \sigma_{ij}} \quad (D.5)$$

Using the chain rule of differentiation, the gradient direction is given as

$$\frac{\partial f}{\partial \sigma_{ij}} = \zeta \frac{\partial I_1}{\partial \sigma_{ij}} + \chi \frac{\partial J_2}{\partial \sigma_{ij}} + \psi \frac{\partial J_3}{\partial \sigma_{ij}} \quad (D.6)$$

where $\zeta = \frac{\partial f}{\partial \bar{\rho}_u} \frac{\partial \bar{\rho}_u}{\partial \xi} \frac{\partial \xi}{\partial I_1}$,

$$\chi = \frac{1}{\sqrt{2J_2}} + \frac{\partial f}{\partial \bar{\rho}_u} \frac{\partial \bar{\rho}_u}{\partial J_2},$$

$$\psi = \frac{\partial f}{\partial \bar{\rho}_u} \frac{\partial \bar{\rho}_u}{\partial J_3},$$

$$\frac{\partial I_1}{\partial \sigma_{ij}} = \delta_{ij},$$

$$\frac{\partial J_2}{\partial \sigma_{ij}} = s_{ij} , \text{ and}$$

$$\frac{\partial J_3}{\partial \sigma_{ij}} = s_{ik}s_{kj} - \frac{2}{3}J_2^\delta_{ij}$$

Therefore

$$\frac{\partial f}{\partial \sigma_{ij}} = \zeta^\delta_{ij} + \chi s_{ij} + \psi (s_{ik}s_{kj} - \frac{2}{3}J_2^\delta_{ij})$$

or

$$\frac{\partial f}{\partial \sigma_{ij}} = \omega^\delta_{ij} + \eta_{ij} \quad (D.7)$$

where

$$\omega = \zeta - \frac{2}{3}\psi J_2 , \text{ and}$$

$$\eta_{ij} = \chi s_{ij} + \psi s_{ik}s_{kj}$$

D.1.1 Calculation of ζ

From Eq. D.6 the expression for ζ is as follows

$$\zeta = \frac{\partial f}{\partial \bar{\rho}_u} \frac{\partial \bar{\rho}_u}{\partial \bar{\xi}} \frac{\partial \bar{\xi}}{\partial I_1} \quad (D.8)$$

Using Eq's. D.2, D.3 and D.4 it is deduced that

$$\frac{\partial f}{\partial \bar{\rho}_u} = -\beta f_{cu} \quad (D.9)$$

$$\frac{\partial \bar{\rho}_u}{\partial \bar{\xi}} = \frac{1}{N^2} \left(\frac{\partial M}{\partial \bar{\xi}} N - \frac{\partial N}{\partial \bar{\xi}} M \right) \quad (D.10)$$

where

$$\frac{\partial M}{\partial \bar{\xi}} = \frac{\partial M}{\partial \bar{\rho}_c} \frac{\partial \bar{\rho}_c}{\partial \bar{\xi}} + \frac{\partial M}{\partial \bar{\rho}_t} \frac{\partial \bar{\rho}_t}{\partial \bar{\xi}} ,$$

$$\frac{\partial N}{\partial \bar{\xi}} = \frac{\partial N}{\partial \bar{\rho}_c} \frac{\partial \bar{\rho}_c}{\partial \bar{\xi}} + \frac{\partial N}{\partial \bar{\rho}_t} \frac{\partial \bar{\rho}_t}{\partial \bar{\xi}} ,$$

$$\frac{\partial M}{\partial \bar{\rho}_c} = \left(\frac{\partial A}{\partial \bar{\rho}_c} \cos\theta + \frac{\partial B}{\partial \bar{\rho}_c} \sin\theta \right) \bar{\rho}_t ,$$

$$\frac{\partial M}{\partial \bar{\rho}_t} = \left(\frac{\partial A}{\partial \bar{\rho}_t} \cos\theta + \frac{\partial B}{\partial \bar{\rho}_t} \sin\theta \right) \bar{\rho}_t + A \cos\theta + B \sin\theta ,$$

$$\frac{\partial N}{\partial \bar{\rho}_c} = \frac{\partial A}{\partial \bar{\rho}_c} \cos^2\theta + \frac{\partial B}{\partial \bar{\rho}_c} \sin\theta \cos\theta ,$$

$$\frac{\partial N}{\partial \bar{\rho}_t} = \frac{\partial A}{\partial \bar{\rho}_t} \cos^2\theta + \frac{\partial B}{\partial \bar{\rho}_t} \sin\theta \cos\theta ,$$

$$\frac{\partial A}{\partial \bar{\rho}_c} = \frac{3[(4\bar{\rho}_c - \bar{\rho}_t)(2\bar{\rho}_t - \bar{\rho}_c) + 2\bar{\rho}_c(2\bar{\rho}_c - \bar{\rho}_t)]}{2(2\bar{\rho}_t - \bar{\rho}_c)^3} ,$$

$$\frac{\partial B}{\partial \bar{\rho}_c} = \frac{3[(5\bar{\rho}_t - 8\bar{\rho}_c)(2\bar{\rho}_t - \bar{\rho}_c) + 2\bar{\rho}_c(5\bar{\rho}_t - 4\bar{\rho}_c)]}{2(2\bar{\rho}_t - \bar{\rho}_c)^3} ,$$

$$\frac{\partial A}{\partial \bar{\rho}_t} = \frac{-3\bar{\rho}_c(7\bar{\rho}_c - 2\bar{\rho}_t)}{2(2\bar{\rho}_t - \bar{\rho}_c)^3} ,$$

$$\frac{\partial B}{\partial \bar{\rho}_t} = \frac{\sqrt{3}\bar{\rho}_c(10\bar{\rho}_c - 11\bar{\rho}_t)}{2(2\bar{\rho}_t - \bar{\rho}_c)^3} , \text{ and}$$

$$\left. \begin{aligned} \frac{\partial \bar{\rho}_t}{\partial \bar{\xi}} &= \frac{a_2 a_4}{2\beta \sqrt{a_3 + a_4 \bar{\rho}_u}} \\ \frac{\partial \bar{\rho}_c}{\partial \bar{\xi}} &= \frac{b_2 b_4}{2\beta \sqrt{b_3 + b_4 \bar{\rho}_u}} \end{aligned} \right\} \text{for } \bar{\xi}_T \geq \bar{\xi}_u > \bar{\xi}_1$$

$$\left. \begin{aligned} \frac{\partial \bar{\rho}_t}{\partial \bar{\xi}} &= - \frac{\bar{\rho}_{t1}^2 (\bar{\xi}_u - \bar{\xi}_1)}{\beta \bar{\rho}_t (\bar{\xi}_1 - \bar{\xi}_c)^2} \\ \frac{\partial \bar{\rho}_c}{\partial \bar{\xi}} &= - \frac{\bar{\rho}_{c1}^2 (\bar{\xi}_u - \bar{\xi}_1)}{\beta \bar{\rho}_c (\bar{\xi}_1 - \bar{\xi}_c)^2} \end{aligned} \right\} \text{for } \bar{\xi}_1 \geq \bar{\xi}_u > \bar{\xi}_c$$

and

$$\frac{\partial \bar{\xi}}{\partial I_1} = \frac{1}{\sqrt{3} f_{cu}} \quad (\text{D.11})$$

D.1.2 Calculation of χ

From Eq. D.6 the expression for χ is as follows

$$\chi = \frac{1}{\sqrt{2} J_2} + \frac{\partial f}{\partial \bar{\rho}_u} \frac{\partial \bar{\rho}_u}{\partial J_2} \quad (\text{D.12})$$

The expression for $\partial f / \partial \bar{\rho}_u$ is obtained from Eq. D.9. Using Eq's. D.3 and D.4 yields

$$\frac{\partial \bar{\rho}_u}{\partial J_2} = \frac{1}{N^2} \left(\frac{\partial M}{\partial J_2} N - \frac{\partial N}{\partial J_2} M \right) \quad (\text{D.13})$$

where

$$\frac{\partial M}{\partial J_2} = \left(\frac{\partial \cos \theta}{\partial J_2} A + \frac{\partial \sin \theta}{\partial J_2} B \right) \bar{p}_t ,$$

$$\frac{\partial N}{\partial J_2} = \frac{\partial \cos^2 \theta}{\partial J_2} A + \frac{\partial \sin \theta \cos \theta}{\partial J_2} B + \frac{\partial \sin^2 \theta}{\partial J_2} ,$$

$$\frac{\partial \cos \theta}{\partial J_2} = -\sin \theta \frac{\partial \theta}{\partial J_2} ,$$

$$\frac{\partial \sin \theta}{\partial J_2} = \cos \theta \frac{\partial \theta}{\partial J_2} ,$$

$$\frac{\partial \cos^2 \theta}{\partial J_2} = -\sin 2\theta \frac{\partial \theta}{\partial J_2} ,$$

$$\frac{\partial \sin^2 \theta}{\partial J_2} = \sin 2\theta \frac{\partial \theta}{\partial J_2} ,$$

$$\frac{\partial \sin \theta \cos \theta}{\partial J_2} = \cos 2\theta \frac{\partial \theta}{\partial J_2} , \text{ and}$$

$$\frac{\partial \theta}{\partial J_2} = -\frac{3\sqrt{3}}{2} \frac{J_3}{J_2^{5/2}} \frac{1}{\sin 3\theta}$$

It should be noted that as $\theta \rightarrow 0^\circ$ or $\theta \rightarrow 60^\circ$, $\frac{\partial \bar{p}_u}{\partial J_2} \rightarrow \frac{0}{0}$,

therefore, from L'hospital rule

$$\text{if } \frac{\partial \bar{p}_u}{\partial J_2} = \frac{f(\theta)}{g(\theta)}$$

where $f(\theta), g(\theta) = \text{functions of } \theta$

the limit of the function when $\theta \rightarrow a$ is given by

$$\lim_{\theta \rightarrow a} \frac{\partial \bar{\rho}_u}{\partial J_2} = \frac{\frac{df(\theta)}{d\theta}}{\frac{dg(\theta)}{d\theta}}$$

Carrying out differentiation and substituting for θ gives

when $\theta \rightarrow 0^\circ$

$$\frac{\partial \bar{\rho}_u}{\partial J_2} \rightarrow \frac{\sqrt{3}}{4} \frac{J_3}{J_2^{5/4}} \bar{\rho}_t \frac{A-2}{A} \quad (D.14)$$

when $\theta \rightarrow 60^\circ$

$$\frac{\partial \bar{\rho}_u}{\partial J_2} \rightarrow -\frac{\sqrt{3}}{2} \frac{J_3}{J_2^{5/4}} \bar{\rho}_t \frac{-5A^2+9B^2-2\sqrt{3}AB+A+\sqrt{3}B}{(A+\sqrt{3}B+3)^2} \quad (D.15)$$

Limiting values of χ at boundaries $\theta = 0^\circ$ and 60° may be obtained by using Eq's. D.14 and D.15 in Eq. D.12.

D.1.3 Calculation of ψ

From Eq. D.6 the expression for ψ is given as follows

$$\psi = \frac{\partial f}{\partial \bar{\rho}_u} \frac{\partial \bar{\rho}_u}{\partial J_3} \quad (D.16)$$

The expression for $\frac{\partial f}{\partial \bar{\rho}_u}$ is obtained from Eq. D.9. Using Eq's. D.4 and D.3 yields

$$\frac{\partial \bar{\rho}_u}{\partial J_3} = \frac{1}{N^2} \left(\frac{\partial M}{\partial J_3} N - \frac{\partial N}{\partial J_3} M \right) \quad (D.17)$$

where
$$\frac{\partial M}{\partial J_3} = \frac{\partial \cos \theta}{\partial J_3} A + \frac{\partial \sin \theta}{\partial J_3} B \bar{\rho}_t ,$$

$$\frac{\partial N}{\partial J_3} = \frac{\partial \cos^2 \theta}{\partial J_3} A + \frac{\partial \sin \theta \cos \theta}{\partial J_3} B + \frac{\partial \sin^2 \theta}{\partial J_3} , \text{ and}$$

The expressions for $\frac{\partial \cos \theta}{\partial J_2}$, $\frac{\partial \sin \theta}{\partial J_2}$, $\frac{\partial \cos^2 \theta}{\partial J_2}$, $\frac{\partial \sin^2 \theta}{\partial J_2}$, $\frac{\partial \sin \theta \cos \theta}{\partial J_2}$,

are obtained in the same way as in Eq. D.13 but replacing $\frac{\partial \theta}{\partial J_2}$

by $\frac{\partial \theta}{\partial J_3}$ where

$$\frac{\partial \theta}{\partial J_3} = \frac{\sqrt{3}}{2} \frac{1}{J_2^{3/2}} \frac{1}{\sin 3\theta} \quad (D.18)$$

It should be noted that as $\theta \rightarrow 0^\circ$ or $\theta \rightarrow 60^\circ$, $\frac{\partial \bar{\rho}_u}{\partial J_3} \rightarrow \frac{0}{0}$,

therefore from L'hospital rule

if
$$\frac{\partial \bar{\rho}_u}{\partial J_3} = \frac{f(\theta)}{g(\theta)}$$

where $f(\theta), g(\theta) = \text{functions of } \theta$

The limit of the function when $\theta \rightarrow a$ is given by

$$\lim_{\theta \rightarrow a} \frac{\partial \bar{\rho}_u}{\partial J_3} = \frac{\frac{df(\theta)}{d\theta}}{\frac{dg(\theta)}{d\theta}}$$

Carrying out differentiation and substituting for θ gives

when $\theta \rightarrow 0^\circ$

$$\frac{\partial \bar{\rho}_u}{\partial J_3} \rightarrow \frac{\sqrt{3}}{6} \frac{1}{J_2^{3/2}} \bar{\rho}_t \frac{A-2}{A} \quad (D.19)$$

when $\theta \rightarrow 60^\circ$

$$\frac{\partial \bar{\rho}_u}{\partial J_3} \rightarrow \frac{\sqrt{3}}{3} \frac{1}{J_2^{3/2}} \bar{\rho}_t \frac{-5A^2+9B^2-2\sqrt{3}AB+A+\sqrt{3}B}{(A+\sqrt{3}B+3)^2} \quad (D.20)$$

Limiting values of ψ at boundaries $\theta = 0^\circ$ and 60° may be obtained by using Eq's. D.19 and D.20 in Eq. D.16.

D.2 Calculation of γ

The relationship for γ is as follows

$$\gamma = - \frac{\partial f}{\partial \beta} \frac{\partial \beta}{\partial \epsilon_p} \quad (D.21)$$

Using Eq's D.2, D.3 and D.4 gives

$$\frac{\partial f}{\partial \beta} = -f_{cu} \left(\bar{\rho}_u + \beta \frac{\partial \bar{\rho}_u}{\partial \beta} \right) \quad (D.22)$$

where
$$\frac{\partial \bar{\rho}_u}{\partial \beta} = \frac{1}{N^2} \left(\frac{\partial M}{\partial \beta} N - \frac{\partial N}{\partial \beta} M \right)$$

$$\frac{\partial M}{\partial \beta} = \frac{\partial M}{\partial \bar{\rho}_c} \frac{\partial \bar{\rho}_c}{\partial \beta} + \frac{\partial M}{\partial \bar{\rho}_t} \frac{\partial \bar{\rho}_t}{\partial \beta},$$

$$\frac{\partial N}{\partial \beta} = \frac{\partial N}{\partial \bar{\rho}_c} \frac{\partial \bar{\rho}_c}{\partial \beta} + \frac{\partial N}{\partial \bar{\rho}_t} \frac{\partial \bar{\rho}_t}{\partial \beta},$$

Expressions for $\frac{\partial M}{\partial \bar{\rho}_c}$, $\frac{\partial M}{\partial \bar{\rho}_t}$, $\frac{\partial N}{\partial \bar{\rho}_c}$ and $\frac{\partial N}{\partial \bar{\rho}_t}$ are given in section

D.1.1. The other derivatives in Eq. D.22 are obtained by differentiating Eq. D.3 as follows

$$\left. \begin{aligned} \frac{\partial \bar{\rho}_t}{\partial \beta} &= \frac{-a_2 a_4 \bar{\xi}_u}{2\beta \sqrt{a_3 + a_4 \bar{\rho}_u}} \\ \frac{\partial \bar{\rho}_c}{\partial \beta} &= \frac{-b_2 b_4 \bar{\xi}_u}{2\beta \sqrt{b_3 + b_4 \bar{\rho}_u}} \end{aligned} \right\} \text{for } \bar{\xi}_T \geq \bar{\xi}_u > \bar{\xi}_1$$

and

$$\left. \begin{aligned} \frac{\partial \bar{\rho}_t}{\partial \beta} &= - \frac{\bar{\rho}_{t1}^2 (\bar{\xi}_u - \bar{\xi}_1) \bar{\xi}_u}{\beta \bar{\rho}_t (\bar{\xi}_1 - \bar{\xi}_c)^2} \\ \frac{\partial \bar{\rho}_c}{\partial \beta} &= - \frac{\bar{\rho}_{c1}^2 (\bar{\xi}_u - \bar{\xi}_1) \bar{\xi}_u}{\beta \bar{\rho}_c (\bar{\xi}_1 - \bar{\xi}_c)^2} \end{aligned} \right\} \text{for } \bar{\xi}_1 \geq \bar{\xi}_u > \bar{\xi}_c$$

As discussed in section 3.5 (Chapter Three) the expression for the hardening parameter β , is derived from the following expressions

$$\beta = c_1 + c_2 X + c_3 X^2 + c_4 X^4 \quad \text{for } 0 \leq X \leq 1.0 \quad (\text{D.23})$$

$$\beta = e^{-c_5 \left(1.0 - \frac{1}{X}\right)^{c_6}} \quad \text{for } X > 1.0 \quad (\text{D.24})$$

where $X = \frac{\epsilon_p}{\epsilon_{p,u}}$
 ϵ_p = effective plastic strain,
 $\epsilon_{p,u}$ = effective plastic strain at peak stress,
 c_1, c_2, c_3, c_4, c_5 and c_6 = material constants
 (see Chapter Three)

Differentiation of the above equations yields

$$\frac{\partial \beta}{\partial \epsilon_p} = \frac{(c_2 + 2c_3 X + 4c_4 X^3)}{\epsilon_{p,u}} \quad \text{for } 0 < X \leq 1.0 \quad (\text{D.25})$$

$$\frac{\partial \beta}{\partial \epsilon_p} = \frac{c_7 (1.0 - X^{-1})^{c_8}}{\epsilon_{p,u} X^2 e^{c_5 (1.0 - X^{-1})^{c_6}}} \quad \text{for } X > 1.0 \quad (\text{D.26})$$

where $c_7 = -c_5 c_6$ and
 $c_8 = c_6 - 1.0$

A P P E N D I X E

DERIVATION OF TENSORIAL ELASTIC-PLASTIC MODULAR MARTIX

E.1 Derivation of Tensorial D-Matrix

The incremental stress-strain relationship of concrete derived in section 3.6 is given by

$$d\sigma_{ij} = \left[D_{ijkl}^e - \frac{D_{ijmn}^e \frac{\partial g}{\partial \sigma_{mn}} \frac{\partial f^T}{\partial \sigma_{rs}} D_{rskl}^e}{h + \frac{\partial f^T}{\partial \sigma_{mn}} D_{mnr s}^e \frac{\partial g}{\partial \sigma_{rs}}} \right] d\epsilon_{kl} \quad (E.1)$$

where $d\sigma_{ij}$ = tensor of stress increment ,
 $d\epsilon_{kl}$ = tensor of strain increment ,
 D_{ijkl}^e = elastic modular matrix ,
 $\frac{\partial f}{\partial \sigma_{ij}}$ = gradient direction of the yield surface,
 $\frac{\partial g}{\partial \sigma_{ij}}$ = gradient direction of the plastic potential surface , and

$$h = \gamma \sqrt{\frac{\partial g}{\partial \sigma_{uv}} \frac{\partial g^T}{\partial \sigma_{uv}}}$$

Assuming associate flow rule, it is required that

$$g = f \quad \text{and} \quad \frac{\partial g}{\partial \sigma_{ij}} = \frac{\partial f}{\partial \sigma_{ij}}$$

E.1.1 Calculation of $D_{ijmn}^e \frac{\partial f}{\partial \sigma_{mn}} \frac{\partial f^T}{\partial \sigma_{rs}} D_{rskl}^e$

The elastic modular matrix D_{ijkl}^e and yield surface gradient could be written in matrix form as follows

$$D_{ijmn}^e = \frac{E}{(1-\nu)(1-2\nu)} \begin{pmatrix} 1-\nu & \nu & 0 & 0 & 0 \\ & 1-\nu & \nu & 0 & 0 & 0 \\ & & 1-\nu & 0 & 0 & 0 \\ \text{Symm.} & & & (1-2\nu)/2 & 0 & 0 \\ & & & & (1-2\nu)/2 & 0 \\ & & & & & (1-2\nu)/2 \end{pmatrix} \quad (\text{E.2})$$

$$\frac{\partial f}{\partial \sigma_{mn}} = \begin{pmatrix} \omega + \eta_{11} \\ \omega + \eta_{22} \\ \omega + \eta_{33} \\ \eta_{12} \\ \eta_{23} \\ \eta_{31} \end{pmatrix} \quad (\text{E.3})$$

where E = Young's modulus ,

ν = Poisson's ratio ,

$$\omega = \zeta - \frac{2}{3} J_2 ,$$

$$\eta_{ij} = \chi s_{ij} + \psi s_{ik} s_{kj} ,$$

J_2 = second invariant of stress deviator, s_{ij} ,

s_{ij} = stress deviator tensor, and

ζ , χ and ψ = given in Appendix D

After some algebra manipulation it can be proved that

$$\eta_{11} + \eta_{22} + \eta_{33} = 2\psi J_2 \quad (\text{E.4})$$

Multiplying Eq. E.2 by Eq. E.3 and substituting Eq. E.4 in the resulting product, yields

$$D_{ijmn}^e \frac{\partial f}{\partial \sigma_{mn}} = \frac{E}{(1-\nu)(1-2\nu)} \left\{ \begin{array}{l} (1+\nu)\omega + 2\psi\nu J_2 + (1-2\nu)\eta_{11} \\ (1+\nu)\omega + 2\psi\nu J_2 + (1-2\nu)\eta_{22} \\ (1+\nu)\omega + 2\psi\nu J_2 + (1-2\nu)\eta_{33} \\ \frac{1}{2}(1-2\nu)\eta_{12} \\ \frac{1}{2}(1-2\nu)\eta_{23} \\ \frac{1}{2}(1-2\nu)\eta_{31} \end{array} \right\} \quad (\text{E.5})$$

Using tensor notation ,Eq. E.5 can be written as

$$D_{ijmn}^e \frac{\partial f}{\partial \sigma_{mn}} = \frac{E}{(1-\nu)(1-2\nu)} \left\{ [(1+\nu) + 2\psi\nu J_2] \delta_{ij} + \frac{1}{2}(1-2\nu)(\delta_{ij} + 1)\eta_{ij} \right\} \quad (\text{E.6})$$

Similarly

$$\frac{\partial f^T}{\partial \sigma_{rs}} D_{rskl}^e = \frac{E}{(1-\nu)(1-2\nu)} \left\{ [(1+\nu) + 2\psi\nu J_2] \delta_{kl} + \frac{1}{2}(1-2\nu)(\delta_{kl} + 1)\eta_{kl} \right\} \quad (\text{E.7})$$

Multiplying Eq. E.6 by Eq. E.7 gives

$$D_{ijmn}^e \frac{\partial f}{\partial \sigma_{mn}} \frac{\partial f^T}{\partial \sigma_{rs}} D_{rskl}^e =$$

$$\left[\frac{E}{(1-\nu)(1-2\nu)} \right]^2 \{ \kappa_1 \delta_{ij} \delta_{kl} + \kappa_2 [(\delta_{ij}+1)\delta_{kl} \eta_{ij} + (\delta_{kl}+1)\delta_{ij} \eta_{kl}] + \kappa_3 (\delta_{ij}+1)(\delta_{kl}+1) \eta_{ij} \eta_{kl} \} \quad (E.8)$$

where

$$\begin{aligned} \kappa_1 &= [(1+\nu) + 2\psi\nu J_2]^2 \\ \kappa_2 &= (1-2\nu)[(1+\nu)\omega + 2\psi\nu J_2]/2 \\ \kappa_3 &= (1-2\nu)^2/4 \end{aligned}$$

E.1.2 Calculation of $\frac{\partial f^T}{\partial \sigma_{mn}} D_{mnr}^e \frac{\partial f}{\partial \sigma_{rs}}$

The product of $D_{mnr}^e \frac{\partial f}{\partial \sigma_{rs}}$ may be obtained in the same way as

the derivation in section E.1.1. Multiplying Eq. E.5 by $\frac{\partial f^T}{\partial \sigma_{mn}}$

and making use of Eq. E.4 gives

$$\frac{\partial f^T}{\partial \sigma_{mn}} D_{mnr}^e \frac{\partial f}{\partial \sigma_{rs}} =$$

$$\frac{E}{(1-\nu)(1-2\nu)} [(1+\nu)(3\omega + 4\psi J_2)\omega + 4(1-\nu)\psi^2 J_2^2 + (1-2\nu)J_4] \quad (E.9)$$

where

$$J_4 = \frac{1}{2}(\eta_{12}^2 + \eta_{23}^2 + \eta_{31}^2) - 2(\eta_{11}\eta_{22} + \eta_{22}\eta_{33} + \eta_{33}\eta_{11})$$

E.1.3 Calculation of h

The expression for h is given in Eq. E.1 as

$$h = \gamma \sqrt{\frac{\partial f}{\partial \sigma_{uv}} \frac{\partial f^T}{\partial \sigma_{uv}}} \quad (\text{E.10})$$

where $\gamma = - \frac{\partial f}{\partial \beta} \frac{\partial \beta}{\partial \epsilon_p}$ (see Appendix D)

The second part of Eq. E.10 is written as

$$\frac{\partial f}{\partial \sigma_{uv}} \frac{\partial f^T}{\partial \sigma_{uv}} = \begin{Bmatrix} \omega + \eta_{11} \\ \omega + \eta_{22} \\ \omega + \eta_{33} \\ \eta_{12} \\ \eta_{23} \\ \eta_{31} \end{Bmatrix} \left\langle \begin{matrix} \omega + \eta_{11} & \omega + \eta_{22} & \omega + \eta_{33} & \eta_{12} & \eta_{23} & \eta_{31} \end{matrix} \right\rangle \quad (\text{E.11})$$

Carrying out multiplication of Eq. E.11 and using Eq. E.4 gives

$$\frac{\partial f}{\partial \sigma_{uv}} \frac{\partial f^T}{\partial \sigma_{uv}} = (3\omega + 4\psi J_2)\omega + 4\psi^2 J_2 + J_5 \quad (\text{E.12})$$

where $J_5 = J_4 + \frac{1}{2}(\eta_{12}^2 + \eta_{23}^2 + \eta_{31}^2)$

Therefore

$$h = \gamma \sqrt{(3\omega + 4\psi J_2)\omega + 4\psi^2 J_2 + J_5} \quad (\text{E.13})$$

E.1.4 Elastic-Plastic Modular Matrix

It has been discussed in section 3.6 that the elastic-plastic modular matrix can be decomposed into elastic and plastic matrices as

$$D_{ijkl}^{ep} = D_{ijkl}^e - D_{ijkl}^p \quad (E.14)$$

$$D_{ijkl}^e = \frac{E}{(1+\nu)(1-2\nu)} C_{ijkl} \quad (E.15)$$

where

$$C_{ijkl} = \frac{1}{2}(1-2\nu)(\delta_{ik}\delta_{jl} + \delta_{il}\delta_{jk}) + \nu\delta_{ij}\delta_{kl} ,$$

E = Young's modulus ,and

ν = Poisson's ratio

Using Eq's. E.8, E.9 and E.13, the plastic modular matrix is expressed as

$$D_{ijkl}^p = \frac{E}{(1+\nu)(1-2\nu)} \mu \phi_{ijkl} \quad (E.16)$$

where

$$\phi_{ijkl} = \kappa_1 \delta_{ij} \delta_{kl} + \kappa_2 [(\delta_{ij}+1)\delta_{kl} \eta_{ij} + (\delta_{kl}+1)\delta_{ij} \eta_{kl}] + \kappa_3 (\delta_{ij}+1)(\delta_{kl}+1) \eta_{ij} \eta_{kl} ,$$

$$\eta_{ij} = \chi^s_{ij} + \psi^s_{im} s_{mj}$$

$$\mu = \frac{E}{\alpha(1+\nu)(1-2\nu)} ,$$

$$\alpha = h + \frac{[(1+\nu)(3\omega+4\psi J_2)\omega+4(1-\nu)\psi^2 J_2^2+(1-2\nu)J_4]}{(1+\nu)(1-2\nu)} E,$$

E = Young's modulus ,and

ν = Poisson's ratio

Substituting for Eq's E.15 and E.16 in Eq. E.14, the elastic-plastic modular matrix is obtained as

$$D^{ep} = \frac{E}{(1+\nu)(1-2\nu)} (C_{ijkl} - \mu \Phi_{ijkl})$$

(E.17)

The incremental elastic-plastic constitutive model for concrete is as follows

$$d\sigma_{ij} = \frac{E}{(1+\nu)(1-2\nu)} (C_{ijkl} - \mu \Phi_{ijkl}) d\epsilon_{kl}$$

(E.18)

**CLASSIFICATION OF DIFFERENT STRESS
ZONES ON THE YIELD SURFACE**

F.1 Introduction

It is required to know the correct state of stress when the stress level reaches the yield surface so that a suitable fracturing procedure can be adopted, e.g. fracture by cracking or crushing of material. A state of stress on the yield surface can be classified into the appropriate stress zones provided the boundaries of the intersection between planes of $\sigma_1 = 0$, $\sigma_2 = 0$ and $\sigma_3 = 0$ with the yield surface are known, Fig. F.1. These boundaries are obtained in the following section .

F.2 Calculation of the Boundaries

Consider the intersection of plane $\sigma_1 = 0$ with the yield surface, Fig. F.2. The points of intersection can be fully defined by the location of points B, C and D in the compressive hydrostatic zone and B', C' and D' in the tensile hydrostatic zone. The intersection points of the planes with one zero principal stress and the yield surface form a π -Plane which is normal to the hydrostatic axis, line $\overline{OO'}$, e.g. points A, B and C or A', B' and C'. A π -Plane is a plane of constant hydrostatic pressure $\bar{\xi}$. The location of the points which lie on a common π -Plane are, therefore, to be defined by the distance of their π -Plane from the origin, i.e. the corresponding value of $\bar{\xi}$.

Consider the two-dimensional representation of the intersection points, Fig. F.3. The locations of A and A' are obtained by the intersection of line $\overline{AA'}$ and meridians $\bar{\rho}_c$ and $\bar{\rho}_t$, respectively. These points correspond to the location of B and C, and B' and C'. The locations of D and D' are obtained by the intersection of the line $\overline{DD'}$ with the meridians $\bar{\rho}_t$ and $\bar{\rho}_c$ respectively. It can be shown that the angle of inclination of $\overline{AA'}$ with the $\bar{\xi}$ -axis (line $\overline{XX'}$) α , using the geometry of tetrahedral OABC, is given by

$$\alpha = \tan^{-1}\sqrt{2} \quad (\text{F.1})$$

Therefore, line $\overline{AA'}$ is defined by

$$\bar{\rho}_{AA'} = \sqrt{2} \bar{\xi} \quad (\text{F.2})$$

The direction of line $\overline{DD'}$ is normal to the direction of line $\overline{AA'}$. The equation of line $\overline{DD'}$ is, therefore, as follows

$$\bar{\rho}_{DD'} = -\frac{1}{\sqrt{2}} \bar{\xi} \quad (\text{F.3})$$

Intersecting lines given by Eq's. F.2 and F.3 and the hydrostatic tensile and compressive meridians $\bar{\rho}_t$ and $\bar{\rho}_c$ (see Eq's. 3.8 and 3.9, Chapter Three), establishes the following values

i) Location of D'

$$\bar{\xi}_{T1} = (-\sqrt{2}b_1 + b_2^2 b_4) \pm \sqrt{(-\sqrt{2}b_1 + b_2^2 b_4)^2 - 2b_2(b_1 - b_2 b_3)} > 0$$

ii) Location of A', B' and C'

$$\bar{\xi}_{T2} = \frac{1}{4} [(2\sqrt{2}a_1 + a_2^2 a_4) \pm \sqrt{(2\sqrt{2}a_1 + a_2^2 a_4)^2 - 8a_2(a_1 - a_2 a_3)}] > 0$$

iii) Location of A, B and C

$$\bar{\xi}_{C2} = \frac{1}{4} [(2\sqrt{2}b_1 + b_2^2 b_4) \pm \sqrt{(2\sqrt{2}b_1 + b_2^2 b_4)^2 - 8b_2(b_1 - b_2 b_3)}] < 0$$

iv) Location of D

$$\bar{\xi}_{C1} = (-\sqrt{2}a_1 + a_2^2 a_4) \pm \sqrt{(-\sqrt{2}a_1 + a_2^2 a_4)^2 - 2a_2(a_1 - a_2 a_3)} < 0$$

F.3 Classification of the Stress Zones

The classification of the different stress zones on the yield surface may be given as follows assuming $\sigma_1 > \sigma_2 > \sigma_3$, where σ_1 , σ_2 and σ_3 are the principal stresses

Stress Value

State of Stress

$$\bar{\xi} \leq \bar{\xi}_{C1}$$

C C C

$$\bar{\xi}_{C1} < \bar{\xi} \leq \bar{\xi}_{C2} \quad \text{and} \quad \begin{cases} \sigma_1 < 0 \\ \sigma_1 > 0 \end{cases}$$

C C C

T C C

$$\bar{\xi}_{C2} < \bar{\xi} \leq 0$$

T C C

$$0 < \bar{\xi} < \bar{\xi}_{T2}$$

T T C

$$\bar{\xi}_{T2} < \bar{\xi} < \bar{\xi}_{T1} \quad \text{and} \quad \begin{cases} \sigma_3 < 0 \\ \sigma_3 > 0 \end{cases}$$

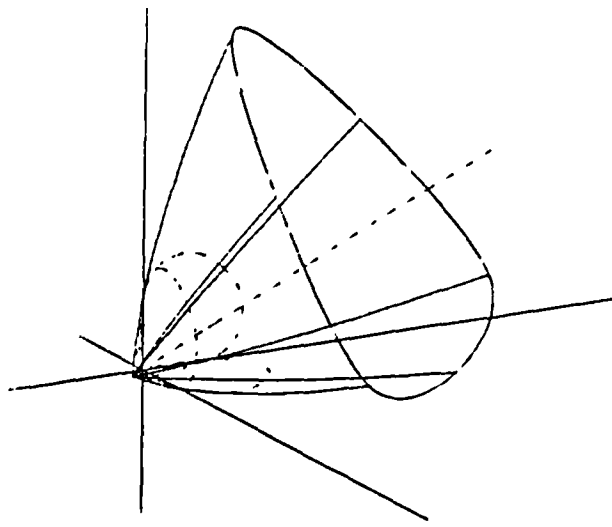
T T C

T T T

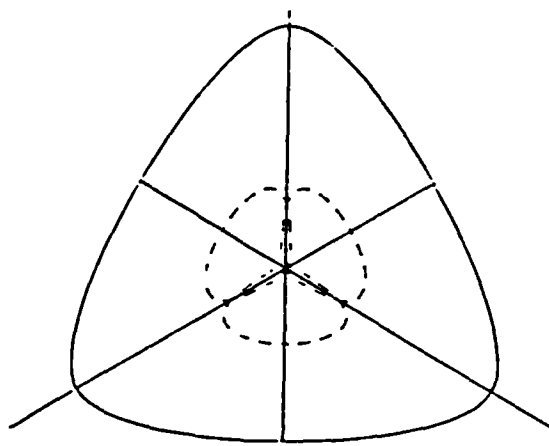
$$\bar{\xi}_{T1} < \bar{\xi}$$

T T T

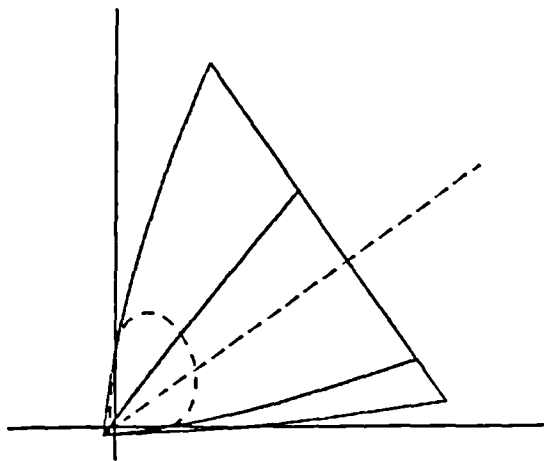
where C = Compression, and
T = Tension



(a) Three-Dimensional View



(b) Deviatoric View



(c) Hydrostatic View

Fig. F.1 Schematic representation of intersection between planes of zero stress and the proposed yield surface.

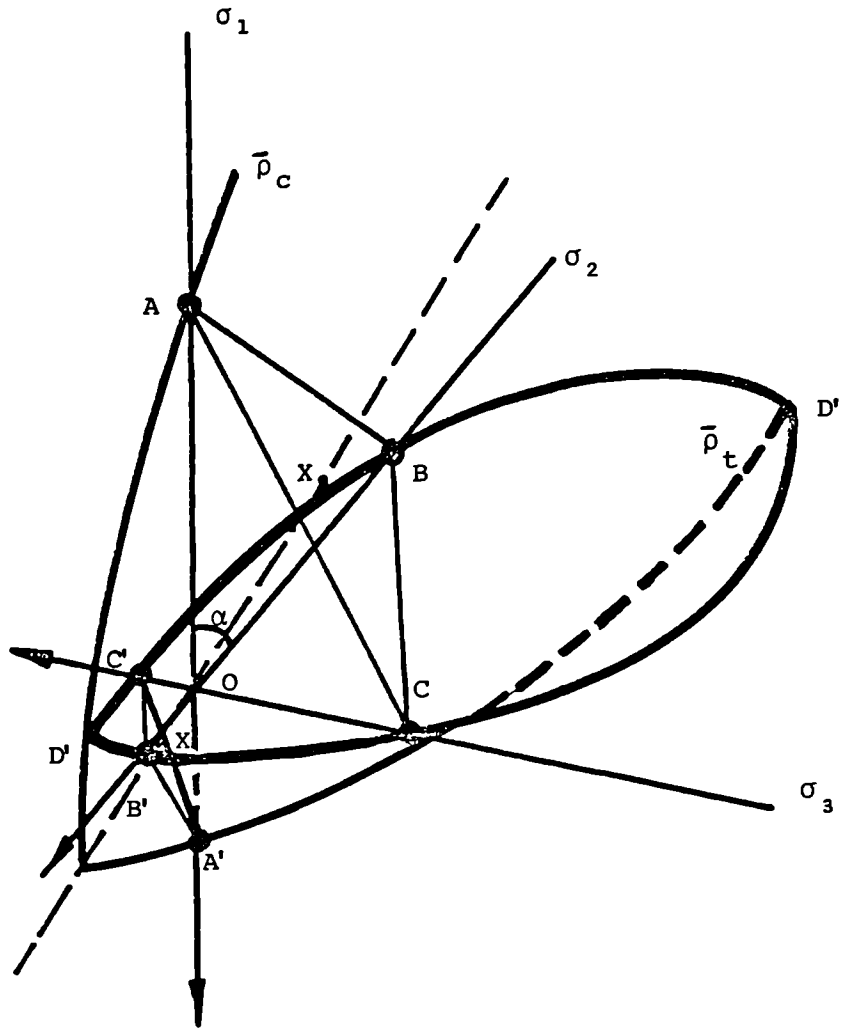


Fig. F.2 Intersection of the plane of $\sigma_1=0$ with the proposed yield surface.

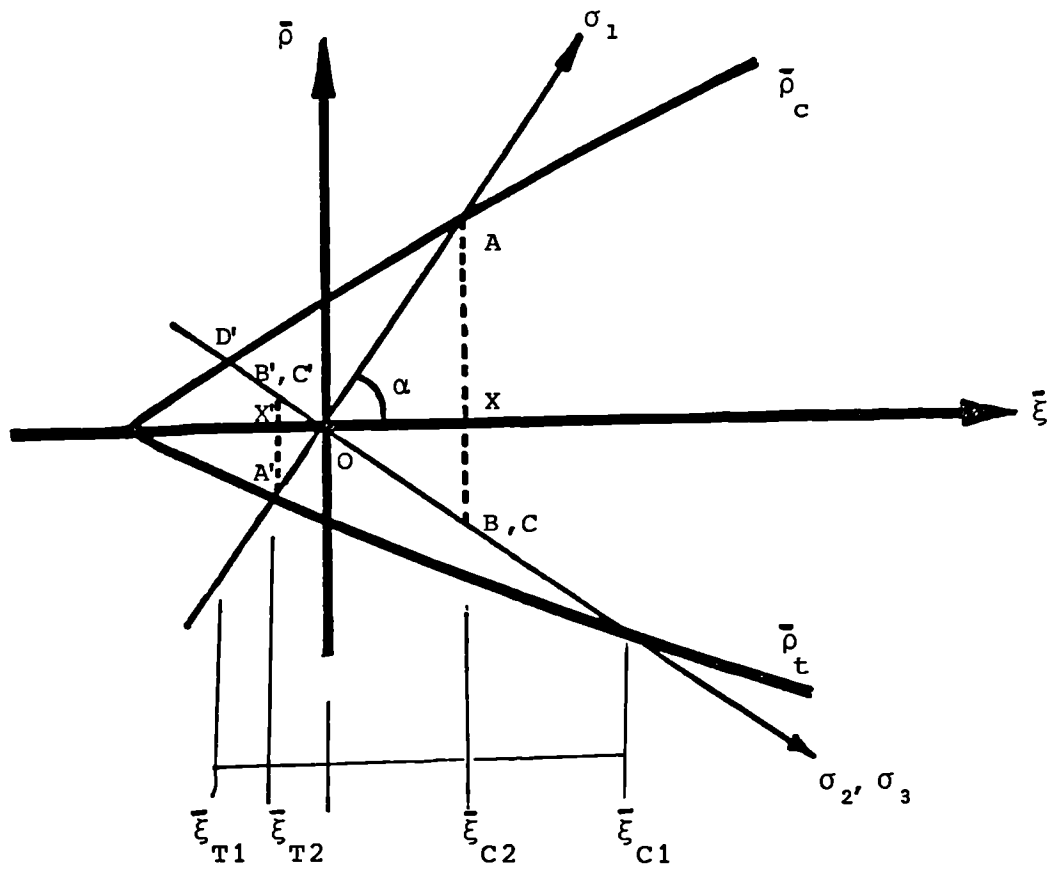


Fig. F.3 Two-dimensional representation of the intersection points on the proposed yield surface.

EXPLICIT EXPRESSIONS FOR CRACK STIFFNESS MATRIX

G.1 Crack Stress-Displacement Relationship

It was discussed in section 4.6.1.2 that crack stresses may be related to crack displacements via a crack stiffness matrix K, as follows

$$\begin{Bmatrix} d\sigma_{nn}^{cr} \\ d\sigma_{nt}^{cr} \end{Bmatrix} = \begin{bmatrix} K_{nn} & K_{nt} \\ K_{tn} & K_{tt} \end{bmatrix} \begin{Bmatrix} d\delta_n \\ d\delta_t \end{Bmatrix} \quad (G.1)$$

where $K_{nn} = \frac{\partial f_n}{\partial \delta_n}$,

$$K_{nt} = \frac{\partial f_n}{\partial \delta_t},$$

$$K_{tt} = \frac{\partial f_t}{\partial \delta_t},$$

$$K_{tn} = \frac{\partial f_t}{\partial \delta_n},$$

$$\sigma_{nt}^{cr} = f_t(\delta_t, \delta_n), \text{ and}$$

$$\sigma_{nn}^{cr} = f_n(\delta_t, \delta_n)$$

The explicit relationships for f_n and f_t are given by Eq's. 4.2a and 4.2b (see Chapter Four).

G.2 Derivation of K_{nn} , K_{nt} , K_{tn} and K_{tt}

The relationships between crack stresses and displacements are given by Eq's. 4.1 and 4.2 as follows

$$\sigma_{nt}^{cr} = \sigma_{nt,u}^{cr} \left(1 - \frac{1}{1 + m_1 \delta_t^{m_2}} \right) \quad (G.2)$$

$$\sigma_{nn}^{cr} = \sigma_{nn,u}^{cr} \left(1 - \frac{1}{1 + n_1 \delta_t^{n_2}} \right) \quad (G.3)$$

where

$$\sigma_{nt,u}^{cr} = \frac{\sigma_{nt,0}^{cr}}{1 + m_3 \delta_n^{m_4}}$$

$$\sigma_{nn,u}^{cr} = \frac{\delta_{nn,0}^{cr}}{1 + n_3 \delta_n^{n_4}}$$

$$\sigma_{nt,0}^{cr} = m_5 f_{cu}^{m_6}$$

$$\sigma_{nn,0}^{cr} = n_5 f_{cu}^{n_6}$$

Differentiating σ_{nn}^{cr} and σ_{nt}^{cr} with respect to δ_n and δ_t , would produce the components of the crack stiffness matrix as follows

$$\begin{aligned}
K_{nn} &= \frac{\partial \sigma_{nn}^{cr}}{\partial \delta_n} \\
&= \frac{[(1+n_3 \delta_n^{n_4}) (n_7 n_8 \delta_n^{n_8-1} + n_1 n_{10} \log \delta_t) - n_1 n_3 n_4 (1+n_1 \delta_t^{n_2}) \delta_n^{n_4-1}] \delta_t^{n_2}}{[(1+n_1 \delta_t^{n_2}) (1+n_3 \delta_n^{n_4})]^2} \sigma_{nn,0}^{cr}
\end{aligned}
\tag{G.4}$$

$$K_{nt} = \frac{\partial \sigma_{nn}^{cr}}{\partial \delta_t} = \frac{n_1 n_2 \delta_t^{n_2-1}}{(1+n_1 \delta_t^{n_2})^2} \sigma_{nn,u}^{cr}
\tag{G.5}$$

$$\begin{aligned}
K_{tn} &= \frac{\partial \sigma_{nt}^{cr}}{\partial \delta_n} \\
&= \frac{[(1+m_3 \delta_n^{m_4}) (m_7 m_8 \delta_n^{m_8-1} + m_1 m_{10} \log \delta_t) - m_1 m_3 m_4 (1+m_1 \delta_t^{m_2}) \delta_n^{m_4-1}] \delta_t^{m_2}}{[(1+m_1 \delta_t^{m_2}) (1+m_3 \delta_n^{m_4})]^2} \sigma_{nt,0}^{cr}
\end{aligned}
\tag{G.6}$$

and

$$K_{tt} = \frac{\partial \sigma_{nt}^{cr}}{\partial \delta_t} = \frac{m_1 m_2 \delta_t^{m_2-1}}{(1+m_1 \delta_t^{m_2})^2} \sigma_{nt,u}^{cr}
\tag{G.7}$$

EXPLICIT EXPRESSIONS FOR DOWEL STIFFNESS MATRIX

H.1 Dowel Force-Displacement Relationship

It was discussed in section 4.6.2.2, that dowel stresses may be related to crack displacements via a dowel stiffness matrix, H, as follows

$$\begin{Bmatrix} d\sigma_{nn}^d \\ d\sigma_{nt}^d \end{Bmatrix} = \begin{bmatrix} H_{nn} & H_{nt} \\ H_{tn} & H_{tt} \end{bmatrix} \begin{Bmatrix} d\delta_n \\ d\delta_t \end{Bmatrix} \quad (H.1)$$

where $H_{nn} = \frac{\partial \sigma_{nn}^d}{\partial \delta_n}$,

$$H_{nt} = \frac{\partial \sigma_{nn}^d}{\partial \delta_t},$$

$$H_{tn} = \frac{\partial \sigma_{nt}^d}{\partial \delta_n},$$

$$H_{tt} = \frac{\partial \sigma_{nt}^d}{\partial \delta_t},$$

$$\sigma_{nt}^d = f_n(\delta_t, \delta_n), \text{ and}$$

$$\sigma_{nt}^d = f_t(\delta_t, \delta_n)$$

The explicit relationships the for f_t and f_n functions above are given by Eq's 4.11 and 4.12 (see Chapter Four).

H.2 Derivation of H_{nn} , H_{nt} , H_{tt} and H_{tn}

The relationships between dowel stresses and crack displacements are given by Eq's. 4.11 and 4.12 as follows

$$\sigma_{nt}^d = \frac{p F_d}{A_b} \quad (H.2)$$

$$\sigma_{nn}^d = \frac{p F_d}{A_b} \tan\theta_{bc} \quad (H.3)$$

where

$$F_d = \frac{R_w t \delta_t^b}{1 + t \delta_t^b} F_{d,u} ,$$

$$R_w = \frac{0.2}{\delta_n + 0.2}$$

t and $F_{d,u}$ = defined in Eq. 4.8 (see Chapter Four)

Differentiating σ_{nn}^d and σ_{nt}^d with respect to δ_n and δ_t respectively, would produce the components of the dowel stiffness matrix H as follows

$$H_{nn} = \frac{\partial \sigma_{nn}^d}{\partial \delta_n} = - \frac{\sigma_{nn}^d}{\delta_n + 0.2} \quad (H.4)$$

$$H_{nt} = \frac{\partial \sigma_{nn}^d}{\partial \delta_t} = \frac{b \sigma_{nn}^d}{\delta_t (1 + t \delta_t^b)} \quad (H.5)$$

$$H_{tn} = \frac{\partial \sigma_{nt}^d}{\partial \delta_n} = \frac{H_{nn}}{\tan\theta_{bc}} \quad (H.6)$$

and

$$H_{tt} = \frac{\partial \sigma_{nt}^d}{\partial \delta_t} = \frac{H_{nt}}{\tan\theta_{bc}} \quad (H.7)$$

A P P E N D I X I

DERIVATION OF THE SLIP FREE LENGTH AND THE TENSION STIFFENING FACTOR

I.1 Derivation of the Slip free Length, L_s

Consider a bar of cross-sectional area A_b , crossing a sharp crack in a block of concrete, Fig. I.1a. The bond stress distribution is non-uniform as shown in Fig. I.1b. The distribution of bond stress is also affected by the normal stresses at the bar-concrete interface. This effect is not included here for simplicity. The idealised uniform bond stress distribution is shown in Fig. I.1c. The actual and idealised shear stress distributions are shown in Fig's. I.1d to e, respectively. By considering the equilibrium conditions along the length of the bar, the steel and concrete stresses at any point along the bar (on the l -axis) may be written as

$$\sigma_s(l) = \sigma_s - \frac{U_b l}{A_b} \quad (I.1)$$

$$\sigma_c(l) = \frac{U_b l}{A_{c1}} \quad (I.2)$$

where

- σ_s = steel stress at crack ,
- $U_b = \pi \phi \tau_b$
= bond force per unit length of bar ,
- ϕ = bar diameter ,
- A_b = cross-sectional area of one bar ,
- $A_{c1} = s_b t_p$,

s_b = bar spacing , and

t_p = plate thickness

The slip free length, L_s , may be obtained from Eq. I.1 by replacing l by L_s to give

$$L_s = \frac{A_b}{U_b} (\sigma_s - \sigma') \quad (I.3)$$

where $\sigma_s' = \sigma_s(L_s)$

The stress σ_s' is obtained from Eq's. I.1 and I.2 by transforming steel and concrete stresses to the corresponding strains and then eliminating $U_b l$ between the resulting equations. The result is as follows

$$E_c \epsilon_c(l) + p E_s \epsilon_s(l) = p \sigma_s \quad (I.4)$$

where $\epsilon_c(l)$ = concrete strain ,

$\epsilon_s(l)$ = steel strain ,

E_c = concrete Young's modulus ,

E_s = steel Young's modulus , and

p = percentage of steel

The strains in steel and concrete are the same at the end of the slipping segment (i.e. L_s from the crack face).
Therefore

$$\epsilon_c(L_s) = \epsilon_s(L_s) \quad (I.5)$$

or

$$\epsilon_c(L_s) = \frac{\sigma_s(L_s)}{E_s} \quad (I.6)$$

It can be deduced from the definition of σ'_s (Eq. I.3) that

$$\epsilon_c(L_s) = \frac{\sigma'_s}{E_s} \quad (I.7)$$

Substituting Eq. I.4 into Eq. I.7 results in

$$\sigma'_s = \frac{np}{1 + np} \sigma_s \quad (I.8)$$

where $n = \frac{E_s}{E_c}$

Combining Eq. I.3 and Eq. I.8 results in

$$L_s = \frac{A_b \sigma_s}{U_b (1 + np)} \quad (I.9)$$

It should be noted that as the stress σ_s increases the slip free length increases until it reaches half the bar length enclosed between two adjacent cracks (L_s approaches $s'/2$).

I.2 Derivation of the Tension Stiffening Factor, α_t

The average steel strain ϵ_s , may be obtained by averaging the total strain in steel enclosed by the cracks over the crack

spacing. This operation may be carried out as follows

$$\epsilon_s = \frac{1}{s'/2} \int_0^{s'/2} \epsilon_s(l) dl \quad (I.10)$$

where l = the distance along the bar measured from
the crack face

The steel strain may be written as follows by rearranging
Eq. I.10

$$\epsilon_s = \frac{1}{s'/2} \int_0^{L_s} \epsilon_s(l) dl + \frac{1}{s'/2} \int_{L_s}^{s'/2} \epsilon_s(l) dl \quad (I.11)$$

Substituting Eq. I.1 and I.8 into Eq. I.11, results

$$\epsilon_s = \frac{2}{s'E_s} \int_0^{L_s} \left(\sigma_s - \frac{U_b}{A_b} \right) dl + \frac{2}{s'E_s} \int_{L_s}^{s'/2} \frac{np}{1+np} \sigma_s dl \quad (I.12)$$

Carrying out the integration, yields

$$\epsilon_s = \frac{2}{s'E_s} \left[\frac{1}{1+np} \sigma_s L_s + \frac{nps'}{2(1+np)} \sigma_s - \frac{U_b}{2A_b} L_s^2 \right] \quad (I.13)$$

Substituting for L_s from Eq. I.9 gives

$$\epsilon_s = \frac{2}{s' E_s} \left[\frac{A_b}{2U_b (1+np)^2} \sigma_s^2 + \frac{np s'}{2(1+np)} \sigma_s \right] \quad (I.14)$$

The incremental constitutive model for steel reinforcement bars with tension-stiffening effect is obtained by differentiating Eq. I.14 with respect to σ_s , therefore

$$d\sigma_s = \frac{s' U_b (1+np)^2}{2A_b \sigma_s + s' U_b np (1+np)} E_s d\epsilon_s \quad (I.15)$$

From Eq. I.15 it can be concluded that steel bar stiffness containing the effect of tension-stiffening E_s^* , is a multiple of the steel tangential stiffness without the effect of tension-stiffening, therefore

$$E_s^* = \alpha_t E_s \quad (I.16)$$

where α_t = the tension-stiffening factor

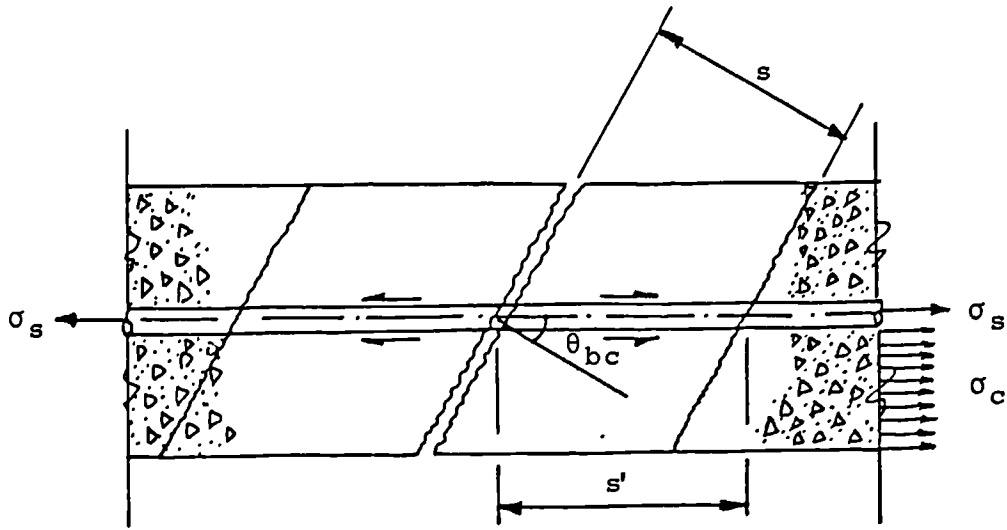
Therefore, α_t is given as follows

$$\alpha_t = \frac{s' U_b (1+np)^2}{2A_b \sigma_s + s' U_b np (1+np)} \quad (I.17)$$

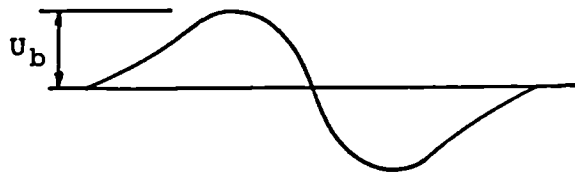
where $s' = \frac{s}{\cos \theta_{bc}}$,

s = crack spacing,

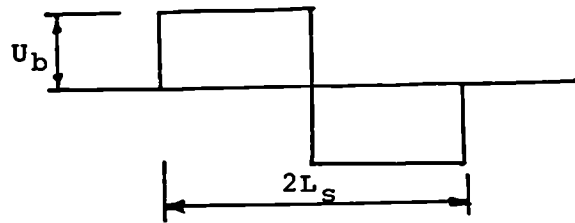
θ_{bc} = angle between the normal to the crack and the reinforcement bar



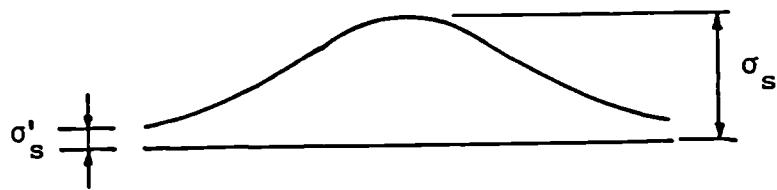
(a) Reinforcement Bar Crossing a Sharp Crack



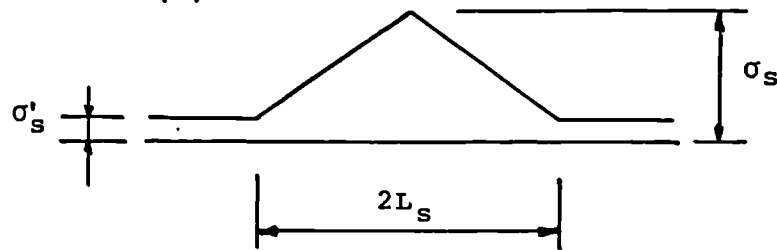
(b) Actual Bond Stress Distribution



(c) Idealised Bond Stress Distribution



(d) Actual Steel Stress Distribution



(e) Idealised Steel Stress Distribution

Fig. I.1 Reinforcement bar crossing a sharp crack and the associated stresses.

REFERENCES

1. Dougill, J.W.,
"On Stable Progressively Fracturing Solid", Zeitschrift
fur Angewandte Mathematik und Physik, Berlin, Germany,
Vol.27, No.4, 1976, pp. 423-431.
2. Bazant, Z.P., and Kim, S.S.,
"Plastic-Fracturing Theory for Concrete", Journal of the
Engineering Mechanics Division, Proceedings of the ASCE,
Vol.105, No.EM3, June 1979, pp. 407-427.
3. Bazant, Z.P.,
"Endochronic Inelasticity and Incremental Plasticity",
International Journal of Solids and Structures, Vol.14,
1978, pp. 691-714.
4. Schapery, R.A.,
"On a Thermodynamic Constitutive Theory and its
Applications to Various Nonlinear Materials", IUTAM
Symposium Kilbride, June 1968, B.A. Boley, ed., Springer
Verlag, New York, 1968.
5. Valanis, K.C.,
"A Theory of Viscoplasticity without a Yield Surface",
Archiwum Mechaniki Stosowanej (Archive of Mechanics,
Warsaw), Vol.23, 1971, pp. 517-551.
6. Bazant, Z.P., and Bhat, P.D.,
"Endochronic Theory of Inelasticity and Failure of
Concrete", Journal of the Engineering Mechanics
Division, Proceedings of the ASCE, Vol.102, No.EM4,
August 1976, pp.701-722.
7. Bazant, Z.P.,
"Work Inequalities for Plastic Fracturing Models",
International Journal of Solids and Structures, Vol.16,
1980, pp. 873-901.

8. **Bazant, Z.P., and Shieh, C.L.,**
"Hysteretic Fracturing Endochronic Theory for Concrete",
Journal of the Engineering Mechanics Division,
Proceedings of the ASCE, Vol.106, No.EM6, October 1980,
pp. 929-950.
9. **Rankine, W.J.M.,**
"On the Stability of Loose Earth", Phil., Transactions,
Royal Society, London 1857.
10. **Tresca, M.H.,**
"Memoire sur l'Ecoulement des Corps Solides Soumis a de
Fortes Pressions", Comptes Rendus des seances de
l'Academie des Sciences, Vol.59, 1864, p. 754.
11. **Von Mises, R.,**
"Mechanik der Plastischen Formanderung von Kristallen",
Zeitschrift fur Angewandte Mathematik und Mechanik,
Vol.8, 1928, pp. 161-185.
12. **Mohr, O.,**
"Welsche Umstande Bedingen die Elastizitatsgrenze und de
Bruch eines Materials", Zeitschrift des Vereines
Deutshcer Ingenieure, Vol.44-II, 1900, pp. 1524-1530,
1572-1577.
13. **Coulomb, C.A.,**
"Essai sur une Application des Regles de Maximis &
Minimis a Quelques Problemes de Statique, Relatifs a
l'Architecture, Memoies de Mathematique & de Physique
Presentes a l'Academie Royale des Sciences, Vol.7, 1776,
pp. 343-382.
14. **Richart, F.E., Brandzaeg, A., and Brown, R.L.,**
"A Study of the Failure of Concrete under Combined
Compressive Stresses", Bulletin No.185, Engineering
Experiment Station, University of Illinois, Urbana,
Illinois, November 1928.
15. **Drucker, D.C., and Prager, W.,**
"Soil Mechanics and Plastic Analysis on Limit Design",
Quarterly of Applied Mathematics, Vol.10, No.2, 1952.

16. **Bresler, B., and Pister, K.S.,**
"Strength of Concrete under Combined Stress", Journal of American Concrete Institute, Proceedings , Vol.55, No.3, September 1958, pp. 321-345.
17. **McHenry, D., and Karni, J.,**
"Strength of Concrete under Combined Tensile and Compressive Stress", Journal of American Concrete Institute, Proceedings , Vol.54, No.10, April 1958, pp. 829-840.
18. **Mikkola, M.J., and Schnobrich, W.C.,**
"Material Behaviour Characteristics for Reinforced Concrete Shells Stressed Beyond the Elastic Range", Civil Engineering Studies, SRS No.367, University of Illinois, Urbana-Champaign, Urbana, Illinois, August 1970.
19. **Bellamy, C.J.,**
"Strength of Concrete under Combined Stresses", Journal of American Concrete Institute, Proceedings , Vol.58, No.4, October 1961, pp. 367-382.
20. **Willam, K.J., and Warnke, E.P.,**
"Constitutive Model of the Triaxial Behaviour of Concrete", IABSE Seminar on Concrete Structures Subjected to Triaxial Stresses, Bergamo, Italy, 1974, pp. 1-30.
21. **Launay, P., and Gachon, H.,**
"Strain and Ultimate Strength of Concrete under Triaxial Stress", Paper 13, American Concrete Institute Special Publication, SP-34, 1972, pp. 269-282.
22. **Kotsovos, M.D.,**
"A Mathematical Description of the Strength Properties of Concrete under Generalised Stress", Magazine of Concrete Research, Vol.31, No.108, September 1979, pp. 151-158.
23. **Kotsovos, M.D.,**
"Failure Criteria for Concrete under Generalised Stress State", Ph.D. Thesis, University of London, 1974, p. 284.

24. Newman, J.B.,
"Criteria for Concrete Strength", Ph.D. Thesis,
University of London, 1973, p. 583.
25. Ottosen, N.S.,
"A Failure Criterion for Concrete", Journal of the
Engineering Mechanics Division, Proceedings of the ASCE,
Vol.103, No.EM4, August 1977, pp. 527-535.
26. Kupfer, H., Hilsdorf, H.K., and Rusch, H.,
"Behaviour of Concrete under Biaxial Stresses", Journal
of American Concrete Institute, Proceedings, Vol.66,
No.8, August 1969, pp. 656-666.
27. Balmer, G.G.,
"Shearing Strength of Concrete under Triaxial Stress -
Computation of Mohrs Envelope as a Curve", Structural
Research Laboratory Report No. SP-23, United State
Department of the Interior, Bureau of Reclamation,
Washington D.C., 1949.
28. Hsieh, S.S., Ting, E.C., and Chen, W.F.,
"An Elastic-Fracture Model for Concrete", Proceedings of
3rd Engineering Mechanics Division Special Conference,
ASCE, Austin, Texas, 1979, pp. 437-440.
29. Mills, L.L., and Zimmerman, R.M.,
"Compressive Strength of Plain Concrete under Multiaxial
Loading Conditions", Journal of American Concrete
Institute, Proceedings, Vol.67, No.10, August 1970,
pp. 802-807.
30. Launay, P., and Gachon, H., and Poiterin, P.
"Deformation et Resistance Ultime du Beton sous Etreinte
Triaxiale", Annals de l'Institut Technique du Batiment
et du Travaux Publics, No.269, May 1970, pp. 21-48.
31. Chen, E.Y.-T., and Schnobrich, W.C.,
"Material Modelling of Plain Concrete", IABSE
Colloquium, Advanced Mechanics of Reinforced Concrete,
Delft, Holand, 1981, pp. 33-51.

32. Nilsson, L., and Glemberg, R.,
"A Constitutive Model for Concrete in High Rate of Loading Conditions", IABSE Colloquium, Advanced Mechanics of Reinforced Concrete, Delft, Holand, 1981, pp. 185-200.
33. Chen, A.C.T., and Chen, W.F.,
"Constitutive Relations for Concrete", Journal of the Engineering Mechanics Division, Proceedings of the ASCE, Vol.101, No.EM4, August 1975, pp. 465-481.
34. Vile, G.W.D.,
"The Strength of Concrete Under Short-Term Static Biaxial Stress", The Structure of Concrete, Cement and Concrete Association, London, England, 1968, pp. 275-288.
35. Chen, W.F., Suzuki, H., and Chang, T.Y.,
"Analysis of Concrete Cylinder Structures under Hydrostatic Loading", Structural Engineering Report No. CE-STR-78-2, School of Civil Engineering, Purdue University, West Lafayette, Indiana, April 1978.
36. Chen, A.C.T., and Chen, W.F.
"Nonlinear Analysis of Concrete Splitting Test", Computers & Structures, Vol.6, 1976, pp. 451-457.
37. Chen, W.F., Suzuki, H., and Chang, T.Y.,
"Nonlinear Analysis of Concrete Cylinder Structures under Hydrostatic Loading", Computers & Structures, Vol.12, 1980, pp. 559-570.
38. Suzuki, H., and Chen, W.F.,
"Elastic-Plastic-Fracture Analysis of Concrete Structures", Computers & Structures, Vol.16, No.6, 1983, pp. 697-705.
39. Argyris, J.H., Faust, G., and Willam, K.J.,
"A Unified Stress-Strain Law for Triaxial Concrete Failure", 3rd Conference on Computational Aspects of the Finite Element Method, Imperial College, London, September 1975, pp. 359-401.

40. Hsieh, E.C., Ting, M., and Chen, W.F.,
"A Plastic-Fracturing Model for Concrete", Proceedings of ASCE National Convension, Holywood, Florida, 1980, pp. 50-64.
41. Kotsovos, M.D., and Newman, J.B.,
"Behaviour of Concrete under Multiaxial Stress", Journal of American Concrete Institute, Proceedings , Vol.74, No.9, September 1977, pp. 443-446.
42. Hsu, T.T.C., Slate, F.O., Sturman, G.M., and Winter, G.,
"Microcracking of Plain Concrete and the Shape of the Stress-Strain Curve", Journal of American Concrete Institute, Proceedings , Vol.60, No.2, February 1963, pp. 209-224.
43. Hsu, T.T.C.,
"Mathematical Analysis of Shrinkage Stresses in a Model of Hardened Concrete", Journal of American Concrete Institute, Proceedings , Vol.60, No.3, March 1963, pp. 371-390.
44. Buyukozturk, O., Nilson, A.H., and Slate, F.O.,
"Stress-Strain Response and Fracture of a Model of Concrete in Biaxial Loading", Journal of American Concrete Institute, Proceedings , Vol.68, No.8, August 1971, pp. 590-599.
45. Kotsovos, M.D., Newman, J.B.,
"Generalised Stress-Strain Relations for Concrete", Journal of the Engineering Mechanics Division, Proceedings of the ASCE, Vol.104, No.EM4, August 1978, pp. 845-856.
46. Kotsovos, M.D., Newman, J.B.,
"A Mathematical Description of the Deformational Behaviour of Concrete under Complex Loading", Magazine of Concrete Research, Vol.31, No.107, June 1979, pp. 77-90.
47. Chen, W.F.,
"Plasticity in Reinforced Concrete", McGraw-Hill Book Company, New York, 1982.

48. Drucker, D.C.,
"A Definition of Stable Inelastic Material", Journal of Applied Mechanics, Vol.26, 1959.
49. Drucker, D.C.,
"Some Implication of Work Hardening and Ideal Plasticity", Quarterly of Applied Mathematics, Vol.7, No.4, January 1950, pp. 411-418.
50. Chinn, J., and Zimmerman, R.M.,
"Behaviour of Plain Concrete under Various High Triaxial Compression Loading Conditions", Technical Report No. WL-TR-64-163 (AD468460), Air Force Weapons Laboratory, New Mexico, August 1965, p. 134.
51. Hobbs, D.W.,
"Strength and Deformation Properties of Plain Concrete Subjected to Combined Stress, Part 3 : Results Obtained on a Range of Flint Gravel Aggregate Concretes", Cement and Concrete Association, Technical Report 42.497, July 1974, p. 19.
52. Palaniswamy, R., and Shah, S.P.,
"Fracture and Stress-Strain Relation for Concrete under Triaxial Compression", Journal of the Structural Division, Proceedings of the ASCE, Vol.100, No.ST5, May 1974, pp. 901-916.
53. Akroyd, N.W.,
"Concrete under Triaxial Stress", Magazine of Concrete Research, Vol.13, No.39, November 1961, pp. 111-118.
54. Gardner, N.J.,
"Triaxial Behaviour of Concrete", Journal of American Concrete Institute, Proceedings, Vol.66, No.2, February 1969, pp. 136-146.
55. Launay, P., and Gachon, H.,
"Strain and Ultimate Strength of Concrete under Triaxial Stress", Paper H1/3, Proceedings of the first International Conference on Structural Mechanics in Reactor Technology, Berlin, Germany, September 1971, pp. 23-34.

56. Hobbs, D.W.,
"Strength and Deformation Properties of Plain Concrete Subjected to Combined Stress, Part 1 : Strength Results Obtained on one Concrete", Cement and Concrete Association, Technical Report 42.451, November 1970, p. 12.
57. Hobbs, D.W.,
"Strength and Deformation Properties of Plain Concrete Subjected to Combined Stress, Part 2 : Strength in Multiaxial Compression", Cement and Concrete Association, Technical Report 42.463, March 1972, p. 7.
58. Ahmad, S.H.,
"Properties of Confined Concrete Subjected to Static and Dynamic Loads", Ph.D. Thesis, University of Illinois, Chicago, Illinois, 1981.
59. Ahmad, S.H., and Shah, S.P.,
"Complete Triaxial Stress-Strain Curves for Concrete", Journal of the Structural Division, Proceedings of the ASCE, Vol.108, No.ST4, April 1982, pp. 728-742.
60. Green, S.J., and Swanson, S.R.
"Static Constitutive Relation for Concrete", Technical Report No. AFWL-TR-72-244 (AD761820), Air Force Weapons Laboratory, New Mexico, April 1973.
61. Ferrara, G., et. al.,
"Dispositivi di Prova per l'Analisi Sperimentale de Comportamento di Conglomerati Cementizi Sotoposti a Stati Triassiali di Sollecitazione", Presented at the 4th AIAS-Congress, Rome, Italy, October 1976.
62. Fung, Y.C.,
"Foundations of Solid Mechanics (Chapter 6), Prentice-Hall, Englewood Cliffs, New Jersey, 1975.
63. Lin, T.H.,
"Theory of Inelastic Structures", Wiley, New York, 1968.

64. **Malvern, L.E.,**
"Introduction to the Mechanics of a Continuous Medium",
Prentice-Hall, Englewood Cliffs, New Jersey, 1969.
65. **Martin, J.B.,**
"Plasticity : Fundamentals and General Results",
M.I.T. Press, Cambridge, Massachusetts, 1975.
66. **Kotsovos, M.D.,**
"A Mathematical Model of the Deformational Behaviour of
Concrete under Generalised Stress Based on Fundamental
Material Properties", *Materials and Structures, RILEM,*
Vol.13, No.76, July-August 1980, pp. 289-298.
67. **Kotsovos, M.D., and Newman, J.B.,**
"Mathematical Description of Deformational Behaviour of
Concrete under Generalised Stress Beyond Ultimate
Strength", *Journal of American Concrete Institute,*
Proceedings , Vol.77, No.5, 1980, pp. 340-346.
68. **Sorensen, S.I., Arensen, A., and Bergan, P.G.,**
"Nonlinear Finite Element Analysis of Reinforced
Concrete Structures Using Endochronic Theory",
P.G. Bergan et. al. (eds.), *Finite Element in Nonlinear
Mechanics* (Tapir Trondheim, 1978).
69. **Suidan, M., and Schnobrich, W.C.,**
"Finite Element Analysis of Reinforced Concrete",
*Journal of the Structural Division, Proceedings of the
ASCE, Vol.99, No.ST10, October 1973, pp. 2109-2122.*
70. **Ngo, D., and Scordelis, A.C.,**
"Finite Element Analysis of Reinforced Concrete Beams",
Journal of American Concrete Institute, Proceedings,
Vol.64, No.3, March 1967, pp. 152-163.
71. **Cedolin, L., and Dei Poli, S.,**
"Nonlinear Plane Stress Analysis of Reinforced Concrete
by the Finite Element Method", *Costruzioni in Cemento
Armato, Studi e Rendiconti, Politecnico di Milano,*
Vol. VIII, 1977, pp. 3-33.

72. Cedolin, L., and Dei Poli, S.,
"Finite Element Studies of Shear Critical Reinforced Concrete Beams", Journal of the Engineering Mechanics Division, Proceedings of the ASCE, Vol.103, No.EM3, June 1977, pp. 395-410.
73. Gervenka, V.,
"Inelastic Finite Element Analysis of Reinforced Concrete Panels under In-plane Loads", Ph.D. Thesis, University of Colorado, 1970.
74. Loov, R.,
"The Determination of Stresses and Deformation of Reinforced Concrete After Cracking", Proceedings of the Southampton, Civil Engineering Materials Conference, 1969, pp. 1257-1260.
75. Franklin, H.A.,
"Nonlinear Analysis of Reinforced Concrete Frames and Panels", Dissertation, University of California, Berkeley, 1970.
76. Zienkiewicz, O.C., Phillips, D.V., and Owen, P.R.J.,
"Finite Element Analysis of Some Concrete Nonlinearities. Theory and Examples", Proceedings of the Seminar 'Concrete Structures Subjected to Triaxial Stresses', Bergamo, Italy, May 1974.
77. Mueller, P.,
"Plastische Berechnung von Stahlbetonscheiben und Balken", Bericht Nr.83, Institut für Baustatik und Konstruktion, ETH-Zurich, July 1978.
78. Lin, C.S., and Scordelis, A.C.,
"Nonlinear Analysis of R/C Shells of General Form", Journal of the Structural Division, Proceedings of the ASCE, Vol.101, No.ST3, October 1975, pp. 523-537.
79. Bazant, Z.P., and Tsubaki, T.,
"Optimum Slip-Free Limit Design of Concrete Reinforcing Net", Journal of the Structural Division, Proceedings of the ASCE, Vol.105, No.ST2, April 1979, pp. 255-276.

80. Bazant, Z.P., and Gambarova, P.G.,
"Rough Cracks in Reinforced Concrete", Journal of the Structural Division, Proceedings of the ASCE, Vol.106, No.ST4, April 1980, pp. 819-842.
81. Gambarova, P.G.,
"On Aggregate Interlock Mechanism in Reinforced Concrete Plates with Extensive Cracking", IABSE Colloquium on Advanced Mechanics of Reinforced Concrete, Delft, Holland, 1981, pp. 106-134.
82. Chen., E.Y.-T., and Schnobrich, W.C.,
"Models for the Post-Cracking Behaviour of Plain Concrete under Short Term Monotonic Loading", Computers & Structures, Vol.13, 1981, pp. 213-221.
83. Walraven, J.C.,
"Experiments on Shear Transfer in Cracks in Concrete. Part II : Analysis of Results", Report No.5-79-10, Sterin Laboratory, Delft University of Technology, The Netherlands, November 1979.
84. Walraven, J.C.,
"Aggregate Interlock : A Theoretical and Experimental Analysis", Ph.D. Thesis, Delft University of Technology, The Netherlands, October 1980.
85. Loeber, P.J.,
"Shear Transfer by Aggregate Interlock", M.Eng. Thesis, University of Canterbury, Christchurch, New Zealand, 1970.
86. Paulay, T., and Loeber, P.J.,
"Shear Transfer by Aggregate Interlock", American Concrete Institutes Special Publication SP-42, 'Shear in Reinforced Concrete', Vol.I, 1974, pp. 1-16.
87. Walraven, J.C., Vos, E., and Reinhardt, H.W.,
"Experiments on Shear Transfer in Cracks in Concrete. Part I : Description of Results", Report No.5-79-3, Sterin Laboratory, Delft University of Technology, Delft, The Netherlands, 1979.

88. Friberg, B.F.,
"Load and Deflection Characteristics of Dowels in Transverse Joints of Concrete Pavements", Highway Research Board, Proceedings, Vol.18, Part I, 1940, pp. 154-173.
89. Walraven, J.C., and Reinhardt, H.W.,
"Theory and Experiments on the Mechanical Behaviour of Cracks in Plain and Reinforced Concrete Subjected to Shear Loading", 'Concrete Mechanics', Heron, Vol.26, No.1A, 1981.
90. Schaefer, H.,
"Anspruche des Konstrukteurs an den Beton", Beton 27, Nr.5, 1977, pp. 195-199.
91. Leonhardt, F.,
"Volesungen uber Massivbau", Viercer Teil, Nachweis der Gebrauchsfahigkeit, Springer Verlag, Berlin, Heidelberg, New York.
92. Dulacscka, H.,
"Dowel Action of Reinforcement Crossing Cracks in Concrete", Journal of American Concrete Institute, Proceedings, Vol.69, No.12, 1972, pp. 754-757.
93. Paulay, T., Park, R., and Phillips, M.H.,
"Horizontal Construction Joints in Cast-in-Place Reinforced Concrete", American Concrete Institute Special Publication, SP-42, 'Shear in Reinforced Concrete', Vol. II, 1974, pp. 599-616.
94. Eleiott, A.F.,
"An Experimental Investication of Shear Transfer Across Cracks in Reinforced Concrete", M.Sc. Thesis, Cornell University, Ithaca, June 1974.
95. Jager, K.
"Zur Theorie der Ri bildung im Stahlbetonbalken", Osterreichische Ingenieur - Zeitschrift, Vol.3, No.11, November 1960, pp. 357-363.

96. Scanlon, A.,
"Time Dependent Deflection of Reinforced Concrete Slabs", Ph.D. Thesis, University of Alberta, Edmonton, Alberta, Canada, 1971.
97. Gilbert, R.I., and Warnner, R.F.,
"Nonlinear Analysis of Reinforced Concrete Slabs with Tension Stiffening", UNICIV Report No.R-167, University of South Wales, Kensington, N.S.W., Australia, January 1977.
98. Mueller, G.,
"Numerical Problems in Nonlinear Analysis of Reinforced Concrete", UC-SESM Report No.77-5, University of California, Berkeley, September 1977.
99. Van Greunen, J.,
"Nonlinear Geometric, Material and Time-Dependent Analysis of Reinforced and Prestressed Concrete Slabs and Panels", UC-SESM Report No.79-3, University of California, Berkeley, October 1979.
100. Bazant, Z.P., and Oh, B.H.,
"Deformation of Cracked Net-Reinforced Concrete Walls", Journal of the Structural Engineering, Proceedings of the ASCE, Vol.109, No.1, January 1983, pp. 93-108.
101. Bazant, Z.P., and Cedolin, L.,
"Fracture Mechanics of Reinforced Concrete", Journal of the Engineering Mechanics Division, Proceedings of the ASCE, Vol.106, No.EM6, December 1980, pp. 1287-1306.
102. F.E.A. Ltd.,
"LUSAS User Manual", Finite Element Analysis Limited, Kingston upon Thames, England.
103. Irons, B.M.,
"A Frontal Solution Programme for Finite Element Analysis", Proceedings of International Journal of Numerical Methods in Engineering, Vol.2, 1970.

104. Nayak, G.C., and Zienkiewicz, O.C.,

"Elasto-Plastic Stress Analysis. A Generalisation for Various Constitutive Relations Including Strain Softening", Proceedings of International Journal of Numerical Method in Engineering, Vol.5, June 1972.

105. Burns, N.H., and Siess, C.P.,

"Load-Deflection Characteristics of Beam-Column Connection in Reinforced Concrete", Structural Research Series No.234, Civil Engineering Studies, University of Illinois, Urbana-Champaign, Illinois, January 1962.

106. Krahl, N.W., Khachaturian, N., and Siess, C.P.,

"Stability of Tensile Cracking in Concrete Beams", Journal of the Structural Division, Proceedings of the ASCE, Vol.93, No.ST1, February 1967, pp. 235-254.

107. Bresler, B., and Scordelis, A.C.,

"Shear Strength of Reinforced Concrete Beams - Series II", SESM Report No.64-2, University of California, Berkeley, May 1965.

108. Sozen, M.A., and Paul, S.L.,

"Structural Behaviour of a Small-Scale Prestressed Concrete Reactor Vessel", Nuclear Engineering and Design, Vol.8, 1968.

**109. Paul, S.L., Sozen, M.A., Schnobrich, W.C.,
Karlsson, B.I., and Zimmer, A.,**

"Strength and Behaviour of Prestressed Concrete Vessels for Nuclear Reactors - Volume I and II", Report No. W-7405-ENG-26, University of Illinois, Urbana, Illinois, July 1969